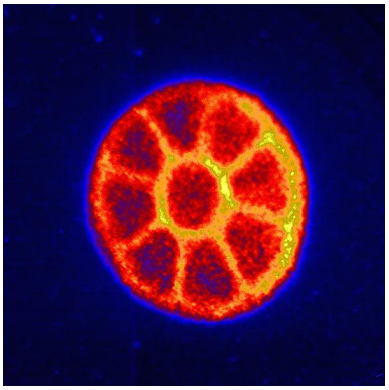

Measurement and Modelling of Intrabeam Coulomb Interactions in Ultracold Ion Bunches

Dene Murphy

ORCID: 0000-0002-6829-8291

Submitted in total fulfilment of the requirements
of the degree of Doctor of Philosophy

February 2017

School of Physics
The University of Melbourne

Supervised by Prof. Robert E. Scholten and Dr Ben M. Sparkes

Cover image: The ‘wagon wheel’, a two-dimensional projection of the charge density of an ultracold ion bunch in the plane transverse to its propagation direction, measured with a phosphor-coupled microchannel plate detector. This image was the first clear demonstration of the use of a cold-atom ion source as a platform for the investigation of space-charge effects. False-colour mapping provided by D. V. Sheludko for data presented in Fig. 2.3. [Electronic copy: provides a clickable shortcut to the table of contents.]

Abstract

Control of Coulomb-induced emittance growth in charged particle beams is of critical importance for applications including electron and ion microscopy, injectors for particle accelerators and in ultrafast electron diffraction, where Coulomb effects constrain the temporal and spatial imaging resolution. The development of techniques to prevent space-charge and disorder-induced emittance growth has been limited by the masking effect of thermal diffusion in conventional beams. In this thesis it is shown that ion bunches from a cold-atom electron and ion source can be used to observe the effects of intrabeam Coulomb interactions with unprecedented detail. Experiments are performed using nanosecond-duration cold ion bunches, which provide data for analogous ultrafast electron systems where the dynamics occur on timescales too short for detailed observation.

Cold ion bunches were produced by photoionising a laser-cooled gas. The intensity profile of the photoionising lasers was controlled using a spatial light modulator, which allowed for shaping of the spatial charge density distribution of the ion bunches. Nonlinear space-charge expansion dynamics were observed in the propagation of the ion bunches. Certain aspects of the observed dynamics were inconsistent with initial modelling attempts. In particular, high-density rings were formed in the transverse density distribution, which were not predicted in particle tracking simulations for the calculated initial ion distributions. Through detailed modelling, it was determined that the rings form in the interaction of the expanding ion beam with a diffuse 'fluorescence halo' of ions. The fluorescence halos were formed by reabsorption of fluoresced light from the sequential photoexcitation and ionisation process. Modelling of the photoexcitation process and particle-tracking simulations reproduced the experimentally observed beam dynamics, confirming the hypothesis of halo formation. The nonlinear transformation of the beam density profile leading to the formation of the fluorescence halo rings is indicative of loss of beam coherence. The fluorescence halo rings were suppressed by controlling the duration of laser overlap during photoionisation, where a shorter overlap reduces the time available for absorp-

tion of fluorescence. Fluorescence halo rings are an issue specific to atomic-gas based sources, but serve as an example of a nonlinear space-charge effect that is observable only because of the non-diffusive cold propagation of the ions. Efforts towards reconstruction of the beam dynamics leading to the ring formation were used to show that the cold ion bunches can be used as a platform to observe space-charge dominated beam dynamics in analogue of high-brightness and ultrafast electron beams.

The cold ion beams were then used as a platform to investigate methods to overcome space-charge-induced beam-quality limitations. Modelling and experimental efforts were contributed to proof-of-principle experiments that demonstrated linearisation of the space-charge effects through beam-shaping. The ion bunches were shaped to uniform transverse distributions to linearise the internal electric field, suppressing the nonlinear space-charge effect. Improvements to the focusing properties of the shaped ion beams were measured, as compared to unshaped bunches, directly demonstrating improvement of beam quality through beam shaping for the first time in any charged particle beam.

Beyond the linearisable space-charge effects are statistical disorder-induced heating (DIH) effects, which set lower-bound achievability limits on particle beam temperature. Models of the DIH process were used to predict the degree to which DIH can be suppressed in cold ion bunches by introducing interparticle spatial correlations in the cold atoms prior to ionisation. Two different methods of introducing correlations were modelled: first, by exploiting the Rydberg blockade effect in the photoexcitation process to excite and ionise atoms with hard-sphere type spatial correlations limited by close-packing effects; and second, by loading the atoms into optical lattices, which have crystalline structural correlations, limited by partial-filling effects. The models predicted that the heating can be significantly suppressed in the cold ion bunches for experimentally achievable degrees of spatial correlation using either of the two correlation methods.

Excitation of Rydberg atoms was implemented in the cold-atom ion source, towards achieving the improvement of beam quality predicted by the DIH modelling. Spectroscopy based on electromagnetically-induced transparency was used to tune photoionising lasers to resonance with Rydberg states. A method was presented for suppressing the formation of fluorescence halos during Rydberg excitation, by using intermediate-state-decoupled stimulated Raman adiabatic passage to excite Rydberg atoms while bypassing population of the fluorescent intermediate state in sequential (ladder) photoexcitation. Measurements of the blockaded photoexcitation dynamics of the Rydberg ion bunches established the

presence of spatial correlations, to a degree consistent with a sevenfold increase in beam brightness compared to a disordered distribution, according to the DIH models.

The models, simulations, methods and measurements presented in this thesis guide the development of charged particle beams towards attaining the necessary coherence, focusability, and brightness to perform single-shot ultrafast electron diffraction of biological molecules. In a surprising twist, slow atoms may underpin progress in high energy and ultrafast physics.

Declaration

I declare that:

i. the thesis comprises only my original work towards the PhD except where indicated in the preface;

ii. due acknowledgement has been made in the text to all other material used;

iii. the thesis is fewer than 100,000 words in length, exclusive of tables, maps, bibliographies and appendices.

Dene Murphy

Preface and acknowledgements

This thesis presents the research contributions of the author (DM) to the published articles included in Appendix A. This preface details the contributions of the author to the work described in each chapter, and that of other members and associates of the Melbourne Atom Optics Group: Simon C. Bell (SCB), Mark Junker (MJ), Andrew J. McCulloch (AJM), Corey T. Putkunz (CTP), Sebastian D. Saliba (SDS), Robert E. Scholten (RES), David V. Sheludko (DVS), Ben M. Sparkes (BMS), Rory W. Speirs (RWS), Richard J. Taylor (RJT), Joshua S. J. Torrance (JSJT), Daniel J. Thompson (DJT) and Rick M. W. van Bijnen (RMWvB). The work in the thesis was supervised and overseen by BMS and RES.

Chapter 1 presents an original review into the development of the cold-atom electron and ion source, and its limitations due to intrabeam Coulomb interactions. The chapter gives an overview of the functions of the Melbourne source, which was originally designed and constructed by SCB, MJ, AJM, SDS and DVS, with later significant modifications and upgrades by CTP, BMS and RWS.

Chapter 2 describes efforts towards measuring and suppressing space-charge effects using cold ions. I performed the experiments of Sec. 2.1.1 with assistance from DVS, CTP and AJM, and in Sec. 2.1.3 with equal contribution in experimental design, execution and analysis from RWS. I developed the models of ion beam laser shaping, and conducted simulations based upon original code provided by CTP, through which I discovered the mechanism of fluorescence halo formation. The work in Sec. 2.3 expands upon preliminary investigations presented in my MSc thesis; the data presented in Fig. 2.3 appeared there originally, all other work presented in the chapter was conducted during the PhD.

Section 2.2 presents investigation of the effects of beam shape on beam focusability in cold ions, as established in Sec. 2.1. The work described in Sec. 2.2 forms part of a published study included as appendix A.5, for which DJT is the principal author. For the elements of that publication that appear in this thesis, I contributed to the design of the experiments, calculations of beam shape

properties, and provided the initial code to simulate the beam propagation. The simulations were performed by DJT, BMS and RWS. Shaping of the laser intensity distributions was performed by BMS and DJT, with code provided by RMWvB. I, BMS and DJT performed the experimental measurements of beam focusability.

Chapter 3 presents modelling and simulation of the effect of spatial correlations on the disorder-induced heating of cold ion bunches. All work presented in the chapter is my own.

Chapter 4 presents implementation of Rydberg-atom excitation in the cold ion source. Section 4.1 describes the excitation of Rydberg atoms in the ion source, in which I performed calculations of laser frequencies and modelling of the electromagnetically-induced transparency effect, which was implemented in a spectroscopy system that I, RJT and BMS constructed. Section 4.2 details investigations of the Rydberg blockade effect in the cold ion bunches, in which I performed calculations of the blockade dynamics and degrees of correlation, and performed experiments with RJT and BMS. Section 4.3 describes a method for preventing formation of the fluorescence halos described earlier (Sec. 2.1) based upon stimulated Raman adiabatic passage, in which I present my original calculations of the effect, and experiments led by BMS, with contributions from myself and RJT. BMS performed the calculations of the transfer efficiencies and interpretation of the experimental data in Fig. 4.10 and 4.11.

This work was supported by the Australian Research Council Centre of Excellence for Coherent X-Ray Science, Australian Research Council Discovery Projects DP1096025 and DP140102102, an Australian Postgraduate Award, the Australian Government Research Training Scheme and an Australian Government Research Training Program Scholarship.

Personal acknowledgements go to each member of the Melbourne Atom Optics group, with whom I have spent a good chunk of my 20s. Thanks to Ben, Andy, Corey and Dave for teaching me a thing or two about how to get things done. Thanks to my officemates, my friends and my colleagues in the School of Physics for all the good times. Thanks to Rob for your guidance, advice and patience, and for the space and trust you've given me to pursue these ideas in my own (at times haphazard) way. Thanks to my parents, Charuwan and Dale, who raised me to be huge nerd in their own image. And, to my Justiney, thank you, you are the best.

Table of contents

List of figures

List of publications

The following publications and presentations resulted from work leading to the PhD. The contributions of each author towards work included in the thesis are described in the preface. Copies of the publications are included in App. A.

Peer reviewed publications

- D. Murphy, R. W. Speirs, D. V. Sheludko, C. T. Putkunz, A. J. McCulloch, B. M. Sparkes & R. E. Scholten, 'Detailed observation of space-charge dynamics using ultracold ion bunches', *Nature Communications* **5**:4489 (2014). [Ref. [1], discussed in Ch. 2 and included as App. A.1]

- D. Murphy, R. E. Scholten & B. M. Sparkes, 'Increasing the brightness of cold ion beams by suppressing disorder-induced heating with Rydberg blockade', *Physical Review Letters* **115**, 214802 (2015). [Ref. [2], discussed in Ch. 3 and included as App. A.2]

- D. Murphy & B. M. Sparkes, 'Disorder-induced heating of ultracold neutral plasmas created from atoms in partially filled optical lattices', *Physical Review E - Rapid Communications* **94**, 021201(R) (2016). [Ref. [3], discussed in Ch. 3 and included as App. A.3]

- B. M. Sparkes, D. Murphy, R. J. Taylor, R. W. Speirs, A. J. McCulloch & R. E. Scholten, 'Stimulated Raman adiabatic passage for improved performance of a cold-atom electron and ion source', *Physical Review A* **94**, 023404 (2016). [Ref. [4], discussed in Ch. 4 and included as App. A.4]

- D. J. Thompson, D. Murphy, R. W. Speirs, R. M. W. van Bijnen, A. J. McCulloch, R. E. Scholten & B. M. Sparkes, 'Suppression of emittance growth using a shaped cold atom electron and ion source', *Physical Review Letters* **117**, 193202 (2016). [Ref. [5], discussed in Ch. 2 and included as App. A.5]

- B. M. Sparkes, D. J. Thompson, A. J. McCulloch, D. Murphy, R. W. Speirs, J. S. J. Torrance & R. E. Scholten, 'High-coherence electron and ion bunches from laser-cooled atoms', *Microscopy and Microanalysis* **20**, 1008 (2014). [Ref. [6], included as App. A.6]

Selected presentations

- D. Murphy, A. J. McCulloch, R. E. Scholten, and B. M. Sparkes, 'Rydberg Blockaded Ion Beams: Fundamental Beam Science With Cold Atoms', The Australian and New Zealand Conference on Optical Physics, Adelaide SA, Australia, November 2015

- D. Murphy, D. J. Thompson, R. W. Speirs, R. J. Taylor, J. S. J. Torrance, A. J. McCulloch, B. M. Sparkes & R. E. Scholten, 'Ultracold electron and ion beams from cold gases: Beating Coulomb effects with beam shaping and Rydberg blockade', invited talks given at William Marsh Rice University, Houston TX, and at University of Wisconsin–Madison, Madison WI, USA, August 2015

- R. E. Scholten, D. Murphy, R. W. Spiers, D. J. Thompson, J. S. J. Torrance, R. J. Taylor, A. J. McCulloch & B. M. Sparkes, 'Ultracold electron and ion bunches via Rydberg excitation and blockade', International conference on Rydbergs at Durham, Durham, UK, June 2015

- D. Murphy, R. W. Speirs, R. J. Taylor, D. V. Sheludko, C. T. Putkunz, A. J. McCulloch, B. M. Sparkes & R. E. Scholten, 'Space-charge and disorder in ultra-cold ion bunches', Australian Institute of Physics Congress, Canberra, ACT Australia, December 2014

- B. M. Sparkes, D. Murphy, R. J. Taylor, R. W. Speirs, D. J. Thompson & R. E. Scholten, Poster: 'Cold Atom Electron/Ion Source with Rydberg Blockade and Electromagnetically Induced Transparency' 45th Annual Meeting of the APS Division of Atomic, Molecular and Optical Physics, Madison, Wisconsin, USA, June 2014

- R. E. Scholten, D. Murphy, R. W. Speirs, D. J. Thompson, B. M. Sparkes & A. J. McCulloch, Poster: 'Space-charge dynamics in ultra-cold ion bunches', 45th Annual Meeting of the APS Division of Atomic, Molecular and Optical Physics, Madison WI, USA, June 2014

- B. M. Sparkes, D. Murphy, R. J. Taylor, R. W. Speirs & R. E. Scholten, 'Ultracold Ion Source with Rydberg Blockade', Australian and New Zealand Conference on Optics and Photonics, Fremantle WA, Australia, December 2013

- D. Murphy, D. V. Sheludko, C. T. Putkunz, A. J. McCulloch & R. E. Scholten, Poster: 'Study of Space-charge dynamics in ultra-fast electron beams using cold ions', International Conference on Laser Spectroscopy, Berkeley CA, USA, June 2013

Chapter 1

Introduction

Charged particle beams underpin progress in many areas of the physical sciences, with applications ranging from high-resolution imaging of biological molecules, to the production and investigation of exotic particles in high-energy collider experiments. Each application is limited by the achievable quality of its charged particle beam, which is in turn fundamentally limited by the charged nature of its particles. This introductory chapter outlines the development of cold-atom based sources of charged particles in which low beam temperature leads to high beam quality, approaching the fundamental limit due to interparticle Coulomb interactions.

1.1 Charged particle beam applications

Beams of electrons and ions have applications for a wide range of beam energies and beam durations. At the low energy scale are focused ion beams and electron microscopes, operating in the 100 keV range with continuous beam current. Focused ion beams are used to manipulate and image matter at the nanometre scale, and are a key system in the semiconductor industry, which requires continually decreasing focal sizes for the miniaturisation of circuit components [7]. State of the art electron cryomicroscopy is used in the structural determination of single biological molecules and proteins for drug design in the pharmaceuticals industry [8, 9]. To achieve atomic resolution, electron and ion microscopes typically image static samples using continuous exposure to the beam, with long exposure times, limiting their applicability to the imaging of dynamic processes.

The 'holy grail' of imaging is ultrafast single-shot coherent diffraction of dynamic structural changes of single molecules. Progress towards this goal has been

made using x-ray free-electron lasers [10], which use high-energy bunched electron beams to produce quasi-coherent x-ray light pulses. The scientific paradigm of research into ultrafast atomic-resolution imaging using electron beams, on the other hand, is the development of stroboscopic single-electron diffraction [11–13]. Developments towards ultrafast imaging have been made using short-duration electron bunches [14, 15], but at present these electron sources have insufficient phase-space density for single-molecule and single-shot imaging. The coherence of bunched electron beams is ultimately limited by the self-field interactions of electrons within the beam, where inter-electron scattering and repulsion can turn a coherent wavefield, akin to a laser beam, into an incoherent wavefield, as from a lightbulb [16].

1.2 Beam emittance considerations

The common desirable quality of charged particle beams in each of their applications is that the beams are highly focusable. Focusability determines probe size for electron and ion microscopes, and is equivalent to (and a result of) beam coherence for electron diffraction, synchrotrons and x-ray free-electron lasers.

The focusability of a charged particle beam is determined by its beam *emittance*. Emittance is the area of a beam's transverse axial position and velocity phase-space profile. In analogy with light optics, charged particle optics can be described as performing linear transformations on beam phase-space [17, 18]. Focusing of an expanding beam by a lens, for example, corresponds to a reflection in a transverse beam velocity axis as illustrated in Fig. 1.1. A beam with uncorrelated spread in its particles' positions and transverse velocities has limited focusability. Arbitrarily small focal spot sizes can be achieved only for beams with a linear relationship between their particles' axial position and velocity, and thus zero phase-space area.

The phase-space area occupied by a beam can be quantified by its emittance, which is defined by convention in normalised root-mean-square (RMS) form [18]

$$\epsilon_\mu = \frac{1}{c}\sqrt{\langle \mathrm{x}_\mu^2 \rangle \langle \mathrm{v}_\mu^2 \rangle - \langle \mathrm{x}_\mu \mathrm{v}_\mu \rangle^2} \tag{1.1}$$

in each spatial axis μ, where c is the speed of light and the delimiters $\langle\,\rangle$ denote averages over the beam particles for quantities involving the μ-axis components of the particle positions, x_μ, and velocities v_μ.

For an axis μ orthogonal to the direction of beam propagation with a beam-

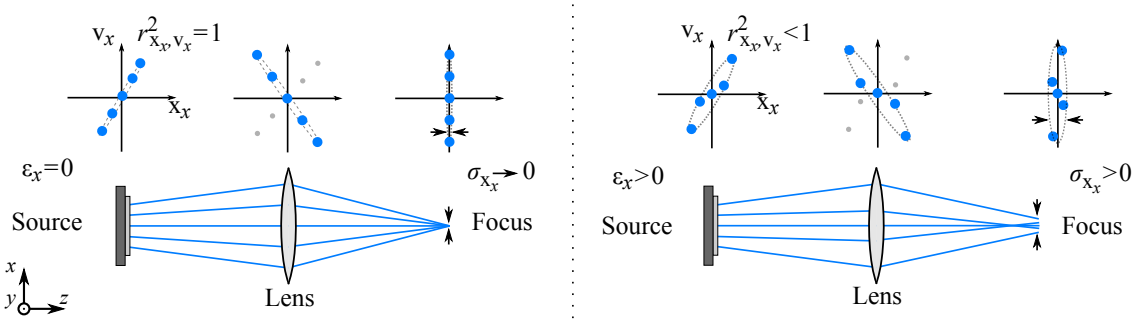

Figure 1.1: Beam phase-space, emittance and focusability. Left: A beam with a linear transverse position and velocity phase space profile and zero emittance, that can be focused to an arbitrarily small spot size, given an aberration-free linear lens. Right: A beam with nonlinear phase-space profile, which cannot be focused by the linear-transformation to its profile imparted by the lens.

centred origin, so that $\langle \mathrm{v}_\mu \rangle = 0$ and $\langle \mathrm{x}_\mu \rangle = 0$, the transverse emittance can be written as

$$\epsilon_\mu = \frac{1}{c}\sigma_{\mathrm{x}_\mu}\sigma_{\mathrm{v}_\mu}\sqrt{1 - r^2_{\mathrm{x}_\mu,\mathrm{v}_\mu}}, \tag{1.2}$$

which uses the RMS beam size $\sigma_{\mathrm{x}_\mu} = \sqrt{\langle \mathrm{x}_\mu^2 \rangle - \langle \mathrm{x}_\mu \rangle^2}$, transverse velocity spread $\sigma_{\mathrm{v}_\mu} = \sqrt{\langle \mathrm{v}_\mu^2 \rangle - \langle \mathrm{v}_\mu \rangle^2}$ and the Pearson product-moment correlation coefficient measuring the linearity of the phase space profile

$$r_{\mathrm{x}_\mu,\mathrm{v}_\mu} = \frac{\sum^N (\mathrm{x}_\mu - \langle \mathrm{x}_\mu \rangle)(\mathrm{v}_\mu - \langle \mathrm{v}_\mu \rangle)}{\sqrt{\sum^N (\mathrm{x}_\mu - \langle \mathrm{x}_\mu \rangle)^2}\sqrt{\sum^N (\mathrm{v}_\mu - \langle \mathrm{v}_\mu \rangle)^2}}, \tag{1.3}$$

where the sums are taken over the x_μ and v_μ quantities of all N particles in the beam, which reduces to

$$r_{\mathrm{x}_\mu,\mathrm{v}_\mu} = \frac{\langle \mathrm{x}_\mu \mathrm{v}_\mu \rangle}{\sqrt{\langle \mathrm{x}_\mu^2 \rangle \langle \mathrm{v}_\mu^2 \rangle}} \tag{1.4}$$

for the chosen coordinates.

Transverse emittance has units of m·rad, where division of the transverse beam velocity spread by the normalisation factor c gives the angular spread for a beam travelling at c using a small-angle approximation. The transverse emittance thereby determines the minimum achievable focal spot size for a beam. At a beam waist, $r_{\mathrm{x}_\mu,\mathrm{v}_\mu} = 0$, as there is no correlation between transverse position and velocity, as shown in Fig. 1.1, so that the emittance becomes the product of the normalised angular divergence (i.e. focusing angle) and beam size.

In the absence of nonlinear electric fields, for example lens aberrations that would distort the distribution in phase-space, beam emittance is a conserved quantity determined by the emission area and uncorrelated velocity spread (i.e.

temperature) of the particle source. By defining a reduced velocity spread

$$\tilde{\sigma}_{\mathrm{v}_\mu} = \sigma_{\mathrm{v}_\mu}\sqrt{1 - r^2_{\mathrm{x}_\mu,\mathrm{v}_\mu}} \tag{1.5}$$

and an axial beam temperature

$$T_\mu = \frac{m\tilde{\sigma}^2_{\mathrm{v}_\mu}}{k_\mathrm{B}}, \tag{1.6}$$

the emittance can be conveniently simplified to

$$\epsilon_\mu = \frac{\sigma_{\mathrm{x}_\mu}}{c}\sqrt{\frac{k_\mathrm{B}T_\mu}{m}}. \tag{1.7}$$

The axial temperature is equal to the emission temperature at the source, prior to expansion, and represents the uncorrelated component of the velocity spread. Minimisation of source emittance to achieve narrow focal spot sizes therefore requires small emission area or low emission temperature.

Low emittance and high focusability is achieved in electron microscopes using field-emission sources, which emit electrons from a very small emission area at the tip of a sharpened tungsten needle [19]. Focused ion beams achieve small spot sizes using field-emission liquid metal ion sources, which emit ions from a metallic needle 'wick' drawing liquid metal, typically gallium, to its tip [7]. Field-emission sources provide beams with the high focusability required for static imaging, or for ultrafast stroboscopic imaging [20], but have limited current and are unable to produce bunched beams required for single-shot imaging, due to the small emission area.

Ultrafast single-shot diffraction studies using electron beams, synchrotron light sources and free-electron lasers require high-current, short-duration electron bunches. These applications typically use photocathode sources that emit electrons at high temperature over large areas, therefore having high emittance and poor source-limited coherence [21, 22]. Applications requiring bunches of ions, for example mass spectrometers and particle collider experiments, use high-temperature plasma-based ion sources [23, 24]. Plasma sources produce ion bunches by ionisation of a solid or gas by electron impact, laser or field ionisation, resulting in high temperature and limited focusability.

The common figure of merit for beams requiring high current and low emittance is the transverse beam brightness, the beam flux density per unit solid

angle, expressed in terms of the beam current I and transverse emittances as [25]

$$B = \frac{I}{4\pi^2 \epsilon_x \epsilon_y}, \tag{1.8}$$

where x and y denote axes orthogonal to the beam propagation axis, z. The brightness of bunched beams is limited by the properties of conventional electron and ion sources, in that to achieve high current and short duration requires both high temperature and large emission area, and thus high emittance. Furthermore, at high charge densities Coulomb interactions can cause heating of a beam after its creation, and thus emittance growth.

1.3 Intrabeam Coulomb effects

At high charge densities, required for time-resolved imaging and beam focusing, the interactions between the charged particles affect beam behaviour in ways that do not occur in light-beams. For a system of N charged particles with positions $\mathbf{x}_i$, masses m_i and charges q_i, where the index $i \in \{1, 2, ..., N\}$ denotes quantities for each ion, the equations of motion are given by Coulomb's law,

$$\frac{d^2\mathbf{x}_i}{dt^2} = \sum_{j \neq i}^{N} \frac{q_i q_j}{4\pi\varepsilon_0 m_i} \frac{(\mathbf{x}_i - \mathbf{x}_j)}{|\mathbf{x}_i - \mathbf{x}_j|^3}, \tag{1.9}$$

where ε_0 is the permittivity of free space. Repulsive interactions in a charged particle beam lead to beam expansion, increasing the focal spot size and beam duration, and while doing so can cause emittance growth, limiting the ability for charged-particle optics to refocus the beam [26].

The degree to which Coulomb interactions impact beam behaviour can be classified using the Debye length in a transverse axis [18],

$$\lambda_{\mathrm{D}} = \frac{\tilde{\sigma}_{\mathrm{v}_\mu}}{\omega_p}, \tag{1.10}$$

the distance over which thermal motion is unperturbed by Coulomb interactions, determined by the thermal reduced velocity $\tilde{\sigma}_{\mathrm{v}_\mu}$ (Eq. 1.5) and the plasma frequency,

$$\omega_p = \sqrt{\frac{ne^2}{\varepsilon_0 m}}, \tag{1.11}$$

which is the characteristic frequency at which particle trajectories are deflected due to Coulomb interactions within a plasma of particle number density n. With

substitution of Eq. 1.6 and 1.11 into Eq. 1.10, λ_D can be written in terms of axial temperature and charge density as

$$\lambda_\mathrm{D} = \sqrt{\frac{\epsilon_0 k_\mathrm{B} T_\mu}{n e^2}}. \tag{1.12}$$

A beam of transverse RMS size σ_{x_μ} is said to be thermally dominated when $\lambda_\mathrm{D} > \sigma_{\mathrm{x}_\mu}$, as thermal motion of the particles is unperturbed by Coulomb interactions over the length scale of the beam size. At low beam temperatures, high beam densities or small transverse beam sizes the Coulomb interactions occur in two distinct classes: space-charge effects and statistical-Coulomb effects.

1.3.1 Space-charge effects

When $\lambda_\mathrm{D} < \sigma_{\mathrm{x}_\mu}$ beam behaviour is space-charge dominated, as the motion of individual particles is strongly perturbed by the spatial charge density of the beam. The evolution of a space-charge dominated beam is dependent on its shape, where density non-uniformities lead to nonlinearities in the space-charge fields and thus to emittance growth. Approximating the beam with a smooth, continuous charge density ρ allows calculation of the electric field $\mathbf{E}$ via Gauss's law

$$\nabla \cdot \mathbf{E} = \frac{\rho}{\varepsilon_0}. \tag{1.13}$$

An example of a density distribution with nonlinear internal fields is a three-dimensional (3D) Gaussian, which could result from thermal diffusion of particles from their source or, for photocathodes, the Gaussian intensity distribution of the laser that induces electron emission. The electric field within a three-dimensional (3D) Gaussian distribution containing charge Q with equal RMS sizes in each axis, $\sigma_{\mathrm{x}_i} = \sigma_{\mathrm{x}_j} = \sigma_{\mathrm{x}_k} \equiv \sigma_\mathrm{x}$, at a position $\mathbf{x} = \mathrm{x}_i\hat{\mathbf{i}} + \mathrm{x}_j\hat{\mathbf{j}} + \mathrm{x}_k\hat{\mathbf{k}}$, where $\hat{\mathbf{i}}$, $\hat{\mathbf{j}}$ and $\hat{\mathbf{k}}$ are orthonormal coordinate axes, is

$$\mathbf{E}_\mathrm{Gauss}(\mathbf{x}) = \frac{Q}{(2\pi)^{3/2}\,\varepsilon_0 \sigma_\mathrm{x}^2 |\mathbf{x}|^2}\left[\sqrt{\frac{\pi}{2}}\,\mathrm{erf}\left(\frac{|\mathbf{x}|}{\sqrt{2}\sigma_\mathrm{x}}\right) - |\mathbf{x}|\exp\left(-\frac{|\mathbf{x}|^2}{2\sigma_\mathrm{x}^2}\right)\right]\hat{\mathbf{x}}. \tag{1.14}$$

The nonlinear relationship between the electric field strength and particle position (illustrated in Fig. 1.2) for a Gaussian distribution leads to nonlinear distortion of the phase-space profile, and emittance growth.

In contrast to a Gaussian distribution, a uniformly-filled spherical distribution has a linear internal electric field. For a sphere containing charge Q with RMS size σ_x in each dimension (i.e. within a spherical boundary of radius $\sqrt{5}\,\sigma_\mathrm{x}$), the

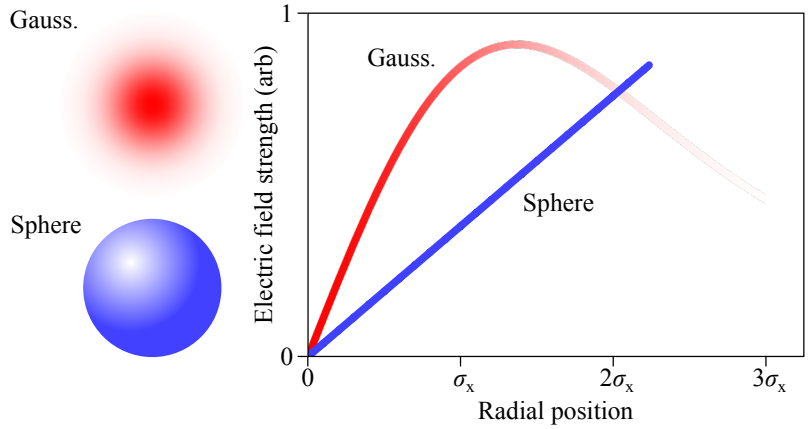

Figure 1.2: Electric field strength within 3D Gaussian and spherical charge distributions of equal charge and equal RMS bunch size σ_x in each dimension. The red-to-white colour map for the Gaussian curve indicates the relative charge density for the radial position in the horizontal plot axis.

linear internal electric field is

$$\mathbf{E}_{\text{sphere}}(\mathbf{x}) = \frac{Q\,|\mathbf{x}|}{4\pi\varepsilon_0 5^{3/2}\sigma_x^3}\,\hat{\mathbf{x}}, \tag{1.15}$$

for $|\mathbf{x}| < \sqrt{5}\,\sigma_x$. Spherical distributions also have a unique property that the component of the electric field along an axis $\hat{\mathbf{i}}$, $\mathbf{E}_i = Q\mathrm{x}_i/(4\pi\varepsilon_0 5^{3/2}\sigma_x^3)\,\hat{\mathbf{i}}$, is dependent only on the axial position x_i and not on the positions in the other orthogonal axes, x_j and x_k. Together, the axial independence and field linearity lead to emittance conservation and self-similar expansion. These properties generalise to ellipsoidal distributions, which have unequal RMS sizes in each dimension. Hard-edged, uniformly-filled, three-dimensional ellipsoidal distributions are the theoretically ideal distributions for a bunched beam [27], but their creation is challenging because conventional photocathode or field-emission sources are two-dimensional emitters.

Luiten et al. [28] proposed a method for the creation of ellipsoidal bunches in photocathode sources, through shaping of the laser intensity profile and therefore the emitted electron bunch density to a 'pancake' transverse radial distribution

$$\rho(r) \propto \sqrt{1 - \left(\frac{r}{R}\right)^2}, \tag{1.16}$$

where r is the transverse radial coordinate, and R is the radial extent of the pancake in the transverse plane. The pancake distribution is a two-dimensional projection of a three-dimensional ellipsoid. When a pancake-distributed bunch is created and accelerated in a short time, so that its length along the propagation direction is small compared to its transverse radius, simulations showed

expansion into a three-dimensional ellipsoid with linear space-charge forces and minimal emittance growth. Another related technique for creating ellipsoidal bunches is the temporal shaping of the laser pulse intensity to create a 'cigar' bunch, with a parabolic temporal profile

$$\rho(t) \propto 1 - \left(\frac{2t}{\tau}\right)^2, \tag{1.17}$$

where τ is the full temporal length of the laser pulse, and with a transverse laser beam size much less than the longitudinal beam length $c\tau$ so that the electron bunch also is longer than it is wide. Cigars, like pancakes, are a projection of the 3D ellipsoidal distribution, but onto a one-dimensional line in the beam propagation direction, and also expand under space-charge forces to form full ellipsoids.

Pancake and cigar bunches have since been created in photocathode electron sources [29–33], but the predicted improvements in brightness associated with the technique have so far not been measured. Conventional sources produce electron bunches which are too hot for nonlinear space-charge effects to be observed in isolation from thermal effects. Space-charge effects are predicted to become the limiting factor for improvements to source brightness, and so it is necessary to conduct proof-of-principle experiments to establish and refine bunch-shaping techniques.

1.3.2 Statistical Coulomb effects

At extremely low beam temperatures, when the Debye length λ_D is less than the average interparticle separation given by the Wigner-Seitz radius

$$a = \left(\frac{3}{4\pi n}\right)^{1/3}, \tag{1.18}$$

particle trajectories are perturbed more by the fields of their nearest-neighbour particles than by the space-charge fields. Beam behaviour in this case is dominated by statistical effects depending on the degree of interparticle spatial correlations.

In electron microscopes and focused ion beams, particles are emitted from a small region at a field-emitting tip, producing a beam with narrow transverse size but random longitudinal particle separation due to the uncorrelated emission times. The irregularity of the separations leads to unpredictable interparticle

scattering, broadening the beam energy spread and spot size at the beam focus, and limitation of the usable beam current [34].

At the high beam densities required for ultrafast, single-shot diffraction and for injection into particle accelerators, disorder-induced heating (DIH) at the beam source limits the achievable beam brightness [35]. Particles emitted into a vacuum with uncorrelated positions repel each other to minimise their interparticle potential energy, gaining thermal kinetic energy and increasing the beam emittance. In a conventional particle source, such as a photocathode electron source, DIH is negligible compared to space charge effects due to the non-uniformity of the charge distribution, and to thermal effects due to the initially high source temperatures. But, because of DIH, efforts to reduce photocathode emittance by decreasing the source temperature and space-charge nonlinearity will be fundamentally limited by source disorder. Maxson et al. [36] wrote:

> '...we expect disorder induced heating to become a major limiting factor in the next generation of photoemission sources delivering dense bunches and employing ultra-cold photoemitters... The full degree to which the effects of DIH can be mitigated remains an open question.'

To overcome the limitations imposed by DIH, it would be necessary to create a beam without disorder in the initial spatial distribution of its particles, which is presently beyond the capability of photocathode electron sources. Demonstrating the suppression of DIH and space-charge-induced emittance growth would therefore be a major milestone in the development of charged-particle beam sources. Progress towards such a demonstration, using a cold-atom ion source, is the major outcome of this thesis.

1.4 Cold-atom electron and ion sources

The cold-atom electron and ion source (CAEIS) was first proposed in 2005 as a method of producing high coherence ultrafast electron bunches [37] and focusable ions [38], using low emission temperature to achieve low emittance. These sources are based upon the photoionisation of a laser-cooled gas to produce an ultracold plasma (UCP), from which an electron or ion beam is extracted using an accelerating electric field. Control over the laser and atom interaction gives control over the beam temperature and emittance, providing the potential

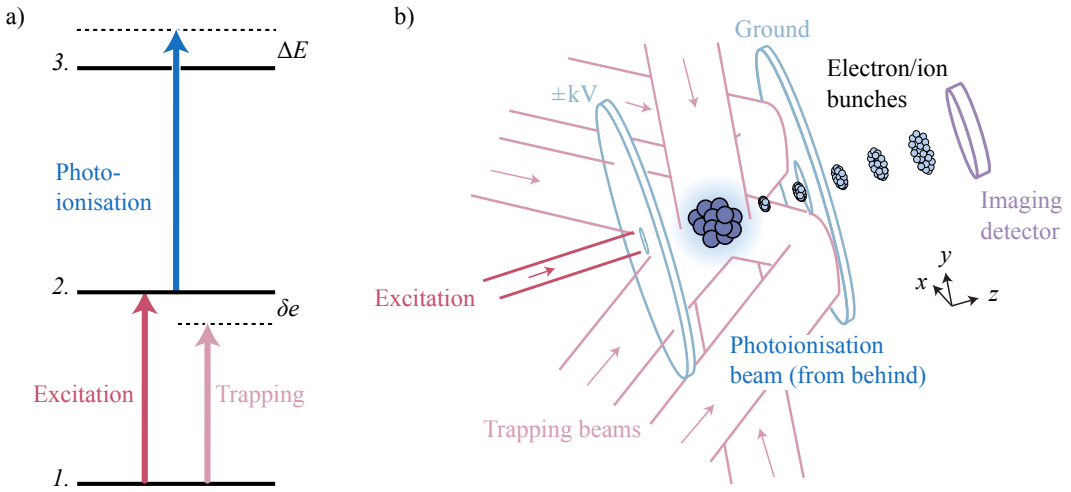

Figure 1.3: Production of cold electron and ion bunches by photoionisation of a laser-cooled gas. Neutral atoms (centre) are laser-cooled with counter-propagating resonance-detuned beams. Two-colour photoionisation produces ultracold plasma (UCP) at the spatial overlap of the two lasers. Charged electrodes accelerate the electron or ion bunches. Adapted from Ref. [39]

for control of the source distribution and correlations to suppress the emittance growth associated with intrabeam Coulomb interactions.

1.4.1 Ultracold plasma

Ultracold plasmas are created by photoionising low-temperature gases [40]. Laser cooling and trapping techniques [41] produce cold atomic gases below 1 mK, which are ionised by laser fields coupling the atoms to near the energy threshold for ionisation. The small excess energy imparted by the ionising laser results in a plasma with electron and ion temperatures on the order of 10 K and 1 mK respectively. UCPs can be used as a source of electron or ion beams with low emittance.

UCPs access the strongly-coupled regime of plasma physics, which occurs elsewhere only in astrophysical environments [42]. Strong coupling occurs when inter-particle Coulomb potential energies exceed the thermal energy, leading to particle localisation and collective behavioural effects within the plasma. Achieving strong coupling in UCP is prevented by plasma heating effects, in particular DIH, which was described for UCPs before it was predicted to affect charged particle beams [43]. DIH limits the beam quality of UCP-based electron and ion beams which, due to their low initial temperatures, fall into the regime of statistical-Coulomb-effect-dominated beam behaviour. Efforts to induce correlations into the initial spatial distributions of the plasma have been predicted to

reduce the DIH effect [44], but the reduction has not been observed experimentally.

See Ref. [45] for a recent review of ultracold neutral plasma research.

1.4.2 Ultracold electron beams

Electrons extracted from UCP have bunch durations determined by the duration of the ionising laser, allowing for ultrafast emission suitable for ultrafast diffraction imaging [37]. A typical setup for an ultracold electron beam source is shown in Fig 1.3, which uses a two-step process to ionise the cold atoms. Ionisation occurs at the overlap of the photo-exciting and photo-ionising lasers, providing control of the initial source distribution. If the laser energies are tuned to excite the atom near to the ionisation threshold then only small, controllable amounts of excess thermal energy are imparted to the photoelectron and the ion, resulting in a beam with small energy spread and thus low temperature and emittance.

Experiments have characterised the high coherence [46] and short duration [47, 48] of UCP-based electron beams, and have demonstrated ultrafast and single-shot diffraction from crystalline samples [49, 50]. Diffraction imaging of non-crystalline, single-molecule samples requires increased electron beam density, which would lead to emittance growth and loss of coherence through intrabeam Coulomb effects. Techniques have been developed to produce arbitrarily-shaped three-dimensional bunches in cold-atom electron sources, to reduce space-charge induced emittance growth [39]. At present however, space-charge effects have not been observed in cold electron beams due to the low charge density of the electron bunches at the source. Further work is therefore needed to demonstrate the suppression of nonlinear space-charge effects using cold atom electron sources.

See Ref. [51] for a recent review of cold electron beam research.

1.4.3 Ultracold ion beams

Ion beams extracted from cold-atom trap sources have small focal spot sizes appropriate for ion microscopy [37, 38]. The wide range of atoms that can be laser cooled allows for choice of ions of different masses and properties, unlike conventional focused-ion beam sources which are typically limited to gallium from liquid metal sources [7] and, more recently, helium from gas field ionisation sources [52]. Lithium ions from cold-atom sources, for example, have been used for microscopy where the low ion mass provides imaging with reduced sample

damage [53]. Cold-atom-based caesium ion beams, on the other hand, have a higher ion mass, and can be used for nanoscale machining and manipulation [54].

Focused ion beam imaging, deposition and machining applications do not typically require time resolution, and so utilise continuous beams rather than pulsed bunches to limit beam charge density, in order to avoid space-charge expansion effects. Cold ion sources operating in continuous mode experience energy broadening from the statistical Coulomb effects associated with the random longitudinal particle separations [55]. Short-duration pulsed ion beams have industrial applications at high beam energies [56] and to the measurement of chemical processes [57]. Bunched ion beams extracted from a cold atom source would be space-charge dominated, and have been predicted to exhibit strong space-charge interactions [58]. This thesis establishes the cold-atom ion source as a platform for the investigation of space-charge and disorder-induced heating effects in analogue to ultrafast electron beams used for imaging of dynamic processes.

See Ref. [59] for a recent review of cold ion beam research.

1.5 Thesis outline

Coulomb interactions limit the brightness of charged particle beams. Controlling the effects of nonlinear beam expansion (space charge) and disordered interparticle scattering is of critical importance for applications ranging from ultrafast electron diffraction to injectors for particle accelerators. In this thesis it is shown that ultra-cold ion bunches extracted from laser-cooled atoms can be used to observe the effects of intrabeam Coulomb interactions with unprecedented detail. This detail allows for the investigation of the fundamental limitations to charged-particle beam quality from Coulomb effects, and the development and testing of techniques to overcome the limitations. Arbitrarily shaped bunches are created to reverse the space-charge problem, and excitation of Rydberg-blockaded or optical-lattice correlated atoms prior to ionisation reduces the disorder-induced heating effect. The University of Melbourne cold-atom electron source is used to produce the ion bunches for this study. Details of the construction and design of the source can be found in the PhD theses of its developers [60–63]; the apparatus and its operation is discussed in this thesis when relevant to the work presented.

Chapter 2 presents a study of the space-charge effect in cold ion bunches,

including detailed observations of the beam dynamics and suppression of space-charge induced emittance growth through beam shaping. It is shown that the higher mass of ions compared to electrons produced with the same source configuration leads to a mass/time/energy scaling that makes the study of cold, low-energy, moderate-duration, high-mass ion bunches applicable as a direct behavioural analogue to high-energy, high-temperature, ultrafast electron bunches. The low temperature of the ions is shown to allow for detailed observation of space-charge effects, free from the masking effects of thermal diffusion present in conventional sources. The detailed experimental observations reveal complex interactions that nonlinearly transform the beam shape, which are found to depend on the atom-laser interaction, closely matching simulations and modelling of the photoionisation and beam-propagation processes. Beam-shaping techniques are then used to make experimental measurement of reduction of space-charge induced emittance growth for shaped bunches compared to unshaped bunches, which are the first such measurements with any particle beam source.

Chapter 3 investigates the disorder-induced heating effect in ultracold ion bunches. As established in chapter 2, ion bunches are used as a behavioural analogue of ultrafast electron bunches. A comprehensive N-body 'molecular-dynamics' simulation is developed to study disorder-induced heating, with theoretical calculations of the thermal equilibration of an initially disordered system of ions. Two different methods for the suppression of disorder-induced heating are then investigated, based on spatially-correlated ions created by ionisation of:

i. a blockaded Rydberg gas, where the inter-atomic interactions of highly-excited states establish a minimum separation between the ions; and

ii. atoms in an optical lattice, which would be completely ordered except for lattice vacancies which introduce disorder.

The suppression of disorder-induced heating is quantified in each case, depending on the degree of correlation, which is discussed in terms of experimental achievability and measurability.

Chapter 4 demonstrates the production of Rydberg-blockaded ion bunches, towards suppression of disorder-induced heating. A laser system and Rydberg spectroscopy system are developed, and used to coherently excite ions to targeted Rydberg states. Inference of the degree of interparticle correlation is then made by measurement of the excitation blockade effect. Methods of coherent population transfer to Rydberg states are implemented in the cold-atom source, showing high excitation transfer efficiency.

In summary, this work determines limits to beam quality for new cold atom electron and ion sources in terms of the particle spatial distributions on macroscopic (beam shape) and microscopic (spatial correlation) scales. Techniques are developed and demonstrated towards suppression of the deleterious aspects of intrabeam Coulomb effects, which otherwise present fundamental limitations to the future development of charged particle beam sources.

Chapter 2

Cold ion beam platform for measuring space-charge effects

The studies presented in this chapter were published as Ref. [1] (Appendix A.1) and Ref. [5] (Appendix A.5).

Coulomb interactions can lead to instabilities and emittance growth in charged particle beams, limiting the ultimate utility of electron and ion microscopes [7, 64] and high energy particle accelerators [65]. In ultrafast electron diffraction (UED) [15, 66, 67], space-charge effects constrain the capacity to obtain diffraction information [68, 69]. For example, in bunches containing just 18 electrons, Coulomb repulsion was shown to increase the bunch duration by 50% and energy spread sevenfold [70]. For strongly coupled systems, Coulomb interactions mediate interesting collective effects including the formation of Wigner crystals [71], self-organisation [72] and shockwave phenomena [73–75]. Although the underlying physics of the two-particle Coulomb interaction is simple, the behaviour of beams with complicated spatial and temporal structure can be difficult to predict. Particle trajectory calculations are straightforward for a few particles or even a few million, but become intractable for high-density high-current systems. The development of useful models of self-field effects has been limited by a lack of detailed comparative experimental data where the space-charge and thermal effects are clearly distinguishable.

In this chapter the cold-atom ion source is established as a platform for the study of space-charge effects. The measurements with ions are directly analogous to high energy and ultrafast electron beams. Detailed space-charge dynamics are observed in the evolution of freely expanding bunches with complex initial distributions. The unique capability of cold-atom sources to produce arbitrarily

shaped and three-dimensional bunch charge distributions is then used to make measurements of the improved brightness for uniform ellipsoidal bunches as compared to Gaussian bunches.

2.1 Detailed observation of space-charge dynamics

Cold charged particle sources based on near-threshold photoionisation of laser-cooled atoms [37–40] produce electrons and ions with temperatures as low as a few kelvin and millikelvin respectively, allowing detailed investigation of self-field and strong coupling effects. The ability to arbitrarily shape the initial charged particle distribution [39] enables flexible investigation of the spatial dependence of interparticle dynamics.

Pioneering work with cold electron bunches found evidence of space charge effects [58, 76] without clear observation of the nonlinear bunch transformation associated with emittance growth. The role of Coulomb interactions in cold ion beams has been studied in detail for continuous-mode low charge density operation [55, 77, 78], but not in pulsed mode where space-charge effects would be present. This section presents an investigation of space-charge effects in arbitrarily shaped nanosecond duration cold ion bunches produced by near-threshold photoionisation of laser-cooled atoms, to gain insight into the effects that would be present in ultrafast cold electron bunches.

The effects of space-charge interactions are enhanced in ion bunches compared to electron bunches. Due to their high mass, they have comparatively low velocities and hence retain a high charge density following the ionisation. The ion temperature is also three to four orders of magnitude lower, allowing distinct measurement of space-charge effects without significant loss of detail due to thermal diffusion.

During an ionising laser pulse of time t_i in the static electric field of the accelerator, the ion bunch will grow longitudinally as the ions are produced. The elongation of the ion bunch is, however, less than that of an electron bunch created over the same duration due to the larger ion mass. The laser-pulse duration t_e that would produce an electron bunch of equivalent length to an ion bunch in the same field is then

$$t_\mathrm{e} = t_\mathrm{i} \sqrt{\frac{m_\mathrm{e}}{m_\mathrm{i}}}, \tag{2.1}$$

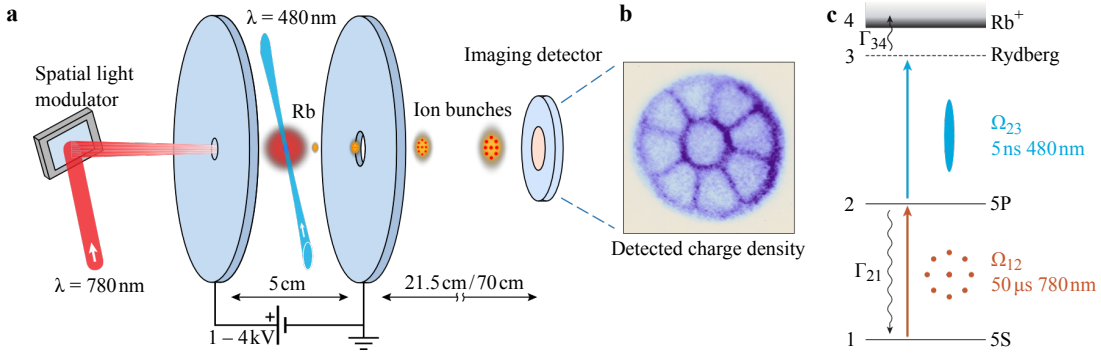

Figure 2.1: (**a**) Cold rubidium atoms are prepared in a magneto-optical trap. Ions are produced by two-colour near-threshold photoionisation. The cold ions are accelerated by a static electric field before drifting 21.5 cm or 70 cm in a zero field region to an imaging detector to record their transverse spatial profile. (**b**) Ion bunch transverse spatial distribution; density shown in false colour. (**c**) Rubidium energy levels with optical couplings labelled by the Rabi rates Ω, decay rates Γ and schematic transverse laser intensity profiles, for relevant states in the two-colour ionisation process.

where $m_{\mathrm{e,i}}$ are the electron and ion mass. The visibility of the space-charge effect is enhanced in ions compared to that in the equivalent-*time* electron bunches because the ion temperature remains low, with the excess ionisation energy predominantly transferred to the photoelectrons. Thus, rubidium ion bunches ($m_i = 1.41 \times 10^{-25}$ kg) created with ionisation pulse durations of a few nanoseconds demonstrate space-charge effects equivalent to those in electron bunches created on picosecond timescales, but without thermal diffusion that has prevented observation of those effects [47, 48].

In addition to the mass-scaling of equivalent bunch durations, beam evolution is also determined by the beam temperature, energy and density. For a beam propagating over a set distance with particle kinetic energy E_k, the degree of Coulomb expansion is proportional to $\sqrt{m/n'E_k}$ (excluding relativistic time dilation effects), where n' is the initial particle density. The thermal Debye length λ_{D} (Eq. 1.10), which measures the relative contribution of space-charge effects compared to thermal effects in beam evolution, is proportional to the temperature and initial density as $\sqrt{T/n'}$. Therefore, the low energy, low temperature, low density, long duration and high mass pulsed ion beams from a CAEIS provide observational data for space-charge effects analogous to high energy, high temperature, high density, ultrafast and low mass electron sources.

2.1.1 Experimental methods and observations

Ion bunches were formed by photoionisation of an ensemble of laser-cooled rubidium atoms in a magneto-optical trap (MOT) (Fig. 2.1). The MOT was

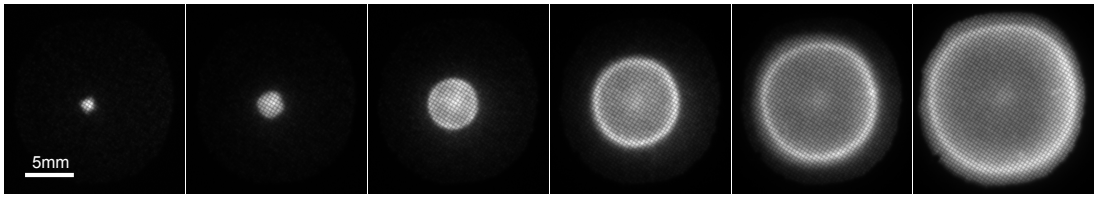

Figure 2.2: Ion beam transverse density profiles projected through the axis of propagation, measured 70 cm (10.8 μs) from the source, each with initial transverse distributions of 100 μm diameter but different bunch charge. The bunch charge was increased with increased laser powers of 6 nW, 38 nW, 140 nW, 410 nW, 1.4 μW and 2.7 μW (left to right), causing space charge expansion and nonlinear transformation of the bunch profile. At higher charges, a dense ring formed at the edge of the expanding bunches.

loaded from an effusive oven source and a Zeeman slower [79], collecting neutral rubidium-85 atoms at a temperature of 70 μK in a region approximately 5 mm in diameter, with a peak number density of $1.2 \times 10^{10}\,\mathrm{cm}^{-3}$. The atoms were ionised by two-step, near-threshold photoionisation. The two-colour ionisation process allows ions to be created in an arbitrary spatial charge density distribution [39]. A $\lambda = 780$ nm laser beam was used to drive the first step excitation transition. This beam consisted of two laser frequencies, with 900 μW of power tuned to the $5^2S_{1/2}(F = 3) \rightarrow 5^2P_{3/2}(F = 4)$ transition and 100 μW acting as a repumper on the $5^2S_{1/2}(F = 2) \rightarrow 5^2P_{3/2}(F = 3)$ transition. The excitation laser beam intensity profile was shaped with a spatial light modulator (SLM) to control the spatial distribution of the intermediate excited-state atoms in two dimensions. Atoms in the 5P state were further excited to an energy level equivalent to a Rydberg state with principal quantum number n = 30 that undergoes field-ionisation due to the accelerator electric field. The Rydberg-coupling laser pulse had a wavelength of $\lambda = 480$ nm, a power of $2 - 6$ mJ and a duration of of 5 ns, focused to a ribbon of 100 μm$\times$8 mm full width at half maximum propagated perpendicularly to the excitation laser beam, thereby defining the profile of the ions along the direction of ion propagation. Control of the bunch charge was varied by changing the excitation laser beam power.

The atoms were excited and ionised in a static electric field of $20 - 80\,\mathrm{kV\,m}^{-1}$ between a pair of parallel plate electrodes. During and shortly after ionisation, heating processes such as disorder-induced heating increase the ion temperature to a few millikelvin [80]. The ion bunches were accelerated over a distance of 2.5 cm, subsequently traversing an aperture in the grounded electrode that expands the beam due to the lensing effect of the divergent electric field [81]. The expanding ion bunches then drifted in a field-free region for 21.5 cm (Fig. 2.3) or 70 cm (Fig. 2.2) to a phosphor-coupled microchannel plate, which was imaged with a CCD camera to measure spatial charge density.

Figure 2.2 shows experimentally measured projected ion bunch densities at the MCP detector at a distance of 70 cm. The ion bunches were created with a 100 μm diameter excitation beam profile and accelerated to 2 keV. At low excitation laser power (low bunch charge; left) the bunch is small at the detector, indicating weak space-charge effects, with a measured distribution after propagation that matching the intensity profile of the excitation laser. With increasing charge (right), rather than the simple expansion and loss of detail that might be expected, Coulomb interactions accelerate the growth and induce nonlinear transformation of the bunch structure.

High-density rings were observed surrounding the high-charge bunches. The rings are visually similar to those formed by the interplay between self-fields and external focusing elements in electron storage rings [82], but in this case are found for all high-density initial distributions regardless of beam size and internal profile. The rings are also suggestive of phase-space wave-breaking phenomena which have been predicted for particle beams [83–85], and similar to shock-shell formation predicted, but not yet experimentally observed, for Coulomb explosion of strongly coupled plasmas formed from cold ions [74] and in laser-irradiated nanoclusters [86–89].

A complex ion distribution was studied in detail as an example of the subtle space-charge dynamics which can be observed. Figure 2.3 shows experimentally measured projected ion bunch densities, for nine small closely-spaced ion bunches, imaged 24 cm from the source at a bunch energy of 500 eV. Collective behaviour was observed in the interactions between the ion bunches, resulting from the nonlinear space-charge fields. At low excitation laser power (low bunch charge; left column) the measured distribution after propagation closely matches the intensity profile of the excitation laser and original bunch shape. Increased laser power and bunch charge induced nonlinear transformation of the beam charge density due to Coulomb interactions within and between the bunches. In particular, the expanding beams were observed to form high density layers at the boundaries of their collision formation, an effect not previously observed in studies of merging electron beams from thermal sources [90]. The detail with which the space-charge effects were observed enabled systematic testing and development of a comprehensive model of the system including self-field effects, illustrating the advantages of observation with minimal thermal diffusion effects.

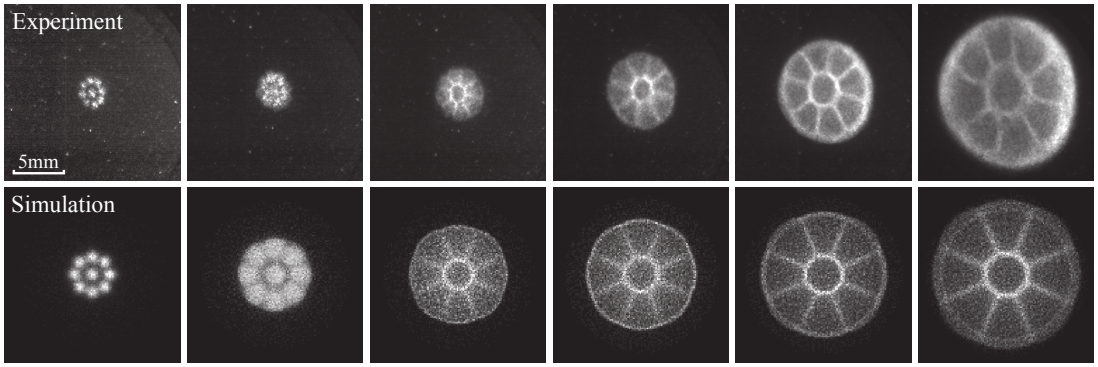

Figure 2.3: Ion beam projected density profiles imaged 24 cm (7.9 μs) from the source region, for nine closely spaced bunches each of 100 μm diameter. Upper: Experimentally measured profiles for increasing bunch charge, showing increased expansion and the emergence of high-density regions due to intrabeam space-charge effects. Left to right: shaped excitation laser beam with total power of $< 1\,\mu$W, 70 μW, 210 μW, 340 μW, 640 μW and 980 μW. Lower: Simulated bunch structure for ion bunches with spatial profiles calculated as described in Sec. 2.1.2 with laser profile and powers as used in the experimental images. Total bunch charges of 0 C, 2 fC, 8 fC, 10 fC, 13 fC, 19 fC. The greyscale density profiles are normalised individually to maximise contrast.

2.1.2 Models and simulations to reconstruct beam dynamics

The evolution of the ion bunches was simulated using General Particle Tracer (GPT) [91], a commercial modelling program that uses numerical solutions to the equations of motion to propagate point particles through the known electrostatic fields in the accelerator structures and the dynamically evolving self-field of the beam. The initial charge distributions were determined from the measured laser spatial profiles by calculation of the atomic excitation. Initial attempts to replicate the observed beam behaviour in simulation were unsuccessful. For calculations of the ion distribution based on a two-level atom model [39] with shaped $\lambda = 780$ nm excitation laser intensities, the simulations did not display formation of the high-density rings (Fig. 2.2) or collision boundaries (Fig. 2.3).

A hint at the required alteration to the model came from the dependence of the ion density on the excitation laser power. The two-level atom model predicts saturation of the ion density for increasing excitation laser power, which was not observed experimentally. The number of ions produced was inferred from the degree of space-charge induced bunch expansion (Fig. 2.3). Saturation of ion production was not observed even at several hundred times saturation intensity for the 780 nm transition. A four-level model of the excitation and ionisation process was developed, including field ionisation included as a loss rate proportional to the population of the field-ionising state. The model is

an extension from the two-level model, accounting for laser-induced transitions from the ground to excited state during the 5 ns ionising laser pulse, such that the ionisation fraction is not limited by the saturated excited-state fraction prior to the ionisation-inducing laser pulse.

The atomic state was described with a four-state density matrix for the electronic ground and intermediate excited states, the resonant self-ionising state, and the final ionised state. The states were coupled by laser fields with position and time dependent intensities, and by spontaneous decay (see Fig. 2.1c). Field ionisation was represented by rate Γ_{34} which was taken to be the electron orbital frequency for the field-ionising state with principle quantum number n from the Bohr model of the atom [92].

The evolution of ρ, the density matrix for the four-level atom, is given by

$$\dot{\rho}_{ij} = -\frac{i}{\hbar}\left[\hat{H},\rho\right]_{ij} + \hat{\mathcal{L}}(\rho)_{ij}, \tag{2.2}$$

using the commutator $[A,B] = AB - BA$, where the subscripted indices are associated with the atomic levels given in Fig. 2.1, and where $\hbar$ is the reduced Planck constant. The optical Bloch equations (OBEs) for the four-level system were derived following standard approaches [93, 94], where the Hamiltonian for the laser-atom interaction is

$$\hat{H} = \frac{\hbar}{2}\begin{bmatrix} 0 & \Omega_{12} & 0 & 0 \\ \Omega_{12} & 0 & \Omega_{23} & 0 \\ 0 & \Omega_{23} & 0 & 0 \\ 0 & 0 & 0 & 0 \end{bmatrix}. \tag{2.3}$$

The decay terms are

$$\begin{aligned} \hat{\mathcal{L}}(\rho) &= \frac{\Gamma_{21}}{2}\begin{bmatrix} 2\rho_{22} & -\rho_{12} & 0 & 0 \\ -\rho_{21} & -2\rho_{22} & -\rho_{23} & -\rho_{24} \\ 0 & -\rho_{32} & 0 & 0 \\ 0 & -\rho_{42} & 0 & 0 \end{bmatrix} \\ &+ \frac{\Gamma_{34}}{2}\begin{bmatrix} 0 & 0 & -\rho_{13} & 0 \\ 0 & 0 & -\rho_{23} & 0 \\ -\rho_{31} & -\rho_{32} & -2\rho_{33} & -\rho_{34} \\ 0 & 0 & -\rho_{43} & 2\rho_{33} \end{bmatrix}, \end{aligned} \tag{2.4}$$

where $\Gamma_{21} = 38.117 \times 10^6\,\mathrm{s}^{-1}$ is the excited to ground state decay rate [95]. The

Rabi rates were calculated as

$$\Omega_{ij} = \sqrt{2d_{ij}^2 I_{ij}/c\varepsilon_0\hbar^2}, \tag{2.5}$$

where I_{ij} is the laser intensity coupling the i and j states, c is the speed of light, ε_0 is the permittivity of free space and $\hbar$ is the reduced Planck constant. The transition dipole matrix elements were $d_{12} = 2.99ea_0$ for the $5S_{1/2} \rightarrow 5P_{3/2}$ excitation transition [95] and $d_{23} = 0.04ea_0$ for the $5P_{3/2} \rightarrow 36D_{5/2}$ Rydberg transition targeted by the ionisation laser [96] where e is the proton charge and a_0 is the Bohr radius. The laser intensity profile for the excitation beam was measured with a CCD camera at an equivalent position to the atoms, and the intensity profile for the ionisation beam was measured using a beam profiler. The diagonal elements of the density matrix represent the atomic state populations. The off-diagonal elements represent the coherences between the atomic states. The OBEs were solved for ρ_{44}, which gives the time dependent spatial charge-density distribution function of the ion bunches.

The four-level model accounted for the non-saturating ion bunch number for increasing laser power, but the calculated bunch distributions still did not display formation of the experimentally-observed high-density rings of Fig. 2.2, for the known laser intensity distributions. Models of Coulomb explosion dynamics for ultracold plasmas [74] and laser-irradiated nanoclusters [86] have predicted density features similar in appearance to the rings observed in Fig. 2.2. In those models, the density features form due to the expansion of charge at the centre of a spatial density distribution into a less-dense 'tail' in the transverse radial distribution. The particle tracking simulations were repeated with the addition of a uniform low-density background of ions to the calculated ion density distribution. The repeated simulations showed formation of the rings, as observed experimentally.

It was postulated that the diffuse 'halo' of background ions could be formed by absorption of scattered excitation beam light, outside of the desired ionisation volume. To model the scattering of the light through the atom cloud, the effects of fluorescence and reabsorption of the quasi-continuous excitation beam were included in the four-level model, using a first-order single-scattering approximation. As illustrated in Fig. 2.4, a background of ions is formed by the re-emission (fluorescence) of $\lambda = 780\,\text{nm}$ photons by the excited atoms in the beam 'core'. The fluoresced light is then reabsorbed by atoms outside of the beam core, forming a 'halo' of background ions. Assuming steady-state conditions prior to the ionising laser pulse, the spatial profile of the core of atoms

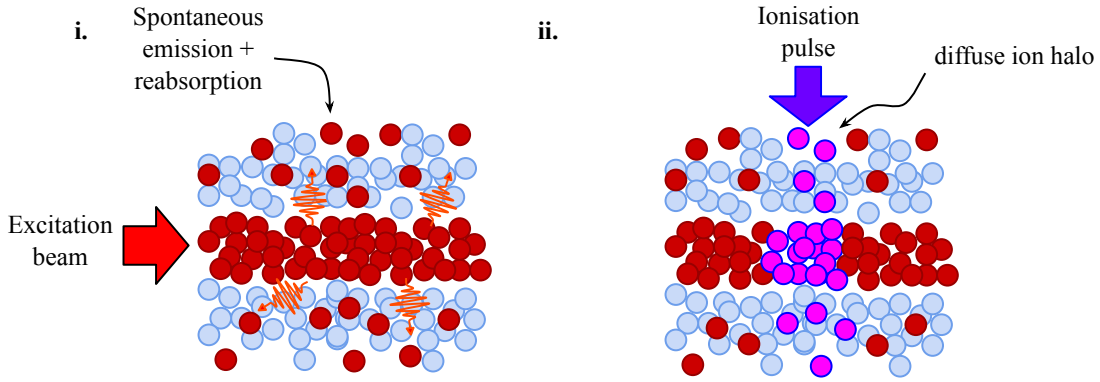

Figure 2.4: Diffuse ion halo formation by excitation fluorescence. **i.** The long-duration shaped excitation beam creates a beam 'core' of excited atoms, which spontaneously re-emit their excitation laser photons. The fluoresced light is reabsorbed outside of the beam core by other atoms in the cloud, creating a diffuse 'halo' of excited atoms. **ii.** On the arrival of the ionisation laser pulse, which propagates orthogonally to the excitation laser, both the core and halo are ionised. Expansion of the core into the halo leads to formation of fluorescence halo rings.

excited by the $\lambda = 780\,\text{nm}$ laser, $\rho_{22}^{c}(\mathbf{x})$, was calculated from the laser intensity, using the steady-state solution to the two-level optical Bloch equations [94]

$$\rho_{22} = \frac{\Omega_{12}^2}{2\Omega_{12}^2 + \Gamma_{21}^2}. \tag{2.6}$$

Excited atoms spontaneously emit photons at the natural decay rate Γ_{21}, so the scattered light intensity is

$$I^{\text{s}}(\mathbf{x}) = \hbar\omega\Gamma_{21} \int_V \frac{n(\mathbf{x}')\rho_{22}^{c}(\mathbf{x}')}{4\pi|\mathbf{x}-\mathbf{x}'|^2}\mathrm{d}^3\mathbf{x}' \tag{2.7}$$

assuming isotropic emission, where $\hbar\omega$ is the energy per photon and $n(\mathbf{x})$ is the number density distribution of the cold atom cloud. The scattered intensity is then used to calculate the profile of beam-core fluorescence excitations, $\rho_{22}^{s}(\mathbf{x})$, again using Eq. 2.6. The total density profile of excited state atoms at time $t = 0$, prior to arrival of the $\lambda = 480\,\text{nm}$ laser beam, is then calculated in the single-scattering approximation as

$$\rho_{22}(\mathbf{x}, t=0) = \rho_{22}^{c}(\mathbf{x}) + \rho_{22}^{s}(\mathbf{x})[0.5 - \rho_{22}^{c}(\mathbf{x})], \tag{2.8}$$

which accounts for depletion of atoms available for excitation by the $\lambda = 780\,\text{nm}$ laser, up to the limit of saturation ($\rho_{22} \to 0.5$). Equation 2.8 was used as the initial conditions for the density matrix in the four-level model of ionisation, with $\rho_{11} = 1 - \rho_{22}$, and all other elements equal to zero.

The experimentally observed high-density rings that surround the ion bunches

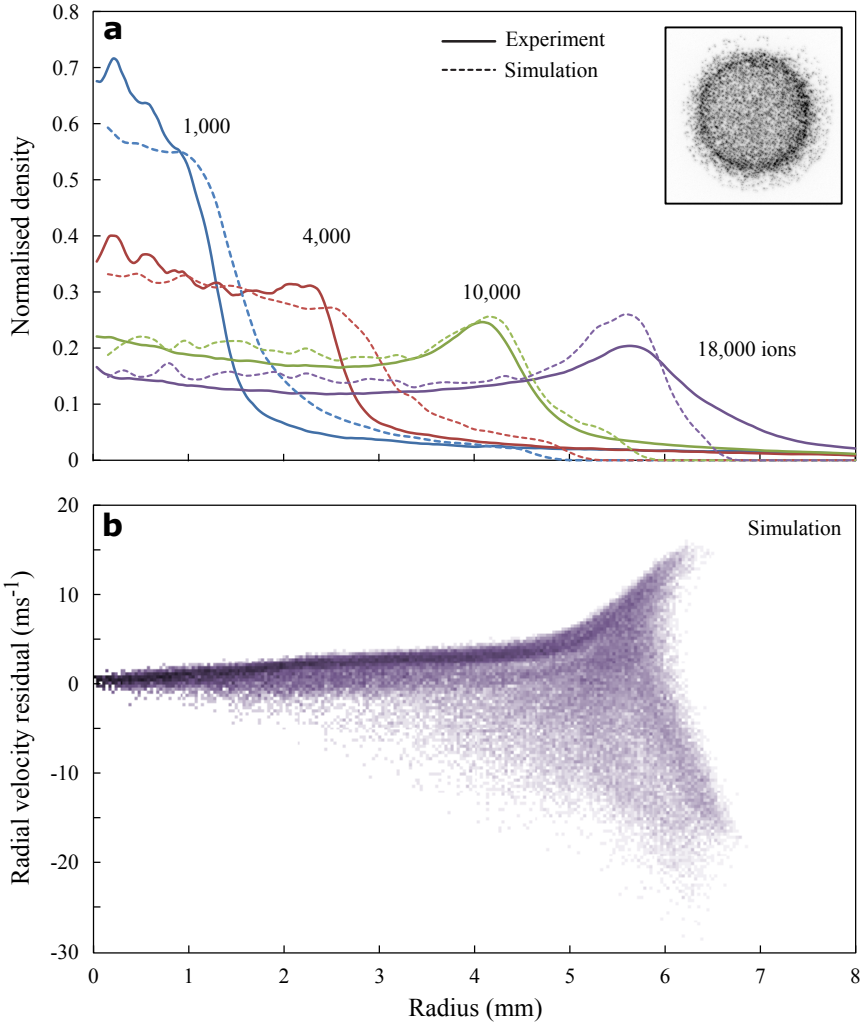

Figure 2.5: (**a**) Measured and calculated radial dependence of the ion density. (**b**) Logarithm of the ion phase space density, showing two orders of magnitude in density from light to dark, for a single bunch of 18,000 cold ions at propagation distance and time of 70 cm and 10.8 μs. The formation of a shock front at the outer edge of the bunch is illustrated by the caustic in the phase space distribution. Inset of (**a**) shows typical measured density profile for a single bunch.

were reproduced in simulation for initial ion distributions that included the fluorescence halo. The total bunch charge was adjusted to optimise the agreement between the propagated simulation and the measured density distribution. Simulations were performed using a 3D particle mesh method to calculate the self-field, and also by calculating the interactions between all ion pairs. The bunch evolution was identical for the two approaches, demonstrating bunch evolution that was dominated by space-charge effects rather than statistical Coulomb effects which would not be apparent with the mesh method. Figure 2.5a shows the axially averaged radial distribution calculated for expanding ion bunches of the same initial size but varying charge density, selected from the 38 nW, 140 nW, 410 nW and 2.7 μW data presented in Fig. 2.2.

The halo atoms excited by beam-core fluorescence decreases in density with power-law dependence out to long distances compared to the beam-core radius. Simulations including fluorescence halos provided detailed agreement with experimentally observed beam behaviour (Fig. 2.3). Simulations showed that the rings observed in experiments form by transverse velocity bunching, where fast-expanding ions from the high-density core of a shaped bunch overrun the more slowly-expanding halo ions. The smooth decrease of halo density with distance from the beam core leads to a bunching up of the expanding ions into high-density rings. The slight peak in density near the bunch centres seen in Fig. 2.2 and 2.3 are low density, non-radially-expanded ions from the bunch head and tail, formed by the tails of the 480 nm laser intensity distribution in the longitudinal $\pm z$-direction.

Figure 2.5b shows the simulated phase-space structure of a high-density bunch, in particular showing the large radius and momentum ring which is akin to shock wave formation in strongly interacting media. The density of the radial velocity residuals is plotted, which are the deviations (in ms^{-1}) for each ion from the best-fit linear relationship between the magnitude of the transverse velocity and the transverse radial position. The plot shows phase-space wave-breaking, where the rapidly-expanding the inner core of ions (with positive velocity residuals) compresses the more slowly expanding halo. The radial density profile of the bunch is the integral of the radial velocity for each radial position, leading to the dense rings observed in Fig. 2.5a.

Simulations repeated for the acceleration of bunches of electrons, rather than ions, with a creation time equal to the mass-scaled equivalence time (Eq. 2.1), showed precisely the same structures forming at very low initial electron temperature, but loss of visibility at a few kelvin, the lowest electron temperatures currently achievable [39, 48]. The equivalence of the beam dynamics in simulation demonstrate the use of the cold ion source as a testbed for the experimental investigation of intrabeam Coulomb effects.

2.1.3 Suppression of fluorescence halo rings

The fluorescence halo rings visible in the high-density bunches of Fig. 2.2 and 2.3 correspond to nonlinear transformation of bunch shape, and therefore also to emittance growth. Preservation of low source emittance requires linearisation of space-charge fields, thus requiring elimination of halo excitation. To prevent formation of the halo requires prevention of the beam-core fluorescence. To do so,

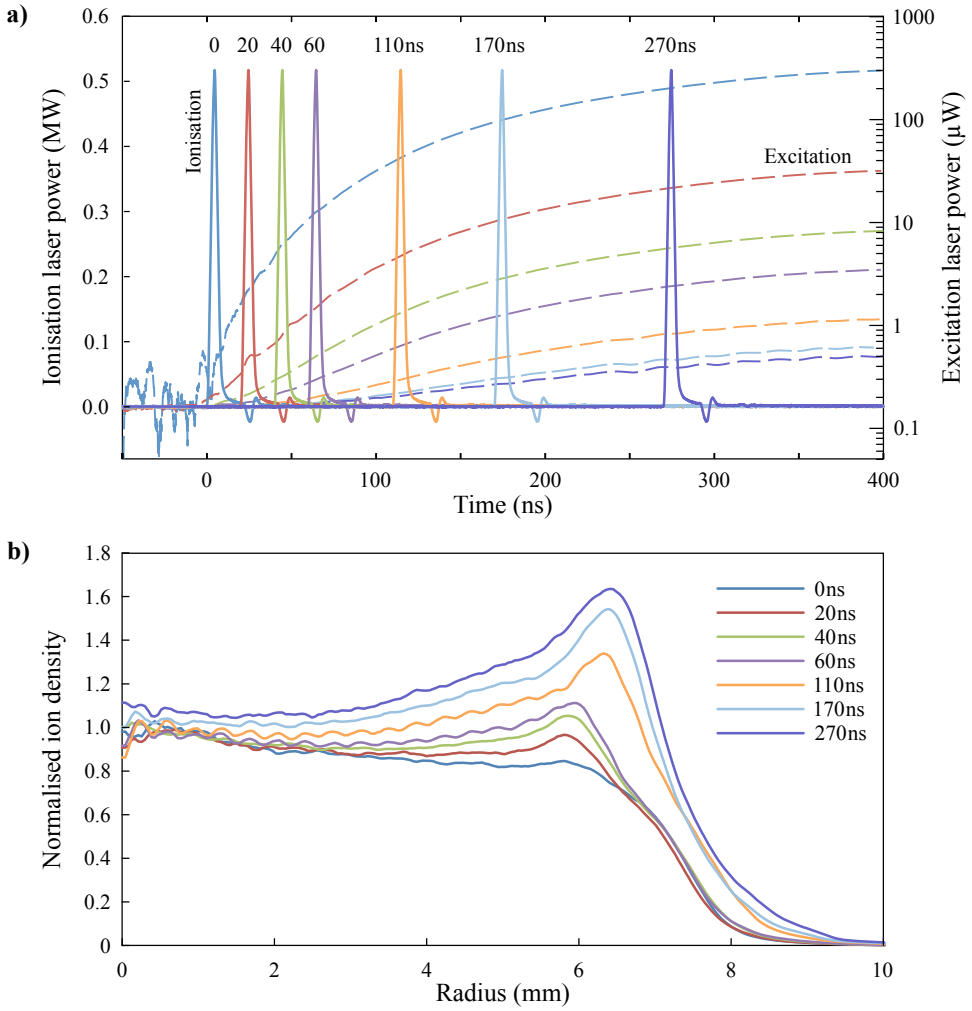

Figure 2.6: Variation in projected transverse density of halo ions with excitation laser pulse temporal separation. (**a**) Solid lines (left) and dashed lines (right) show the blue ionisation and red excitation laser pulse timing. The excitation laser rise time is limited by the acousto-optical modulator used to modulate the laser beam. (**b**) Measured ion bunch radial profiles for varying ionisation delay, for free propagation distance of 70 cm. Due to the slow rise of the excitation laser intensity, the charge density of the beam 'core' was kept constant for different timings by adjusting the power of the excitation laser. With a constant core density the expansion rate is approximately constant, but with longer delay times the fluorescence increases, increasing the halo density.

the time that beam-core atoms spend in the excited state prior to ionisation was reduced, thereby reducing the amount of fluorescence. The spontaneous emission time was determined by the delay between the 780 nm and 480 nm laser pulses used in the two-step ionisation process. The first laser excites atoms to the $5P_{3/2}$ state which has a mean lifetime of 26 ns. The second laser, with pulse-length of 5 ns, excites the 5P atoms to a resonant auto-ionising state in the static ambient electric field. The fluorescence from the intermediate 5P state can therefore be controlled by varying the delay between the two laser pulses, allowing variation of the density of excited and subsequently ionised atoms in the halo.

To demonstrate the suppression of halo rings, bunches were created with equal degrees of space-charge expansion (i.e. core charge), but different laser-delay times. The excitation laser was switched on and off using an acousto-optical modulator, which had a rise-time on the order of 100 ns. The slow rise time meant that bunches excited with a low delay time needed higher excitation laser beam power to have equal bunch charge, illustrated in Fig. 2.6a. Figure 2.6b shows the variation in visibility of the outer rings with changing time between pulses, showing decreased density of the fluorescence halo ring with decreased duration of spontaneous emission.

Suppression of fluorescence halos using control of will be required in the future development of cold-atom electron and ion bunch source technology and applications, to prevent emittance space-charge induced growth. The fluorescence halo effect is specific to cold-atom based sources, but serves to demonstrate the usefulness of the cold ion beam platform to investigate subtle space-charge effects that would be masked by thermal effects in a conventional source.

2.2 Bunch-shaping to linearise space-charge

The principal author of Ref. [5] is D. J. Thompson, who led the project to which the work described in this section contributes. I contributed calculations of the beam profile properties used in the work described by Sec. 2.2.1, and contributed to the preparation of the manuscript for Ref. [5]. I contributed, to a degree equal to DJT and Ben M. Sparkes, to the design and execution of the knife-edge measurement of beam focal sizes, described in Sec. 2.2.2.

Charged particle beams operating via photoemission, including photocathode-based electron sources and cold-atom electron and ion sources, typically operate with unshaped Gaussian laser beam profiles. The beams produced therefore have

non-uniform charge density profiles which experience nonlinear space-charge effects and emittance growth. Bunch-shaping techniques to linearise space-charge and prevent emittance growth (described in Sec. 1.3.1) were first proposed [28] and demonstrated [29] in photocathode sources, and were subsequently adopted for cold-atom sources [39]. So far, however, the improved focusability and brightness predicted for shaped electron bunches has not been demonstrated experimentally, due to the relative weakness of space-charge effects in comparison to thermal effects in conventional sources.

This section presents direct measurements of improved focusability for shaped ion bunches as compared to Gaussian distributions. The charge densities of the ion beams were shaped to uniform distributions, to linearise space-charge, using the unique three-dimensional bunch-shaping capability of the cold atom source. The beams were focused using an electrostatic lens and the beam size at the focus was measured, and compared to the beam size for un-shaped Gaussian bunches, to experimentally demonstrate suppression of emittance growth.

2.2.1 Beam-profile shaping

The excitation beam coupling the $5S^2_{1/2} \rightarrow 5P^2_{3/2}$ states of the rubidium atoms was shaped using the SLM with iterative feedback [97] using images acquired with a CMOS camera, as illustrated in Fig. 2.7. For excitation Rabi frequencies Ω_{12} on the order of the excited state decay rate Γ_{21}, the ionised-state population ρ_{44} approaches linear dependence on Ω_{12}, and thus dependence on the excitation laser intensity as $\sqrt{I_{12}}$. To shape the density of the excited atoms, the laser intensity distributions were therefore set as the square of the desired bunch distribution functions, $I_{12}(x, y) \propto \Omega^2_{12}(x, y)$. Bunch distribution dimensions were set with the same initial root-mean-square (RMS) sizes in each orthogonal transverse axis, so that initial thermal emittance was the same for all bunches. Further detail regarding the bunch-shaping procedure is given in Ref. [5] (Appendix A.5).

Gaussian distributed bunches were created with standard deviation $\sigma = 67\,\mu$m in the transverse x and y directions orthogonal to the beam propagation direction. The maximum usable initial bunch size was limited by the expansion of the ions during propagation to the detector. The pancake distribution, which is predicted to expand to a fully three-dimensional ellipsoidal bunch [28], is a two-dimensional projection of a three-dimensional ellipsoid with a transverse radial particle-density distribution of the form $\rho(r) \propto \sqrt{1 - r^2/R^2}$ for a hard-edge boundary radius of R, which has an RMS beam size $\sigma_x = R/\sqrt{5}$. A flat-topped

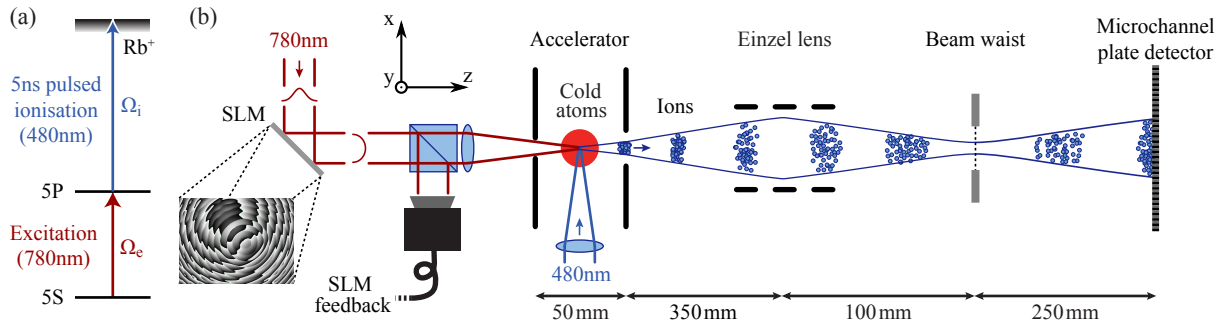

Figure 2.7: Experimental setup for measurement of improved focusability for shaped bunches. Shaping of the excitation laser beam using a spatial light modulator (SLM) produces ion bunches with uniform transverse density profiles. The ions were focused using an electrostatic ion lens, and their focal sizes were measured at the beam waist.

distribution of uniform density within a hard-edged transverse boundary was also studied, which is used in conventional sources due to their ease of production and complementary application to ellipsoidal distributions [98]. Flat-topped distributions with transverse boundary radius R have $\sigma_x = R/2$. Excited bunches were coupled to high-lying Rydberg states using $\lambda = 480\,\text{nm}$ 5 ns duration laser pulses following 500 ns of excitation laser exposure. Fluorescence halos were not observed to form at the below-saturation intensities used in this experiment. The near-threshold atoms were ionised with a static uniform field of 240 kV/m, and accelerated over a distance of 2.5 cm to an energy of 6 keV.

2.2.2 Measurements of shaped-beam focusability

The ion bunches drifted 350 mm in a field-free region from the accelerator exit aperture, expanding and experiencing emittance growth as determined by their initial bunch distributions. The ions then entered a commercial (Dreebit DN 100 CF D30) electrostatic three-electrode unipotential 'einzel' lens. The lens focused the beam with a 12.2 kV centre-electrode potential to a waist at a distance of 100 mm from the lens centre. At the beam focus was an aluminium plate of 2 mm thickness tapered to a sharp edge on a precision translation stage, used in other experiments [50] as a diffraction sample mount. The 'knife edge' of the aluminium plate was used to scan through the focal waist of the ion beam in the transverse x-direction, blocking a fraction of the beam depending on its position. After the knife edge, the transmitted fraction of the ion beam drifted to the phosphor-coupled MCP detector, which measured the bunch charge as a relative fraction of the unobstructed beam. The knife edge was also translated in the z-direction to measure the beam size at longitudinal positions in the vicinity of the focus.

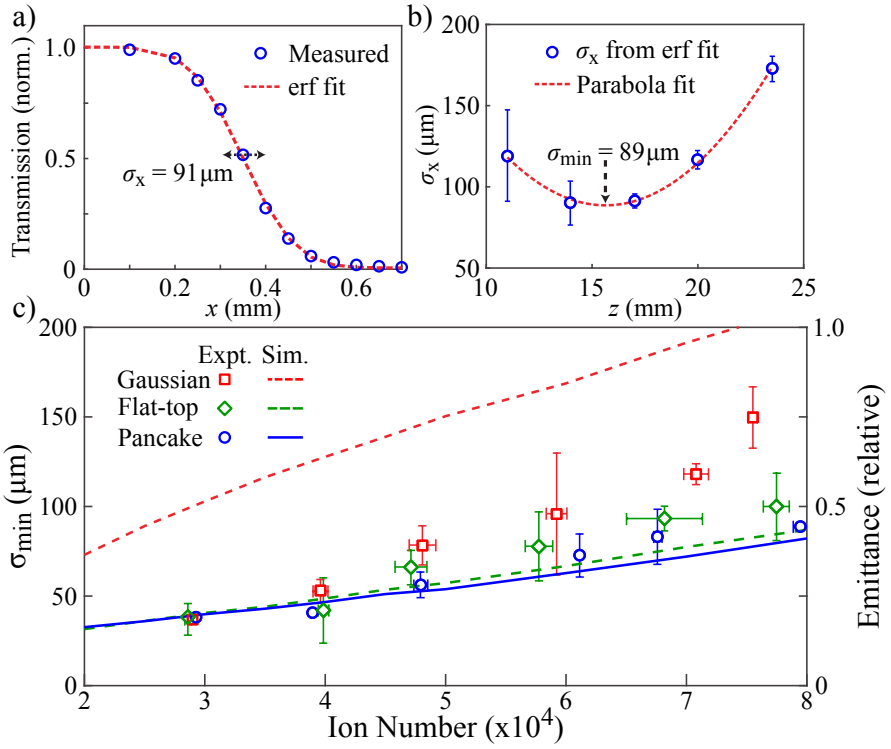

Figure 2.8: Knife-edge measurements of beam focal spot sizes. a) Individual knife-edge scan for one longitudinal position, with error-function fit to determine beam spot size. b) Spot size measurements at different longitudinal positions to determine the minimum spot size at the beam waist. c) Minimum spot sizes at the beam waist for Gaussian, flat-topped and pancake-distributed bunches for different ion number, with implied relative emittance compared to simulation results.

Bunch charges were measured from the integrated brightness of 8-bit greyscale images of the phosphor screen taken with a CCD camera. The bunch charge measurements were calibrated using a Faraday cup beam monitoring system [99] to measure the absolute beam current for the different laser beam powers. The camera-based measurements allowed for visual inspection of the knife-edge positioning. The experimental cycle was locked to the $10\,\mathrm{s}^{-1}$ repetition rate of the 480 nm ionisation laser. Measurements of the bunch charge were averaged over 100 shots for each excitation beam power, initial distribution and knife-edge position.

The bunch size in the vicinity of the focus was measured as one standard deviation in one transverse direction, by fitting the error function for a Gaussian distribution (i.e. its corresponding cumulative distribution along one dimension) to the knife-edge scan data, as illustrated in Fig. 2.8a. The minimum focal size was then determined by fitting a parabola to the bunch sizes as they varied along the longitudinal z-direction, illustrated in Fig. 2.8b. The parabola-fitting accounted for variations in focal position between bunches with different charge and initial distribution.

Minimum focal sizes were determined for Gaussian, flat-topped and pancake-distributed bunches for a range of ion numbers, controlled by the excitation beam power. The excitation beam power was varied only below the level of saturation of the 5S $\rightarrow$ 5P excitation transition so that the initial bunch shapes remained constant for the different bunch charges. The data, presented in Fig. 2.8 show that at low ion number all shapes have the same focal size, as beam emittance is determined mostly by accelerator aberrations. At higher ion numbers, the 'un-shaped' Gaussian bunches had larger focal sizes, indicating increased emittance due to nonlinear space charge.

Particle-tracking simulations using General Particle Tracer (GPT) [91] were performed with free space-charge expansion for shaped bunches propagating to the position of the einzel lens. The simulations were performed for the same range of ion numbers used in the experiment. The emittance at the lens plane determined the minimum focal size of the bunches, varying with bunch charge and beam distribution. For a constant beam divergence, the minimum focal size is directly proportional to the beam emittance. Figure 2.8c shows the lower emittance of bunches with flat-topped and pancake initial charge distributions relative to Gaussian-distributed bunches. The experimentally-measured relative emittance was not reduced by beam shaping to the same degree as in simulations, which was attributed to imprecision in the beam shaping, as well as the presence of residual fluorescence halos. Further improvements to the bunch focusability may be possible through the use of a higher-resolution SLM, allowing finer control of the bunch charge distributions, and by reducing the width of the pulsed blue laser beam to better satisfy the requirements for the pancake distribution to transform into a uniformly-filled ellipsoid [28]. Nevertheless this is the first such direct experimental measurement of lowered emittance due to beam shaping, representing a proof-of-principle measurement of the technique.

2.3 Discussion

Cold atom charged particle sources are a promising new approach to producing high brightness beams for applications in ultrafast imaging and high resolution nanoscale fabrication. Achieving that promise will require detailed understanding of the beam-quality degrading Coulomb interactions within charge bunches. Here it has been shown that cold ion bunches can be a powerful tool for investigating such charged particle beam behaviour. The detailed measurements that are possible with cold ions allowed testing of the predictions of complex interac-

tions in high-density charge bunches, which highlight the importance of correctly calculating the initial charge density resulting from the photoionisation process.

A particular example of a subtle space-charge effect was discovered, resulting from the fluorescent re-emission of laser light used in the photoexcitation process. The fluorescence halo effect led to formation of high-density rings associated with nonlinear transformation of the bunch shape, and emittance growth. A method to suppress the halo was demonstrated, by carefully timing the laser pulses used for generating the ion bunches to reduce the fluorescence.

The work presented in this chapter establishes the use of cold ions as a platform for the investigation and observation of space-charge dynamics. The ability to arbitrarily shape the bunches in three dimensions has made it possible to mimic the density distributions for complex and diverse source configurations, and probe the associated beam quality degradation related to space-charge effects. With beam shaping and space-charge dominated behaviour, the first measurements were made of improved focusability for hard-edge, uniform-density shaped bunches. The low temperature of cold ion sources, and the scaling of time due to the electron/ion mass ratio, allow precise measurement of previously inaccessible space-charge dynamics relevant to high density electron bunches used in accelerators and ultrafast electron diffraction imaging. The dynamics of the 5 ns ion bunches used in these experiments are equivalent to those of a 13 ps ultrafast electron bunch. Demonstrating the suppression of space-charge-induced emittance growth through shaping of the initial bunch profile is, therefore, a critical milestone in the development of cold electron sources, necessary for harnessing their inherent coherence, focusability, and brightness to perform single-shot ultrafast diffraction with atomic resolution.

Chapter 3

Suppressing disorder-induced heating through correlation

The studies presented in this chapter were published as Ref. [2] (Appendix A.2) and Ref. [3] (Appendix A.3).

For beams created with uniform charge distributions (Sec. 2.2), the minimum achievable source temperature will ultimately be limited by statistical Coulomb effects resulting from the discrete nature of the charged particles. Bunches of charged particles with uncorrelated initial positions have interparticle repulsive forces that are random in direction and magnitude, leading to disorder-induced heating (DIH) [44, 100].

Once space-charge induced emittance growth is prevented using the methods discussed in Ch. 2, the brightness of cold-atom electron and ion sources (CAEISs) will become limited by DIH. Many studies of ultracold neutral plasma (UCNP) have investigated the effects of initial disorder on the equilibrium plasma temperature following DIH [40]. DIH can be suppressed in UCNP by inducing atomic spatial correlations prior to ionisation, for example by ionisation of a degenerate Fermi gas [101], or trapping atoms in an optical lattice [102], or using blockaded Rydberg atom ensembles [103]. Simulations of the suppression of DIH in these pre-correlated plasmas have been performed only in the absence of expansion. Free expansion prevents establishment of thermal equilibrium due to the effects of adiabatic cooling [104, 105]. UCNPs are weakly expanding due to their neutrality, but CAEIS beams expand rapidly due to internal Coulomb forces. Models of DIH suppression through inducement of spatial correlations in cold charged particle bunches, where rapid Coulomb expansion is unavoidable, are needed to establish limitations to beam quality on the basis of achievable experimental

parameters.

In this chapter, the suppression of DIH in Coulomb-expanding cold ion beams with initial position correlations is calculated and compared to detailed molecular dynamics simulations of the particle beam dynamics. The theory behind the simulations is discussed in Secs. 3.1 and. 3.2, followed by discussion of two methods of preventing DIH: through ionisation of a blockaded Rydberg gas (Sec. 3.3) where spatial correlations are introduced by inter-atomic interactions that prevent excitation of pairs of atoms that are in close proximity, and through ionisation of atoms trapped in the sites of optical lattices (Sec. 3.4) formed in the high-intensity antinodes of standing waves of counter-propagating light fields.

3.1 Calculation of post-DIH equilibrium

The internal structure and DIH dynamics of a plasma can be described in terms of its temperature using the Coulomb coupling parameter [106]

$$\Gamma = \frac{e^2}{4\pi\varepsilon_0 a k_\mathrm{B} T}, \tag{3.1}$$

which is the ratio of potential to thermal energy, where e is the elementary charge, ε_0 is the vacuum permittivity, the Wigner-Seitz radius $a = (3/4\pi n)^{1/3}$ (Eq. 1.18) is the average interparticle separation for ion number density n, k_B is the Boltzmann constant and T is the plasma temperature. For strong coupling ($\Gamma > 1$) the motion of individual particles is determined by the interparticle interactions rather than by thermal diffusion. For an initially disordered cold ion plasma, Γ will initially be high due to the low temperature. However, it is not the initial Γ but the Γ following thermal equilibration through DIH that determines beam temperature and emittance. DIH occurs with a characteristic timescale

$$\tau_\mathrm{DIH} = \frac{2\pi}{\omega_p}, \tag{3.2}$$

the inverse of the (angular) plasma frequency $\omega_p = \sqrt{ne^2/\varepsilon_0 m}$ (Eq. 1.11), as the system develops interparticle spatial correlations at the expense of increased temperature. DIH limits the system to an equilibrium coupling parameter $\Gamma_\mathrm{eq} \sim 2$ in the absence of expansion [107]. At an ion density $n = 10^{16}\,\mathrm{m}^{-3}$, typical of a CAEIS using a magneto-optical trap (MOT) atom source, $\Gamma_\mathrm{eq} \sim 2$ implies rapid equilibration to a 'correlation' temperature $T_c = 2\,\mathrm{K}$ as the ions develop correlations during DIH, nearly five orders of magnitude higher than the temperature of the atoms before ionisation.

$\Gamma_{\rm eq}$ can be calculated via conservation of energy between the potential energy of the initial ion distribution and the thermal and binding energy of the equilibrium distribution of a strongly coupled plasma [108]. For the calculations presented here at densities $n = 1 \times 10^{16}\,\mathrm{m}^{-3}$, it is assumed that the cold-ion plasma is created in times much less than the DIH timescale $\tau_{\rm DIH} = 4 \times 10^{-7}\,\mathrm{s}$, which can be achieved using ultrafast photoionising lasers or pulsed external electric fields [103]. A system of infinite spatial extent was modelled without edge effects, approximating a plasma with dimensions greatly exceeding the interparticle separation.

The initial potential energy per particle u_i of the ion system is taken to be the potential with which a single ion is positionally bound to the static structure of the ion distribution. For a disordered distribution, the ion is unbound, with zero initial binding energy $u_i = 0$. The binding energy for the strongly coupled fluid phase of a one-component plasma (OCP), occurring for $1 < \Gamma_{\rm eq} < 170$, is given by the equation of state in thermal equilibrium,

$$u_{\rm eq} = -\frac{e^2}{4\pi\varepsilon_0 a}\left(A + B\,\Gamma_{\rm eq}^{-2/3} + C\,\Gamma_{\rm eq}^{-1}\right), \tag{3.3}$$

where the factor $A = 0.9$ gives the Lieb-Narnhofer lower bound to the OCP energy [109] and the factors $B = -0.590673$ and $C = 0.26569$ are given by fits of the known form of the equation of state to the results of plasma simulations [110]. The total energy per particle in equilibrium is $u_{\rm eq}$ plus the equilibrium kinetic energy k_e, written in terms of the equilibrium coupling parameter from Eq. 3.1 as $k_{\rm eq} = 3e^2/8\pi\varepsilon_0 a\Gamma_{\rm eq}$. An initially disordered ion distribution at zero temperature has initial binding energy $u_i = 0$ and initial kinetic energy $k_i = 0$. For conservation of energy, $u_{\rm i} + k_{\rm i} = u_{\rm eq} + k_{\rm eq}$, the solution for the equilibrium coupling parameter can calculated numerically (i.e. root-finding) as $\Gamma_{\rm eq} = 2.23$ for a disordered distribution. For ions with initial temperatures $T_i < 1\,\mathrm{mK}$, as would be expected in a magneto optical trap, excluding the relatively small initial kinetic energy term has negligible effect on the prediction of $\Gamma_{\rm eq}$.

For spatially-correlated initial ion distributions, u_i will take negative values and reduce DIH, increasing $\Gamma_{\rm eq}$. This calculation is repeated in Sec. 3.3 and 3.4 for correlations associated with Rydberg-blockaded and optical-lattice-trapped atoms, which increase the binding energy and so also increase $\Gamma_{\rm eq}$ to reduce beam emittance.

3.2 Molecular dynamics simulations of disorder-induced heating

To quantify suppression of DIH in an expanding beam, an N-body 'molecular dynamics' (MD) simulation was developed, which solves the equations of motion for a system of particles by tracking all pairwise interactions. DIH was simulated in an infinite homogeneous system of ions with linear expansion by using periodic boundary conditions (PBCs) with a cubic geometry, in a 'comoving' (self-similarly expanding) coordinate system [111], using equations of motion from the direct Ewald summation method [112]. This comoving frame Ewald method was chosen rather than simpler reflective-boundary or minimum-image methods, as the latter were found to have greater numerical errors associated with particle-boundary crossings, for similar computation time.

In a comoving coordinate frame, self-similar uniform expansion is accounted for using a scale factor α, calculated for the free Coulomb expansion of ions of mass m at an initial number density n', using Gauss' law for a uniform-density sphere of charge, as

$$\frac{d^2\alpha}{dt^2} = \frac{n'e^2}{3\varepsilon_0 m\alpha^2}, \tag{3.4}$$

where $\alpha = 1$ immediately following ionisation and $\alpha = 2$ would, for example, indicate doubling of the system dimensions. The comoving frame spatial coordinates $\mathbf{x}'_i$ for ion $i \in \{1, 2, ..., N\}$ of a system of N ions is related to its 'proper' (laboratory frame) spatial coordinates $\mathbf{x}_i$ as

$$\mathbf{x}'_i = \frac{1}{\alpha}\mathbf{x}_i, \tag{3.5}$$

with comoving velocity

$$\frac{d\mathbf{x}'_i}{dt} = \frac{1}{\alpha}\left(\frac{d\mathbf{x}_i}{dt} - \frac{d\alpha}{dt}\mathbf{x}'_i\right) \tag{3.6}$$

and acceleration

$$\frac{d^2\mathbf{x}'_i}{dt^2} = \frac{1}{\alpha}\left[\frac{d^2\mathbf{x}_i}{dt^2} - \frac{d^2\alpha}{dt^2}\mathbf{x}'_i\right] - \frac{2}{\alpha}\frac{d\alpha}{dt}\frac{d\mathbf{x}'_i}{dt}. \tag{3.7}$$

The square-bracketed [...] terms of Eq. 3.7 include the inter-ionic Coulomb interactions in the proper frame, Eq. 1.9, with subtraction of linear expansion forces. The last term of Eq. 3.7 represents adiabatic expansion damping of the comoving velocity.

Ewald transformation gives inter-particle potentials that lead to convergent

non-expanding force sums where, otherwise, the long-ranged nature of the Coulomb interaction would cause the sum in Eq. 1.9 to diverge (see Ref. [113] for derivation of the potentials). The Ewald method involves placing Gaussian negative-charge distributions of comoving standard deviation γ' around each positive point charge to allow the sum of the forces in real space to converge, then adding a sum in reciprocal space of equally-placed positive shielding potentials to counteract their effect in the real-space sum. Taking the gradient of these potentials in the comoving coordinates gives the interparticle forces (see Refs. [114, 115] for derivation) that become the square-bracketed terms of the comoving acceleration (Eq. 3.7) as

$$\left[\frac{d^2\mathbf{x}_i}{dt^2} - \frac{d^2\alpha}{dt^2}\mathbf{x}'_i\right] = \frac{1}{m}\left(\mathbf{F}_i^{(1)} + \mathbf{F}_i^{(2)}\right), \tag{3.8}$$

where the real-space force sum

$$\mathbf{F}_i^{(1)} = \frac{e^2}{4\pi\varepsilon_0\alpha^2}\sum_{j\neq i}\sum_{\mathbf{n}}\frac{\mathbf{r}'_{i,j\mathbf{n}}}{\left|\mathbf{r}'_{i,j\mathbf{n}}\right|^3}\left\{\operatorname{erfc}\left(\frac{\left|\mathbf{r}'_{i,j\mathbf{n}}\right|}{\sqrt{2}\gamma'}\right) + \sqrt{\frac{2}{\pi}}\frac{\left|\mathbf{r}'_{i,j\mathbf{n}}\right|}{\gamma'}\exp\left(-\frac{\left|\mathbf{r}'_{i,j\mathbf{n}}\right|^2}{2\gamma'^2}\right)\right\}, \tag{3.9}$$

which uses the complementary error function $\operatorname{erfc}(z) = 1 - \operatorname{erf}(z)$, is taken over all $j \neq i$ ions and their $\mathbf{n} \in \mathbb{Z}^3$ periodic images ($\mathbb{Z} = \{..., -2, -1, 0, 1, 2, ...\}$) with comoving separations $\mathbf{r}'_{i,j\mathbf{n}} = \mathbf{x}'_i - \left(\mathbf{x}'_j + \mathbf{n}L_0\right)$. The side length of the periodic boundary for a simulation of N ions at initial density n' is $L_0 = (N/n')^{1/3}$. The reciprocal space force sum

$$\mathbf{F}_i^{(2)} = \frac{2e^2}{4\pi\varepsilon_0\alpha^2 L_0^2}\sum_{j\neq i}\sum_{\mathbf{h}\neq\mathbf{0}}\frac{\mathbf{h}}{|\mathbf{h}|^2}\exp\left(-2\left(\frac{\gamma'\pi}{L_0}\right)^2|\mathbf{h}|^2\right)\sin\left(\frac{2\pi}{L_0}\mathbf{h}\cdot\mathbf{r}'_{i,j\mathbf{0}}\right) \tag{3.10}$$

is taken over the reciprocal lattice vector, $\mathbf{h} \in \mathbb{Z}^3$, of the simple-cubic periodic boundary. The approximation of Ref. [114] was used, where the sums converge for the choice of parameters $\gamma' = L_0/\sqrt{2}$ with sums over $\mathbf{n}$ so that $\left|\mathbf{r}'_{i,j\mathbf{n}}\right| \leq 2.6\, L_0$ and sums over $|\mathbf{h}| \leq 8$.

The ions were generated with zero initial temperature. Simulations showed no observable differences when repeated with initial temperatures of 100 μK, the typical temperature of atoms in a MOT. The comoving equations of motion were integrated numerically using the Bulirsch-Stoer method with polynomial extrapolation [116].

Adaptive time steps in the Bulirsch-Stoer integrator were constrained to limit the integration errors for the comoving velocities to less than one part in 10^6 of

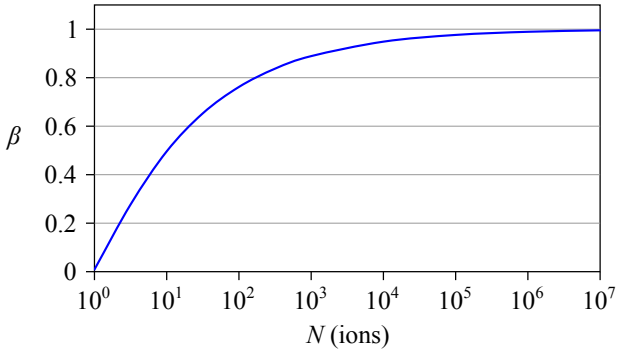

Figure 3.1: Variation of the temperature correction factor β, which corrects for periodic-boundary-induced correlation in molecular dynamics simulations of the disorder-induced heating of one-component plasma, and its variation with the simulated ion number N.

a comoving velocity scale

$$\Delta v' = \frac{e^2}{\sqrt{4\pi\varepsilon_0 \alpha a' k_B \Gamma_{\mathrm{eq}} m}}, \tag{3.11}$$

defined by the root-mean square velocity of a Maxwell-Boltzmann distribution for a plasma of initial Wigner-Seitz radius a' with $\Gamma_{\mathrm{eq}} = 2$, providing a constant error for the emittance in the expanding frame. A limit on the length of a time step was also placed to give a plasma phase difference of at most 1/20th of a full plasma oscillation between steps to ensure visibility of the kinetic energy oscillations.

The key parameter extracted from the simulations is the temperature of the system and its variation in time. The equilibrium temperature is dependent on the interparticle spatial correlations, but periodic boundaries introduce cubic spatial correlations at the repeating boundary length scale, so that the effect of the periodicity must be included. These correlations can be included in the calculation of DIH by adding to the binding energy of a simple cubic lattice with boundary-length lattice-site separation [117]

$$u_{\mathrm{PBC}} = -\frac{e^2}{4\pi\varepsilon_0 a} \frac{M_{\mathrm{sc}}}{2N^{1/3}}, \tag{3.12}$$

to the initial binding energy, where $M_{\mathrm{sc}} = 1.76012$ is the Madelung constant of a simple-cubic lattice. u_{PBC} gives the potential with which an ion is bound in position to the static structure defined by the cubic periodicity of the boundary conditions with lattice constant L_0. For the periodic-boundary simulations with $N = 1000$, addition of the periodic initial binding energy in the calculation of

DIH equilibration results in an equilibrium coupling parameter of $\Gamma_{\rm eq} = 2.51$, increased from the prediction of $\Gamma_{\rm eq} = 2.23$ for an infinite distribution.

The ratio of the coupling parameters predicted for a PBC simulation to an infinite non-periodic simulation, $\beta = \Gamma_{\rm eq}(N \to \infty)/\Gamma_{\rm eq}(N)$, gives the factor by which the equilibrium temperature is lowered for a PBC simulation compared to the expected theoretical result for an infinite distribution. This factor β, plotted against N, in Fig. 3.1, was used to correct the temperature recorded from the N-body simulations to remove the influence of the periodic boundaries. The simulations thereby represent, and can be used to verify, theoretical calculations of DIH equilibration for an infinite distribution. The temperature recorded at each time step in the simulation was calculated from the comoving velocities, accounting for the effects of adiabatic cooling and periodic-boundary correlation, as

$$T = \frac{k_B m_i \alpha^2}{3\beta N} \sum_i^N \left| \frac{d\mathbf{x}_i'}{dt} \right|^2 . \tag{3.13}$$

Simulations were performed first without expansion by setting $\alpha = 1$ and $d\alpha/dt = 0$, at zero initial temperature. Figure 3.2 shows the results of a simulation performed for non-expanding, disordered ions at particle density $n = 10^{16}\,\mathrm{m}^{-3}$. The results show kinetic energy oscillations [40] of the temperature T in time t at the plasma frequency $\omega_{\rm p}$, as the initially cold ions accelerate towards and overshoot positions of local potential minima. By plotting the Coulomb coupling parameter Γ against the plasma phase $\varphi = \omega_{\rm p} t$, the simulation becomes dimensionless and independent of the ion mass or density, thereby being applicable to any uncorrelated source of particles. The ions rapidly reach and oscillate about a correlation temperature of 2.6 K for an equilibrium coupling parameter of $\Gamma_{\rm eq} = 2.23$. Simulations repeated with initial temperatures of 100 μK showed negligible difference in $\Gamma_{\rm eq}$.

Ions with unrestricted Coulomb expansion were then simulated in the comoving frame of reference, to calculate the beam emittance. The definition of emittance (Eq. 1.7) was generalised to a form independent of the initial bunch size

$$\tilde{\epsilon} \equiv \frac{\alpha}{c}\sqrt{\frac{k_B T}{m}} \tag{3.14}$$

such that a spherical ion bunch of initial RMS size $\sigma_{\rm x}'$ expanded to a size $\alpha\sigma_{\rm x}'$ would have an emittance $\epsilon = \sigma_{\rm x}'\tilde{\epsilon}$. Expanding ion bunches cool adiabatically, with decreasing plasma frequency for increasing system size as $\omega_p \propto \alpha^{-3/2}$. For a time-varying plasma frequency, the generalised plasma phase $\varphi = \int_0^t \omega_p dt'$ converges to $\varphi = 1.2\pi$, as $t \to \infty$ for the free Coulomb expansion (Eq. 3.4) of ions of

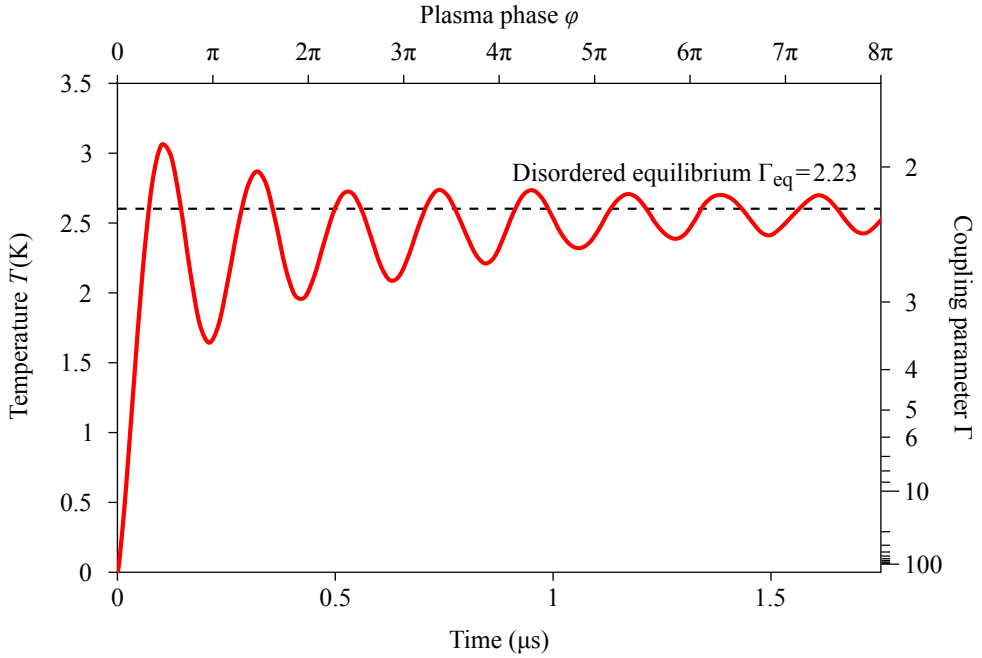

Figure 3.2: Disorder-induced heating for a confined (non-expanding) system of initially disordered ions at density $n = 10^{16}\,\mathrm{m}^{-3}$. The ions experience damped temperature oscillations about an equilibrium Coulomb coupling parameter $\Gamma_{\mathrm{eq}} = 2.23$.

any mass or initial density. Convergence of the plasma phase implies freezing of the ion motion in the expanding reference frame, so it may be expected that the emittance would reach an equilibrium value, as adiabatic expansion cooling preserves bunch emittance, decreasing the temperature as $T \propto \alpha^{-2}$ [36]. Instead, the simulations presented in Fig. 3.3 show unbound logarithmic emittance growth subsequent to the first temperature oscillation minimum at $\varphi = \pi$.

A model presented in Ref. [36] for the adiabatically-cooled temperature of an expanding system also predicted unbounded emittance growth, but did not capture the asymptotic behaviour of the system. For reference, the emittance is plotted in Fig. 3.3 alongside an effective source temperature $\alpha^2 T$ of equivalent-emittance non-interacting particles in the ion source region. The data show that for a bunch propagation time of $10\,\mu$s, typical of a CAEIS, initially cold ions would reach an emittance equivalent to that of ions produced from atoms with a temperature of 10 K, which would not experience DIH. To take advantage of the initially low temperatures of cold-atom sources producing bunched beams, DIH must therefore be suppressed through introduction of interparticle correlations.

To ensure that the emittance growth was not the result of the chosen boundary-conditions for the simulation, the Ewald-boundary results were compared to predictions for unbounded freely-expanding spherical distributions of ions. Ions were randomly placed within the spherical distributions of varying initial radius at the

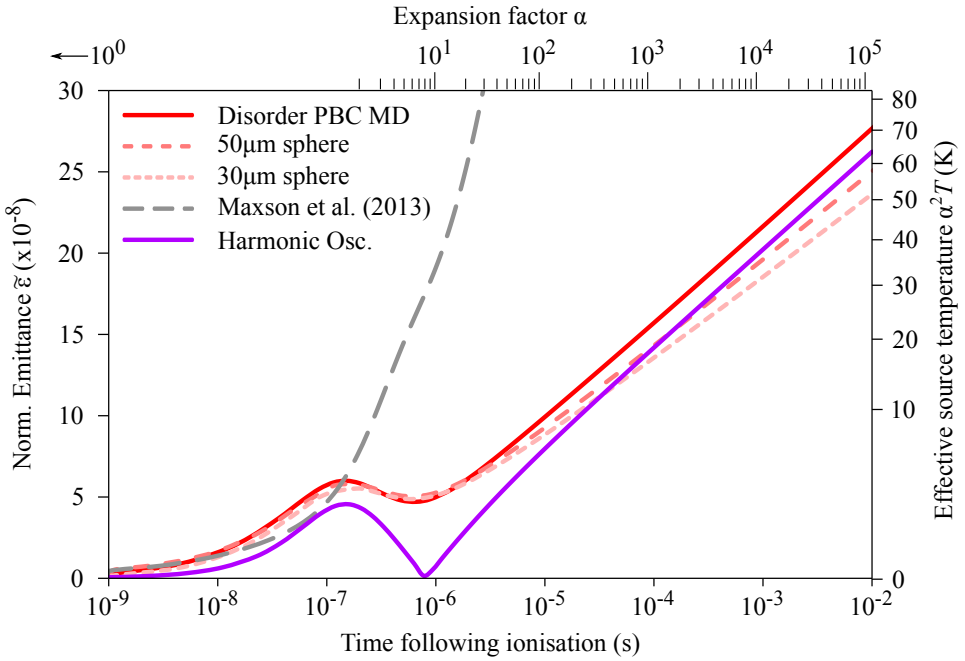

Figure 3.3: Disorder-induced emittance growth for initially disordered ions at density $n = 10^{16}\,\mathrm{m}^{-3}$, with free uniform space-charge expansion. A model for the bunch temperature evolution [36] is found to over-predict the emittance growth at times beyond the first oscillation maxima. Non-periodic simulations for spherical ion bunches of $30\,\mu$m and $50\,\mu$m radius show convergence to the results of periodic boundary condition (PBC) molecular-dynamics (MD) simulation. The harmonic oscillator model for DIH in expanding coordinates qualitatively matched the features of the simulations.

same initial density of $n' = 10^{16}\,\mathrm{m}^{-3}$. For these open-boundary simulations, the equations of motion were solved in the proper frame, from Eq. 1.9 only. The spherically-distributed ions converged to the periodic-boundary results with increasing radius, as shown in Fig. 3.3. Spherical distributions of smaller radius had lower emittance due to their higher surface-to-volume ratio, as ions at the surface of the expanding sphere have fewer adjacent ions with which to undergo disorder-induced heating.

DIH results from harmonic motion of individual, initially stationary ions about local dynamic (rather than fixed) equilibrium positions. Ion kinetic energy oscillations can be modelled, in a mean-field treatment, as harmonic oscillation of one particle in one dimension at the plasma frequency ω_p. For a single ion, taking an initial displacement

$$x_0 = \frac{2e^2}{\sqrt{4\pi\varepsilon_0 a k_B \Gamma_{\mathrm{eq}} m \omega_p^2}} \tag{3.15}$$

from an equilibrium position with restoring acceleration $d^2x/dt^2 = -\omega_p^2 x$ results in a temperature oscillation about an equilibrium value determined by the non-

expanding equilibrium coupling parameter Γ_{eq}. Fig. 3.3 shows the emittance for a harmonic oscillator with expansion in the comoving coordinates, with logarithmic asymptotic behaviour matching that for the expanding ion bunches.

Having established simulations predicting the asymptotic behaviour of expanding disordered ion bunches, investigations were performed into using positional correlations for the suppression of the emittance growth in ion bunches.

3.3 Suppressing DIH with Rydberg blockade

In this section, an investigation is presented into the suppression of DIH in cold ion beams created through the ionisation of a blockaded Rydberg gas, where spatial correlations are introduced by inter-atomic interactions that prevent excitation of pairs of atoms that are in close proximity [118]. The DIH process was modelled using 'hard sphere' initial correlations [119, 120] to derive the equilibrium temperature. Detailed molecular-dynamics (MD) simulations show that the suppression of DIH calculated in equilibrium holds during the emittance non-conserving, non-equilibrium expansion process for uniform bunches.

Previous simulations have suggested that equilibrium coupling parameters as high as $\Gamma_{\mathrm{eq}} = 35$, corresponding to much lower temperatures, may be reached in neutral non-expanding plasmas produced through ionisation of blockaded Rydberg atoms [103]. A pair of Rydberg atoms in a low angular momentum state with separation R interact, to leading order, via the van der Waals (vdW) potential $V(R) = -C_6/R^6$ [121]. In an ensemble of atoms exposed to radiation coupling a ground state to a Rydberg level, with power-broadened linewidth ν, any ground-state atom within the blockade radius $r_b = |C_6/\nu|^{1/6}$ of a Rydberg atom is prevented from being excited to the Rydberg level by the effect of vdW interaction on the resonance condition. For two rubidium atoms in the 60S state that have $C_6 = -140\,\mathrm{GHz}\,\mu\mathrm{m}^6$ excited from the 5P intermediate state with linewidth $\nu = 6\,\mathrm{MHz}$, the blockade radius of $r_b = 5\,\mu\mathrm{m}$ [122] exceeds the mean interparticle separation a of a random distribution at the typical ion density of $n = 10^{16}\,\mathrm{m}^{-3}$. Under such conditions, a blockaded Rydberg atom ensemble has spatial correlations resembling those of a gas of randomly-packed hard spheres of radius $r_b/2$ [119]. Blockade therefore provides a mechanism for spatially correlating the atoms used to produce a cold ion beam, towards suppression of DIH and consequent reduction of the effective source temperature. See Sec. 4.2 for further discussion of the mechanism of Rydberg blockade.

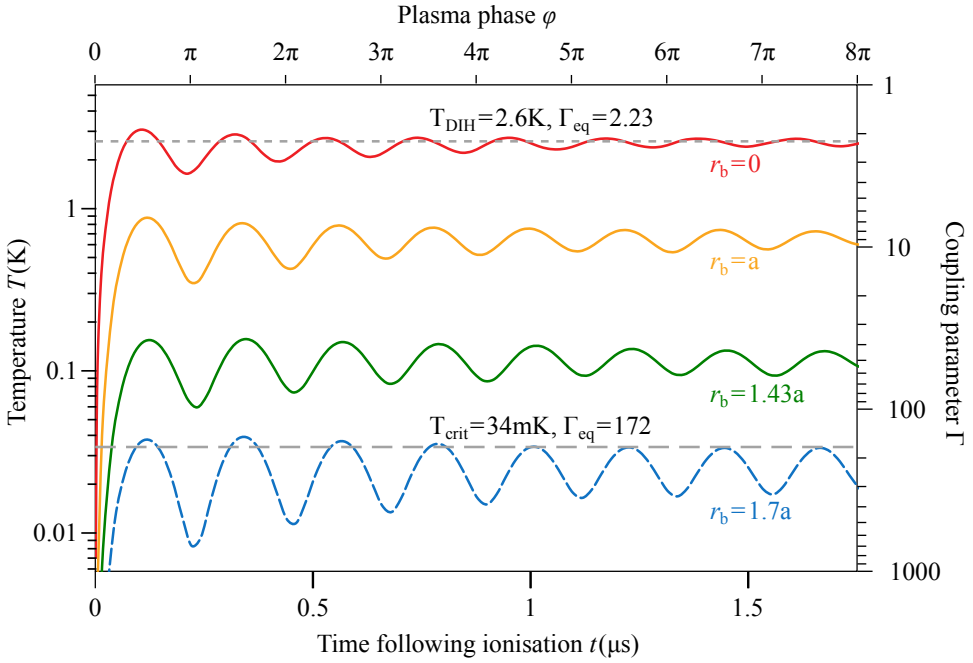

Figure 3.4: Disorder induced heating of non-expanding ion bunches with hard-sphere initial correlations, labelled by the blockade parameter r_b/a. Emittance and temperature are calculated in time and in plasma phase φ, which is 2π times the number of plasma periods after ionization, for ^{85}Rb ions at density $n' = 10^{16}\,\mathrm{m}^{-3}$. Damped kinetic energy oscillations at twice the plasma frequency ω_p due to harmonic ion motion are observed. Hard-sphere Rydberg blockade reduces the equilibrium temperatures from the disordered ($r_b = 0$) correlation temperature $T_{\mathrm{corr}} = 2.6\,\mathrm{K}$, to near the crystallisation phase-boundary at $T_{\mathrm{crit}} = 34\,\mathrm{mK}$.

The thermal equilibrium properties of a non-expanding ion bunch with Rydberg blockade correlations are considered first. Following creation of a blockaded Rydberg ensemble created in a volume defined by a two-laser excitation process [39], the model assumes complete ionisation of the Rydberg atoms by a switched electrostatic field in a time much less than the DIH timescale $\tau_{\mathrm{DIH}} = 2\pi/\omega_p$ (Eq. 3.2), which is achievable in existing MOT-based CAEIS accelerators [123]. The field accelerates the ions, and removes electrons from the system on a much shorter timescale than the ionic motion, such that the electrons have negligible effect on the ion temperature. Hard-sphere approximations for the vdW interaction have been shown to adequately approximate the spatial correlations [119] and excitation fractions [120] of high density blockaded Rydberg ensembles. The hard-sphere approximation allows calculation of the internal energy of the ion configuration as a function of a dimensionless blockade parameter r_b/a, to derive the equilibrium coupling parameter after DIH.

Ions with correlated initial positions have a non-zero initial binding energy so that less kinetic energy is gained per particle during thermal equilibration than

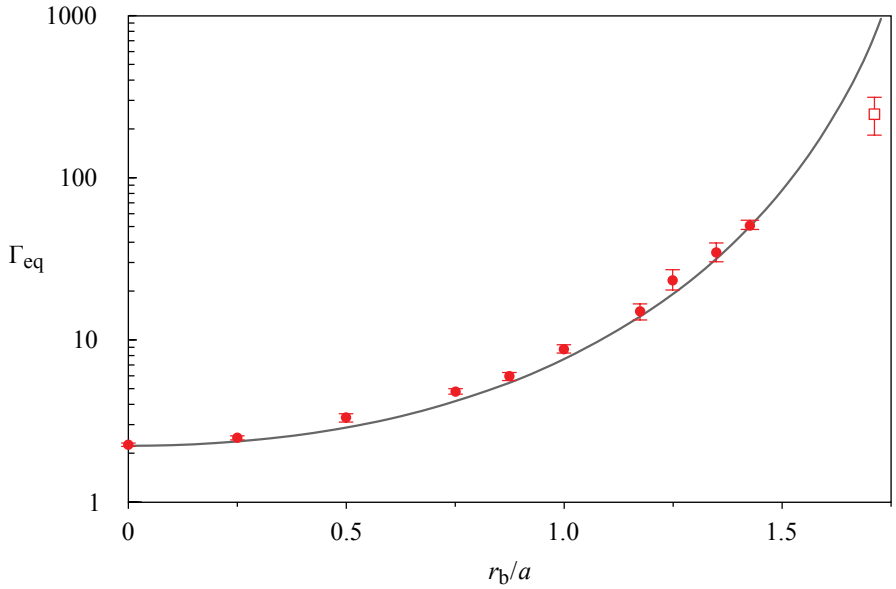

Figure 3.5: Equilibrium Coulomb coupling parameter Γ_{eq} of cold ion bunches with hard-sphere blockade parameter r_b/a calculated using the Percus-Yevick hard-sphere distribution function Γ_{PY} (solid line), and by molecular dynamics simulation for configurations generated by random sequential addition (circles) and for a random-close-packed distribution at $r_b/a = 1.7$ (square). Uncertainties in the MD data result from residual kinetic energy oscillations.

for a disordered distribution, leading to an increase in the Coulomb coupling parameter in the final state. The calculations of thermal equilibration outlined in Sec. 3.1 are modified to include this initial binding energy. For hard-sphere correlations, the Percus-Yevick (PY) equation gives a radial distribution function [124] that permits calculation of an analytic expression for the internal energy under Coulomb interactions [125],

$$u_{PY} = -\frac{3e^2\eta^{2/3}}{4\pi\varepsilon_0 a}\,\frac{1-\frac{1}{5}\eta+\frac{1}{10}\eta^2}{1+2\eta} \tag{3.16}$$

where $\eta = \frac{1}{8}(r_b/a)^3$ is the packing fraction of spheres of diameter r_b in the hard-sphere approximation. Conservation of energy with $u_i = u_{PY}$ then gives the PY hard-sphere equilibrium coupling parameter Γ_{PY} as a function of the blockade parameter r_b/a (Fig. 3.5). For a blockade parameter of $r_b/a = 1.2$ reported by experiments [120], $\Gamma_{PY} = 16$. The solution of Γ_{PY} for blockade parameters r_b/a underpins the 'universal' behaviour of the coupling parameter and its dependence on atomic density observed in the Rydberg-UCNP simulations of Ref. [103].

In experiments where ordering is established through blockade, for the same initial atomic density the bunch charge will be smaller. In the presence of linear

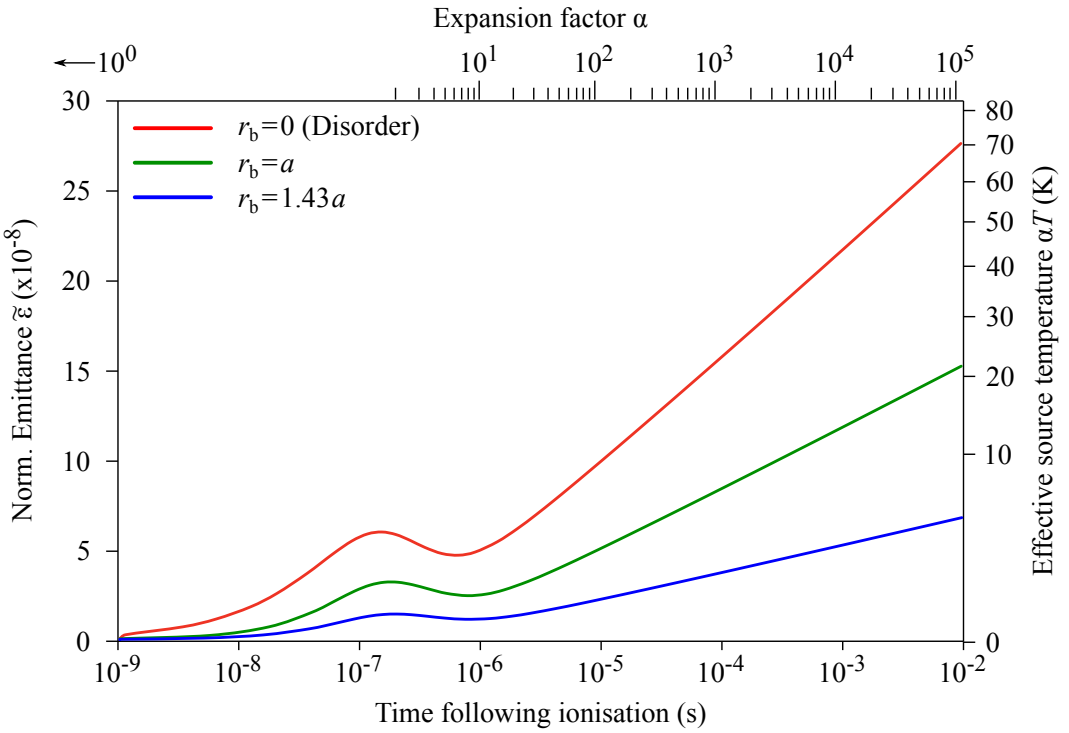

Figure 3.6: Dimensionless emittance $\tilde{\epsilon}$ and effective temperature growth caused by disorder-induced heating in freely expanding $^{85}Rb^{+}$ ion bunches at $10^{16}\,m^{-3}$ initial density, calculated by molecular-dynamics simulation. The presence of Rydberg blockade, labelled by the blockade radius in terms of the Wigner-Seitz radius, increases the initial ion correlations thereby reducing the heating.

space-charge expansion, higher density bunches expand more rapidly, however the beam brightness (Eq. 1.8) is independent of bunch charge for a fixed source temperature [126]. Bunches were simulated with equal initial ion densities $n' = 1 \times 10^{16}\,m^{-3}$ for the ordered and disordered cases, with equal expansion rates, to allow for fair comparison of beam emittance. To compare the behaviour of the Rb ion bunches that were simulated to other bunches of charged particles at different densities, including electrons, the timescales of the kinetic energy oscillations (Eq. 1.11), heating (Eq. 3.2) and expansion (Eq. 3.4) scale as $\sqrt{m/n'}$, with the emittance scaling as $\epsilon \propto \sqrt{n'^{1/3}/m}$ (Eq. 1.7 and 3.1).

$N = 1000$ ions were generated in simulation by random sequential addition of hard spheres in the periodic comoving cubic volume of side length $L_0 = (N/n')^{1/3}$, which generated configurations with blockade parameters up to $r_b/a = 1.43$, close to the saturation limit [127]. To illustrate the behaviour of bunches with higher blockade parameters, a packing algorithm [128] was used to generate ion configurations close to the random hard-sphere close packing limit of $r_b/a \sim 1.72$.

Simulations were initially performed in the absence of expansion (setting $d\alpha/dt = 0$) to calculate the equilibrium coupling parameters Γ_{eq} for varying

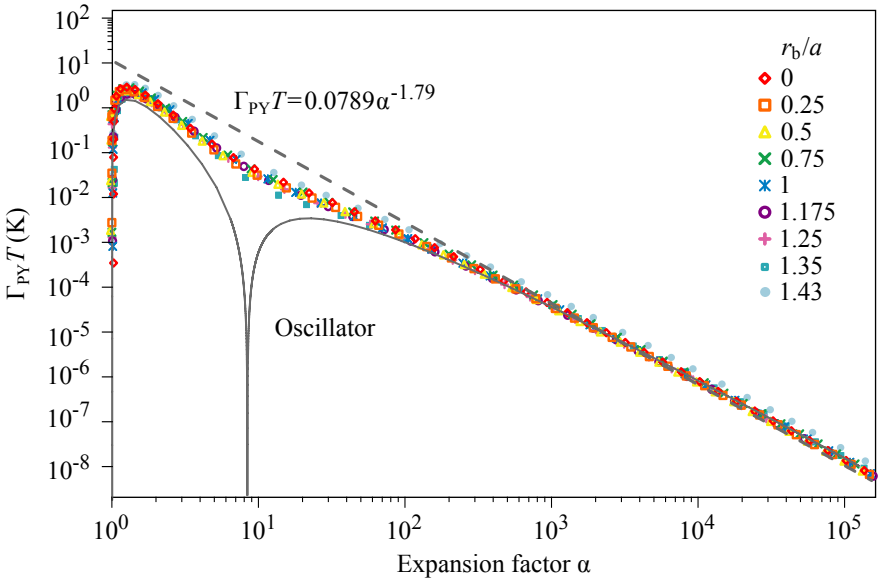

Figure 3.7: Universal asymptotic temperature behavior in the free Coulomb expansion of Rydberg-blockaded initial ion configurations, showing non-adiabatic power-law dependence of the temperature that matches the asymptotic behaviuor (dashed line) of simple harmonic motion (solid line) in the expanding coordinate system.

blockade parameters r_b/a in order to verify the PY prediction, shown in Fig. 3.4. The ion temperature was evaluated at each time-step using Eq. 3.13 with the $N = 1000$ correction factor $\beta = 2.23/2.51$, as calculated for a disordered distribution of $r_b/a = 0$ (Sec. 3.2), for all blockade parameters. The correction factor of a disordered distribution for the blockaded distributions was found to be sufficient for all blockade parameters to give agreement between the simulations and the theoretical predictions for an infinite-size distribution. The equilibrium emittance and temperature were observed to decrease as the blockade parameter was increased. The equilibrium coupling parameters for each simulation were found by averaging over the plasma phase, which for a non-expanding bunch is the product of plasma frequency and time, between 8π and 16π. The MD simulations verify the PY-OCP theory (Fig. 3.5) for distributions generated up to $r_b/a = 1.43$ in non-expanding thermal equilibrium.

The simulations were then repeated for freely expanding ion bunches. The results, presented in Fig. 3.6, showed clear reduction in the magnitude of the emittance growth for blockaded initial distributions. No equilibrium is reached for an expanding system, but the ratio of emittances for a blockaded to disordered system can be determined from the results of the the non-expanding equilibrium calculations shown in Fig. 3.5. According to the harmonic oscillator description

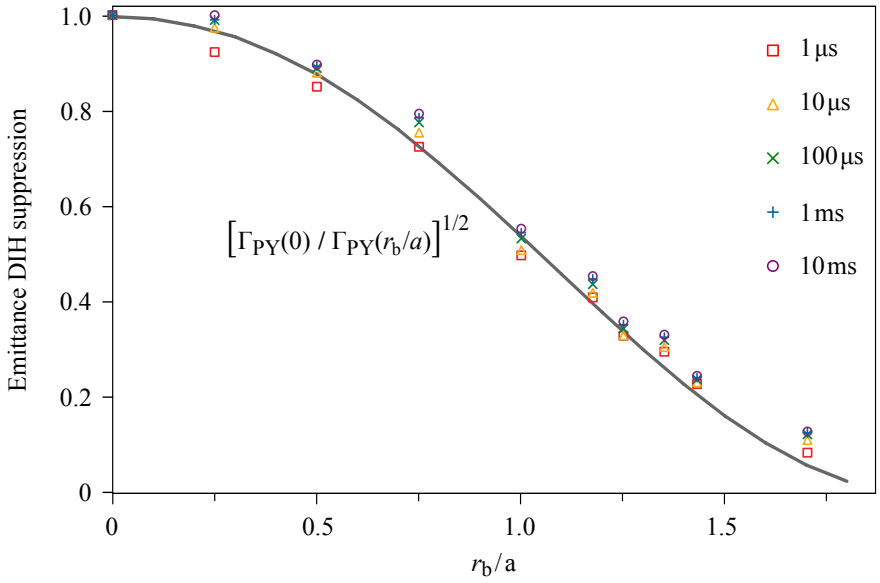

Figure 3.8: Suppression of disorder-induced heating, expressed as the ratio of blockaded to disordered emittance for different blockade parameters at different expansion times. The suppression remains constant throughout the linear Coulomb expansion process, as predicted with the hard-sphere model for the thermal equilibrium coupling parameter (solid line).

of DIH, the magnitude of the plasma temperature during expansion (Fig. 3.3) is proportional to the predicted equilibrium coupling parameter (Eq. 3.15), here Γ_{PY}, for each blockade parameter.

Figure 3.7 shows that the oscillator model predicts the asymptotic behaviour of the temperature for all simulations in the range of validity for the Percus-Yevick prediction as $T \propto \Gamma_{PY}^{-1}\alpha^{-1.79}$. The non-adiabatic temperature scaling with expansion (exponent $\neq -2$) leads to the emittance growth shown in Fig. 3.3. The reduction of the emittance, and the suppression of DIH, can then be quantified using the proportionality of beam emittance to equilibrium coupling parameter $\epsilon \propto \Gamma_{eq}^{-1/2}$, to give the ratio of the emittance for a blockaded system with equilibrium coupling $\Gamma_{eq} = \Gamma_{PY}(r_b/a)$ to the emittance of a disordered system which has $\Gamma_{eq} = 2.23$ as

$$\frac{\epsilon_{\text{blockade}}}{\epsilon_{\text{disorder}}} = \sqrt{\frac{2.23}{\Gamma_{PY}(r_b/a)}}. \tag{3.17}$$

The MD results of Fig. 3.8 verified that the suppression is unaffected by the expansion. The limit of the suppression depends on the extent of blockade. For an ion beam created from a system with $r_b/a = 1.2$ [120], an equilibrium coupling parameter $\Gamma_{eq} = 16$ was predicted, with an emittance lowered by a

factor of 2.6. This emittance reduction would lead to a sevenfold increase in transverse brightness (Eq. 1.8), which is proportional to ϵ^{-2}.

3.4 Suppressing DIH with optical lattices

It has been shown, in the context of ultracold neutral plasmas (UCNPs), that DIH can be entirely prevented through ionisation of atoms trapped in optical lattices, which have a crystal-like structure formed in the interference of high-intensity laser beams [102]. Prevention of DIH requires that single atoms occupy a high fraction ($f > 0.99$) of the optical lattice sites. However, preparation of single atoms in lattice sites is typically limited to $f \leq 0.5$, as lattice sites initially holding many atoms lose those atoms in pairs through collisions [129]. It may be possible to excite (and subsequently ionize) single Rydberg atoms with high effective filling fraction in a lattice with many ground-state atoms per lattice site [130], overcoming the requirement of single-atom trapping. Models to date have been applied only to the high filling fraction limit, and have not been extended to predict the equilibrium value of the Coulomb coupling parameter for lattice-correlated UCNP at filling fractions $0 < f < 0.99$. In this section, the suppression of DIH is calculated for ion beams created from single-atom site-occupancy optical lattices for $f < 0.99$. The calculations are performed for experimentally relevant initial ion temperatures using the equation of state of the strongly-coupled one-component plasma (OCP).

Equilibration of the Coulomb coupling parameter after DIH can be calculated via conservation of energy between the electrostatic potential energy of the initial lattice distribution, and the thermal and binding energy of the OCP equilibrium distribution. The initial potential energy for the partially-filled lattice can be derived considering the scaling the energy compared to a fully-filled lattice. A fully-filled lattice system of N' point charges with Wigner-Seitz radius a' occupying the sites of a lattice has a total electrostatic energy $N'u_M$, with electrostatic potential energy per particle [113]

$$u_M = -\frac{e^2}{4\pi\varepsilon_0 a'}\frac{M}{2}, \tag{3.18}$$

where M is the Madelung constant for the lattice. If only a fraction f of the lattice sites are charged, then the electrostatic energy is scaled as f^2, which is shared between the reduced number of charges $N = fN'$ that have Wigner-Seitz radii scaling to the full-lattice value as $a = f^{1/3}a'$. Accounting for the various

scaling factors[1], the internal binding energy per particle of a system of charged particles with Wigner-Seitz radius a occupying a fraction f of the sites of a lattice structure with Madelung constant M can therefore be written as

$$u_i = -\frac{e^2}{4\pi\varepsilon_0 a}\frac{f^{2/3}M}{2}. \tag{3.19}$$

Atoms with initial temperature T_i in lattice sites with harmonic trapping angular frequency ν are displaced from the lattice sites by standard deviation $\sigma = \sqrt{k_\mathrm{B}T_i/(m\nu^2)}$ in each axis. Thermal displacement reduces the initial binding of the ions compared to the zero-temperature case by addition of a value that can be written for small displacements to first order in $(\sigma/a')^2$ as [102]

$$\Delta = \frac{e^2}{4\pi\varepsilon_0 a}\frac{3f^{2/3}}{2}\left(\frac{\sigma}{a'}\right)^2, \tag{3.20}$$

which includes the scaling with f as in Eq. 3.19, in terms of the Wigner-Seitz radius for the *lattice* sites, a'.

Equating the initial and equilibrium energies for conservation of energy as in Sec. 3.1, excluding the relatively small k_i, results in the expression

$$\frac{1}{2}f^{2/3}\left(M - 3\left(\frac{\sigma}{a'}\right)^2\right) = A + B\,\Gamma_\mathrm{eq}^{-2/3} + \left(C - \frac{3}{2}\right)\Gamma_\mathrm{eq}^{-1}, \tag{3.21}$$

from which Γ_eq can be calculated in terms of M, f and σ/a', and the equilibrium plasma parameters from Eq. 3.3. At typical CAEIS densities of $n = 10^{16}\,\mathrm{m}^{-3}$ and initial temperatures $T_i < 1\,\mathrm{mK}$, excluding the small initial kinetic energy term has negligible effect on the results of the calculation for $f < 0.99$, which then gives results for Γ_eq only in terms of the dimensionless lattice constant M, filling fraction f and displacement parameter σ/a'.

Molecular dynamics simulations were performed to verify the calculations of DIH for the partially filled lattices, initially without expansion. Simulations were performed for simple cubic (SC), face-centred cubic (FCC) and body-centred cubic (BCC) lattices, which are experimentally realisable with suitable choices of laser geometry [131–133], and have Madelung constants $M_\mathrm{sc} = 1.76012$, $M_\mathrm{fcc} = 1.79175$ and $M_\mathrm{bcc} = 1.79186$ respectively [134]. Ion positions were set at the lattice sites for a range of filling fractions, choosing the cubic lattice dimensions so that the number of occupied sites was closest to 1000 for con-

[1] On this point, the calculations presented here using $u_i \propto f^{2/3}$ (Eq. 3.19) differ from the calculations in Ref. [102] that use $u_i \propto f^{5/3}$. The latter calculations are not consistent with the MD simulations for $0 < f < 0.99$ that follow here.

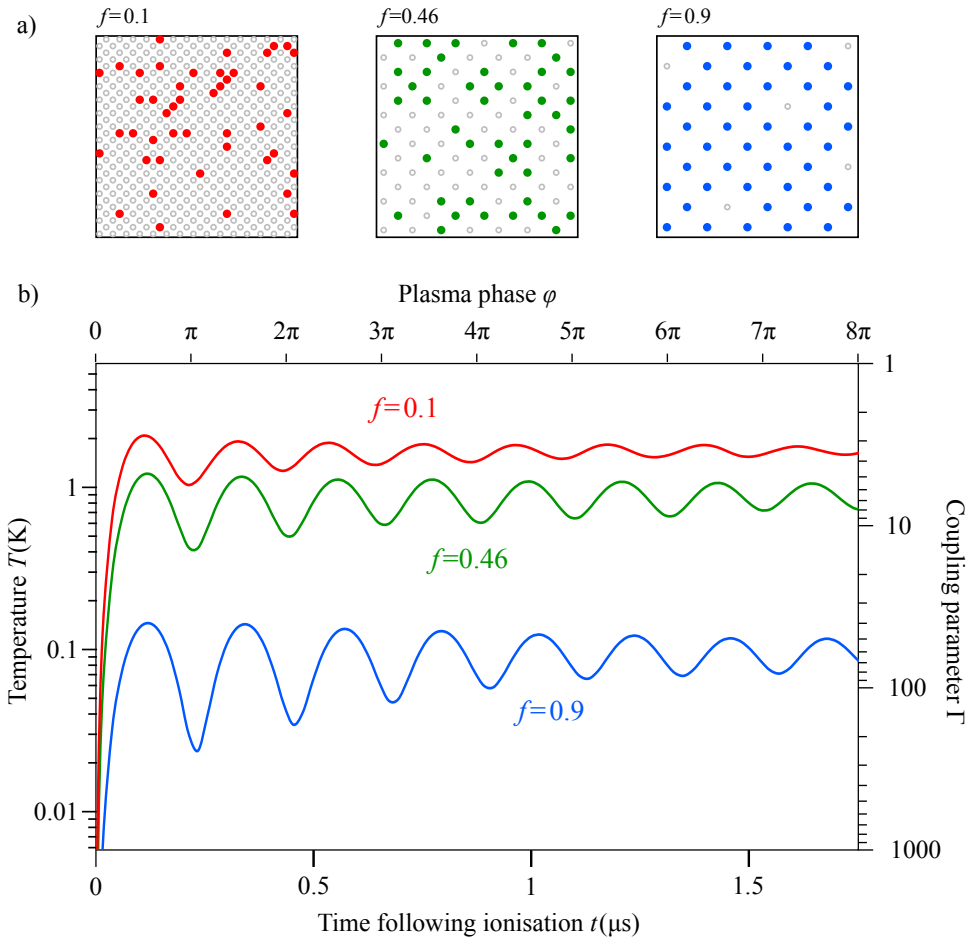

Figure 3.9: a) Two-dimensional lattices of different filling fraction f with the same atom density. The filled circles represent the position of atoms, and the empty circles represent vacancies within the lattice. b) Simulations of disorder induced heating in ionised rubidium atoms located at the sites of a three-dimensional body-centred cubic lattice with filling fraction f. Lattices of high filling fraction equilibrate to lower temperature and higher coupling parameter, reflecting increased interparticle spatial correlations in the initial distribution.

sistency. All simulations were performed for singly-charged ^{85}Rb ions of mass $m = 1.41 \times 10^{-25}\,\mathrm{kg}$, for the same ion number density $n = 10^{16}\,\mathrm{m}^{-3}$ by letting the lattice spacing vary. For simplicity, it was assumed that photoionisation is instantaneous, though negligible differences were observed in the equilibria of simulations repeated with ionisation times up to $\varphi < 0.1$ or 7 ns, typical of the duration of pulsed lasers used to ionise the atoms. Experimentally, lattice spacings are set by the laser wavelength and geometry. Low filling fraction typically corresponds to low density, but as the main results are dimensionless the density was fixed for notational convenience, allowing one-to-one correspondence between the temperature and coupling parameter. Figure. 3.9a) shows a two-dimensional representation of the initial positions for ions of different filling fraction but equal density.

The periodicity correction factor β for evaluating the ion temperature with Eq. 3.13 was calculated for each simulation for its given boundary length, filling fraction and lattice geometry. Correcting the simulations for each filling fraction is required because in the initial binding energy calculation, Eq. 3.19, it is assumed that the lattice vacancies are distributed randomly, but the periodic boundary conditions give the vacancies a simple-cubic repeating structure. The repeating images of the system introduce effective correlations into the ion position distribution at the scale of the boundary length [135]. Each ion that is 'removed' from a lattice site under periodic boundaries causes the remaining ions to retain one unit of simple-cubic binding energy relative to the removal of an equivalent fraction of ions from an infinite distribution. This residual binding energy can be accounted for in the calculations of the binding energy for a lattice-correlated system by introducing an additional term in the calculation of the initial energy

$$u_{\mathrm{PBC}}^{\mathrm{lattice}} = -\frac{e^2}{4\pi\varepsilon_0 a}\frac{(1-f)M_{\mathrm{sc}}}{2N^{1/3}}, \tag{3.22}$$

which is the vacant fraction lattice energy for the simple-cubic structure of the periodic boundaries, for a simulated ion number N. Calculations of Γ_{eq} including the boundary-correction term (Eq. 3.22) in the initial energy of the system can accurately predict the results of the simulations with finite size effects. Instead, to give results for a system without periodic boundary conditions, finite size effects were compensated for by calculating the correction factor for the evaluated simulation temperature (Eq. 3.13). The correction factor β is equal to the expected ratio of the predicted Γ_{eq} for an infinite system with $u_{\mathrm{PBC}} \to 0$ to the prediction of Γ_{eq} for a periodic-boundary system. Simulations for different lattice geometries and filling fractions differ slightly in ion number N due to the cubic scaling of N with lattice dimensions, and therefore also differ in correction factor.

Simulations of ions with zero initial temperature created in a 3-dimensional BCC lattice with different filling fractions are shown for example in Fig. 3.9b, corrected for the influence of the periodic boundaries. The ion temperature is plotted against time following ionisation, or in dimensionless terms plotted for the coupling parameter against plasma phase φ, exhibiting damped kinetic energy oscillations expected of equilibrating UCNP. Ions bunches created from atoms with high lattice filling fraction equilibrate to a lower temperature and higher coupling parameter than ions with low filling fraction, reflecting the increased initial correlations.

The equilibrium coupling parameter, Γ_{eq}, was evaluated from the simulations

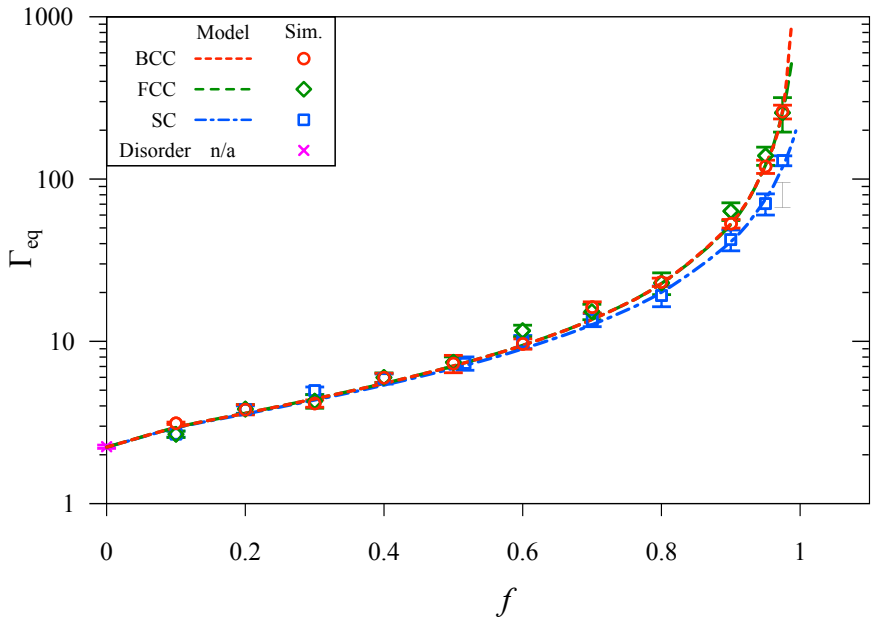

Figure 3.10: Calculated and simulated equilibrium coupling parameters Γ_{eq} for body-centred cubic (BCC), face-centred cubic (FCC) and simple-cubic (SC) lattices at different atomic filling fractions f, for atoms of zero initial temperature. Differences in equilibrium coupling between lattices result from the different binding energies in the initial state, with the BCC and FCC lattices reaching higher coupling than the SC lattice at fixed f. High filling fractions lead to increased Γ_{eq} compared to random (disordered) initial placement, which is equivalent to $f = 0$. Γ_{eq} was evaluated in simulation over plasma phases φ between 8π and 16π, with uncertainty as one standard deviation in that period.

by taking the average of the periodicity-corrected coupling parameters at each time step between plasma phases 8π and 16π. Figure 3.10 shows the simulated results for zero initial temperature ions of $\sigma/a' = 0$ for the body-centred, face-centred and simple cubic lattices at different filling fractions. These give strong agreement to the theoretical predictions calculated with Eq. 3.21 for the dependence of the equilibrium coupling parameter on the filling fraction for each lattice, and to the results for a disordered distribution with randomly placed ions, equivalent to a lattice with $f = 0$, which has $\Gamma_{eq} = 2.23$. Uncertainties in the simulation data result from residual kinetic energy oscillations during the evaluation period for Γ_{eq}. The BCC and FCC lattice results are similar, owing to their nearly-equal binding energies represented by the Madelung constants, while the SC lattice tended to have lower Γ_{eq} at high values of f due to its lower Madelung constant.

Ions with initial thermal displacement from the lattice sites have lowered equilibrium Coulomb coupling parameters compared to ions from lattices of the same f with zero initial temperature, because the displacements reduce the initial in-

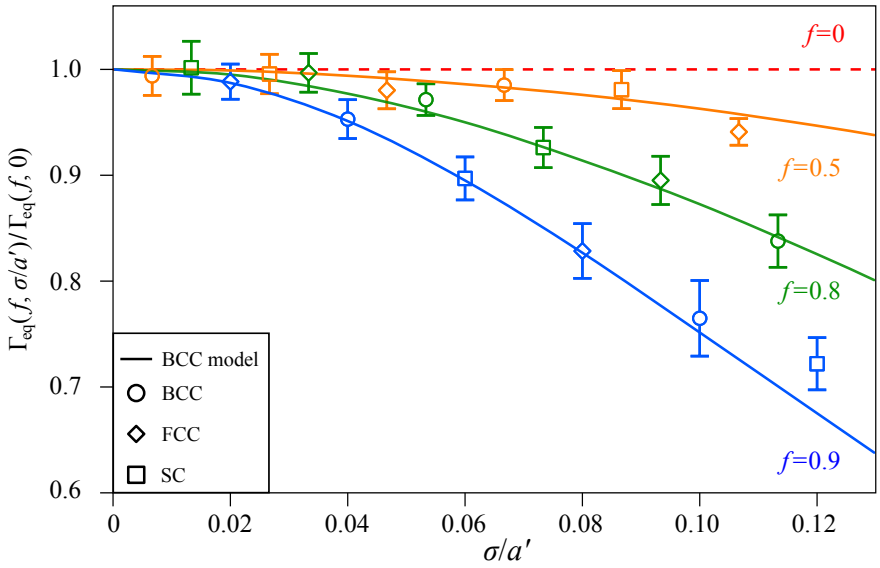

Figure 3.11: Lowering of the equilibrium coupling parameter due to thermal broadening of lattice sites, expressed as the ratio of the equilibrium coupling parameters for displaced to non-displaced atoms in lattices with filling fraction f. The atomic displacement σ is normalised to the Wigner-Seitz radius a' for the lattice sites. Simulations (data points) are performed for the simple cubic (SC), face-centred cubic (FCC) and body-centred cubic (BCC) lattices, and the theoretical calculations (solid lines) are shown for the BCC lattice only.

terparticle correlations. Simulations were repeated with thermal displacement parameters σ/a' for initial temperature $T_i = m\sigma^2\nu^2/k_\mathrm{B}$ for a typical trapping frequency of 15 kHz (i.e. $\nu = 94.25 \times 10^3\,\mathrm{s}^{-1}$). Each particle was assigned a random velocity using a Gaussian thermal distribution, for the chosen σ/a' parameter, and a random phase for the oscillatory harmonic motion in each axis, which together define a spatial displacement from the particle's lattice site.

Figure 3.11 shows theoretical predictions and simulation results for the factor by which Γ_eq is reduced for atoms with displacement parameter σ/a' compared to the zero-temperature result. The data points are the averages of the coupling parameter ratios for the displaced and zero-temperature simulations at each time step over the $8\pi < \varphi < 16\pi$ evaluation period, with uncertainties as one standard deviation. Simulations were performed for the SC, FCC and BCC lattices, however only predictions for the BCC lattice are shown as the ratios are not strongly dependent on the Madelung constant. Thermal displacements have greater impact on Γ_eq for lattices of high f, reducing the otherwise high spatial correlations, than for lattices of low f. For example, distributions with $f \to 0$ gain no additional disorder when the atoms are displaced. The predictions and simulations

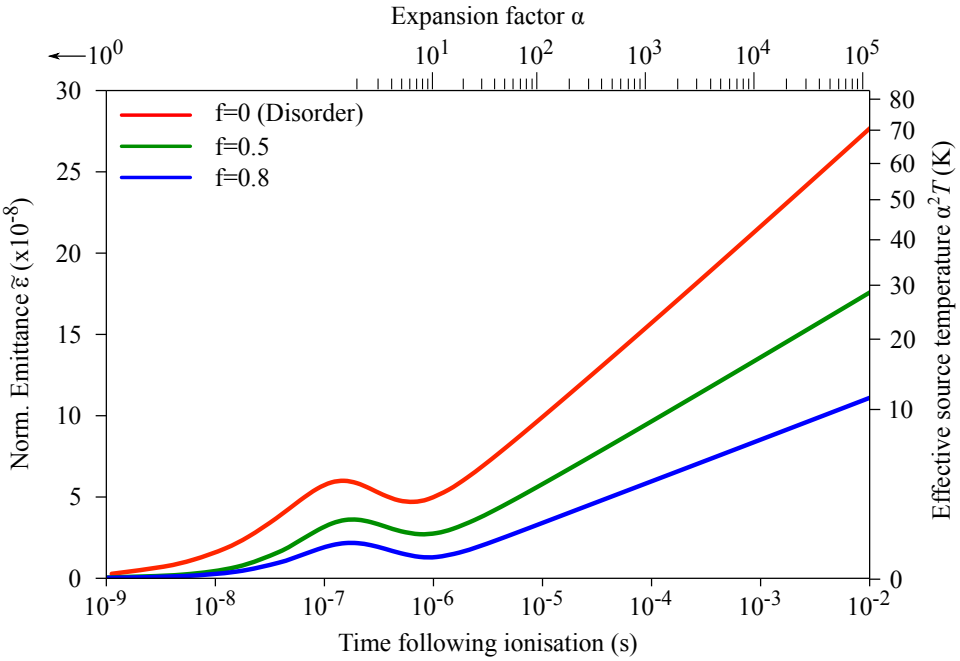

Figure 3.12: Disorder-induced emittance growth of an expanding BCC-correlated ion beam for different lattice filling fractions.

agreed up to $\sigma/a' = 0.1$, a relatively high parameter for lattice-trapped atoms. For example, $\sigma/a' = 0.087$ for caesium atoms at 10 μK in a 4.9 μm site-separation ($a' = 3.0\,\mu$m) simple-cubic lattice with 15 kHz trapping frequency [136].

The simulations for the BCC-correlated lattice were then repeated with free Coulomb expansion, shown for different filling fractions in Fig. 3.12. From these simulations, the suppression of the emittance growth (Eq. 3.17) was calculated as discussed in Sec. 3.3, at different times during beam expansion and compared to the theoretical calculations (Fig. 3.13). The results predict the degree of suppression of disorder-induced heating for freely-expanding ion bunches created from atoms in partially-filled optical lattices, dependent on the filling fraction f.

Previous calculations of the equilibrium Coulomb coupling parameter $\Gamma_{\rm eq}$ with partially-filled lattice correlations [102] suggested that only small improvements would be possible for experimentally achievable filling fractions $f \sim 0.5$. As a result, lattice correlations have not been pursued in the study of ultracold neutral plasmas as a method of achieving strong coupling. However, the results presented here show that by creating ion bunches from optical-lattice trapped atoms, even with imperfect filling fraction, an increase in $\Gamma_{\rm eq}$ may be achieved that is comparable to the expected increases using doubly-ionised atoms [137] or Rydberg-blockade correlated atoms [103]. Optical lattices are therefore a viable method for the reduction of DIH in ultracold neutral plasmas, with application to the production of low-emittance ion bunches.

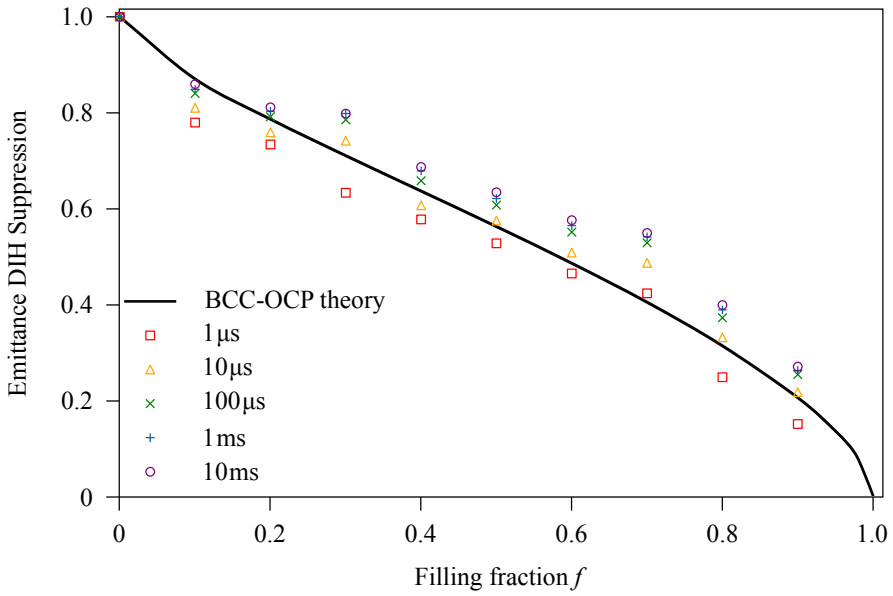

Figure 3.13: Suppression of DIH in an expanding beam using BCC optical lattice correlations for different filling fractions.

An ion beam created from the SC lattice example discussed above, at the single-atom occupancy limit of $f = 0.5$ with $\sigma/a' = 0.087$, would have $\Gamma_{\rm eq} = 6.7$, compared to $\Gamma_{\rm eq} = 2.2$ for disordered atoms, and therefore an emittance suppressed by a factor of 0.57. Increasing f beyond the single-atom occupancy limit may be achieved by exciting and then ionising Rydberg atoms within multiple-atom occupancy lattices, where the blockade mechanism would ensure that only one ion is created per lattice site [130]. Achieving an order of magnitude increase in $\Gamma_{\rm eq}$ would require $f = 0.76$ and cooling of the atoms within the lattice sites to eliminate thermal displacement effects.

3.5 Discussion

The potential for suppressing DIH in cold ion bunches using Rydberg blockade and optical lattices was calculated. The key parameters for quantifying the degree of initial atomic correlations were identified, and linked to experimental achievability: the blockade parameter r_b/a for Rydberg-blockade correlations, and the filling fraction f for optical lattices. The models presented here predict suppression of DIH that would enable strong coupling conditions to be established in ultracold neutral plasma studies, to provide a laboratory-based resource for the study of regimes of plasma physics occurring elsewhere only in astrophys-

ical environments such as the dense high-temperature interiors of gas giants and in white-dwarf stars [40].

Suppression of DIH in cold ions would be a significant milestone in the advancement of charged particle beam source technology, as the DIH effect otherwise presents a fundamental limitation to beam focusability and brightness [36]. The effects of Coulomb interactions within an ion bunch are equivalent to those in an electron bunch, but occur on a longer timescale due to the larger ion mass. The models presented in this chapter therefore place an experimental limit on the reduction of emittance for any high-density charged particle bunch, such as electrons used for single-shot, ultrafast diffraction studies. Ultimately, single-shot ultrafast electron diffraction may require electron beams of a phase-space density close to the quantum degeneracy limit [16], which will not be possible unless DIH is negligible. In conclusion, the results presented here quantitatively predict the extent to which disorder-induced emittance growth can be suppressed using Rydberg blockade and lattice correlations, and guide further development of high-brightness cold charged particle beams for applications including ultrafast electron diffraction.

In the following chapter, the Rydberg blockade method of correlation is implemented in the experimental production of ion beams from a cold atom source.

Chapter 4

Rydberg-atom ion bunches and their applications

The study presented in Sec. 4.3 of this chapter was published as Ref. [4] (Appendix A.4).

This chapter presents efforts towards the creation of a spatially correlated cold ion source through the ionisation of Rydberg blockaded atoms. Rydberg atoms are atoms with an electron excited to a state with high principal quantum number n. The high-n atom, with an electron weakly bound to the nucleus, is sensitive to external fields and inter-atomic interactions, which has made Rydberg atoms important in studies of quantum-based sensing, computing and information processing [138, 139].

Chapter 3 presented calculations of the disorder-induced heating (DIH) effect, showing that DIH is suppressed in strongly-blockaded Rydberg atom ensembles with large blockade radii r_b and small interparticle separations a (i.e. at high density). Experiments have demonstrated the production of blockaded cold atomic ensembles [140] and ultracold neutral plasmas [120], but to date have not measured the expected reduction of temperature associated with the increased spatial correlations and suppression of DIH [141].

Creation of a blockaded ion source would enable the first demonstration of the suppression of DIH in a charged particle beam through source correlations. This chapter presents three achievements towards this goal: implementation of Rydberg spectroscopy and excitation in the Melbourne cold-atom electron and ion source (CAEIS); measurements of the excitation blockade effect; and implementation of a coherent excitation scheme to prevent formation of the fluorescence halos described in Sec. 2.1.

4.1 Rydberg excitation and spectroscopy

Atoms in the CAEIS were photoexcited to Rydberg states using narrow-bandwidth continuous-wave lasers, and field-ionised to produce ion bunches. This section presents the implementation of spectroscopic techniques to identify and target Rydberg states, in particular the nS ($L = 0$) states, which have isotropic interactions leading to spherical blockade.

4.1.1 Rydberg energy levels and transition wavelengths

Singly-excited Rydberg states have hydrogenic energy levels approximated by the Rydberg formula

$$E_{\mathrm{n}} = E_\infty - \frac{hcR_M}{\mathrm{n}^{*2}}, \tag{4.1}$$

where E_∞ is the ionization energy of the atom, h is Planck's constant, c is the speed of light, $R_M = R_\infty/(1+m_e/M)$ is the Rydberg constant for an atom with nuclear mass M where $R_\infty = 10973731.568508(65)\,\mathrm{m}^{-1}$ is the Rydberg constant for an infinite-mass nucleus and $m_e = 9.10938356(11)\times10^{-31}\,\mathrm{kg}$ is the electron mass [142]. The effective principal quantum number n^* accounts for deviation from the energy levels of hydrogen due to the non-pointlike screened charge of the nucleus, given by $\mathrm{n}^* = \mathrm{n} - \mu_{\mathrm{n}}$ with quantum defect

$$\mu_{\mathrm{n}} = \sum_{j=0}^{\infty} \frac{\nu_j}{(\mathrm{n}-\nu_0)^{2j}}. \tag{4.2}$$

The leading terms for the quantum defect of the ^{85}Rb ($M = 1.409993418(17)\times10^{-25}\,\mathrm{kg}$) Rydberg spectra have been tabulated from experimental data [143], which for the $\mathrm{n}^2\mathrm{S}_{1/2}$ ($E_\infty = 6.69249468(1)\times10^{-19}\,\mathrm{J}$) series gives $\nu_0 = 3.13109(2)$, $\nu_1 = 0.204(8)$ and $\nu_2 = -1.8$ for $\mathrm{n} > 14$.

The quantum defects allow quick calculation of the laser wavelengths to target different Rydberg states. The $5\mathrm{P}_{3/2}$ ($E = 2.5459372(4)\times10^{-19}\,\mathrm{J}$ [144])$\rightarrow 60\mathrm{S}_{1/2}$ transition used in the blockade experiments later in the chapter, for example, has a transition energy of $4.13981\times10^{-19}\,\mathrm{J}$, or a vacuum wavelength of 479.839 nm.

4.1.2 Production and ionisation of Rydberg atoms

Rydberg atoms were excited at the overlap of two lasers within the atom cloud, as illustrated in Fig. 4.1 (cf. Fig. 2.1 and 2.7). The $5\mathrm{S}_{1/2}\,(\mathrm{F}=3) \rightarrow 5\mathrm{P}_{3/2}\,(\mathrm{F}=4)$ excitation transition was induced by a laser beam shaped to a uniform circular

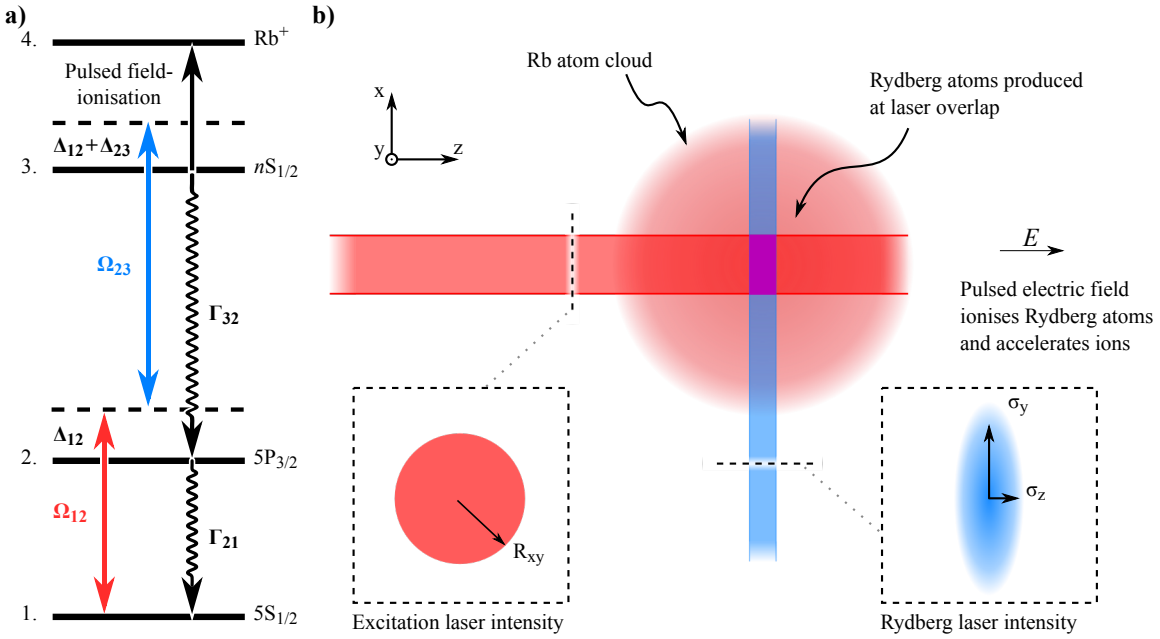

Figure 4.1: Production of Rydberg atoms within a CAEIS. a) Laser coupling energy level diagram. b) Laser geometry, with uniform intermediate-state excitation laser field with transverse radius R_{xy}, and transverse-propagation of Rydberg-coupling laser field with elliptical Gaussian intensity profile.

intensity distribution propagating along the z-axis direction (in the direction of eventual ion acceleration), defining the transverse profile of the overlap region as described in Ch. 2. The $5P_{3/2} \rightarrow nS_{1/2}$ transition was induced by an amplified and frequency-doubled $\lambda = 960\,\text{nm}$ diode laser system[2], which output continuous-wave $\lambda = 480\,\text{nm}$ light at up to 1 W power focused to an elliptical Gaussian ribbon propagating perpendicularly to the excitation beam, defining the longitudinal profile of the laser overlap region. The Rydberg-coupling pump laser was initially tuned to wavelengths calculated through the quantum-defects, with picometre accuracy measurement provided by an interferometric wavelength meter[3].

Rydberg continuous-wave-laser excitation and pulsed-field ionisation was described by a three-level ladder process, presuming complete ionisation of the Rydberg atoms at times following the establishment of steady-state conditions. To predict the Rydberg excitation fraction and describe the laser-dependent excitation dynamics, the time evolution of the density matrix was used,

$$\dot{\rho}_{ij} = -\frac{i}{\hbar}\left[\hat{H}, \rho\right]_{ij} + \hat{\mathcal{L}}(\rho)_{ij}, \qquad \text{(2.2 revisited)}$$

[2] Toptica TA-SHG Pro, linewidth <500 kHz
[3] High Finesse WS-6

for the three-level system with Hamiltonian

$$\hat{H} = \frac{\hbar}{2}\begin{bmatrix} 0 & \Omega_{12} & 0 \\ \Omega_{12} & -2\Delta_{12} & \Omega_{23} \\ 0 & \Omega_{23} & -2\left(\Delta_{12}+\Delta_{23}\right) \end{bmatrix}, \tag{4.3}$$

and decay terms

$$\begin{aligned} \hat{\mathcal{L}}(\rho) &= \frac{\Gamma_{21}}{2}\begin{bmatrix} 2\rho_{22} & -\rho_{12} & 0 \\ -\rho_{21} & -2\rho_{22} & -\rho_{23} \\ 0 & -\rho_{32} & 0 \end{bmatrix} \\ &+ \frac{\Gamma_{32}}{2}\begin{bmatrix} 0 & 0 & -\rho_{13} \\ 0 & 2\rho_{33} & -\rho_{23} \\ -\rho_{31} & -\rho_{32} & -2\rho_{33} \end{bmatrix}. \end{aligned} \tag{4.4}$$

As introduced in chapter 2, the diagonal terms of the density matrix describe the fractional occupancies of the ground, excited and Rydberg states, and the off-diagonal terms represent the cross-state coherences. Excitation fractions can therefore be calculated from the spatially- and temporally-varying laser intensities I_{ij}, using the Rabi frequencies

$$\Omega_{ij} = \sqrt{2d_{ij}^2 I_{ij}/c\varepsilon_0\hbar^2}, \tag{2.5 revisited}$$

with dipole matrix elements tabulated as $d_{12} = 2.99ea_0$ for the $5S_{1/2} \rightarrow 5P_{3/2}$ excitation transition [95] and $d_{23} = 4.508ea_0 n^{*-3/2}/\sqrt{3}$ for the $5P_{3/2} \rightarrow (n \geq 30)S_{1/2}$ Rydberg state [145, 146].

The spontaneous transition rates of the rubidium nS Rydberg states for radiative transitions to the 5P state are [147]

$$\Gamma_{32} = \frac{8.3261\times10^8}{n^{*3}}\left(\frac{0.079342}{n^*} + \frac{3.5508}{n^{*2}} - \frac{24.694}{n^{*3}}\right), \tag{4.5}$$

with coefficients for an approximated functional form given by fits to tabulated theoretical calculations for $10 < n < 1000$, which are verified by experiments for $28 < n < 45$ [148].

The Rydberg atoms were field-ionised by an external accelerator field potential, switched with rise times on the order of 100 ns (Fig. 4.9) following a period of laser exposure. For an atom in a static, uniform electric field $F\hat{\mathbf{z}}$, and thus an external potential $U = -Fz$, the combined Coulomb-Stark potential has a

saddle point energy $E_{\mathrm{sp}} = E_{\infty} - \sqrt{e^3 F/\pi\epsilon_0}$ relative to the ground state, above which the electron trajectories are unbound from the ionic core [47,92,149]. The threshold field strength to ionise ^{85}Rb atoms in the $60S_{1/2}$ state for example is 3 kV/m, corresponding to a potential of 150 V applied across the 5 cm-separated accelerator electrodes in the Melbourne cold atom ion source.

4.1.3 Spectroscopy using electromagnetically-induced transparency

To tune the wavelength of the Rydberg-coupling laser to resonance with the desired transitions, a spectroscopy setup based on electromagnetically-induced transparency (EIT), similar to that of Ref. [150], was used. EIT spectroscopy was used rather than absorption spectroscopy due to the weak transition strength of the Rydberg transition. EIT occurs when an intense 'pump' laser field renders an atomic medium transparent to a 'probe' field [151]. Here, the probe and pump fields couple the $5S \rightarrow 5P$ and $5P \rightarrow$ Rydberg states respectively. EIT is a resonant effect, occurring only when the pump and probe laser frequencies are tuned precisely to the atomic transition frequencies.

EIT provides a method for measuring the relative detuning of the lasers used in Rydberg excitation. In a spectroscopy setup with counter-propagating pump and probe lasers, thermal motion of the atoms relative to the laser propagation directions lead to a velocity-dependent Doppler-shifted detuning. In the three-level ladder system represented by the Hamiltonian Eq. 4.3, the detuning can be written as a function of atomic velocity as

$$\Delta_{ij} = \delta_{ij} - \omega_{ij}\left(1 - \sqrt{\frac{1 - v_{ij}}{1 + v_{ij}}}\right), \tag{4.6}$$

where δ_{ij} is the detuning of the laser coupling the i and j states from resonance for a stationary atom, ω_{ij} is the optical frequency of the transition and v_{ij} is the velocity component of an atom along the direction of the laser propagation. EIT occurs for dual resonance of both pump and probe fields, $\Delta_{12} = \Delta_{23} = 0$. For a probe laser detuning of δ_{12}, dual resonance occurs for atoms of a velocity class $v_{12} = -v_{23}$ resonant for pump laser detuning

$$\delta_{23} = -\frac{\omega_{23}\,\delta_{12}}{\omega_{12} - \delta_{12}}. \tag{4.7}$$

For small detunings relative to the transition frequencies ($\delta_{ij} \ll \omega_{ij}$), and with

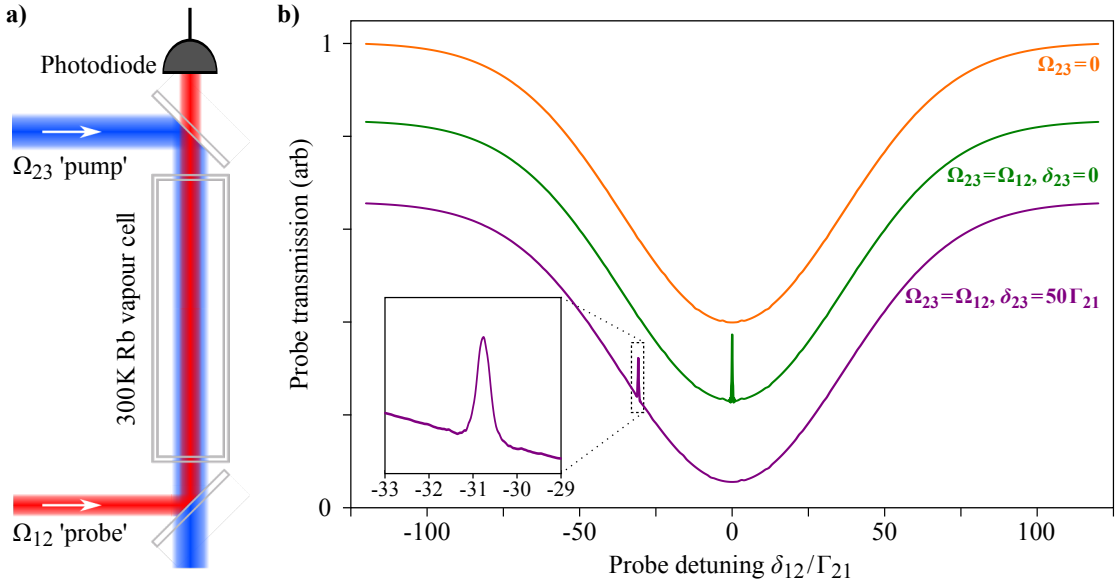

Figure 4.2: a) Experimental setup for electromagnetically-induced transparency (EIT) vapour-cell spectroscopy, for rubidium atoms in a ladder excitation scheme illustrated in Fig. 4.1a with n = 60, using counter-propagating pump and probe lasers. b) Calculated probe laser transmission spectrum as a function of probe laser detuning, as would be measured by the photodiode, for different combinations of pump laser strengths and detunings. For $\delta_{23} = 50\,\Gamma_{21}$, EIT occurs at probe laser detuning $\delta_{12} = -(\lambda_{23}/\lambda_{12})\delta_{23} = 30.75\,\Gamma_{21}$ within the Doppler-broadened absorption profile. Spectra vertically offset for clarity.

transition wavelengths $\lambda_{ij} = 2\pi c/\omega_{ij}$, Eq. 4.7 simplifies to

$$\delta_{23} = -\frac{\lambda_{23}}{\lambda_{12}}\,\delta_{12}. \tag{4.8}$$

The detuning of the pump laser can therefore be determined using Eq. 4.8 by measurement of the probe laser detuning frequency at which EIT appears within a Doppler-broadened absorption spectrum.

Figure 4.2b shows calculated EIT spectra for different combinations of laser parameters, for the experimental geometry illustrated in Fig. 4.2a with an atomic ensemble of rubidium at 300 K, where the Rydberg state is the 60S state. The transmission of the probe laser was calculated from the steady-state solution of the time evolution of the density matrix (Eq. 2.2) using the three-level ladder Hamiltonian (Eq. 4.3) and decay terms (Eq. 4.4), with velocity-dependent Doppler-induced detunings (Eq. 4.6). In steady-state conditions, the photon absorption rate of the probe laser is equal to the rate of fluorescence from the probe-coupled state [93], which is proportional to the occupancy of that state, ρ_{22}. The transmission of the probe laser is therefore proportional to $1 - \rho_{22}$. The probe transmission, which is dependent on the atomic velocity due to the Doppler shift, was convolved with a Maxwell-Boltzmann distribution for the axial velocity

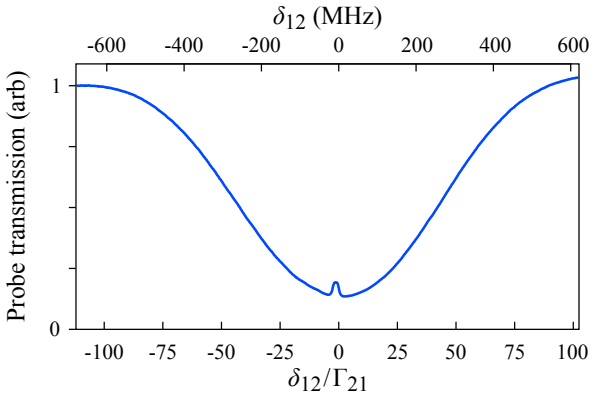

Figure 4.3: Experimentally attained electromagnetically-induced transparency spectrum, shown here for pump laser coupling to the rubidium $33D_{5/2}$ state, from data first appearing in Ref. [152].

for rubidium atoms at 300 K, to obtain the ensemble-averaged absorption as a function of the Rabi frequencies Ω_{12} and Ω_{23}, and detunings δ_{12} and δ_{23}.

The 5S $\rightarrow$ 5P probe laser, used in Ch. 2, was frequency-scanned over the excitation resonance, and counter-propagated with the 5P $\rightarrow$ 60S pump laser through a room-temperature rubidium vapour cell as illustrated in Fig. 4.2a. The absorption of the probe laser was measured on a photodiode, which showed EIT depending on the pump-laser detuning. Quarter-wave plates were used to circularly polarise the beams for maximum visibility of the EIT peak. An example of an EIT spectrum obtained experimentally is shown in Fig. 4.3, taken for the $33D_{5/2}$ state. Approximately 10% of the pump laser power was committed to the EIT setup, with the majority of the available power sent to the cold-atom apparatus for the production of Rydberg atoms.

EIT spectroscopy allowed for precise tuning of the pump laser with an atomic reference. Frequency offsets were used to compensate for acousto-optical modulator (AOM) based switching of the laser intensities, and were used in the following section to offset the relative frequency of the two Rydberg-exciting lasers. Stabilisation of the EIT-tuned laser frequency was performed using the Pound-Drever-Hall technique, locking the laser wavelength to a high-finesse, temperature-stabilised vacuum-enclosed optical cavity[4].

[4] Stable Laser Systems PDH-1000-5B

4.2 Rydberg blockade correlated ion bunches

The energy levels of Rydberg atoms are sensitive to the dipole fields of other nearby Rydberg atoms. The sensitivity can be exploited to induce spatial correlations in Rydberg atom ensembles during their photoexcitation. In a semiclassical Bohr model of a highly-excited Rydberg state, the valence electron is far from the atomic nucleus, giving the atom a large dipole moment. The van der Waals (vdW) interaction of the Rydberg atomic dipoles shifts the energy levels of the Rydberg states depending on the inter-Rydberg distance R, given to leading order as

$$V(R) = -\frac{C_6}{R^6}. \tag{4.9}$$

The interaction of two rubidium atoms excited to nS states is isotropic, with

$$C_6 = \mathrm{n}^{11}(c_0 + c_1\mathrm{n} + c_2\mathrm{n}^2), \tag{4.10}$$

where $c_0 = 1.729 \times 10^{-18}\,\mathrm{GHz}\,\mu\mathrm{m}^6$, $c_1 = -1.226 \times 10^{-19}\,\mathrm{GHz}\,\mu\mathrm{m}^6$ and $c_2 = 4.891 \times 10^{-22}\,\mathrm{GHz}\,\mu\mathrm{m}^6$ [121].

The effect of the vdW shift in the excitation of an ensemble of Rydberg atoms is illustrated in Fig. 4.4. In ladder-configuration coupling to a Rydberg state (Fig. 4.1), the effective linewidth of the 5P $\rightarrow$ Rydberg transition is the intermediate-state decay rate Γ_{21} (assuming $\Omega_{23} < \Gamma_{21}$ to avoid power broadening). When two atoms are within one blockade radius $r_b = |C_6/\Gamma_{12}|^{1/6}$, the energy level of the Rydberg state is shifted off resonance with the laser field for one of the atoms, so that only one of the atoms can be excited. Rydberg blockade leads to spatial correlations in Rydberg atom ensembles, which can prevent DIH as outlined in Ch. 3.

4.2.1 Excitation blockade model

The key signature of the presence of Rydberg blockade is the suppression of excitation. For excitation of Rydberg atoms when there is no Rydberg blockade, the spatial density of Rydberg atoms n_R should be linearly dependent on the total density of atoms n_T. This can be written as $n_R = \rho_{33} n_T$, where the blockade-free Rydberg-excited fraction can be calculated using the optical Bloch equations (Eq. 2.2, 4.3 and 4.4) for exposure to continuous laser fields with Rabi frequencies Ω_{12} and Ω_{23} (Eq. 2.5). The steady state solution for resonant conditions ($\Delta_{12} =$

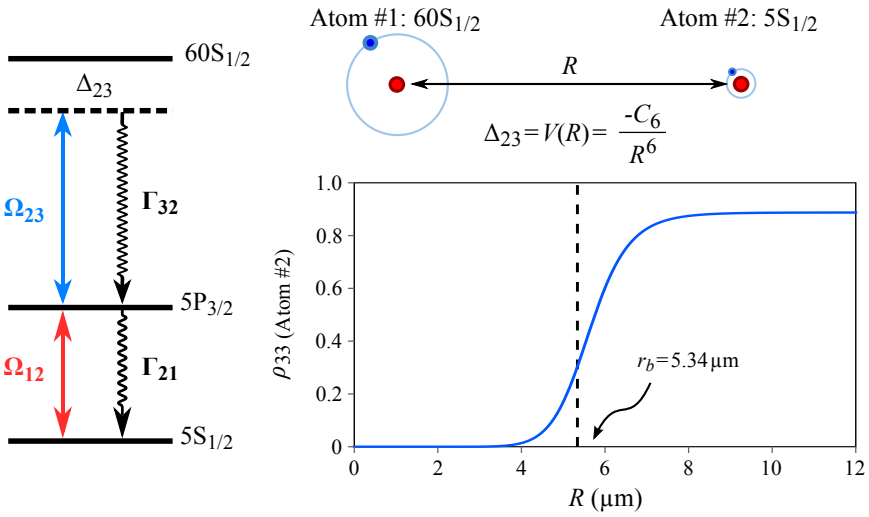

Figure 4.4: Blockade of Rydberg-excitation. Left: Energy level diagram for coupling of atoms to the 60S Rydberg state, resonant in the lower transition but detuned in the upper transition. Top right: A Rydberg atom (#1) in the 60S state shifts the energy levels of a ground state atom (#2), inducing a detuning Δ_{23} in its coupling to the same Rydberg level. Bottom right: Rydberg-excitation probability ρ_{33} of atom #2 (solid line) calculated from the steady-state solution to the three-level system as a function of the inter-atom distance R, for the experimentally-relevant parameters $\Omega_{12} = 73.2 \times 10^6\,\mathrm{s}^{-1}$, $\Omega_{23} = 25.8 \times 10^6\,\mathrm{s}^{-1}$, $\Gamma_{21} = 38.116 \times 10^6\,\mathrm{s}^{-1}$, $\Gamma_{32} = 4.85 \times 10^3\,\mathrm{s}^{-1}$ and $C_6 = 140\,\mathrm{GHz}\,\mu\mathrm{m}^6$. The approximated blockade radius used in the hard-sphere models, $r_b = (C_6/\Gamma_{21})^{1/6} = 5.34\,\mu\mathrm{m}$ is indicated with the dashed line.

$\Delta_{23} = 0$) is

$$\rho_{33} = (\Gamma_{21}+\Gamma_{32})\Omega_{12}^2\Omega_{23}^2 \Big/ \Big[\Gamma_{21}\Omega_{23}^2(\Omega_{12}^2+\Omega_{23}^2) + \Gamma_{21}\Gamma_{32}^2(2\Omega_{12}^2+\Omega_{23}^2) + \Gamma_{21}^2\Gamma_{32}(\Gamma_{32}^2+\Omega_{12}^2+2\Omega_{23}^2) + 2\Gamma_{32}\Omega_{12}^2(\Gamma_{32}^2+\Omega_{12}^2+\Omega_{23}^2) + \Gamma_{21}^3\Gamma_{32}^2\Big], \quad (4.11)$$

which simplifies to

$$\rho_{33} \simeq \frac{\Omega_{12}^2}{\Omega_{12}^2+\Omega_{23}^2} \quad (4.12)$$

for $\Gamma_{21} \gg \Gamma_{32}$. When there is Rydberg blockade, however, there will be a point at which the density of Rydberg atoms saturates and stops increasing regardless of increased atom density, as the hard spheres of excitation become closely packed.

The density-limiting effects of Rydberg blockade were described in a model described in Ref. [120], presented here (Eq. 4.13 – 4.17) with modification to explicitly incorporate the spatial variation of the Rydberg atom density as a function of the spatially-varying laser intensities (Eq. 4.11). Approximating the three-level, two-step Rydberg excitation process as a two-level, direct excitation process, the Einstein rate equation for the spatial number density n_R of atoms

in excited to the Rydberg state without blockade is

$$\frac{dn_R}{dt} = An_g - Bn_R, \tag{4.13}$$

where A is the excitation rate from the ground state density n_g, and B is the de-excitation rate, and the total density of atoms in any state is conserved as $n_T = n_g + n_R$. In steady-state conditions, when $dn_R/dt = 0$, Eq. 4.13 gives the density as

$$n_R = \frac{A}{A+B} n_T, \tag{4.14}$$

where $A/(A+B) = \rho_{33}$ from Eq. 4.11.

In the presence of hard-sphere type blockade, however, a fraction of the ground state atoms will be blocked from excitation by the vdW interaction. In an ensemble of ground state atoms and hard-sphere Rydberg atoms with blockade radius r_b, the fraction of ground state atoms *not* within r_b of a Rydberg atom, ϕ, can be approximated using the Carnahan-Starling model for hard spheres of radius $r_b/2$, with packing fraction $\eta = \frac{\pi}{6} n_R r_b^3$, as

$$\phi = \exp\left(\frac{-8\eta + 9\eta^2 - 3\eta^3}{(1-3\eta)^3}\right). \tag{4.15}$$

The reduction of available and excitable ground state atoms modifies the Einstein rate equation (4.13) to

$$\frac{dn_R}{dt} = A\phi n_g - Bn_R. \tag{4.16}$$

Assuming that the excitation fraction of atoms outside of one blockade radius from a Rydberg atom remains the same as the isolated-atom case, so that $A/(A+B) = \rho_{33}$, the steady-state solution to Eq. 4.16 gives the total atom density as a function of the Rydberg atom density as

$$n_T = \left(\frac{1-\rho_{33}}{\phi\rho_{33}} + 1\right) n_R. \tag{4.17}$$

The inverse of Eq. 4.17, for n_R as a function of n_T, r_b and ρ_{33}, gives the characteristic saturation of the Rydberg atom density plotted in Fig. 4.5.

The blockaded excitation of Rydberg atoms is illustrated in Fig. 4.5, for different Rydberg states in rubidium excited by three-level excitation via the $5P_{3/2}$ state, assuming $\rho_{33} = 1/3$. Rydberg excitation of states with low principal quantum number have small blockade radii, shown for example with the 30S state, and exhibit a linear relationship $n_R \to \rho_{33} n_T$ as the excitation is uninhibited

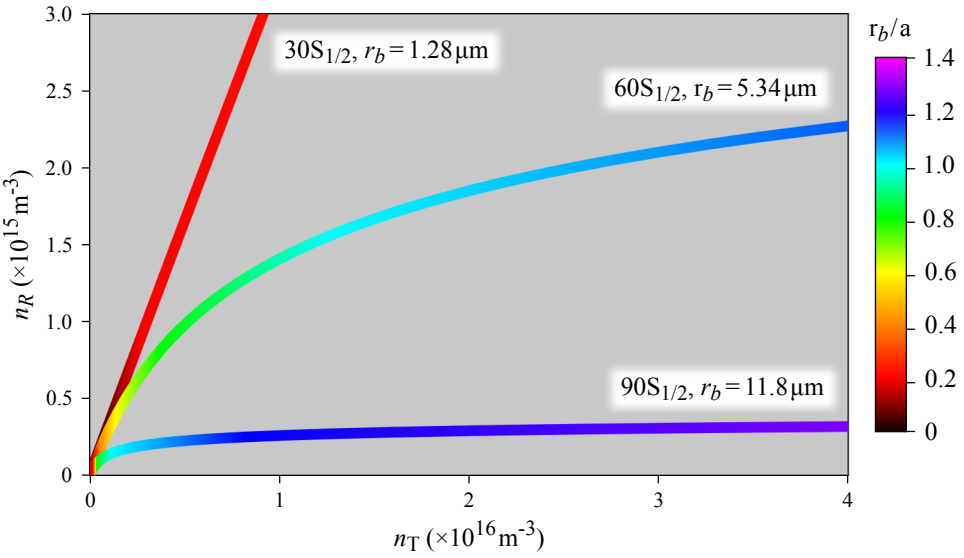

Figure 4.5: Rydberg blockade of excitation, showing saturation of the Rydberg atom density n_R in the presence of blockade with radiui r_b as a function of the total atom density n_T, assuming an excitation probability of $\rho_{33} = 1/3$ in the absence of blockade. The degree of correlation is indicated by the colour map, measured by the blockade parameter r_b/a where a is the mean inter-Rydberg distance (Wigner-Seitz radius).

by blockade. Excitation to states with with low blockade exhibits low degrees of correlation. For excitation to states of higher principal quantum number, blockade limits the density of the Rydberg atoms while increasing the degree of correlation and, as discussed in Ch. 3, leads to suppression of DIH.

4.2.2 Blockade measurements

Ion bunches were created from Rydberg atoms in the $60S_{1/2}$ state, which has blockade radius $r_b = 5.33\,\mu$m (Fig. 4.4). Laser excitation to field-ionising Rydberg states (Fig. 4.1) was used with Rabi frequency Ω_{34} less than the intermediate-state linewidth Γ_{12}, to avoid power-broadening effects. Measurements were made of the density-limiting blockade effect, described in Sec. 4.2.1, using a variable-density atom cloud to determine the degree of spatial correlations for the resulting ion bunches.

Rubidium atoms were prepared in the magneto-optical trap (see Ch. 2) for a period of 100 ms, at density of $n_T = 10^{16}\,\mathrm{m}^{-3}$, after which the trapping laser and magnetic fields were switched off. Two different methods were used to increase and to decrease the density from $10^{16}\,\mathrm{m}^{-3}$. Reduction of the atom density was achieved using a period of free thermal expansion of up to 15 ms prior to photo-excitation. Alternatively, an increase in the density was achieved with polarisation gradient cooling (PGC) and magnetic compression, using an increase

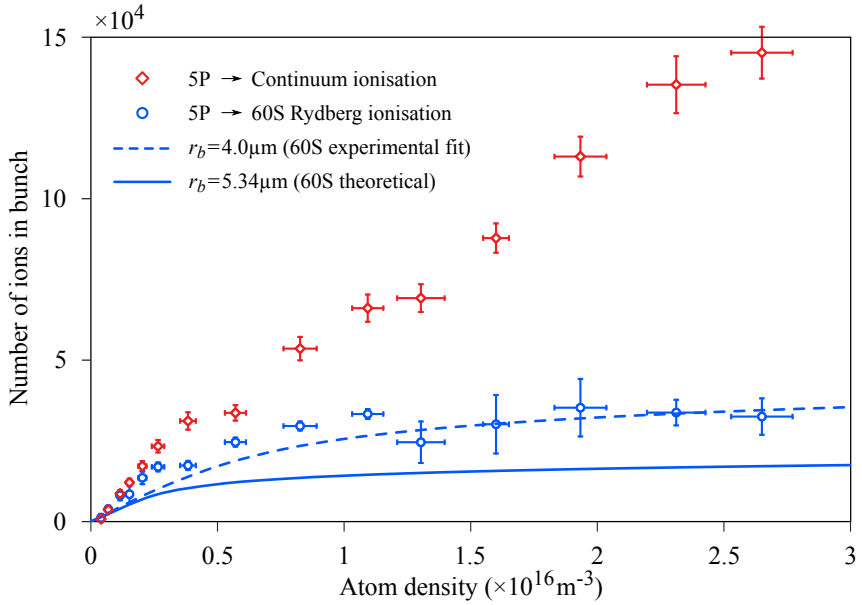

Figure 4.6: Detected number of ions in bunches created with varying initial atomic density. For direct photoionisation without blockade, ion number is linearly dependent on the atom density. For excitation to the 60S Rydberg state, blockade causes saturation of the ion number, with theoretical calculations fit to the data consistent with $4\,\mu$m blockade radius.

in magnetic field gradient coupled with a decrease in trapping laser frequency. The density of the atom cloud was measured for varying time delay and degree of compression using absorption imaging.

Atoms were photoexcited by AOM-switched lasers for a period of $1\,\mu$s. The $5S_{1/2} \rightarrow 5P_{3/2}$ excitation transition was driven by an $11.86\,\mu$W laser with a uniform circular profile of radius $R_{xy} = 143\,\mu$m resulting in $\Omega_{12} = 7.32 \times 10^7 \mathrm{s}^{-1}$, shaped using a spatial light modulator. The $5P_{3/2} \rightarrow 60S_{1/2}$ transition was driven by a 255 mW laser with an elliptical Gaussian intensity profile of RMS size $\sigma_z = 10\,\mu$m along the axis of ion propagation and $\sigma_y = 1.5\,$mm in the vertical transverse axis, with peak Rabi frequency $\Omega_{34} = 2.2 \times 10^7\,\mathrm{s}^{-1}$. The Rydberg atoms were ionised by a 4 kV potential applied between the 5 cm-separated accelerator plates, for an electric field of 80 kV/m, with a switching time measured as 100 ns.

The ion bunch charges were measured from the integrated brightness of CCD camera images of a phosphor-coupled microchannel-plate detector, calibrated using a Faraday cup charge measurement device as described in Ch. 2. The experiment was performed with a repetition rate of $10\,\mathrm{s}^{-1}$. For each delay time and measured atom density, the ion number was measured 100 times, from which the averaged ion number is plotted in Fig. 4.6. This figure plots the data as ion number, rather than as density used in Fig. 4.5, as the non-uniformity of the

laser field intensities causes spatial variation of the density of Rydberg atoms. In the curve of ion number versus atom density (Fig. 4.6), saturation is clear. A non-blockaded control set was generated experimentally by using the pulsed 480 nm laser (see Ch. 2) tuned to directly ionise the atoms. Continuum ionisation bypasses the blockade effect, generating a linear relationship between the number of ions and the atom density. The vertical error bars in the experimental curve reflect one standard deviation of the ion numbers collected over the 100-shot experimental average. The horizontal error bars represent one standard deviation of uncertainty in the calculation of the atom density from the absorption imaging. For recorded densities above 1.25×10^{16} which used PGC, there were increased fluctuations in the ion number, attributed to movement of the atom cloud peak density region between experimental runs.

To generate a comparative theoretical curve in Fig. 4.6, the non-uniformity of the light field was taken into account in the calculation of the isolated-atom Rydberg excitation fraction (Eq. 4.11). The theoretical number of ions was calculated for a given atom density by integrating the blockaded-Rydberg density from the inverse of Eq. 4.17 over the three-dimensional laser volume with spatially-varying Rabi frequencies. These calculations were fit to the experimental data, which implied a blockade radius of $r_b = 4.0\,\mu$m, indicated with the dashed line. This blockade radius was smaller than the calculated $5.34\,\mu$m radius calculated using the intermediate-state lifetime as the linewidth, indicated with the solid line. The discrepancy is attributable to power broadening of the transition, which would lower the blockade radius compared to the calculation of r_b with the natural linewidth, and to the presence of low-density ion halos outside of the laser overlap volume that would increase the measured number of ions. The general trend of the experimental data otherwise matched the theoretical model, in particular showing suppression of excitation at higher atom densities, supporting the premise of Rydberg-blockaded ion bunches.

The degree of correlation measured by the blockade parameter r_b/a (Sec. 3.3) was calculated for the highest atom density $n_T = 2.65 \times 10^{16}\text{m}^{-3}$ achieved in Fig. 4.6 with $r_b = 4.0\,\mu$m using the hard-sphere model. The non-uniformity of the Rydberg-coupling laser beam causes spatial variation of the Rydberg atom density, and thus variation of r_b/a. The z-axial variation of r_b/a within the transverse radius R_{xy} of the excitation laser is plotted in Fig. 4.7, showing $r_b/a \sim 1.2$ within $30\,\mu$m of the centre of the Rydberg laser beam at $z = 0$. The decrease of r_b/a near $z = 0$ is due to the nonlinear dependence of ρ_{33} on Ω_{23}. For the inferred level of correlation within the centre of the Rydberg-atom cloud, $r_b/a = 1.2$, the calculations of Ch. 3 presented in Fig. 3.8 predict suppression of disorder-induced

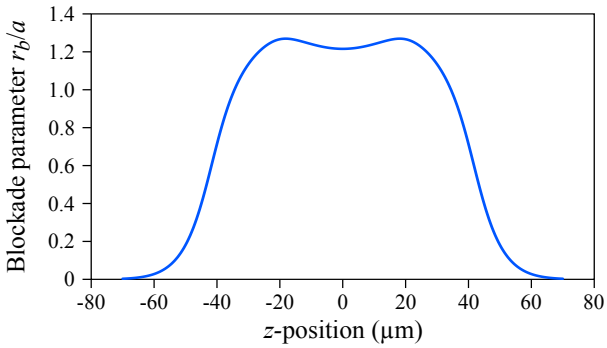

Figure 4.7: Calculated spatial variation in the blockade parameter within the region of laser overlap illustrated in Fig. 4.1, produced with an atom density of $2.65 \times 10^{16}\,\mathrm{m}^{-3}$ and a blockade radius of $4\,\mu$m inferred by the fits to experimental data in Fig. 4.6.

heating with reduction of bunch emittance to 0.38 times that of a disordered bunch at the same density, or a sevenfold increase in brightness.

4.3 High-efficiency Rydberg excitation via stimulated Raman adiabatic passage

The emittance growth caused by disorder-induced heating occurs alongside the emittance growth caused by space-charge nonlinearity. Measuring the suppression of DIH with Rydberg blockade, as predicted in Ch. 3, for the degree of spatial correlations inferred in Sec. 4.2, would therefore also require simultaneous alleviation of space-charge effects. Techniques to linearise space-charge and suppress emittance growth using beam shaping, as demonstrated in Sec. 2.2, are readily applicable to the Rydberg excitation techniques demonstrated in this chapter. With improvements to the precision and spatial resolution of the shaping techniques, space-charge effects could be fully linearised to the point where DIH becomes the dominant factor in determining beam quality. However, the methods to circumvent formation of fluorescence halos established in Sec. 2.1 are not immediately applicable to the excitation of Rydberg atoms.

Fluorescence halos are caused by spontaneous emission of intermediate-state excited atoms and reabsorption of the emitted photons outside of the desired photoionisation volume. Formation of the halos leads to nonlinear transformation of bunch shape, and therefore to emittance growth. Section 2.1.3 showed that for pulsed photoionisation directly to the continuum, halos can be prevented by adjusting the timing of the delay between the slow, long duration excitation laser and the fast pulse of the ionisation laser. That method is not applicable to

the excitation of blockaded Rydberg atoms as it requires fast laser pulses for the Rydberg-coupling transition, which lead to large laser frequency bandwidths that would prevent blockade. In this section, a method is presented for the prevention of fluorescence halos in the production of Rydberg-atom ion bunches, using coherent population transfer via stimulated Raman adiabatic passage (STIRAP) to avoid populating the fluorescent intermediate state.

4.3.1 Theoretical description

STIRAP is a procedure by which atomic population is coherently transferred between states using time-offset light pulses. For a comprehensive discussion of the process, see Ref. [153]. For excitation in a three-level ladder system (Fig. 4.1), STIRAP allows transfer of population into the third state, bypassing the second intermediate state. Bypassing the fluorescent intermediate state prevents formation of beam halos. A key feature of the STIRAP process is the 'counterintuitive' pulse sequence, in which the Rydberg laser pulse precedes the intermediate-state laser, establishing a coherence between the first and third states that evolves adiabatically to transfer the state population as the relative laser intensities change. Altering the delay between the two lasers affects the overall transfer efficiency, which is an effect that be used to establish the presence of STIRAP experimentally (Sec. 4.3.2). The STIRAP technique is robust to differences in Rabi frequencies, pulse delays and beam shapes, provided that the adiabatic condition $\Omega_{\text{eff}}\tau > 10$ is met, where $\Omega_{\text{eff}} = \sqrt{\Omega_{12}^2 + \Omega_{23}^2}$ is the effective Rabi frequency and τ is duration of the laser overlap.

A calculation of excitation using the STIRAP process is shown in Fig. 4.8a. The optical Bloch equations (Eq. 2.2, 4.3 and 4.4) were applied to the ladder-excitation scheme with intermediate $5P_{3/2}$ state, with $\Gamma_{21} = 38 \times 10^6\,\text{s}^{-1}$, using laser pulses with peak Rabi frequency $\Omega_{12} = \Omega_{23} = 10\,\text{MHz}$ of Gaussian time-dependence of standard deviation 200 ns, separated by 200 ns. The calculations show transfer of population from ρ_{11} to ρ_{33}, with ρ_{22} remaining depopulated throughout the process. The STIRAP process is insensitive to the relative detuning of the laser fields from the intermediate state. The calculations were performed for conditions where both lasers are on resonance with their respective transitions, and also when the relative detunings are decoupled from the intermediate state while remaining in two-photon resonance with the Rydberg state ($\Delta_{12} = +27\,\text{MHz}$ and $\Delta_{23} = -27\,\text{MHz}$). In either case, high efficiency in the transfer process is maintained. Decoupling the relative laser frequencies from the intermediate state is required to avoid population of the intermediate-state exci-

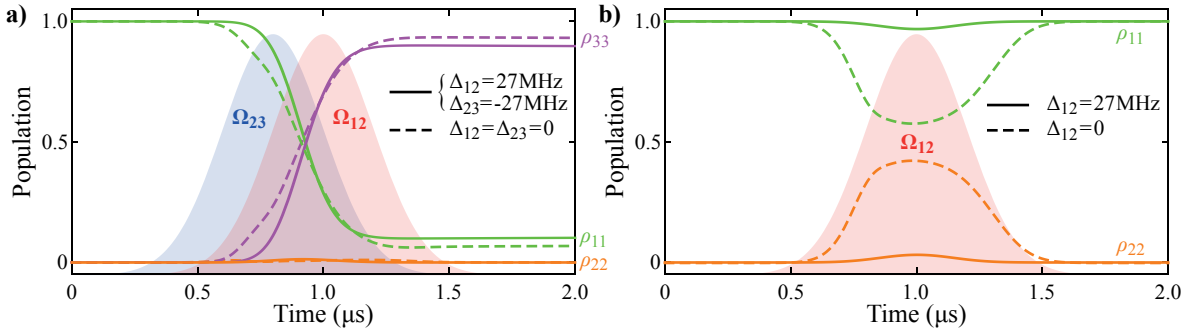

Figure 4.8: Calculation of Rydberg STIRAP excitation for the three-level ladder system in rubidium, using Gaussian time-dependent Rabi frequencies of 10 MHz peak, 200 ns standard deviation and 200 ns STIRAP delay (indicated in the shaded regions). a) Atomic population is transferred from ground to the Rydberg state, bypassing the intermediate state. The STIRAP process is insensitive to detuning from the intermediate state, for two-photon resonance $\Delta_{12} = -\Delta_{23}$. b) Population of the intermediate state in a region with $\Omega_{23} = 0$, as would occur outside of the region of laser overlap, showing suppressed excitation for off-resonant coupling. Resonance decoupling can therefore be used to avoid population of the intermediate state throughout the entire volume, with minimal effect on the STIRAP efficiency.

tation outside of the volume of laser overlap. Figure 4.8b shows the calculation of Fig. 4.8a repeated with $\Omega_{23} = 0$, corresponding to atoms within the excitation laser but away from the centre of the ionisation volume in Fig. 4.1, showing suppressed intermediate-state excitation. Intermediate-state-detuned STIRAP could therefore be used to avoid populating the intermediate state throughout the atomic volume, and thus prevent the formation of fluorescence halos.

4.3.2 Experimental implementation

STIRAP was implemented in the cold atom ion source by shaping of the laser pulse durations and timings using radio frequency (RF) acousto-optic modulators (AOMs). Waveform generators programmed to produce rectangular pulses were used to control the power supplied to the AOM RF amplifiers. The spatial profiles of the lasers were as illustrated in Fig. 4.1 with $R_{xy} = 150\,\mu$m, $\sigma_y = 150\,\mu$m and $\sigma_z = 20\,\mu$m. The Rydberg laser was tuned to the $28S_{1/2}$ state, with relative detuning for the two lasers set to $\Delta_{12} = +27$ MHz and $\Delta_{23} = -27$ MHz. The cold atom cloud was loaded in the magneto-optical trap to a density of $5 \times 10^{15}\,\mathrm{m}^{-3}$. Excitation to the $28S_{1/2}$ state should have no appreciable excitation blockade at experimental densities (see, e.g., Fig. 4.5), and should therefore not affect the measurement of excitation efficiency.

To measure the efficiency of the STIRAP process, a 'two-pulse' method [146, 154] was used, in which STIRAP excitation occurs twice in quick succession. The

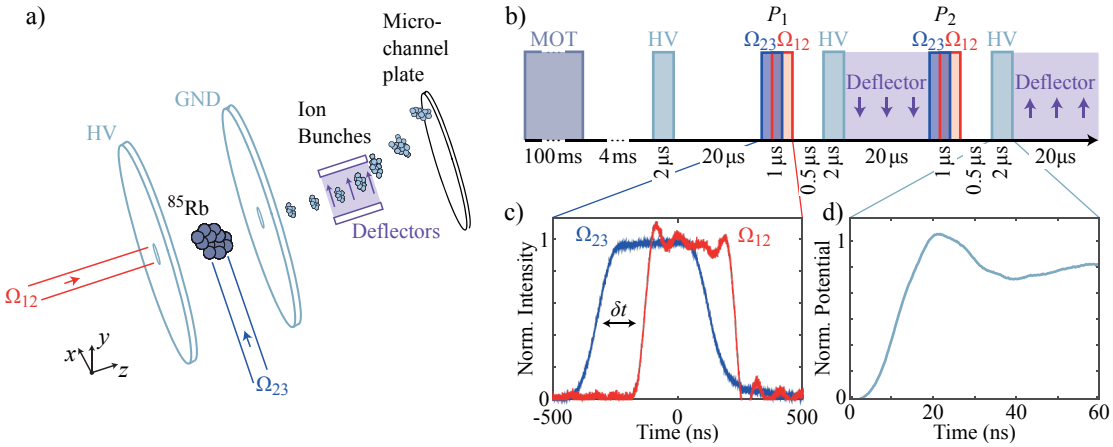

Figure 4.9: Schematic of STIRAP experimental setup (a) and timing sequence (b). Rydberg atoms produced at the laser overlap (as in Fig. 4.1) with time-dependent laser pulses are ionised by switched high-voltage electric fields. The charge of the ion bunches were measured individually by spatially separating them at the micro-channel plate detector using transverse deflecting electric fields.

Rydberg atoms excited in each STIRAP pulse are ionised by electric fields that accelerate the resultant ions towards the MCP detector, measuring the charge and thus relative Rydberg population in each pulse. Depletion of the atom cloud by removal of Rydberg atoms with the first pulse reduces the number of atoms available to the second pulse. The excitation efficiency in the region of the laser overlap can be determined by comparing the relative ion number in each pulse, as described below.

The experimental setup, laser geometry, and timing sequence used in the two-pulse method is shown in Fig. 4.9. An example measurement of the laser intensities corresponding to the intermediate and Rydberg lasers is shown inset (Fig. 4.9c), alongside the measured rise-time of the high-voltage (HV) accelerator pulse that ionises the Rydberg atoms (Fig. 4.9d). The HV pulse was applied before the first set of laser pulses, to ensure equal residual electric field conditions in the two measurements. The accelerator field was 1400 kV cm^{-1}, which ionised the Rydberg atoms produced by STIRAP, and accelerated the ions towards the MCP detector. Transverse electric fields provided by parallel-plate electrodes downstream of the source (Ref. [63] p. 77) were used to deflect each ion pulse to a different region on the phosphor-coupled MCP, so that their bunch charges could be measured independently.

The two-pulse method measures the overall integrated efficiency over the ionisation volume, bounded in the plane transverse to ion propagation by the circular profile of the intermediate excitation laser ($x^2 + y^2 < R_{xy}^2$) within which its intensity does not vary. Within the cylindrical volume of the intermediate laser,

the efficiency of population transfer to the Rydberg state $\mathcal{E}(y,z)$ is dependent only on the spatial variation of the Rydberg-coupling laser intensity, in the y and z axes. The total charges in the first and second ion bunches produced in the two-pulse STIRAP process, N_1 and N_2 respectively, are

$$N_1 = \iiint_V \mathcal{E}(y,z)\, n(x,y,z)\, dx\, dy\, dz, \tag{4.18}$$

and

$$N_2 = \iiint_V \mathcal{E}(y,z)\big[1-\mathcal{E}(y,z)\big]\, n(x,y,z)\, dx\, dy\, dz, \tag{4.19}$$

where $n(x,y,z)$ is the spatial density of the atom cloud prior to the STIRAP process, and the interaction volume V is bounded by the intermediate laser beam. The equation for N_2 accounts for the depletion of the atom density by the first STIRAP pulse, assuming negligibe thermal atomic motion in the time between the two pulses. Using Eq. 4.18 and 4.19, the STIRAP efficiency averaged over the interaction volume can be written in terms of N_1 and N_2 as

$$\mathcal{E}_{\text{int}} = 1 - \frac{N_1}{N_2}, \tag{4.20}$$

which requires only the ratio of the measured charges, relaxing requirements on both detector calibration and the consistency of atomic density between measurements.

Images of the MCP taken to measure the bunch charges are shown for example in Fig. 4.10a, for the STIRAP pulses P_1 and P_2 (Fig. 4.9). The relative proportionality of N_1 and N_2 was determined by area integration of the 8-bit count of intensity in each CCD pixel for each pulse. To remove the influence of spatial variation in the MCP sensitivity, measurements of N_1 were taken from pulse sequences (Fig. 4.9) containing only P_2. N_2 was measured by integration over the same area as N_1 for pulses containing both P_1 and P_2. The characteristic signature of STIRAP is enhanced efficiency at negative delay times δt between the intermediate and Rydberg-coupling lasers. The bunch charges were measured for varying STIRAP delay δt, shown in Fig. 4.10b averaged across 100 measurements, with error bars as one standard deviation.

Calculations of STIRAP were performed using the OBEs (Eq. 2.2, 4.3 and 4.4), with rectangular laser pulses of 200 ns peak intensity duration and 100 ns linear rise and fall times, with peak Rabi frequencies $\Omega_{12} = \Omega_{23} = 15\,\text{MHz}$ and detunings $\Delta_{12} = +27\,\text{MHz}$ and $\Delta_{23} = -27\,\text{MHz}$, for varying delay times. The two-pulse sequence was included in the calculations with removal of the Rydberg-

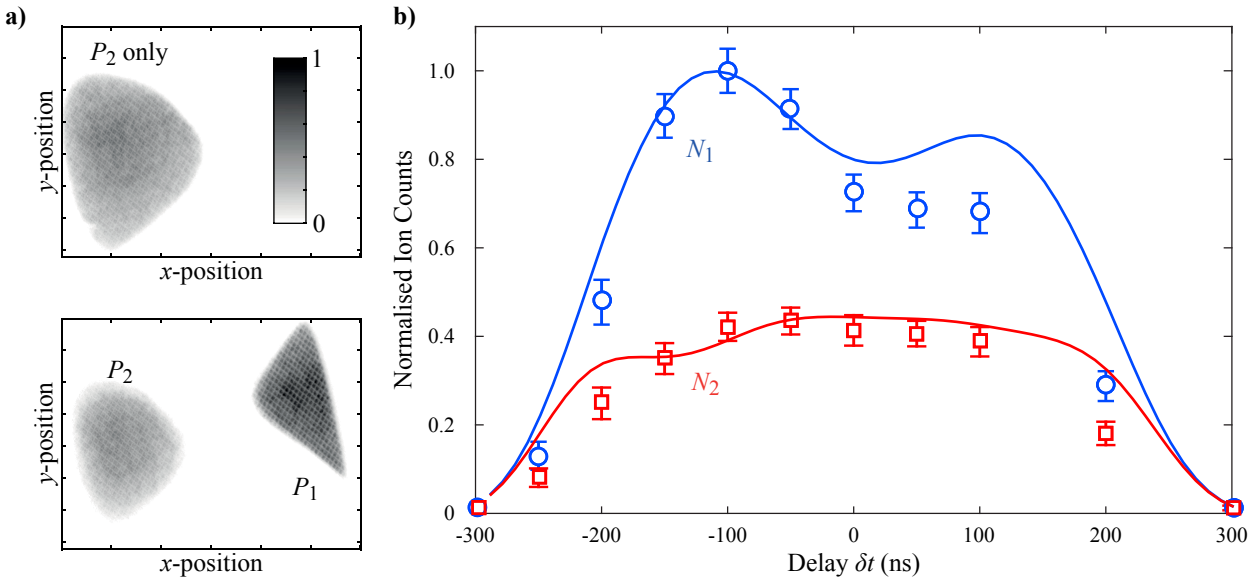

Figure 4.10: Experimental measurements of STIRAP ion bunch charges. a) Images of the phosphor-coupled MCP detector for ion bunches created with STIRAP pulses P_1 and P_2 (Fig. 4.9). Top: ion bunch created in a sequence containing only the second STIRAP pulse P_2 (top), integrated to measure N_1. Bottom: ion bunches created with both pulses P_1 and P_2, integrated over the same region as the top image to measure N_2. b) Normalised experimental measurement of relative bunch charges in N_1 and N_2 (data points), and theoretical calculations using the optical Bloch equations (lines).

excited atomic population between the laser pulses. The Rydberg populations of each pulse were calculated by integration of the calculated population over the Gaussian spatial intensity distribution of the Rydberg-coupling laser in the $y-z$ plane. The calculations are shown in Fig. 4.10b compared to the experimental results, with each normalised to the peak value of N_1.

The volume-averaged efficiencies (Eq. 4.20) are shown in Fig. 4.11 for the experimental results and for the theoretical calculations. Both the results and calculations show peaks in efficiency at negative delays: the characteristic signature of STIRAP. The maximum volume-averaged efficiency was measured to be 60% at $\delta t = -150\,\text{ns}$. At that delay time, the corresponding peak efficiency inferred from the OBE calculations is 82%, at the position of peak intensity of the Rydberg-coupling laser. The relationship between averaged and peak efficiency is illustrated in the inset of Fig. 4.11. The inset shows the volume-averaged STIRAP efficiency calculated only for atoms within an oblate spheroidal volume centred on the interaction region with semi-minor axial radius r_z in the z direction and semi-major axial radius $r_{xy} = r_z\,\sigma_y/\sigma_z$ in the $x-y$ plane, given the Rydberg-laser beam sizes $\sigma_y = 150\,\mu\text{m}$ and $\sigma_z = 20\,\mu\text{m}$. The volume-averaged calculations were performed taking into account the cylindrical boundaries of the interaction volume, $\Omega_{12} \to 0$ for $x^2 + y^2 > R_{xy}^2$. Averaging over a spheroidal

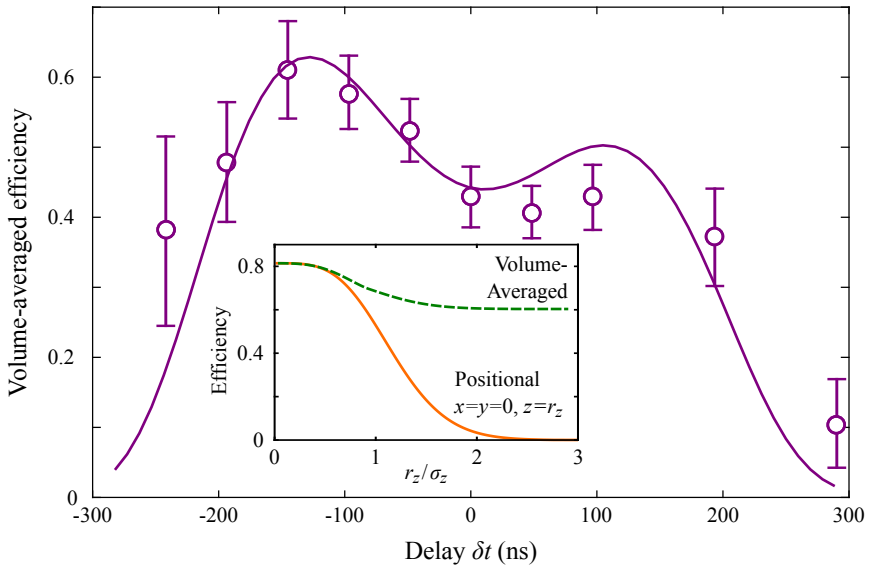

Figure 4.11: Calculated interaction-volume-averaged efficiency (Eq. 4.20) from the experimental and theoretical data of Fig. 4.10. Inset: relationship between the averaged efficiency and positionally-dependent efficiency for the optimal delay time of −150 ns, showing convergence to a peak efficiency of 82% at the centre of the interaction volume.

region accounts for the unequal beam sizes in the y and z axes. The volume averaged-efficiency for r_z is shown in comparison to the exact efficiency at r_z from the centre of the interaction region, in the z-direction, normalised to σ_z. The comparison illustrates the convergence of the volume-averaged result to the peak efficiency at the position of maximum Ω_{23} at the centre of the interaction region.

Measurement of the characteristic efficiency peak at negative delay times demonstrates the implementation of STIRAP in the production of Rydberg-atom ion bunches from a cold source, with off-resonant intermediate-state coupling to prevent the formation of fluorescence halos.

4.4 Discussion

Rydberg atom photoexcitation was implemented in the cold atom ion source to produce ion bunches with inter-particle spatial correlations. Spectroscopy using electromagnetically-induced transparency was used to tune the wavelength of the Rydberg-coupling laser to resonance with states up to a principal quantum number n = 60. Ion bunches were created by excitation to the 60S state, with an experimentally inferred blockade radius $r_b = 4\,\mu$m. At the highest achieved bunch densities, the corresponding blockade parameter was $r_b/a = 1.2$, for which the calculations of Ch. 3 predict suppression of disorder-induced heating with

emittance reduced to 0.38 times that of a disordered bunch.

In future experiments, measuring the reduced emittance associated with the Rydberg-blockade correlation demonstrated here will require simultaneous suppression of nonlinear space-charge effects. Towards this goal, Rydberg ion bunches were produced with resonance-detuned stimulated Raman adiabatic passage, to prevent the formation of fluorescence halos that contribute to nonlinear space-charge effects and emittance growth. Further research will be needed to shape the Rydberg ion bunches to linearise space-charge, using laser distributions calculated with incorporation of the hard-sphere model for blockade.

As established in Ch. 2, cold ion bunches serve as a platform for the study of intrabeam Coulomb effects. The Rydberg excitation techniques introduced in this chapter progress cold-atom ion sources towards overcoming the fundamental limit to beam quality from disorder-induced heating, a major milestone not yet achieved in the development of high brightness charged particle beams.

Chapter 5

Conclusions and outlook

The research presented in this thesis establishes the cold-atom ion source as a platform for the measurement of intrabeam, interparticle Coulomb interactions. Coulomb interactions limit the brightness of charged particle beam sources used for single-shot ultrafast diffraction imaging of biomolecules, and for injection into accelerators for synchrotrons, x-ray free electron lasers and particle colliders. Increasing the brightness of particle sources is critical for progress in those applications, but there has been limited detail in experimental measurements of Coulomb interactions in conventional sources, due to the masking effects of thermal diffusion.

Cold-atom electron sources are being developed towards the goal of attaining ultrafast electron diffraction, but they have not yet achieved Coulomb-interaction limited brightness. Cold-atom ion sources, on the other hand, have been operated to produce continuous streams of ions with low charge density in order to avoid the loss of focusability due to Coulomb interactions. Here it was shown that the propagation dynamics of cold ion bunches are dominated by intrabeam Coulomb effects. The beam dynamics exhibited by the ion bunches are the same as for high-density electron bunches created with shorter durations and lower temperatures than have been achieved to date. Ion bunches can therefore be used in the present day to develop and test methods for overcoming the Coulomb-associated brightness limits for future electron sources.

Two distinct classes of intrabeam Coulomb effects were studied using the cold-atom ion source: macroscopic space-charge effects, where beam evolution is determined by the the bulk electric field of the spatial distribution of the beam charge, and microscopic statistical Coulomb effects, where the randomness of the electric field experienced by each ion leads to beam heating, dependent on the

interparticle spatial correlations.

Detailed observations of space-charge dynamics using cold ion bunches were presented in Sec. 2.1. It was shown that a rubidium ion bunch created over a 5 ns duration in an external accelerator field has the same initial space-charge density and beam evolution as an ultrafast electron bunch with 13 ps duration. The unique three-dimensional beam shaping capability of the cold-atom electron and ion source was used to produce ion bunches with complex initial distributions, which evolve with nonlinear transformation of beam shape. High-density rings were observed to form in the transverse charge-density distributions of the ion bunches, measured with a charged particle detector after 70 cm of free-space propagation. The rings were not predicted by particle tracking simulations for the initial ion distributions calculated using a two-level atom model with known laser intensity distributions. Simulations were repeated using a four-level model of photoexcitation including fluorescence from the intermediate state, which reproduced the experimentally observed distributions including the high-density rings. It was discovered that the rings form from velocity bunching of fast-expanding ions at a beam core with a low density background 'halo' of ions. The halo was produced by reabsorbed light fluoresced from the intermediate excited state during the laser excitation process. Suppression of the fluorescence halo rings was demonstrated by elimination of the time delay between excitation and ionisation. The fluorescence halo rings are an example of complex beam behaviour that is specific to the cold atom source, but also a complex behaviour that was only observable due to the low temperature of the ions, behaviour which would be masked by thermal diffusion at only a few tens of kelvin.

Space-charge effects present a limit to beam quality that can be overcome through linearisation of the internal electric field within a charged particle bunch. Beam shaping techniques for suppressing nonlinear space-charge expansion effects have been developed for photocathode electron sources and implemented in cold atom electron sources, but to date there has been no experimental confirmation of improved beam quality with the technique, due to thermal diffusion effects. Section 2.2 describes contributions towards the creation of cold ion bunches with transverse profiles shaped to produce ellipsoidal bunches with linear internal electric fields, and also with unshaped Gaussian transverse distributions. The relative beam quality of each distribution was quantified by measurement of the minimum beam size at a focus. Shaped bunches were shown to have improved focusing properties, demonstrating suppression of space-charge induced emittance growth through beam shaping for the first time in any charged particle beam.

Amelioration of space-charge induced limits to beam brightness through beam shaping in a CAEIS will produce bunches that are limited instead by statistical Coulomb effects dependent on the interparticle spatial correlations. In a cold ion beam, disorder-induced heating (DIH) arising from randomness of inter-particle electrostatic potentials can cause an increase in beam temperatures by many orders of magnitude compared to the source-atom temperatures. Chapter 3 presents research into the capacity for cold-atom ion beams to overcome DIH by introduction of interparticle spatial correlations into the atomic distribution, prior to ionisation. Models and simulations have previously established the possibility of preventing DIH in ultracold neutral plasmas (UCNPs), but not in charged particle beams undergoing space-charge expansion. Here, a model of the equilibration of DIH in a non-expanding one-component plasma was shown to predict the degree to which DIH emittance growth can be suppressed, for partial degrees of correlation. The model describes suppression of DIH for ion bunches created with Rydberg-blockade correlations (Sec. 3.3) and optical lattice correlations (Sec. 3.4) for experimentally achievable physical parameters. These predictions show that cold atom ion sources are the most promising candidate for exceeding otherwise fundamental limits of charged particle beam brightness.

Motivated by the need to suppress DIH, chapter 4 presents experimental efforts towards creation of a spatially-correlated ion source using Rydberg blockade. Rydberg-excited atoms interact strongly via van der Waals interactions when in close proximity. The interaction leads to Rydberg blockade in the photoexcitation of ensembles of Rydberg atoms, which can be exploited to induce interparticle spatial correlations in the resultant ion bunches. Rydberg-blockade correlated ion bunches have reduced disorder-induced heating compared to disordered ion bunches at the same density. A vapour-cell spectroscopy system using electromagnetically-induced transparency was constructed and used to tune the frequencies of lasers used in the cold-atom ion source to resonance with Rydberg energy levels. Measurements of the excitation blockade effect in ion bunches created using the Rydberg-coupling lasers established the presence of interparticle spatial correlations. The degree of spatial correlation measured in the blockaded ion bunches is predicted to suppress disorder-induced heating and reduce bunch emittance to 38% of that for a disordered bunch, i.e. an increase in beam brightness by a factor of 7.

Section 4.3 presents a method for creating Rydberg-atom ion bunches with implicit suppression of the fluorescence halo effect. A coherent, stimulated Raman adiabatic passage (STIRAP) excitation scheme was implemented to excite the Rydberg atoms with high efficiency and to bypass the fluorescent intermedi-

ary states in the photoexcitation process. Models presented in Sec. 4.3 showed that detuning of the STIRAP lasers from resonance with the fluorescent intermediate state can be used to avoid its population throughout the entire atomic volume, while maintaining high transfer efficiency to the Rydberg state. With implementation of control over the laser pulse durations and timings, experimental measurements of the characteristic high transfer efficiency established the presence of STIRAP in the creation of the Rydberg-atom ion bunches.

Combining the methods presented in this thesis to suppress space-charge and disorder-induced emittance growth would allow for creation of an ion source limited only by its source thermal emittance. To do so would require shaping of the beam spatial charge density to linearise space-charge expansion, while also correlating the interparticle separations with Rydberg blockade or with an optical lattice. Further studies would be required in order to create shaped and correlated Rydberg ion bunches, as the blockade effect reduces the efficiency of photoexcitation, altering the shape of the ion beam distribution for a given laser intensity distribution compared to the excitation of non-blockaded ensembles. The production of spherical-shaped, crystalline-ordered ensembles of Rydberg atoms using spatially, temporally, and frequency-varying laser fields [130, 155], if created at sufficient density to be used for producing particle beams, would fulfil the requirements for the goal of suppressing both space-charge and disorder-induced heating. The models and experimental demonstrations presented in this thesis progress the CAEIS towards that goal.

Direct measurement of the suppression of DIH through correlation for a beam with linearised space-charge fields is, at present, beyond the capabilities of the CAEIS. As an example, the emittance of a disordered, spherical, 1 keV rubidium ion bunch of initial density $n = 10^{16}\,\mathrm{m}^{-3}$ and 100 μm initial transverse RMS beam size is $\epsilon = 10\,\mathrm{pm{\cdot}rad}$ after 10 μs (50 cm) of free-space propagation (Fig. 3.6). A blockade-correlated bunch of $r_b/a = 1$ has a lower beam emittance of $\epsilon = 5\,\mathrm{pm{\cdot}rad}$. The bunches expand under linear space-charge forces to transverse RMS size $\sigma = 1\,\mathrm{cm}$ after the 10 μs of propagation, so that with subsequent focusing over a 10 cm focal distance (0.1 rad focusing angle), the DIH-limited beam focal sizes for the disordered and blockaded bunches can be estimated from their emittances as 100 pm and 50 pm respectively. At present, the spatial resolution for measurement of beam focal sizes, using the knife edge method as in Fig. 2.8, is on the order of 10 μm. Experiments that measure the emittance of CAEIS beams using phase-space sampling have a measurement resolution on the order of 10 nm·rad [47]. Future improvement of detector sensitivity in the sampling of beam phase-space, or design of experiments to measure beam focal

sizes at the picometre scale, will enable a CAEIS to demonstrate suppression of DIH through spatial correlations.

The cold ions have been used in this thesis as an analogue for cold, ultrafast electron bunches. The methods presented here for suppressing emittance growth for cold ion bunches are directly applicable to the production of cold electron bunches, as each ionisation event within the cold atom source produces an electron and an ion at the same point in space. Repetition of the experiments of this thesis with cold electron bunches would face several challenges: First, the temperature of the electron bunches would need to be reduced in order to reduce thermal diffusion, so that the nonlinear space-charge effects become visible. Experiments to date have measured electron source temperatures on the order of 10 K, which is above the disorder-induced heating equilibrium temperature. Reducing the temperature of the electrons would require careful control over the photoexcitation laser bandwidths and polarisations [156], and management of the scattering of the electrons from their parent ions [92]. Secondly, electron bunches will only exhibit space-charge effects when created with short duration, necessary to achieve high charge density. Ultrafast photoionisation tends to create high-temperature electrons due to the large laser bandwidths of ultrafast pulses, and competing photoionisation processes can significantly lengthen the electron pulse duration [157]. If these problems in ultrafast electron generation can be overcome, the source brightness will be limited by the nonlinear space-charge expansion and the disorder-induced heating effects that were studied here using cold ions.

In conclusion, the studies presented in this thesis progress cold atom electron and ion sources towards exceeding Coulomb-induced beam brightness limits. Suppression of space-charge and disorder-induced emittance growth will be crucial for the development of high-brightness electron beams capable of ultrafast single-shot diffraction of biological molecules, which may require beam phase-space densities close to the quantum degeneracy limit [16]. Therefore, ultracold ion bunches can be used in the present day to prepare for future challenges in charged-particle beam source research and development.

Bibliography

[1] D. Murphy, R. W. Speirs, D. V. Sheludko, C. T. Putkunz, A. J. McCulloch, B. M. Sparkes & R. E. Scholten, 'Detailed observation of space-charge dynamics using ultracold ion bunches', *Nat. Commun.* **5**, 4489 (2014). [Cited on pages xvii and 15]

[2] D. Murphy, R. E. Scholten & B. M. Sparkes, 'Increasing the brightness of cold ion beams by suppressing disorder-induced heating with Rydberg blockade', *Phys. Rev. Lett.* **115**, 214802 (2015). [Cited on pages xvii and 33]

[3] D. Murphy & B. M. Sparkes, 'Disorder-induced heating of ultracold neutral plasmas created from atoms in partially filled optical lattices', *Phys. Rev. E* **94**, 021201(R) (2016). [Cited on pages xvii and 33]

[4] B. M. Sparkes, D. Murphy, R. J. Taylor, R. W. Speirs, A. J. McCulloch & R. E. Scholten, 'Stimulated Raman adiabatic passage for improved performance of a cold atom electron and ion source', *Phys. Rev. A* **94**, 023404 (2016). [Cited on pages xvii and 57]

[5] D. J. Thompson, D. Murphy, R. W. Speirs, R. M. W. van Bijnen, A. J. McCulloch, R. E. Scholten & B. M. Sparkes, 'Suppression of emittance growth using a shaped cold atom electron and ion source', *Phys. Rev. Lett.* **117**, 193202 (2016). [Cited on pages xvii, 15, 27, and 28]

[6] B. M. Sparkes, D. J. Thompson, A. J. McCulloch, D. Murphy, R. W. Speirs, J. S. Torrance & R. E. Scholten, 'High-coherence electron and ion bunches from laser-cooled atoms', *Microsc. Microanal.* **20**, 1008 (2014). [Cited on page xviii]

[7] J. Orloff, 'High-resolution focused ion beams', *Rev. Sci. Instrum.* **64**, 1105 (1993). [Cited on pages 1, 4, 11, and 15]

[8] J. L. S. Milne, M. J. Borgnia et al., 'Cryo-electron microscopy–a primer for the non-microscopist', *FEBS J.* **280**, 28 (2013). [Cited on page 1]

[9] Y. Cheng, N. Grigorieff, P. A. Penczek & T. Walz, 'A primer to single-particle cryo-electron microscopy', *Cell* **161**, 438 (2015). [Cited on page 1]

[10] K. J. Gaffney & H. N. Chapman, 'Imaging atomic structure and dynamics with ultrafast x-ray scattering', *Science* **316**, 1444 (2007). [Cited on page 2]

[11] W. E. King, G. H. Campbell, A. Frank, B. Reed, J. F. Schmerge, B. J. Siwick, B. C. Stuart & P. M. Weber, 'Ultrafast electron microscopy in materials science, biology, and chemistry', *J. Appl. Phys.* **97**, 8 (2005). [Cited on page 2]

[12] K. W. Urban, 'Studying atomic structures by aberration-corrected transmission electron microscopy', *Science* **321**, 506 (2008). [Cited on page 2]

[13] D. A. Plemmons, P. K. Suri & D. J. Flannigan, 'Probing structural and electronic dynamics with ultrafast electron microscopy', *Chem. Mater.* **27**, 3178 (2015). [Cited on page 2]

[14] T. LaGrange, M. R. Armstrong et al., 'Single-shot dynamic transmission electron microscopy', *App. Phys. Lett.* **89**, 044105 (2006). [Cited on page 2]

[15] J. R. Dwyer, C. T. Hebeisen, M. Ernstorfer, R. Harb, V. B. Deyirmenjian, R. E. Jordan & R. J. D. Miller, 'Femtosecond electron diffraction: "making the molecular movie"', *Phil. Trans. R. Soc. A* **364**, 741 (2006). [Cited on pages 2 and 15]

[16] B. W. Reed, M. R. Armstrong, N. D. Browning, G. H. Campbell, J. E. Evans, T. LaGrange & D. J. Masiel, 'The evolution of ultrafast electron microscope instrumentation', *Micros. Microanal.* **15**, 272 (2009). [Cited on pages 2, 56, and 83]

[17] E. Hecht, Optics, Chapter 6: More on Geometrical Optics, pp. 243–280, (Addison-Wesley, 2002). [Cited on page 2]

[18] M. Reiser, Theory and Design of Charged Particle Beams, (John Wiley & Sons, 2008). [Cited on pages 2 and 5]

[19] D. B. Williams & C. B. Carter, The Transmission Electron Microscope, Chapter 3: Electron Sources, pp. 73–89, (Springer, 1996). [Cited on page 4]

[20] M. Gulde, S. Schweda, G. Storeck, M. Maiti, H. K. Yu, A. M. Wodtke, S. Schäfer & C. Ropers, 'Ultrafast low-energy electron diffraction in transmission resolves polymer/graphene superstructure dynamics', *Science* **345**, 200 (2014). [Cited on page 4]

[21] G. Sciaini & R. J. D. Miller, 'Femtosecond electron diffraction: heralding the era of atomically resolved dynamics', *Rep. Prog. Phys.* **74**, 096101 (2011). [Cited on page 4]

[22] C. Hernandez-Garcia, P. G. O'Shea & M. L. Stutzman, 'Electron sources for accelerators', *Phys. Today* **61**, 44 (2008). [Cited on page 4]

[23] R. E. March & J. F. J. Todd, Practical Aspects of Ion Trap Mass Spectrometry: Chemical, Environmental, and Biomedical Applications, Volume V: Applications of Ion Trapping Devices, (CRC press, 1995). [Cited on page 4]

[24] I. G. Brown, Ed. The Physics and Technology of Ion Sources, Second Edition, (Wiley-VCH, 2004). [Cited on page 4]

[25] C. A. Brau, 'What brightness means', in The Physics and Applications of High Brightness Electron Beams J. Rosenzweig, G. Travish & L. Serafini, Eds. pp. 20–27 (World Scientific, 2002). [Cited on page 5]

[26] P. Kruit & G. H. Jansen, 'Space charge and statistical Coulomb effects', in Handbook of Charged Particle Optics Chapter 7, J. Orloff, Ed. (CRC Press, 1997). [Cited on page 5]

[27] I. M. Kapchinskij & V. V. Vladimirskij, 'Limitations of proton beam current in a strong focusing linear accelerator associated with the beam space charge', in Proceedings, 2nd International Conference on High-Energy Accelerators and Instrumentation 274 (CERN, Geneva, 1959). [Cited on page 7]

[28] O. J. Luiten, S. B. van der Geer, M. J. de Loos, F. B. Kiewiet & M. J. van der Wiel, 'How to realize uniform three-dimensional ellipsoidal electron bunches', *Phys. Rev. Lett.* **93**, 094802 (2004). [Cited on pages 7, 28, and 31]

[29] P. Musumeci, J. T. Moody, R. J. England, J. B. Rosenzweig & T. Tran, 'Experimental generation and characterization of uniformly filled ellipsoidal electron-beam distributions', *Phys. Rev. Lett.* **100**, 244801 (2008). [Cited on pages 8 and 28]

[30] J. T. Moody, P. Musumeci, M. S. Gutierrez, J. B. Rosenzweig & C. M. Scoby, 'Longitudinal phase space characterization of the blow-out regime of rf photoinjector operation', *Phys. Rev. ST Accel. Beams* **12**, 070704 (2009). [Cited on page 8]

[31] B. O'Shea, J. B. Rosenzweig et al., 'Measurement of self-shaped ellipsoidal bunches from a photoinjector with postacceleration', *Phys. Rev. ST Accel. Beams* **14**, 012801 (2011). [Cited on page 8]

[32] R. K. Li, K. G. Roberts, C. M. Scoby, H. To & P. Musumeci, 'Nanometer emittance ultralow charge beams from rf photoinjectors', *Phys. Rev. ST Accel. Beams* **15**, 090702 (2012). [Cited on page 8]

[33] P. Piot, Y.-E. Sun, T. J. Maxwell, J. Ruan, E. Secchi & J. C. T. Thangaraj, 'Formation and acceleration of uniformly filled ellipsoidal electron bunches obtained via space-charge-driven expansion from a cesium-telluride photocathode', *Phys. Rev. ST Accel. Beams* **16**, 010102 (2013). [Cited on page 8]

[34] G. H. Jansen, 'Coulomb interactions in particle beams', *J. Vac. Sci. Technol. B* **6**, 1977 (1988). [Cited on page 9]

[35] C. Coleman-Smith, H. A. Padmore & W. Weishi, 'Limits to electron beam emittance from stochastic Coulomb interactions', Advanced Light Source, Ernst Orlando Lawrence Berkeley National Laboratory, Berkeley, CA (US) Tech. Rep. LBNL-1824E (2009). [Cited on page 9]

[36] J. M. Maxson, I. V. Bazarov, W. Wan, H. A. Padmore & C. E. Coleman-Smith, 'Fundamental photoemission brightness limit from disorder induced heating', *New J. Phys.* **15**, 103024 (2013). [Cited on pages 9, 40, 41, and 56]

[37] B. J. Claessens, S. B. van der Geer, G. Taban, E. J. D. Vredenbregt & O. J. Luiten, 'Ultracold electron source', *Phys. Rev. Lett.* **95**, 164801 (2005). [Cited on pages 9, 11, and 16]

[38] J. L. Hanssen, E. A. Dakin, J. J. McClelland & M. Jacka, 'Using laser-cooled atoms as a focused ion beam source', *J. Vac. Sci. Technol. B* **24**, 2907 (2006). [Cited on pages 9, 11, and 16]

[39] A. J. McCulloch, D. V. Sheludko, S. D. Saliba, S. C. Bell, M. Junker, K. A. Nugent & R. E. Scholten, 'Arbitrarily shaped high-coherence electron bunches from cold atoms', *Nature Phys.* **7**, 785 (2011). [Cited on pages 10, 11, 16, 18, 20, 25, 28, and 43]

[40] T. C. Killian, 'Ultracold neutral plasmas', *Science* **316**, 705 (2007). [Cited on pages 10, 16, 33, 39, and 56]

[41] W. D. Phillips, 'Nobel lecture: laser cooling and trapping of neutral atoms', *Rev. Mod. Phys.* **70**, 721 (1998). [Cited on page 10]

[42] D. Comparat, T. Vogt, N. Zahzam, M. Mudrich & P. Pillet, 'Star cluster dynamics in a laboratory: electrons in an ultracold plasma', *Mon. Not. R. Astron. Soc.* **361**, 1227 (2005). [Cited on page 10]

[43] S. G. Kuzmin & T. M. O'Neil, 'Numerical simulation of ultracold plasmas: how rapid intrinsic heating limits the development of correlation', *Phys. Rev. Lett.* **88**, 065003 (2002). [Cited on page 10]

[44] D. O. Gericke & M. S. Murillo, 'Disorder-induced heating of ultracold plasmas', *Contrib. Plasma Phys.* **43**, 298 (2003). [Cited on pages 11 and 33]

[45] M. Lyon & S. L. Rolston, 'Ultracold neutral plasmas', *Rep. Prog. Phys.* **80**, 017001 (2016). [Cited on page 11]

[46] S. D. Saliba, C. T. Putkunz, D. V. Sheludko, A. J. McCulloch, K. A. Nugent & R. E. Scholten, 'Spatial coherence of electron bunches extracted from an arbitrarily shaped cold atom electron source', *Opt. Express* **20**, 3967 (2012). [Cited on page 11]

[47] A. J. McCulloch, D. V. Sheludko, M. Junker & R. E. Scholten, 'High-coherence picosecond electron bunches from cold atoms', *Nat. Commun.* **4**, 1692 (2013). [Cited on pages 11, 17, 61, and 82]

[48] W. J. Engelen, M. A. van der Heijden, D. J. Bakker, E. J. D. Vredenbregt & O. J. Luiten, 'High-coherence electron bunches produced by femtosecond photoionization', *Nat. Commun.* **4**, 1693 (2013). [Cited on pages 11, 17, and 25]

[49] M. W. van Mourik, W. J. Engelen, E. J. D. Vredenbregt & O. J. Luiten, 'Ultrafast electron diffraction using an ultracold source', *Struct. Dyn.* **1**, 034302 (2014). [Cited on page 11]

[50] R. W. Speirs, C. T. Putkunz, A. J. McCulloch, K. A. Nugent, B. M. Sparkes & R. E. Scholten, 'Single-shot electron diffraction using a cold atom electron source', *J. Phys. B: At. Mol. Opt. Phys.* **48**, 214002 (2015). [Cited on pages 11 and 29]

[51] A. J. McCulloch, B. M. Sparkes & R. E. Scholten, 'Cold electron sources using laser-cooled atoms', *J. Phys. B: At. Mol. Opt. Phys.* **49**, 164004 (2016). [Cited on page 11]

[52] M. S. Joens, C. Huynh et al., 'Helium ion microscopy (HIM) for the imaging of biological samples at sub-nanometer resolution', *Sci. Rep.* **3**, (2013). [Cited on page 11]

[53] K. A. Twedt, L. Chen & J. J. McClelland, 'Scanning ion microscopy with low energy lithium ions', *Ultramicroscopy* **142**, 24 (2014). [Cited on page 12]

[54] M. Viteau, M. Reveillard et al., 'Ion microscopy based on laser-cooled cesium atoms', *Ultramicroscopy* **164**, 70 (2016). [Cited on page 12]

[55] A. V. Steele, B. Knuffman & J. J. McClelland, 'Inter-ion Coulomb interactions in a magneto-optical trap ion source', *J. Appl. Phys.* **109**, 104308 (2011). [Cited on pages 12 and 16]

[56] G. E. Remnev, I. F. Isakov et al., 'High intensity pulsed ion beam sources and their industrial applications', *Surf. Coat. Technol.* **114**, 206 (1999). [Cited on page 12]

[57] C. Höhr, D. Fischer, R. Moshammer, A. Dorn & J. Ullrich, 'A subnanosecond pulsed ion source for micrometer focused ion beams', *Rev. Sci. Instrum.* **79**, 053102 (2008). [Cited on page 12]

[58] M. P. Reijnders, P. A. van Kruisbergen, G. Taban, S. B. van der Geer, P. H. A. Mutsaers, E. J. D. Vredenbregt & O. J. Luiten, 'Low-energy-spread ion bunches from a trapped atomic gas', *Phys. Rev. Lett.* **102**, 034802 (2009). [Cited on pages 12 and 16]

[59] J. J. McClelland, A. V. Steele, B. Knuffman, K. A. Twedt, A. Schwarzkopf & T. M. Wilson, 'Bright focused ion beam sources based on laser-cooled atoms', *Appl. Phys. Rev.* **3**, 011302 (2016). [Cited on page 12]

[60] D. V. Sheludko, 'Shaped electron bunches from ultracold plasma', PhD thesis, School of Physics, The University of Melbourne (2010). Available: http://hdl.handle.net/11343/35765 [Cited on page 12]

[61] S. C. Bell, 'Cold electrons extracted from an ultracold plasma', PhD thesis, School of Physics, The University of Melbourne (2011). [Cited on page 12]

[62] S. D. Saliba, 'A cold atom electron source for diffractive imaging', PhD thesis, School of Physics, The University of Melbourne (2011). Available: http://hdl.handle.net/11343/36823 [Cited on page 12]

[63] A. J. McCulloch, 'Generation of shaped cold electron bunches for ultrafast electron diffraction', PhD thesis, School of Physics, The University of Melbourne (2013). Available: http://hdl.handle.net/11343/37862 [Cited on pages 12 and 73]

[64] N. M. Buckanie, J. Göhre, P. Zhou, D. Von der Linde, M. Horn-von Hoegen & F.-J. Meyer zu Heringdorf, 'Space charge effects in photoemission electron microscopy using amplified femtosecond laser pulses', *J. Phys. Condens. Matter* **21**, 314003 (2009). [Cited on page 15]

[65] S. Bernal, H. Li et al., 'Beam experiments in the extreme space-charge limit on the University of Maryland electron ring', *Phys. Plasmas* **11**, 2907 (2004). [Cited on page 15]

[66] B. J. Siwick, J. R. Dwyer, R. E. Jordan & R. J. D. Miller, 'Ultrafast electron optics: propagation dynamics of femtosecond electron packets', *J. Appl. Phys.* **92**, 1643 (2002). [Cited on page 15]

[67] B. L. Qian & H. E. Elsayed-Ali, 'Electron pulse broadening due to space charge effects in a photoelectron gun for electron diffraction and streak camera systems', *J. Appl. Phys.* **91**, 462 (2002). [Cited on page 15]

[68] Z. Tao, H. Zhang, P. M. Duxbury, M. Berz & C. Ruan, 'Space charge effects in ultrafast electron diffraction and imaging', *J. Appl. Phys.* **111**, 044316 (2012). [Cited on page 15]

[69] R. P. Chatelain, V. Morrison, C. Godbout, S. B. van der Geer, M. de Loos & B. J. Siwick, 'Ultrafast electron diffraction with radio-frequency compressed electron pulses', *Ultramicroscopy* **116**, 86 – 94 (2012). [Cited on page 15]

[70] F. O. Kirchner, A. Gliserin, F. Krausz & P. Baum, 'Laser streaking of free electrons at 25 keV', *Nature Photon.* **8**, 52 (2014). [Cited on page 15]

[71] T. B. Mitchell, J. J. Bollinger, X.-P. Huang & W. M. Itano, 'Direct observations of the structural phases of crystallised ion plasmas', *Phys. Plasmas* **6**, 1751 (1999). [Cited on page 15]

[72] N. L. Kugland, D. D. Ryutov et al., 'Self-organized electromagnetic field structures in laser-produced counter-streaming plasmas', *Nature Phys.* **8**, 809 (2012). [Cited on page 15]

[73] B. A. Remington, D. Arnett, R. P. Drake & H. Takabe, 'Modeling astrophysical phenomena in the laboratory with intense lasers', *Science* **284**, 1488 (1999). [Cited on page 15]

[74] D. Feldbaum, N. V. Morrow, S. K. Dutta & G. Raithel, 'Coulomb expansion of laser-excited ion plasmas', *Phys. Rev. Lett.* **89**, 173004 (2002). [Cited on pages 15, 19, and 22]

[75] S. Kulin, T. C. Killian, S. D. Bergeson & S. L. Rolston, 'Plasma oscillations and expansion of an ultracold neutral plasma', *Phys. Rev. Lett.* **85**, 318 (2000). [Cited on page 15]

[76] B. J. Claessens, M. P. Reijnders, G. Taban, O. J. Luiten & E. J. D. Vredenbregt, 'Cold electron and ion beams generated from trapped atoms', *Phys. Plasmas* **14**, 093101 (2007). [Cited on page 16]

[77] B. Knuffman, A. V. Steele & J. J. McClelland, 'Cold atomic beam ion source for focused ion beam applications', *J. Appl. Phys.* **114**, 044303 (2013). [Cited on page 16]

[78] L. Kime, A. Fioretti et al., 'High-flux monochromatic ion and electron beams based on laser-cooled atoms', *Phys. Rev. A* **88**, 033424 (2013). [Cited on page 16]

[79] S. C. Bell, M. Junker, M. Jasperse, L. D. Turner, Y.-J. Lin, I. B. Spielman & R. E. Scholten, 'A slow atom source using a collimated effusive oven and a single-layer variable pitch coil Zeeman slower', *Rev. Sci. Instrum.* **81**, 013105 (2010). [Cited on page 18]

[80] N. Debernardi, M. P. Reijnders, W. J. Engelen, T. T. J. Clevis, P. H. A. Mutsaers, O. J. Luiten & E. J. D. Vredenbregt, 'Measurement of the temperature of an ultracold ion source using time-dependent electric fields', *J. Appl. Phys.* **110**, 024501 (2011). [Cited on page 18]

[81] C. J. Davisson & C. J. Calbick, 'Electron lenses', *Phys. Rev.* **42**, 580 (1932). [Cited on page 18]

[82] R. A. Kishek, S. Bernal et al., 'Simulations and experiments with space-charge-dominated beams', *Phys. Plasmas* **10**, 2016 (2003). [Cited on page 19]

[83] O. A. Anderson, 'Internal dynamics and emittance growth in space charge dominated beams', *Part. Accel.* **21**, 197 (1987). [Cited on page 19]

[84] R. L. Gluckstern, 'Analytic model for halo formation in high current ion linacs', *Phys. Rev. Lett.* **73**, 1247 (1994). [Cited on page 19]

[85] F. B. Rizzato, R. Pakter & Y. Levin, 'Wave breaking and particle jets in intense inhomogeneous charged beams', *Phys. Plasmas* **14**, 110701 (2007). [Cited on page 19]

[86] A. E. Kaplan, B. Y. Dubetsky & P. L. Shkolnikov, 'Shock shells in Coulomb explosions of nanoclusters', *Phys. Rev. Lett.* **91**, 143401 (2003). [Cited on pages 19 and 22]

[87] F. Peano, R. A. Fonseca & L. O. Silva, 'Dynamics and control of shock shells in the Coulomb explosion of very large deuterium clusters', *Phys. Rev. Lett.* **94**, 033401 (2005). [Cited on page 19]

[88] V. F. Kovalev & V. Y. Bychenkov, 'Quasimonoenergetic ion bunches from exploding microstructured targets', *Phys. Plasmas* **14**, 053103 (2007). [Cited on page 19]

[89] U. Saalmann, A. Mikaberidze & J. M. Rost, 'Laser-driven nanoplasmas in doped helium droplets: local ignition and anisotropic growth', *Phys. Rev. Lett.* **110**, 133401 (2013). [Cited on page 19]

[90] I. Haber, D. Kehne, M. Reiser & H. Rudd, 'Experimental, theoretical, and numerical investigation of the homogenisation of density nonuniformities in the periodic transport of a space-charge dominated electron beam', *Phys. Rev. A* **44**, 5194 (1991). [Cited on page 19]

[91] 'General particle tracer', http://www.pulsar.nl/gpt/ Pulsar Physics. [Cited on pages 20 and 31]

[92] W. J. Engelen, E. J. D. Vredenbregt & O. J. Luiten, 'Analytical model of an isolated single-atom electron source', *Ultramicroscopy* **147**, 61–69 (2014). [Cited on pages 21, 61, and 83]

[93] L. P. Maguire, R. M. W. van Bijnen, E. Mese & R. E. Scholten, 'Theoretical calculation of saturated absorption spectra for multi-level atoms', *J. Phys. B: At. Mol. Opt. Phys.* **39**, 2709 (2006). [Cited on pages 21 and 62]

[94] L. Allen & J. H. Eberly, Optical Resonance and Two-Level Atoms, (Dover Publications, 1987). [Cited on pages 21 and 23]

[95] D. A. Steck, 'Rubidium 85 D line data', http://steck.us/alkalidata/. [Cited on pages 21, 22, and 60]

[96] M. J. Piotrowicz, C. MacCormick, A. Kowalczyk, S. Bergamini, I. I. Beterov & E. A. Yakshina, 'Measurement of the electric dipole moments for transitions to rubidium Rydberg states via autler-townes splitting', *New J. Phys.* **13**, 093012 (2011). [Cited on page 22]

[97] R. M. W. van Bijnen, C. Ravensbergen, D. J. Bakker, G. J. Dijk, S. J. J. M. F. Kokkelmans & E. J. D. Vredenbregt, 'Patterned Rydberg excitation and ionization with a spatial light modulator', *New J. Phys.* **17**, 023045 (2015). [Cited on page 28]

[98] S. B. van der Geer, M. J. de Loos & O. J. Luiten, 'Pancakes versus beer-cans in terms of 6D phase-space density', in Proceedings of EPAC08, Genoa, Italy MOPC036, p. 151 (2008). [Cited on page 29]

[99] K. L. Brown & G. W. Tautfest, 'Faraday-cup monitors for high-energy electron beams', *Rev. Sci. Instrum.* **27**, 696 (1956). [Cited on page 30]

[100] G. ten Haaf, S. H. W. Wouters, S. B. van der Geer, E. J. D. Vredenbregt & P. H. A. Mutsaers, 'Performance predictions of a focused ion beam from a laser cooled and compressed atomic beam', *J. Appl. Phys.* **116**, 244301 (2014). [Cited on page 33]

[101] M. S. Murillo, 'Using Fermi statistics to create strongly coupled ion plasmas in atom traps', *Phys. Rev. Lett.* **87**, 115003 (2001). [Cited on page 33]

[102] T. Pohl, T. Pattard & J. M. Rost, 'On the possibility of "correlation cooling" of ultracold neutral plasmas', *J. Phys. B: At. Mol. Opt. Phys.* **37**, L183 (2004). [Cited on pages 33, 48, 49, and 54]

[103] G. Bannasch, T. C. Killian & T. Pohl, 'Strongly coupled plasmas via Rydberg blockade of cold atoms', *Phys. Rev. Lett.* **110**, 253003 (2013). [Cited on pages 33, 35, 42, 44, and 54]

[104] T. Pohl, T. Pattard & J. M. Rost, 'Relaxation to nonequilibrium in expanding ultracold neutral plasmas', *Phys. Rev. Lett.* **94**, 205003 (2005). [Cited on page 33]

[105] P. McQuillen, T. Strickler, T. Langin & T. C. Killian, 'Ion temperature evolution in an ultracold neutral plasma', *Phys. Plasmas* **22**, 033513 (2015). [Cited on page 33]

[106] J. T. Mendonça & H. Terças, Physics of Ultra-Cold Matter, Chapter 14: Ultra-cold plasmas, (Springer, 2012). [Cited on page 34]

[107] S. D. Bergeson, A. Denning, M. Lyon & F. Robicheaux, 'Density and temperature scaling of disorder-induced heating in ultracold plasmas', *Phys. Rev. A* **83**, 023409 (2011). [Cited on page 34]

[108] M. Lyon, S. D. Bergeson & M. S. Murillo, 'Limit of strong ion coupling due to electron shielding', *Phys. Rev. E* **87**, 033101 (2013). [Cited on page 35]

[109] M. Baus & J. P. Hansen, 'Statistical mechanics of simple Coulomb systems', *Phys. Rep.* **59**, 1 (1980). [Cited on page 35]

[110] D. H. E. Dubin & T. M. O'Neil, 'Trapped nonneutral plasmas, liquids, and crystals (the thermal equilibrium states)', *Rev. Mod. Phys.* **71**, 87 (1999). [Cited on page 35]

[111] D. W. Hogg, 'Distance measures in cosmology', arXiv:astro-ph/9905116v4 (2000). [Cited on page 36]

[112] A. Y. Toukmaji & J. A. Board Jr., 'Ewald summation techniques in perspective: a survey', *Comput. Phys. Commun.* **95**, 73 (1996). [Cited on page 36]

[113] C. Kittel & P. McEuen, Introduction to Solid State Physics, (Wiley New York, 1986). [Cited on pages 37 and 48]

[114] M. J. L. Sangster & M. Dixon, 'Interionic potentials in alkali halides and their use in simulations of the molten salts', *Adv. Phys.* **25**, 247 (1976). [Cited on page 37]

[115] L. Hernquist, F. R. Bouchet & Y. Suto, 'Application of the Ewald method to cosmological N-body simulations', *Astrophys. J. Suppl. Ser.* **75**, 231 (1991). [Cited on page 37]

[116] W. H. Press et al., Numerical Recipes in C, (Cambridge University Press, 2012). [Cited on page 37]

[117] R. T. Farouki & S. Hamaguchi, 'Thermodynamics of strongly-coupled yukawa systems near the one-component-plasma limit. II. Molecular dynamics simulations', *J. Chem. Phys.* **101**, 9885 (1994). [Cited on page 38]

[118] E. Urban, T. A. Johnson, T. Henage, L. Isenhower, D. D. Yavuz, T. G. Walker & M. Saffman, 'Observation of Rydberg blockade between two atoms', *Nature Phys.* **5**, 110 (2009). [Cited on page 42]

[119] D. Petrosyan, M. Höning & M. Fleischhauer, 'Spatial correlations of Rydberg excitations in optically driven atomic ensembles', *Phys. Rev. A* **87**, 053414 (2013). [Cited on pages 42 and 43]

[120] M. Robert-de-Saint-Vincent, C. S. Hofmann, H. Schempp, G. Günter, S. Whitlock & M. Weidemüller, 'Spontaneous avalanche ionization of a strongly blockaded Rydberg gas', *Phys. Rev. Lett.* **110**, 045004 (2013). [Cited on pages 42, 43, 44, 47, 57, and 65]

[121] K. Singer, J. Stanojevic, M. Weidemüller & R. Côté, 'Long-range interactions between alkali Rydberg atom pairs correlated to the ns–ns, np–np

and nd–nd asymptotes', *J. Phys. B: At. Mol. Opt. Phys.* **38**, S295 (2005). [Cited on pages 42 and 64]

[122] J. D. Pritchard, D. Maxwell, A. Gauguet, K. J. Weatherill, M. P. A. Jones & C. S. Adams, 'Cooperative atom-light interaction in a blockaded Rydberg ensemble', *Phys. Rev. Lett.* **105**, 193603 (2010). [Cited on page 42]

[123] G. Taban, M. P. Reijnders, S. C. Bell, S. B. van der Geer, O. J. Luiten & E. J. D. Vredenbregt, 'Design and validation of an accelerator for an ultracold electron source', *Phys. Rev. ST Accel. Beams.* **11**, 050102 (2008). [Cited on page 43]

[124] G. Stell, 'The Percus-Yevick equation for the radial distribution function of a fluid', *Physica* **29**, 517 (1963). [Cited on page 44]

[125] H. E. DeWitt & Y. Rosenfeld, 'Derivation of the one component plasma fluid equation of state in strong coupling', *Phys. Lett. A* **75**, 79 (1979). [Cited on page 44]

[126] O. J. Luiten, 'Beyond the RF photogun', in The physics and applications of high brightness electron beams **1**, 108 (2003). [Cited on page 45]

[127] S. Torquato, O. U. Uche & F. H. Stillinger, 'Random sequential addition of hard spheres in high Euclidean dimensions', *Phys. Rev. E* **74**, 061308 (2006). [Cited on page 45]

[128] W. S. Jodrey & E. M. Tory, 'Computer simulation of close random packing of equal spheres', *Phys. Rev. A* **32**, 2347 (1985). [Cited on page 45]

[129] M. T. DePue, C. McCormick, S. L. Winoto, S. Oliver & D. S. Weiss, 'Unity occupation of sites in a 3D optical lattice', *Phys. Rev. Lett.* **82**, 2262 (1999). [Cited on page 48]

[130] J. Schachenmayer, I. Lesanovsky, A. Micheli & A. J. Daley, 'Dynamical crystal creation with polar molecules or Rydberg atoms in optical lattices', *New J. Phys.* **12**, 103044 (2010). [Cited on pages 48, 55, and 82]

[131] I. Bloch, 'Ultracold quantum gases in optical lattices', *Nature Phys.* **1**, 23 (2005). [Cited on page 49]

[132] G. Grynberg, B. Lounis, P. Verkerk, J.-Y. Courtois & C. Salomon, 'Quantized motion of cold cesium atoms in two-and three-dimensional optical potentials', *Phys. Rev. Lett.* **70**, 2249 (1993). [Cited on page 49]

[133] C. S. Adams, S. G. Cox, E. Riis & A. S. Arnold, 'Laser cooling of calcium in a "golden ratio" quasi-electrostatic lattice', *J. Phys. B: At. Mol. Opt. Phys.* **36**, 1933 (2003). [Cited on page 49]

[134] R. M. Martin, Electronic Structure: Basic Theory and Practical Methods, (Cambridge University Press, 2004). [Cited on page 49]

[135] G. Makov & M. C. Payne, 'Periodic boundary conditions in ab initio calculations', *Phys. Rev. B* **51**, 4014 (1995). [Cited on page 51]

[136] K. D. Nelson, X. Li & D. S. Weiss, 'Imaging single atoms in a three-dimensional array', *Nature Phys.* **3**, 556 (2007). [Cited on page 54]

[137] M. Lyon & S. D. Bergeson, 'Towards stronger Coulomb coupling in an ultracold neutral plasma', *Contrib. Plasma Phys.* **55**, 399 (2015). [Cited on page 54]

[138] J. A. Sedlacek, A. Schwettmann, H. Kübler, R. Löw, T. Pfau & J. P. Shaffer, 'Microwave electrometry with Rydberg atoms in a vapour cell using bright atomic resonances', *Nature Phys.* **8**, 819–824 (2012). [Cited on page 57]

[139] M. Saffman, T. G. Walker & K. Mølmer, 'Quantum information with Rydberg atoms', *Rev. Mod. Phys.* **82**, 2313 (2010). [Cited on page 57]

[140] D. Comparat & P. Pillet, 'Dipole blockade in a cold Rydberg atomic sample [invited]', *J. Opt. Soc. Am. B* **27**, A208 (2010). [Cited on page 57]

[141] S. D. Bergeson & M. Lyon, 'Measurements of the ion velocity distribution in an ultracold neutral plasma derived from a cold, dense Rydberg gas', arXiv:1601.07439v1 [physics.atom-ph] (2016). [Cited on page 57]

[142] 'The NIST reference on constants, units, and uncertainty', http://physics.nist.gov/cuu/Constants/ National Institute of Standards and Technology. [Cited on page 58]

[143] C. J. Lorenzen & K. Niemax, 'Quantum defects of the $n^2P_{1/2,3/2}$ levels in ^{39}K I and ^{85}Rb I', *Phys. Scripta* **27**, 300 (1983). [Cited on page 58]

[144] J. E. Sansonetti, 'Wavelengths, transition probabilities, and energy levels for the spectra of rubidium (Rb I through Rb XXXVII)', *J. Phys. Chem. Ref. Data* **35**, 301 (2006). [Cited on page 58]

[145] J. D. Pritchard, 'Cooperative optical non-linearity in a blockaded Rydberg ensemble', PhD thesis, Department of Physics, Durham University (2011). Available: http://etheses.dur.ac.uk/782/ [Cited on page 60]

[146] J. Deiglmayr, M. Reetz-Lamour, T. Amthor, S. Westermann, A. de Oliveira & M. Weidemüller, 'Coherent excitation of Rydberg atoms in an ultracold gas', *Opt. Commun.* **264**, 293 (2006). [Cited on pages 60 and 72]

[147] V. D. Ovsiannikov, I. L. Glukhov & E. A. Nekipelov, 'Radiative lifetime and photoionization cross-section for Rydberg states in alkali-metal atoms', *Opt. Spectrosc.* **111**, 25 (2011). [Cited on page 60]

[148] D. B. Branden, T. Juhasz, T. Mahlokozera, C. Vesa, R. O. Wilson, M. Zheng, A. Kortyna & D. A. Tate, 'Radiative lifetime measurements of rubidium Rydberg states', *J. Phys. B: At. Mol. Opt. Phys.* **43**, 015002 (2009). [Cited on page 60]

[149] F. Merkt, A. Osterwalder, R. Seiler, R. Signorell, H. Palm, H. Schmutz & R. Gunzinger, 'High Rydberg states of argon: Stark effect and field-ionization properties', *J. Phys. B: At. Mol. Opt. Phys.* **31**, 1705 (1998). [Cited on page 61]

[150] R. P. Abel, A. K. Mohapatra, M. G. Bason, J. D. Pritchard, K. J. Weatherill, U. Raitzsch & C. S. Adams, 'Laser frequency stabilization to excited state transitions using electromagnetically induced transparency in a cascade system', *Appl. Phys. Lett.* **94**, 071107 (2009). [Cited on page 61]

[151] M. Fleischhauer, A. Imamoglu & J. P. Marangos, 'Electromagnetically induced transparency: optics in coherent media', *Rev. Mod. Phys.* **77**, 633 (2005). [Cited on page 61]

[152] R. J. Taylor, 'Rydberg excitation of rubidium to produce an ultra-cold plasma', MSc thesis, School of Physics, The University of Melbourne (2013). [Cited on page 63]

[153] K. Bergmann, H. Theuer & B. W. Shore, 'Coherent population transfer among quantum states of atoms and molecules', *Rev. Mod. Phys.* **70**, 1003 (1998). [Cited on page 71]

[154] T. Cubel, B. K. Teo, V. Malinovsky, J. Guest, A. Reinhard, B. Knuffman, P. Berman & G. Raithel, 'Coherent population transfer of ground-state atoms into Rydberg states', *Phys. Rev. A* **72**, 023405 (2005). [Cited on page 72]

[155] R. M. W. van Bijnen, S. Smit, K. A. H. van Leeuwen, E. J. D. Vredenbregt & S. J. J. M. F. Kokkelmans, 'Adiabatic formation of Rydberg crystals

with chirped laser pulses', *J. Phys. B: At. Mol. Opt. Phys.* **44**, 184008 (2011). [Cited on page 82]

[156] W. J. Engelen, D. J. Bakker, O. J. Luiten & E. J. D. Vredenbregt, 'Polarization effects on the effective temperature of an ultracold electron source', *New J. Phys.* **15**, 123015 (2013). [Cited on page 83]

[157] R. W. Speirs, A. J. McCulloch, B. M. Sparkes & R. E. Scholten, 'Identification of competing ionisation processes in the generation of ultrafast electron bunches from cold atom electron sources', submitted to *New J. Phys.*, under review (2017). [Cited on page 83]

Appendix A

Publications

This section contains published articles to which I have been an author during the PhD, described in this thesis as detailed in the list of publications (p. xvii). The contributions of each author towards work included in the thesis are described in the preface (p. ix).

nature COMMUNICATIONS

ARTICLE

Received 9 May 2014 | Accepted 24 Jun 2014 | Published 17 Jul 2014

DOI: 10.1038/ncomms5489

Detailed observation of space-charge dynamics using ultracold ion bunches

D. Murphy[1], R.W. Speirs[1], D.V. Sheludko[1], C.T. Putkunz[1], A.J. McCulloch[1], B.M. Sparkes[1] & R.E. Scholten[1]

Control of Coulomb expansion in charged particle beams is of critical importance for applications including electron and ion microscopy, injectors for particle accelerators and in ultrafast electron diffraction, where space-charge effects constrain the temporal and spatial imaging resolution. The development of techniques to reverse space-charge-driven expansion, or to observe shock waves and other striking phenomena, have been limited by the masking effect of thermal diffusion. Here we show that ultracold ion bunches extracted from laser-cooled atoms can be used to observe the effects of self-interactions with unprecedented detail. We generate arrays of small closely spaced ion bunches that interact to form complex and surprising patterns. We also show that nanosecond cold ion bunches provide data for analogous ultrafast electron systems, where the dynamics occur on timescales too short for detailed observation. In a surprising twist, slow atoms may underpin progress in high-energy and ultrafast physics.

[1] ARC Centre of Excellence for Coherent X-ray Science, School of Physics, The University of Melbourne, Parkville, Victoria 3010, Australia. Correspondence and requests for materials should be addressed to R.E.S. (email: scholten@unimelb.edu.au).

Coulomb interactions can lead to instabilities and emittance growth in charged particle beams, limitting the ultimate performance of electron and ion microscopes[1,2] and high-energy particle accelerators[3]. In ultrafast electron diffraction[4–6], space–charge effects constrain the capacity to obtain diffraction information. For example, in bunches containing just 18 electrons, Coulomb repulsion was shown to increase the bunch duration by 50% and energy spread sevenfold[7]. Coulomb repulsion before[8] and after[9] the specimen thus place an ultimate limit on the ability to extract useful diffraction information. For strongly coupled systems, Coulomb interactions mediate interesting collective effects including the formation of Wigner crystals[10], self-organization[11] and shock wave phenomena[12–14]. Thus, although the underlying physics of the two-particle Coulomb interaction is simple, the behaviour of beams with complicated spatial and temporal structure can be difficult to predict. Particle trajectory calculations are straightforward for a few particles or even a few million, but become intractable for high-density high-current systems. The development of useful models of self-field effects has been limited by a lack of detailed comparative experimental data where the space–charge and thermal effects are clearly distinguishable.

Cold charged particle sources based on near-threshold photoionization of laser-cooled atoms[15–18] produce electrons and ions with temperatures as low as a few kelvin and millikelvin, respectively, allowing detailed investigation of self-field and strong coupling effects. The ability to arbitrarily shape the initial charged particle distribution[18] enables flexible investigation of the spatial dependence of inter-particle dynamics.

The effects of space–charge interactions are enhanced in ion bunches compared with electron bunches. Owing to their high mass, they have comparatively low velocities and hence retain a high charge density following the ionization. The ion temperature is also three to four orders of magnitude lower, allowing distinct measurement of space–charge effects without significant loss of detail due to thermal expansion.

During an ionizing laser pulse of time t_i in a static electric field, the ion bunch will grow longitudinally as the ions are produced, but the elongation is less than that of an electron bunch created over the same duration due to the larger ion mass. The equivalent-length electron bunch pulse duration t_e in the same field is then $t_e = t_i\sqrt{m_e/m_i}$, where $m_{e,i}$ are the electron and ion mass. The visibility of the space–charge effect is enhanced in ions compared with that in the equivalent-time electron bunches because the ion temperature remains low, with the excess ionization energy predominantly transferred to the photoelectrons. Thus, ion bunches created with ionization pulse durations of a few nanoseconds demonstrate space–charge effects equivalent to those in electron bunches created on picosecond timescales, comparable to the fast electron beams created using cold atom sources[19,20].

Pioneering work with cold atom sources has shown evidence of space–charge effects[21,22], and the role of Coulomb interactions in cold ion beams has been studied in detail for continuous-mode low charge density operation[23–25]. In this paper we investigate space–charge effects in arbitrarily shaped nanosecond duration cold ion bunches produced by near-threshold photoionization of laser-cooled atoms. We study in detail a complex ion distribution as an example of the subtle space–charge dynamics that can be observed, in particular the formation of shock wave structures where a halo of cold ions is compressed by the space–charge-driven expansion of a small high-density ion bunch. We observe collective behaviour including high-density caustics and the formation of complex patterns from long-range interaction between small charge bunches. The detail allowed us to systematically test and develop a comprehensive model of the system including self-field effects, illustrating the advantages of observation without thermal diffusion.

Results

Generating ultracold ion bunches. In our experiments (see Methods), ion bunches were formed by photoionization of an ensemble of laser-cooled rubidium atoms in a magneto-optical trap (Fig. 1). The two-colour ionization process allows ions to be created in an arbitrary charge density profile[18]. The intensity profile of an excitation laser beam (wavelength $\lambda = 780$ nm, Ω_{12}) was shaped using a reflective phase-shifting spatial light modulator. A second tunable laser (wavelength $\lambda = 480$ nm, Ω_{23}) was used to couple the excited atoms to a selectable Rydberg state. With the addition of an external static electric field (20–80 kV m^{-1}) the atoms are ionized in the region of overlap of the two laser beams. Control of the bunch charge was varied by changing the excitation laser beam power. The ions were accelerated in the static field over a distance of 2.5 cm before drifting 21.5 or 70 cm to a phosphor-coupled microchannel-plate and CCD camera to image the charge density profile of each bunch.

Ring formation. At low charge densities, the bunches expand linearly, driven by thermal diffusion. With increasing charge,

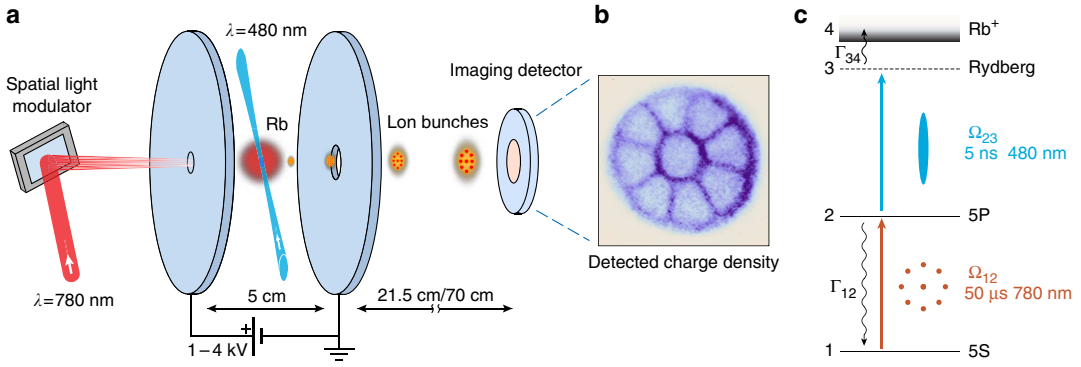

Figure 1 | Measurement of space-charge dynamics in ultracold ion bunches. (**a**) Cold rubidium atoms are prepared in a magneto-optical trap. Ions are produced by two-colour near-threshold photoionization. The cold ions are accelerated by a static electric field before drifting 21.5 or 70 cm in a zero-field region to an imaging detector to record their transverse spatial profile. (**b**) Ion bunch transverse spatial distribution; density shown in false colour. (**c**) Rubidium energy levels with optical couplings labelled by the Rabi rates Ω, decay rates Γ and schematic transverse laser intensity profiles for relevant states in the two-colour ionization process.

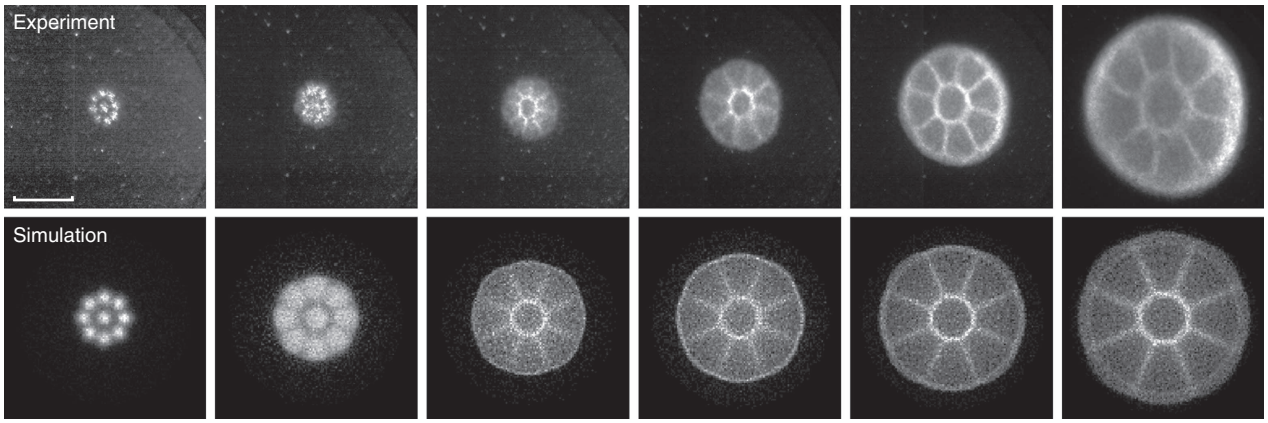

Figure 2 | Space-charge interactions between ion bunches. Ion beam density profiles imaged 24 cm (7.9 μs) from the source region, for nine closely spaced bunches each of 100 μm diameter. Upper panel: experimentally measured profiles for increasing bunch charge, showing increased expansion and the emergence of high-density regions due to intra-beam space-charge effects. Left to right: shaped excitation laser beam with total power of <1, 70, 210, 340, 640 and 980 μW. Lower panel: simulated bunch structure for ion bunches with spatial profiles calculated with laser profile and powers as used in the experimental images. Total bunch charges of 0 C, 2 fC, 8 fC, 10 fC, 13 fC and 19 fC. The greyscale density profiles are normalized individually to maximize contrast. Scale bar, 5 mm.

rather than the simple expansion and loss of detail that might be expected, Coulomb interactions accelerate the growth and induce nonlinear transformation of the bunch structure. Figure 2 shows experimentally measured projected ion bunch densities, for nine small closely spaced ion bunches. At low-excitation laser power (low bunch charge; left column) the measured distribution after propagation closely matches the intensity profile of the excitation laser and original bunch shape. Increased laser power and bunch charge induce surprisingly complex structure due to Coulomb interactions within and between the bunches. In particular, we observe the formation of high-density rings and collision boundaries between bunches.

The rings are visually similar to those formed by the interplay between self-fields and external focusing elements in electron storage rings[26], but in our case are found for all high-density initial distributions regardless of beam size and internal profile. The rings are also suggestive of phase–space wave-breaking phenomena, which have been predicted for particle beams[27–29], and similar to shock-shell formation predicted, but not yet experimentally observed, for Coulomb explosion of strongly coupled plasmas formed from cold ions[13] and in laser-irradiated nanoclusters[30].

We also observe high-density layers at the collision between expanding bunches. These layers have an apparent stickiness or adherence, in that the separate rings do not expand through each other, but compress to form collision boundaries. The compression layers have not been observed in studies of merging electron beams[31], illustrating the insight available through investigation of space–charge effects with cold and heavy ions.

Simulation and modelling. The evolution of the ion bunches was simulated using General Particle Tracer[32], which propagates point particles through the known accelerator field structures and the dynamically evolving self-field. The initial charge distributions were determined from the measured laser spatial profiles by calculation of the atomic excitation. For two-step ionization at a high 480-nm pulse energy, the probability of ionization is proportional to the probability of being in the intermediate 5P state before the 480-nm laser pulse[18,24,33], but the usual expectations of saturation for a two-level transition[34] are not applicable since we must include loss via field ionization. Indeed, experimentally, we can infer the number of ions produced from the space–charge-induced bunch expansion (Fig. 2) and we did not observe saturation of ion production even at several hundred times saturation intensity for the 480-nm transition. We developed a four-level model of the excitation and ionization process (see Methods), with field ionization included as a fixed rate loss. The extension accounts for laser-induced transitions from the ground to excited state during the 5-ns ionizing laser pulse, such that the ionization fraction is not limited by the saturated excited-state fraction before the ionization pulse. The spatial charge distribution of the ion bunches was calculated by numerical solution of four-level optical Bloch equations, given the known laser intensity profiles. We included the effects of fluorescence and reabsorption of the 780-nm photons, which lead to the formation of a halo of ions at large distances from the laser intensity maxima. The overall effect for a Gaussian excitation beam is an ion charge distribution that is radially broadened from the laser profile with a long, smoothly decreasing tail at large radius.

The experimentally observed high-density rings that surround the ion bunches were reproduced in simulation. Figure 3a shows the axially averaged radial distribution calculated for expanding ion bunches of varying charge density. The rings are formed by the dense inner core of ions, expanding rapidly due to Coulomb repulsion, until they interact with cold low-density ions in the halo generated by the reabsorption of fluorescence during the excitation phase. This behaviour is consistent with analytic predictions of the Coulomb explosion of dense nanoclusters irradiated by ultra-intense laser fields on very short timescales, which are studied in the context of laser-triggered nuclear fusion[30,35–37].

Figure 3b shows the simulated phase–space structure of a high-density bunch, in particular showing the large radius and momentum ring that are akin to shock wave formation in strongly interacting media. Modelling of a similar initial distribution of cold ions, in one dimension and without the halo formed by reabsorption of spontaneous emission, has also predicted an expanding shock front[13], but the formation of high-density boundary layers at the collision of the expanding ion shells has not been previously reported[31]. The negligible thermal diffusion of the ions in our experiments allows direct observation

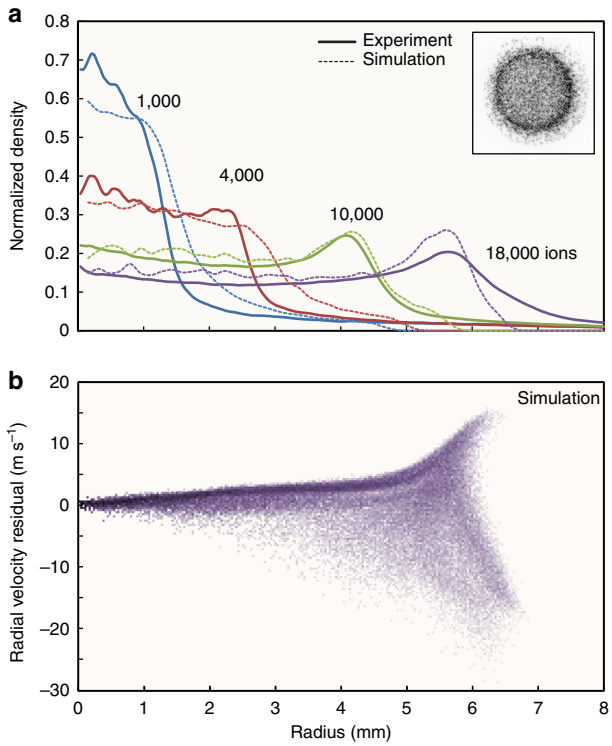

Figure 3 | Ion bunch profiles. (**a**) Measured and calculated radial dependence of the ion density. (**b**) Logarithm of the ion phase-space density, showing two orders of magnitude in density from light to dark, for a single bunch of 18,000 cold ions at propagation distance and time of 70 cm and 10.8 μs, respectively. The formation of a shock front at the outer edge of the bunch is illustrated by the caustic in the phase-space distribution. Inset of **a** shows typical measured density profile for a single bunch.

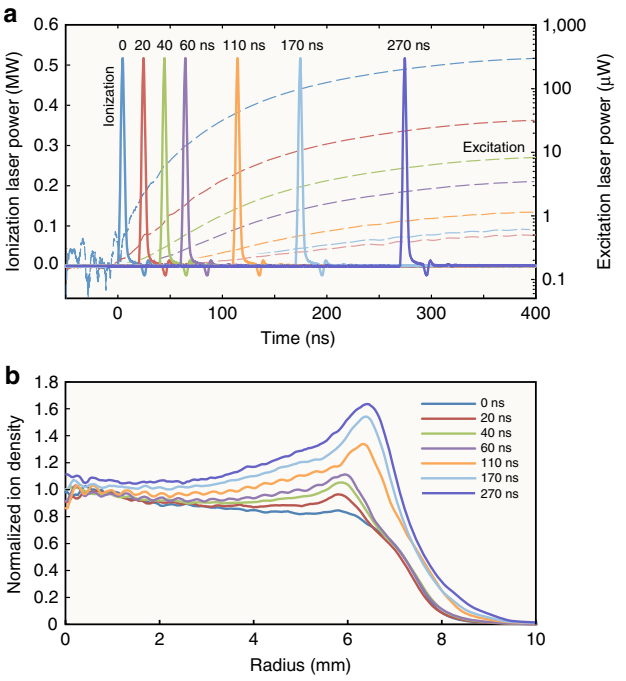

Figure 4 | Halo formation via fluorescence. Variation in density of halo ions with excitation laser pulse temporal separation. (**a**) Solid lines (left) and dashed lines (right) show the blue ionization and red excitation laser pulse timing. The excitation laser rise time is limited by the acousto-optical modulator used to modulate the laser beam. (**b**) Measured ion bunch radial profiles for varying ionization delay, for free-propagation distance of 70 cm. Owing to the slow rise of the excitation laser intensity, the charge density of the beam 'core' was kept constant for different timings by adjusting the power of the excitation laser. With a constant core density the expansion rate is approximately constant, but the 5P–5S fluorescence increases with pre-ionization excitation delay, increasing the halo density.

of the shells and high-density boundary layers despite the comparatively low density and long timescales. Simulations of the equivalent-time electron bunches show the same structures forming at very low initial electron temperature, but loss of visibility at a few kelvin, the lowest electron temperatures currently achievable[18,20].

Model verification. The high-density rings of our ion bunches are formed as the expanding core interacts with a halo of surrounding cold ions produced from reabsorbed spontaneous emission. The link between spontaneous emission and ring structure was tested by varying the duration of spontaneous emission before ionization and measuring the effect on ring density. The spontaneous emission time was determined by the delay between the 780- and 480-nm laser pulses used in the two-step ionization process. The first laser excites atoms to the $5P_{3/2}$ state, which has a natural lifetime of 26 ns. The second laser, with pulse length of 5 ns, excites the 5P atoms to a resonant auto-ionizing state in the static ambient electric field. The fluorescence from the intermediate 5P state can therefore be controlled by varying the delay between the two laser pulses, allowing variation of the density of excited and subsequently ionized atoms in the halo. Figure 4 shows the variation in visibility of the outer rings in the propagated bunch with changing time between pulses, showing increasing visibility with increased duration of spontaneous emission.

The evolution of the multi-beamlet ion bunch is shown in an animation (Supplementary Movie 1), where each frame is the calculated charge density profile for one charge bunch, in a plane transverse to the bunch propagation direction. The simulated ion bunch contains nine mini-bunches of 10^4 ions each, plus 2×10^4 simulated halo ions, for an accelerating field of 20 kV m^{-1} over 2.5 cm and free propagation of 14 cm (5 μs). The space–charge-driven bunch expansion and formation of the halo rings and colliding beamlets are readily apparent.

Discussion

Cold atom-charged particle sources are a promising new approach to producing high-brightness beams for applications in ultrafast imaging and high-resolution nanoscale fabrication. Achieving that promise will require detailed understanding of the Coulomb interactions within charge bunches and we have shown here that cold ion bunches can be a powerful tool for investigating such charged particle beam behaviour. The detailed measurements that are possible with cold ions have allowed us to test predictions of complex interactions in high-density charge bunches. Our observations highlight the importance of the initial charge density resulting from the photoionization process and identify the origin of features such as high-density caustics and inter-bunch boundary layers, which indicate nonlinear fields that lead to the emittance growth. The ability to arbitrarily shape the bunches in three dimensions has made it possible to mimic the

density distributions for complex and diverse source configurations and probe the associated beam quality degradation related to space–charge effects. The low temperature of cold ion sources, and the scaling of time due to the electron/ion mass ratio, allows precise measurement of previously inaccessible space–charge dynamics relevant to high-density electron bunches used in accelerators and ultrafast electron diffraction imaging.

Methods

Experimental apparatus and techniques. A magneto-optical trap loaded from an effusive oven source and a Zeeman slower[38] was used to collect neutral rubidium-85 atoms at a temperature of 70 μK in a region ~5 mm in diameter, with a peak density of $1.2\times10^{10}\,\mathrm{cm}^{-3}$. The atoms were ionized by two-step, near-threshold photoionization. A $\lambda=780$ nm laser beam was used to drive the first-step excitation transition. This beam consisted of two laser frequencies, with 900 μW of power tuned to the $5^2S_{1/2}(F=3)\rightarrow5^2P_{3/2}(F=4)$ transition and 100 μW acting as a repumper on the $5^2S_{1/2}(F=2)\rightarrow5^2P_{3/2}(F=3)$ transition. The excitation laser beam intensity profile was shaped with a spatial light modulator to control the spatial distribution of the intermediate excited-state atoms in two dimensions. Atoms in the 5P state were then excited to a field-ionizing state, equivalent in energy to an $n\simeq30$ Rydberg state in a null field, by a $\lambda=480$ nm, 2–6 mJ laser pulse of 5 ns duration focused to a 100 μm × 8 mm (full width at half maximum) ribbon propagated perpendicular to the excitation laser beam, defining the profile of the ions along the direction of ion propagation. The atoms were excited and ionized in a static electric field of 20–80 kV m^{-1} between a pair of parallel plate electrodes. During and shortly after ionization, heating processes such as disorder-induced heating increase the ion temperature to a few millikelvin[39]. The ion bunches were accelerated over a distance of 2.5 cm, traversed an aperture in the grounded electrode and expanded due to the strong lens effect of the aperture, then drifted in a field-free region for 21.5 (Fig. 2) or 70 cm (Figs 3 and 4) to a phosphor-coupled microchannel plate and the spatial charge density was imaged with a CCD camera.

Modelling and simulation. To simulate the propagation of the cold ions with space–charge effects included, we first calculated the initial spatial profile of the bunches. The atomic state was described with a four-state density matrix for the electronic ground and intermediate excited states, the resonant self-ionizing state and the final ionized state. The states were coupled by laser fields with position- and time-dependent intensities and by spontaneous decay (see Fig. 1c). Field ionization was represented by rate Γ_{34}, which was determined from calculated near-threshold ionization cross-sections[40].

The evolution of ρ, the density matrix for the four-level atom, is given by

$$\dot{\rho}=-\frac{i}{\hbar}[\hat{H},\rho]+\hat{\mathcal{L}}(\rho) \tag{1}$$

where the indices are associated with the atomic levels given in Fig. 1. The Hamiltonian for the laser–atom interaction is

$$\hat{H}=\frac{\hbar}{2}\begin{bmatrix}0&\Omega_{12}&0&0\\ \Omega_{12}&0&\Omega_{23}&0\\ 0&\Omega_{23}&0&0\\ 0&0&0&0\end{bmatrix}. \tag{2}$$

The decay terms are:

$$\hat{\mathcal{L}}(\rho)=\frac{\Gamma_{21}}{2}\begin{bmatrix}2\rho_{22}&-\rho_{12}&0&0\\ -\rho_{21}&-\rho_{22}&-\rho_{23}&-\rho_{24}\\ 0&-\rho_{32}&0&0\\ 0&-\rho_{42}&0&0\end{bmatrix}+\frac{\Gamma_{34}}{2}\begin{bmatrix}0&0&-\rho_{13}&0\\ 0&0&-\rho_{23}&0\\ -\rho_{31}&-\rho_{32}&-\rho_{33}&-\rho_{34}\\ 0&0&-\rho_{43}&2\rho_{33}\end{bmatrix} \tag{3}$$

The optical Bloch equations for the four-level system were derived following standard approaches[34,41] and solved numerically for the spatially varying time derivative of the population of the ionized state. The total bunch charge was adjusted to optimize the agreement with the measured density distribution.

Particle tracking simulations[32] were used to calculate the evolution of the ion bunches under the influence of the external accelerator fields and internal Coulomb self-fields, as shown in the animation (Supplementary Movie 1). The tracking simulations reveal the time dependence of the bunch evolution, and two-dimensional projections of the particle density can be compared with experimental results as in Fig. 2. The essential features of the calculated initial bunch profiles produced good qualitative agreement with the observed bunch behaviour.

Simulations were performed using a three-dimensional particle mesh method to calculate the self-field, and also by calculating the interactions between all ion pairs. The bunch evolution was identical for the two approaches, showing that for our initial distributions, the evolution was dominated by space–charge effects rather than statistical Coulomb (Boersch) effects, which would not be apparent with the mesh method.

The effects of fluorescence and reabsorption of the quasi-continuous excitation beam were included using a first-order single-scattering approximation. Assuming steady-state conditions before the ionizing laser pulse, the excited-state spatial profile without fluorescence $\rho_{22}(\mathbf{x})$ was calculated from the laser intensity. Excited atoms spontaneously emit photons at the natural decay rate Γ_{21}, so the scattered light intensity is

$$I_{\mathrm{scat}}(\mathbf{x}')=\hbar\omega\Gamma_{21}\int\frac{N(\mathbf{x})\rho_{22}(\mathbf{x})}{4\pi|\mathbf{x}'-\mathbf{x}|^2}\mathrm{d}V \tag{4}$$

assuming isotropic emission, where $\hbar\omega$ is the energy per photon and $N(\mathbf{x})$ is the atomic number density. The scattered intensity is then added to the laser intensity to calculate the initial conditions of the excited-state profile corrected for reabsorption. Saturation and reabsorption cause broadening of the excited-state profile compared with the excitation laser profile, and the appearance of a halo of excited-state atoms that decrease in density smoothly from the beam core out to long distances. This excitation halo is ionized, becoming responsible for the formation of a density wave at the edge of an exploding ion bunch.

References

1. Buckanie, N. M. *et al.* Space charge effects in photoemission electron microscopy using amplified femtosecond laser pulses. *J. Phys. Condens. Matter* **21,** 314003 (2009).
2. Orloff, J. High-resolution focused ion beams. *Rev. Sci. Instrum.* **64,** 1105–1130 (1993).
3. Bernal, S. *et al.* Beam experiments in the extreme space-charge limit on the University of Maryland electron ring. *Phys. Plasmas* **11,** 2907–2915 (2004).
4. Dwyer, J. R. *et al.* Femtosecond electron diffraction: 'making the molecular movie'. *Philos. Trans. A Math. Phys. Eng. Sci.* **364,** 741–778 (2006).
5. Siwick, B. J., Dwyer, J. R., Jordan, R. E. & Miller, R. D. Ultrafast electron optics: Propagation dynamics of femtosecond electron packets. *J. Appl. Phys.* **92,** 1643–1648 (2002).
6. Qian, B.-L. & Elsayed-Ali, H. E. Electron pulse broadening due to space charge effects in a photoelectron gun for electron diffraction and streak camera systems. *J. Appl. Phys.* **91,** 462–468 (2002).
7. Kirchner, F. O., Gliserin, A., Krausz, F. & Baum, P. Laser streaking of free electrons at 25 kev. *Nat. Photon.* **8,** 52–57 (2014).
8. Tao, Z., Zhang, H., Duxbury, P. M., Berz, M. & Ruan, C. Space charge effects in ultrafast electron diffraction and imaging. *J. Appl. Phys.* **111,** 044316 (2012).
9. Chatelain, R. P. *et al.* Ultrafast electron diffraction with radio-frequency compressed electron pulses. *Ultramicroscopy* **116,** 86–94 (2012).
10. Mitchell, T. B., Bollinger, J. J., Huang, X.-P. & Itano, W. M. Direct observations of the structural phases of crystallised ion plasmas. *Phys. Plasmas* **6,** 1751–1758 (1999).
11. Kugland, N. L. *et al.* Self-organized electromagnetic field structures in laser-produced counter-streaming plasmas. *Nat. Phys.* **8,** 809–812 (2012).
12. Remington, B. A., Arnett, D., Drake, R. P. & Takabe, H. Modeling astrophysical phenomena in the laboratory with intense lasers. *Science* **284,** 1488–1493 (1999).
13. Feldbaum, D., Morrow, N. V., Dutta, S. K. & Raithel, G. Coulomb expansion of laser-excited ion plasmas. *Phys. Rev. Lett.* **89,** 173004 (2002).
14. Kulin, S. *et al.* Plasma oscillations and expansion of an ultracold neutral plasma. *Phys. Rev. Lett.* **85,** 318–321 (2000).
15. Killian, T. C. Ultracold neutral plasmas. *Science* **316,** 705–708 (2007).
16. Claessens, B. J., van der Geer, S. B., Taban, G., Vreden-bregt, E. J. D. & Luiten, O. J. Ultracold electron source. *Phys. Rev. Lett.* **95,** 164801 (2005).
17. Hanssen, J. L., Dakin, E. A., McClelland, J. J. & Jacka, M. Using laser-cooled atoms as a focused ion beam source. *J. Vac. Sci. Technol. B* **24,** 2907–2910 (2006).
18. McCulloch, A. J. *et al.* Arbitrarily shaped high-coherence electron bunches from cold atoms. *Nat. Phys.* **7,** 785–788 (2011).
19. McCulloch, A. J., Sheludko, D. V., Junker, M. & Scholten, R. E. High-coherence picosecond electron bunches from cold atoms. *Nat. Commun.* **4,** 1692 (2013).
20. Engelen, W. J., van der Heijden, M. J., Bakker, D. J., Vre-denbregt, E. J. D. & Luiten, O. J. High-coherence electron bunches produced by femtosecond photoionization. *Nat. Commun.* **4,** 1693 (2013).
21. Claessens, B. J., Reijnders, M. P., Taban, G., Luiten, O. J. & Vredenbregt, E. J. D. Cold electron and ion beams generated from trapped atoms. *Phys. Plasmas* **14,** 093101 (2007).
22. Reijnders, M. P. *et al.* Low-energy-spread ion bunches from a trapped atomic gas. *Phys. Rev. Lett.* **102,** 034802 (2009).
23. Steele, A. V., Knuffman, B. & McClelland, J. J. Inter-ion coulomb interactions in a magneto-optical trap ion source. *J. Appl. Phys.* **109,** 104308 (2011).
24. Knuffman, B., Steele, A. V. & McClelland, J. J. Cold atomic beam ion source for focused ion beam applications. *J. Appl. Phys.* **114,** 044303 (2013).

25. Kime, L. *et al.* High-flux monochromatic ion and electron beams based on laser-cooled atoms. *Phys. Rev. A* **88,** 033424 (2013).
26. Kishek, R. A. *et al.* Simulations and experiments with space-charge-dominated beams. *Phys. Plasmas* **10,** 2016–2021 (2003).
27. Anderson, O. A. Internal dynamics and emittance growth in space charge dominated beams. *Part. Accel.* **21,** 197–226 (1987).
28. Gluckstern, R. L. Analytic model for halo formation in high current ion linacs. *Phys. Rev. Lett.* **73,** 1247–1250 (1994).
29. Rizzato, F. B., Pakter, R. & Levin, Y. Wave breaking and particle jets in intense inhomogeneous charged beams. *Phys. Plasmas* **14,** 110701 (2007).
30. Kaplan, A. E., Dubetsky, B. Y. & Shkolnikov, P. L. Shock shells in coulomb explosions of nanoclusters. *Phys. Rev. Lett.* **91,** 143401 (2003).
31. Haber, I., Kehne, D., Reiser, M. & Rudd, H. Experimental, theoretical, and numerical investigation of the homogenization of density nonuniformities in the periodic transport of a space-charge dominated electron beam. *Phys. Rev. A* **44,** 5194–5205 (1991).
32. General Particle Tracer http://www.pulsar.nl/gpt/.
33. Killian, T. C., Pattard, T., Pohl, T. & Rost, J. M. Ultracold neutral plasmas. *Phys. Rep.* **449,** 77–130 (2007).
34. Allen, L. & Eberly, J. H. *Optical Resonance and Two-Level Atoms* (Dover, 1987).
35. Peano, F., Fonseca, R. A. & Silva, L. O. Dynamics and control of shock shells in the coulomb explosion of very large deuterium clusters. *Phys. Rev. Lett.* **94,** 033401 (2005).
36. Kovalev, V. F. & Bychenkov, V. Y. Quasimonoenergetic ion bunches from exploding microstructured targets. *Phys. Plasmas* **14,** 053103 (2007).
37. Saalmann, U., Mikaberidze, A. & Rost, J. M. Laser-driven nanoplasmas in doped helium droplets: local ignition and anisotropic growth. *Phys. Rev. Lett.* **110,** 133401 (2013).
38. Bell, S. C. *et al.* A slow atom source using a collimated effusive oven and a single-layer variable pitch coil Zeeman slower. *Rev. Sci. Instrum.* **81,** 013105 (2010).
39. Debernardi, N. *et al.* Measurement of the temperature of an ultracold ion source using time-dependent electric fields. *J. Appl. Phys.* **110,** 024501 (2011).
40. Petrov, I. D., Sukhorukov, V. L., Leber, E. & Hotop, H. Near threshold photoionization of excited alkali atoms Ak(np) (Ak = Na, K, Rb, Cs; n = 3-6). *Eur. Phys. J. D* **10,** 53–65 (2000).
41. Maguire, L. P., van Bijnen, R. M. W., Mese, E. & Scholten, R. E. Theoretical calculation of saturated absorption spectra for multi-level atoms. *J. Phys. B At. Mol. Opt. Phys.* **39,** 2709–2720 (2006).

Acknowledgements

This work was supported by the Australian Research Council Discovery Project DP1096025.

Author contributions

D.M., R.W.S., D.V.S., C.T.P. and A.J.M. executed the experiments, acquired and analysed the data; BMS contributed to the execution of the experiments; D.V.S. and A.J.M. designed and constructed the apparatus; D.M. generated the simulations; D.M., C.T.P. and R.E.S. wrote the manuscript with contributions from all authors; RES conceived and directed the project.

Additional information

Supplementary Information accompanies this paper at http://www.nature.com/naturecommunications

Competing financial interests: The authors declare no competing financial interests.

Reprints and permission information is available online at http://npg.nature.com/reprintsandpermissions/

How to cite this article: Murphy, D. *et al.* Detailed observation of space–charge dynamics using ultracold ion bunches. *Nat. Commun.* 5:4489 doi: 10.1038/ncomms5489 (2014).

Increasing the Brightness of Cold Ion Beams by Suppressing Disorder-Induced Heating with Rydberg Blockade

D. Murphy, R. E. Scholten,* and B. M. Sparkes
School of Physics, The University of Melbourne, Victoria 3010, Australia
(Received 27 July 2015; published 20 November 2015)

A model for the equilibrium coupling of an ion system with varying initial hard-sphere Rydberg blockade correlations is used to quantify the suppression of disorder-induced heating in Coulomb-expanding cold ion bunches. We show that bunches with experimentally achievable blockade parameters have an emittance reduced by a factor of 2.6 and increased focusability and brightness compared to a disordered bunch. Demonstrating suppression of disorder-induced heating is an important step in the development of techniques for the creation of beam sources with sufficient phase-space density for ultrafast, single-shot coherent diffractive imaging.

DOI: 10.1103/PhysRevLett.115.214802 PACS numbers: 29.27.Bd, 07.77.Ka, 37.10.-x, 52.27.Jt

Nanoscale material manipulation with focused ion beams [1], high resolution electron microscopy [2,3], and ultrafast and coherent electron diffraction imaging [4] require high flux low emittance sources of charged particles. The emittance, or focusability, of the beam determines important imaging capabilities such as the resolution and image acquisition time. Cold-atom electron and ion sources (CAEIS) [5,6] based on the photoionization of laser-cooled atomic gases are being developed for the production of low emittance beams, achieving source temperatures below 10 K for electrons [7] and 1 mK for ions [8]. These sources produce charged particle bunches with arbitrarily shaped spatial profiles, short durations and high coherence [9–11], and high resolution focus suitable for ion microscopy [12].

Intrabeam Coulomb effects limit usable beam densities in applications that require short bunch duration, such as single-shot ultrafast electron diffraction where the expansion effects constrain the imaging capability of bunches with more than a few tens of particles [13]. At high beam densities, the nonlinear Coulomb expansion of bunches with nonuniform space-charge densities leads to loss of beam quality [14]. CAEIS ion bunches have been used as a platform for the study of space-charge effects, since low source temperature and high mass enable detailed measurements analogous to much shorter bunch durations appropriate to ultrafast electron beams [15]. The initial source distribution of CAEIS beams can be shaped to produce uniform charge distributions, which is predicted to alleviate space-charge induced emittance growth [14,16].

For beam sources with uniform charge distributions, the minimum achievable source temperature is ultimately limited by statistical Coulomb effects resulting from the discrete nature of the charged particles [17]. Particle beams cooled from initially high temperatures, such as electron-cooled heavy ion beams in storage rings, encounter a cooling limit due to intrabeam scattering when operated at high beam density [18]. Bunches of initially cold charged particles created with uncorrelated initial positions, as from a CAEIS, have interparticle repulsive forces that are random in orientation and magnitude, leading to disorder-induced heating (DIH) [19,20]. DIH can, in principle, be suppressed by establishing spatial correlations in the initial particle distribution, for example, by ionization of a degenerate Fermi gas [21], or atoms in an optical lattice [22], or blockaded Rydberg-atom ensembles [23]. Simulations of the suppression of DIH in these precorrelated plasmas have been performed only in the absence of expansion, which, otherwise, prevents establishment of thermal equilibrium due to the effects of adiabatic cooling [24,25]. Models of DIH suppression through correlation in cold charged particle bunches, where rapid Coulomb expansion is unavoidable, are needed to establish limitations to beam quality on the basis of achievable experimental parameters.

In this Letter, we investigate the suppression of DIH in Coulomb-expanding cold ion beams with initial position correlations created through the ionization of a shaped blockaded Rydberg gas, where spatial correlations are introduced by interatomic interactions that prevent excitation of pairs of atoms that are in close proximity [26]. We model the DIH process using hard-sphere initial correlations [27,28] to derive the equilibrium temperature and show, through detailed molecular-dynamics (MD) simulations, that the suppression of DIH calculated in equilibrium holds during the emittance nonconserving, nonequilibrium expansion process for uniform bunches. The effects of Coulomb interactions within an ion bunch are equivalent to those in an electron bunch, but occur on a longer time scale due to the larger ion mass [15]. Therefore, our model places an experimental limit on the reduction of emittance through hard-sphere correlations for any high-density charged particle bunch, such as electrons used for single-shot, ultrafast diffraction studies.

Emittance is a measure of the phase-space area occupied by a beam, and can be expressed in each spatial dimension x as

$$\epsilon = \frac{\sigma_x}{c}\sqrt{\frac{k_B T}{m}}, \tag{1}$$

where σ_x is the root-mean-square (rms) beam size, c the speed of light, k_B the Boltzmann constant, m the mass of one particle. The thermal energy is $k_B T = m\sigma_{v_x}^2(1 - r_{x,v_x}^2)$ where σ_{v_x} is the rms velocity spread and r_{x,v_x} is the correlation coefficient of the x-axis position and velocity phase-space profile. At a beam waist, emittance is the product of the beam size and angular divergence, thereby determining the minimum focal size for a given focusing system. Achieving high beam brightness and coherence requires low beam emittance and, thus, low temperature. The internal structure and dynamics of a plasma can be described in terms of its temperature using the Coulomb coupling parameter Γ, which is the ratio of potential to thermal energy

$$\Gamma = \frac{e^2}{4\pi\varepsilon_0 a k_B T}, \tag{2}$$

where e is the elementary charge, ε_0 is the vacuum permittivity and the Wigner-Seitz radius $a = (3/4\pi n)^{1/3}$ is the average interparticle separation for ion density n. For strong coupling ($\Gamma > 1$), the motion of individual particles is determined by the interparticle interactions rather than thermal diffusion.

For an initially disordered cold-ion plasma, Γ may be high initially due to the low temperature, but DIH occurs with a characteristic time scale on the order of the inverse of the plasma frequency $\omega_p = \sqrt{ne^2/\varepsilon_0 m}$, limiting the system to an equilibrium coupling parameter $\Gamma_{\rm eq} \sim 2$ in the absence of expansion [29]. At an ion density $n = 10^{16}$ m^{-3}, typical of a CAEIS using a magneto-optical trap (MOT) atom source, this implies rapid equilibration to a temperature $T_c = 2$ K, 5 orders of magnitude higher than the temperature of the atoms before ionization.

Previous simulations have suggested that equilibrium coupling parameters as high as $\Gamma_{\rm eq} = 35$, corresponding to much lower temperatures, may be reached in neutral nonexpanding plasmas produced through ionization of blockaded Rydberg atoms [23]. A pair of Rydberg atoms in a low angular momentum state with separation R interact, to leading order, via the van der Waals (VDW) potential $V(R) = -C_6/R^6$. In an ensemble of atoms exposed to radiation coupling a ground state to a Rydberg level, with power-broadened linewidth ν, any ground-state atom within the blockade radius $r_b = |C_6/\nu|^{1/6}$ of a Rydberg atom is prevented from being excited to the Rydberg level by the VDW interaction. For two rubidium atoms in the 60S state that have $C_6 = -140$ GHz μm^6 and linewidth $\nu = 3$ MHz, the blockade radius of $r_b = 6$ μm [30] exceeds the mean interparticle separation a of a random distribution at the typical ion density of $n = 10^{16}$ m^{-3}. Therefore, the blockade provides a mechanism for suppression of DIH and consequent reduction of the effective source temperature.

First, we consider the thermal equilibrium properties of a nonexpanding ion bunch with Rydberg blockade correlations. Following creation of a blockaded Rydberg ensemble created in a volume defined by a two-laser excitation process [9], our model assumes complete ionization of the Rydberg atoms by a switched electrostatic field in a time much less than the DIH time scale ω_p^{-1}, which is achievable in existing MOT-based CAEIS accelerators [31]. The field accelerates the ions, and removes electrons from the system on a much shorter time scale than the ionic motion, such that they have a negligible effect on the ion temperature. Hard-sphere approximations for the VDW interaction have been shown to adequately approximate the spatial correlations [27] and excitation fractions [28] of high density blockaded Rydberg ensembles. The hard-sphere approximation allows calculation of the internal energy of the ion configuration as a function of a dimensionless blockade parameter r_b/a, which we use to derive the equilibrium coupling parameter after DIH.

Using the approach for a disordered system [32], we calculate the equilibrium Coulomb coupling parameter $\Gamma_{\rm eq}$ of a nonexpanding ion system by, first, considering the conservation of energy per particle in the initial and final (equilibrium) ionic configurations. For potential energy, we use the internal binding energy per particle in a one-component plasma (OCP) system $u_{\rm OCP}$ [33]. In equilibrium, this is given by the OCP equation of state in the equilibrium strongly coupled fluid phase ($\Gamma_{\rm eq} \lesssim 170$) [34]

$$u_{\rm OCP} = \frac{e^2}{4\pi\varepsilon_0 a}(-0.9 + 0.590673\,\Gamma_{\rm eq}^{-2/3} - 0.26569\,\Gamma_{\rm eq}^{-1}). \tag{3}$$

For an initially disordered distribution, the initial internal binding energy $u_i = 0$, as the ions have no structure and experience no initial confining force. Within one plasma period, the ions develop short-ranged OCP correlations with negative binding energy $u_{\rm OCP}$ balanced by a gain of kinetic energy. Conservation of energy for an initially cold, disordered distribution with a final thermal equilibrium potential $u_f = u_{\rm OCP}$ gives an equilibrium coupling parameter $\Gamma_{\rm eq} = 2.23$ [17]. Ions with correlated initial positions have a nonzero initial binding energy so that less kinetic energy is gained per particle during thermal equilibration, leading to an increase in the Coulomb coupling parameter in the final state. For hard-sphere correlations, the Percus-Yevick (PY) equation gives a radial distribution function [35] that permits calculation of an analytical form of the internal energy under Coulomb interactions [36]

$$u_{\rm PY} = -\frac{3e^2\eta^{2/3}}{4\pi\varepsilon_0 a}\frac{1 - \frac{1}{5}\eta + \frac{1}{10}\eta^2}{1 + 2\eta}, \tag{4}$$

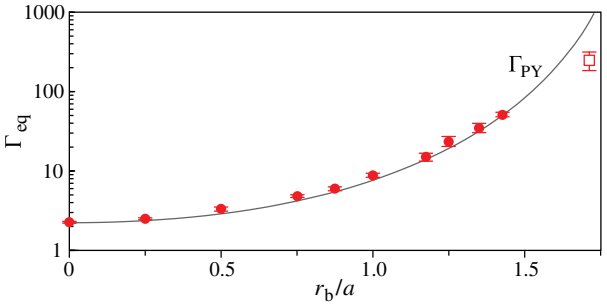

FIG. 1 (color online). Equilibrium Coulomb coupling parameter Γ_{eq} of cold ion bunches with hard-sphere blockade parameter r_b/a calculated using the Percus-Yevick hard-sphere distribution function Γ_{PY} (solid line) and by molecular dynamics simulation for configurations generated by random sequential addition (circles) and for a random-close-packed distribution at $r_b/a = 1.7$ (square). Uncertainties in the MD data result from residual kinetic energy oscillations.

where $\eta = \frac{1}{8}(r_b/a)^3$ is the packing fraction of spheres of diameter r_b in the hard-sphere approximation. Conservation of energy with $u_i = u_{PY}$ then gives the PY hard-sphere equilibrium coupling parameter Γ_{PY} as a function of the blockade parameter r_b/a (Fig. 1). For a blockade parameter of $r_b/a = 1.2$ reported by experiments [28], $\Gamma_{PY} = 16$. The solution of Γ_{PY} for blockade parameters r_b/a underpins the behavior of the coupling parameter observed in simulations of neutral plasmas with Rydberg blockade [23].

To quantify suppression of DIH in an expanding beam, we performed an N-body MD simulation of DIH in an infinite homogeneous system of ions with linear expansion by using periodic boundary conditions in a comoving cubic geometry with equations of motion from the direct Ewald summation method [37] (see Supplemental Material [38]). In the comoving coordinate frame, the effects of linear expansion, including adiabatic cooling, are described by scale factor α calculated for the free uniform Coulomb expansion of ions at an initial density n'

$$\frac{d^2\alpha}{dt^2} = \frac{n'e^2}{3\varepsilon_0 m\alpha^2}, \tag{5}$$

where $\alpha = 1$ immediately following ionization.

In experiments where ordering is established through blockade, for the same initial atomic density, the bunch charge will be smaller. In the presence of linear space-charge expansion, higher density bunches expand more rapidly, so that brightness is independent of the bunch charge for a fixed source temperature [42]. Therefore, we simulate bunches with equal initial densities $n' = 1 \times 10^{16}$ m^{-3} for the ordered and disordered cases, with equal expansion rates, to allow for fair comparison. To compare the behavior of the Rb ion bunches that we simulate to other bunches of charged particles at different densities, including electrons, the time scales of the kinetic energy oscillations, heating and expansion scale as $\sqrt{m/n'}$ and the emittance as $\tilde{\epsilon} \propto \sqrt{n'^{1/3}/m}$.

$N = 1000$ ions were generated in simulation by the random sequential addition of hard spheres in the periodic comoving cubic volume of side length $L = (N/n')^{1/3}$, which generated configurations with blockade parameters up to $r_b/a = 1.43$, close to the saturation limit [43]. To illustrate the behavior of bunches with higher blockade parameters, we use a packing algorithm [44] to generate ion configurations close to the random hard-sphere close packing limit of $r_b/a \sim 1.72$. The ions were generated with zero initial temperature. Simulations showed no observable differences when repeated with initial temperatures of 100 μK, the typical temperature of atoms in a MOT. The comoving equations of motion were integrated through the Bulirsch-Stoer method with polynomial extrapolation [45]. Adaptive time steps were calculated to provide a constant error metric for the emittance. The scale factor α, expansion rate $d\alpha/dt$, and the temperature of the ions were evaluated (see Supplemental Material [38]) to determine a dimensionless emittance

$$\tilde{\epsilon} \equiv \frac{\alpha}{c}\sqrt{\frac{k_B T}{m}}, \tag{6}$$

such that a spherical ion bunch of initial rms size σ_x' expanded to a size $\alpha\sigma_x'$ will have an emittance $\epsilon = \sigma_x'\tilde{\epsilon}$.

Simulations were initially performed in the absence of expansion (setting $d\alpha/dt = 0$) to calculate the equilibrium coupling parameters Γ_{eq} for varying blockade parameters r_b/a in order to verify the PY prediction. The regular kinetic energy oscillations at twice the plasma frequency (seen in Fig. 2) result from the harmonic motion of ions about dynamic local potential minima. The equilibrium emittance and temperature decreases as the blockade parameter increases. The equilibrium coupling parameters for each simulation were found by averaging over plasma phases, which, for a nonexpanding bunch, is the product of plasma frequency and time, between 8π and 16π. The MD simulations verify the PY OCP theory (Fig. 1) for distributions generated up to $r_b/a = 1.43$ in nonexpanding thermal equilibrium.

Expanding ion bunches cool adiabatically, with decreasing plasma frequency for decreasing density as $\omega_p \propto \alpha^{-3/2}$. Asymptotically, the kinetic energy oscillations cease as the plasma phase $\varphi = \int_0^t \omega_p dt'$ converges to $\varphi = 1.2\pi$ as $t \to \infty$, for the free Coulomb expansion (Eq. (5) of ions of any mass or initial density. Convergence of the plasma phase implies freezing of the ion motion in the expanding reference frame, so that we may expect the emittance to reach an equilibrium value, as adiabatic expansion cooling preserves bunch emittance, decreasing the temperature as $T \propto \alpha^{-2}$ [17]. Instead, we observe unbound emittance growth subsequent to the first temperature oscillation minimum at $\varphi = \pi$ (Fig. 3). The results, presented in terms of an effective source temperature $T' = \alpha^2 T$ of equivalent-emittance noninteracting particles in the ion source region,

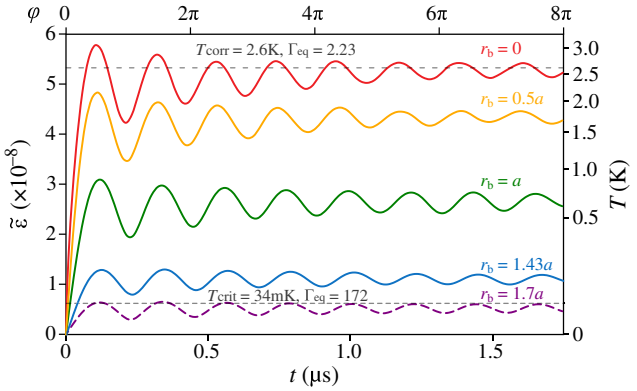

FIG. 2 (color online). Disorder-induced heating of nonexpanding ion bunches with hard-sphere initial correlations, labeled by the blockade parameter r_b/a. Emittance and temperature are calculated in time and in plasma phase φ, which is 2π times the number of plasma periods after ionization, for ^{85}Rb ions at density $n' = 10^{16}$ m^{-3}. Damped kinetic energy oscillations at twice the plasma frequency ω_p due to harmonic ion motion are observed. Hard-sphere Rydberg blockade reduces the equilibrium temperatures from the disordered ($r_b = 0$) correlation temperature $T_{\rm corr} = 2.6$ K, to near the crystallization phase boundary at $T_{\rm crit} = 34$ mK.

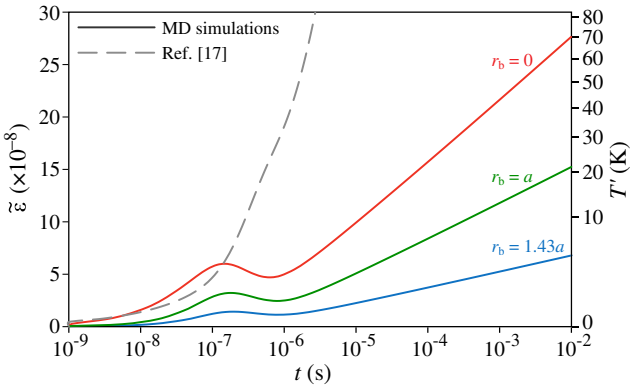

FIG. 3 (color online). Dimensionless emittance $\tilde{\epsilon}$ and effective temperature growth caused by disorder-induced heating in freely expanding ^{85}Rb$^+$ ion bunches at 10^{16} m^{-3} initial density, calculated by molecular-dynamics simulation. A model for the bunch temperature evolution [17] is found to overpredict the emittance growth at times beyond the first oscillation maxima. The presence of Rydberg blockade, labeled by the blockade radius in terms of the Wigner-Seitz radius, increases the initial ion correlations thereby reducing the heating.

show clear reduction in the magnitude of the emittance growth for blockaded initial distributions.

Modeling the harmonic ion motion about local potential minima in the expanding frame yields a nonadiabatic asymptotic temperature dependence of $T \propto \Gamma_{\rm eq}^{-1}\alpha^{-1.8}$ (see Supplemental Material [38]). According to the harmonic oscillator description, the temperature dynamics during expansion are proportional to the predicted equilibrium coupling parameter $\Gamma_{\rm PY}$ for each blockade parameter. The reduction of the emittance, and the suppression of DIH, can then be quantified as the ratio of the emittance of the blockaded system with equilibrium coupling $\Gamma_{\rm eq} = \Gamma_{\rm PY}(r_b/a)$ to the emittance of a disordered system which has $\Gamma_{\rm eq} = 2.23$

$$\frac{\epsilon_{\rm blockade}}{\epsilon_{\rm disorder}} = \sqrt{\frac{2.23}{\Gamma_{\rm PY}(r_b/a)}}. \tag{7}$$

The MD results of Fig. 4 verify that the suppression is unaffected by the expansion. The limit of the suppression depends on the extent of the blockade. For an ion beam created from a system with $r_b/a = 1.2$ [28], we predict an equilibrium coupling parameter $\Gamma_{\rm eq} = 16$, and an emittance lowered by a factor of 2.6. This emittance reduction would lead to a sevenfold increase in transverse brightness, which is proportional to ϵ^{-2}. The minimum focal spot size d would be 0.62 times the size with disorder, where $d \propto \epsilon^{1/2}$.

Suppression of DIH in cold ions would be a significant milestone in the advancement of charged particle beam source technology, as the DIH effect, otherwise, presents a limitation to beam focusability and brightness. Ultimately, single-shot ultrafast electron diffraction may require electron beams of a phase-space density close to the quantum degeneracy limit [46], which will not be possible unless DIH is negligible. For ions, creating bunches with higher blockade parameters and further reduced emittance may be possible through precise variation of the laser frequency and intensity during the Rydberg excitation process [47], Rydberg excitation of atoms in an optical lattice with high filling fraction [22,48], or ionization of atoms in spatially tailored microtrap arrays [49].

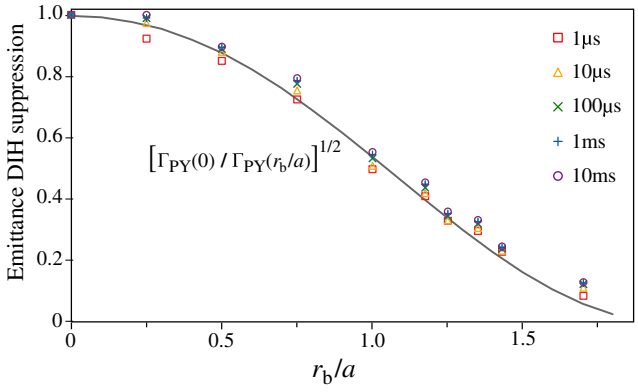

FIG. 4 (color online). Suppression of disorder-induced heating, expressed as the ratio of blockaded to disordered emittance for different blockade parameters at different expansion times. The suppression remains constant throughout the linear Coulomb expansion process, as predicted with the hard-sphere model for the thermal equilibrium coupling parameter (solid line).

In conclusion, the results presented here quantitatively predict the extent to which disorder-induced emittance growth can be suppressed using Rydberg blockade, and guide further development of high-brightness cold charged particle beams for applications including ultrafast electron diffraction.

B. M. S. gratefully acknowledges the support of a University of Melbourne McKenzie Fellowship. This work was supported by the Australian Research Council Discovery Project No. DP140102102.

*scholten@unimelb.edu.au

[1] J. Orloff, High-resolution focused ion beams, Rev. Sci. Instrum. **64**, 1105 (1993).
[2] T. LaGrange, M. R. Armstrong, K. Boyden, C. G. Brown *et al.*, Single-shot dynamic transmission electron microscopy, Appl. Phys. Lett. **89**, 044105 (2006).
[3] K. W. Urban, Studying Atomic Structures by Aberration-Corrected Transmission Electron Microscopy, Science **321**, 506 (2008).
[4] J. C. Williamson, J. Cao, H. Ihee, H. Frey, and A. H. Zewail, Clocking transient chemical changes by ultrafast electron diffraction, Nature (London) **386**, 159 (1997).
[5] B. J. Claessens, S. B. van der Geer, G. Taban, E. J. D. Vredenbregt, and O. J. Luiten, Ultracold Electron Source, Phys. Rev. Lett. **95**, 164801 (2005).
[6] J. L. Hanssen, E. A. Dakin, J. J. McClelland, and M. Jacka, Using laser-cooled atoms as a focused ion beam source, J. Vac. Sci. Technol. B **24**, 2907 (2006).
[7] W. J. Engelen, E. P. Smakman, D. J. Bakker, O. J. Luiten, and E. J. D. Vredenbregt, Effective temperature of an ultracold electron source based on near-threshold photoionization, Ultramicroscopy **136**, 73 (2014).
[8] N. Debernardi, M. P. Reijnders, W. J. Engelen, T. T. J. Clevis, P. H. A. Mutsaers, O. J. Luiten, and E. J. D. Vredenbregt, Measurement of the temperature of an ultracold ion source using time-dependent electric fields, J. Appl. Phys. **110**, 024501 (2011).
[9] A. J. McCulloch, D. V. Sheludko, S. D. Saliba, S. C. Bell, M. Junker, K. A. Nugent, and R. E. Scholten, Arbitrarily shaped high-coherence electron bunches from cold atoms, Nat. Phys. **7**, 785 (2011).
[10] A. J. McCulloch, D. V. Sheludko, M. Junker, and R. E. Scholten, High-coherence picosecond electron bunches from cold atoms, Nat. Commun. **4**, 1692 (2013).
[11] M. W. van Mourik, W. J. Engelen, E. J. D. Vredenbregt, and O. J. Luiten, Ultrafast electron diffraction using an ultracold source, Struct. Dyn. **1**, 034302 (2014).
[12] K. A. Twedt, L. Chen, and J. J. McClelland, Scanning ion microscopy with low energy lithium ions, Ultramicroscopy **142**, 24 (2014).
[13] F. O. Kirchner, A. Gliserin, F. Krausz, and P. Baum, Laser streaking of free electrons at 25 keV, Nat. Photonics **8**, 52 (2014).
[14] O. J. Luiten, S. B. Van der Geer, M. J. De Loos, F. B. Kiewiet, and M. J. van der Wiel, How to Realize Uniform Three-Dimensional Ellipsoidal Electron Bunches, Phys. Rev. Lett. **93**, 094802 (2004).
[15] D. Murphy, R. W. Speirs, C. T. Putkunz, A. J. McCulloch, B. M. Sparkes, and R. E. Scholten, Detailed observation of space-charge dynamics using ultracold ion bunches, Nat. Commun. **5**, 4489 (2014).
[16] P. Musumeci, J. T. Moody, R. J. England, J. B. Rosenzweig, and T. Tran, Experimental Generation and Characterization of Uniformly Filled Ellipsoidal Electron-Beam Distributions, Phys. Rev. Lett. **100**, 244801 (2008).
[17] J. M. Maxson, I. V. Bazarov, W. Wan, H. A. Padmore, and C. E. Coleman-Smith, Fundamental photoemission brightness limit from disorder induced heating, New J. Phys. **15**, 103024 (2013).
[18] M. Steck, K. Beckert, H. Eickhoff, B. Franzke, F. Nolden, H. Reich, B. Schlitt, and T. Winkler, Anomalous Temperature Reduction of Electron-Cooled Heavy Ion Beams in the Storage Ring ESR, Phys. Rev. Lett. **77**, 3803 (1996).
[19] D. O. Gericke and M. S. Murillo, Disorder-induced heating of ultracold plasmas, Contrib. Plasma Phys. **43**, 298 (2003).
[20] G. ten Haaf, S. H. W. Wouters, S. B. van der Geer, E. J. D. Vredenbregt, and P. H. A. Mutsaers, Performance predictions of a focused ion beam from a laser cooled and compressed atomic beam, J. Appl. Phys. **116**, 244301 (2014).
[21] M. S. Murillo, Using Fermi Statistics to Create Strongly Coupled Ion Plasmas in Atom Traps, Phys. Rev. Lett. **87**, 115003 (2001).
[22] T. Pohl, T. Pattard, and J. M. Rost, On the possibility of 'correlation cooling' of ultracold neutral plasmas, J. Phys. B **37**, L183 (2004).
[23] G. Bannasch, T. C. Killian, and T. Pohl, Strongly Coupled Plasmas via Rydberg Blockade of Cold Atoms, Phys. Rev. Lett. **110**, 253003 (2013).
[24] T. Pohl, T. Pattard, and J. M. Rost, Relaxation to Nonequilibrium in Expanding Ultracold Neutral Plasmas, Phys. Rev. Lett. **94**, 205003 (2005).
[25] P. McQuillen, T. Strickler, T. Langin, and T. C. Killian, Ion temperature evolution in an ultracold neutral plasma, Phys. Plasmas **22**, 033513 (2015).
[26] E. Urban, T. A. Johnson, T. Henage, L. Isenhower, D. D. Yavuz, T. G. Walker, and M. Saffman, Observation of Rydberg blockade between two atoms, Nat. Phys. **5**, 110 (2009).
[27] D. Petrosyan, M. Höning, and M. Fleischhauer, Spatial correlations of Rydberg excitations in optically driven atomic ensembles, Phys. Rev. A **87**, 053414 (2013).
[28] M. Robert-de-Saint-Vincent, C. S. Hofmann, H. Schempp, G. Günter, S. Whitlock, and M. Weidemüller, Spontaneous Avalanche Ionization of a Strongly Blockaded Rydberg Gas, Phys. Rev. Lett. **110**, 045004 (2013).
[29] S. D. Bergeson, A. Denning, M. Lyon, and F. Robicheaux, Density and temperature scaling of disorder-induced heating in ultracold plasmas, Phys. Rev. A **83**, 023409 (2011).
[30] J. D. Pritchard, D. Maxwell, A. Gauguet, K. J. Weatherill, M. P. A. Jones, and C. S. Adams, Cooperative Atom-Light Interaction in a Blockaded Rydberg Ensemble, Phys. Rev. Lett. **105**, 193603 (2010).

[31] G. Taban, M. P. Reijnders, S. C. Bell, S. B. van der Geer, O. J. Luiten, and E. J. D. Vredenbregt, Design and validation of an accelerator for an ultracold electron source, Phys. Rev. ST Accel. Beams **11**, 050102 (2008).
[32] M. Lyon, S. D. Bergeson, and M. S. Murillo, Limit of strong ion coupling due to electron shielding, Phys. Rev. E **87**, 033101 (2013).
[33] G. Zwicknagel, Molecular Dynamics Simulations of the Dynamics of Correlations and Relaxation in an OCP, Contrib. Plasma Phys. **39**, 155 (1999).
[34] D. H. E. Dubin and T. M. Oneil, Trapped nonneutral plasmas, liquids, and crystals (the thermal equilibrium states), Rev. Mod. Phys. **71**, 87 (1999).
[35] G. Stell, The Percus-Yevick equation for the radial distribution function of a fluid, Physica (Utrecht) **29**, 517 (1963).
[36] H. E. DeWitt and Y. Rosenfeld, Derivation of the one component plasma fluid equation of state in strong coupling, Phys. Lett. A **75**, 79 (1979).
[37] A. Y. Toukmaji and J. A. Board, Jr., Ewald summation techniques in perspective: a survey, Comput. Phys. Commun. **95**, 73 (1996).
[38] See Supplemental Material at http://link.aps.org/supplemental/10.1103/PhysRevLett.115.214802 for derivation of the equations of motion, and for details of the evaluation of ion temperature in the simulations and the asymptotic temperature dependence of the expanding ions, which contains Refs. [39–41].
[39] C. Kittel and P. McEuen, *Introduction to Solid State Physics* (Wiley, New York, 1986).
[40] M. J. L. Sangster and M. Dixon, Interionic potentials in alkali halides and their use in simulations of the molten salts, Adv. Phys. **25**, 247 (1976).
[41] R. T. Farouki and S. Hamaguchi, Thermodynamics of strongly-coupled Yukawa systems near the one-component-plasma limit. II. Molecular dynamics simulations, J. Chem. Phys. **101**, 9885 (1994).
[42] O. J. Luiten, Beyond the RF Photogun in *The Physics and Applications of High Brightness Electron Beams: Proceedings of the ICFA Workshop, Chia Laguna, Sardinia, 2002*, Vol. 1 (World Scientific, Singapore, 2003), pp. 108–126.
[43] S. Torquato, O. U. Uche, and F. H. Stillinger, Random sequential addition of hard spheres in high Euclidean dimensions, Phys. Rev. E **74**, 061308 (2006).
[44] W. S. Jodrey and E. M. Tory, Computer simulation of close random packing of equal spheres, Phys. Rev. A **32**, 2347 (1985).
[45] W. H. Press, B. P. Flannery, S. A. Teukolsky, and W. T. Vetterling, *Numerical Recipes in C* (Cambridge University Press, Cambridge, England, 1992).
[46] B. W. Reed, M. R. Armstrong, N. D. Browning, G. H. Campbell, J. E. Evans, T. LaGrange, and D. J. Masiel, The Evolution of Ultrafast Electron Microscope Instrumentation, Microsc. Microanal. **15**, 272 (2009).
[47] T. Pohl, E. Demler, and M. D. Lukin, Dynamical Crystallization in the Dipole Blockade of Ultracold Atoms, Phys. Rev. Lett. **104**, 043002 (2010).
[48] J. Schachenmayer, I. Lesanovsky, A. Micheli, and A. J. Daley, Dynamical crystal creation with polar molecules or Rydberg atoms in optical lattices, New J. Phys. **12**, 103044 (2010).
[49] F. Nogrette, H Labuhn, S. Ravets, D. Barredo, L. Béguin, A. Vernier, T. Lahaye, and A. Browaeys, Single-Atom Trapping in Holographic 2D Arrays of Microtraps with Arbitrary Geometries, Phys. Rev. X **4**, 021034 (2014).

Reducing the emittance of cold ion beams through suppression of disorder-induced heating with Rydberg blockade

Supplemental Material

D. Murphy, R. E. Scholten,* and B. M. Sparkes
School of Physics, The University of Melbourne, Victoria, 3010, Australia

Comoving equations of motion

In the comoving frame with scale factor α, the coordinate of the i'th ion $\mathbf{x}'_i$ is related to its proper spatial coordinates $\mathbf{x}_i$ as

$$\mathbf{x}'_i = \frac{1}{\alpha}\mathbf{x}_i, \tag{1}$$

with comoving velocity

$$\frac{d\mathbf{x}'_i}{dt} = \frac{1}{\alpha}\left(\frac{d\mathbf{x}_i}{dt} - \frac{d\alpha}{dt}\mathbf{x}'_i\right) \tag{2}$$

and acceleration

$$\frac{d^2\mathbf{x}'_i}{dt^2} = \frac{1}{\alpha}\left[\frac{d^2\mathbf{x}_i}{dt^2} - \frac{d^2\alpha}{dt^2}\mathbf{x}'_i\right] - \frac{2}{\alpha}\frac{d\alpha}{dt}\frac{d\mathbf{x}'_i}{dt} \tag{3}$$

where the square-bracketed terms are the inter-ionic Coulomb interactions with subtraction of linear expansion, and the last term represents adiabatic expansion damping of the comoving velocity.

The inter-ionic forces in periodic boundaries were calculated using Ewald transformation, which involves placing Gaussian negative-charge distributions of comoving standard deviation γ' around each positive point charge to allow the sum of the potentials in real space to converge, then adding a sum in reciprocal space of positive-sign shielding potentials to counteract their effect in the real-space sum [39]. Taking the gradient of these potentials in the comoving coordinates gives the forces that become the square-bracketed terms of Eq. 3,

$$\left[\frac{d^2\mathbf{x}_i}{dt^2} - \frac{d^2\alpha}{dt^2}\mathbf{x}'_i\right] = \frac{1}{m_i}\left(\mathbf{F}_i^{(1)} + \mathbf{F}_i^{(2)}\right), \tag{4}$$

where the real-space sum

$$\mathbf{F}_i^{(1)} = \frac{e^2}{4\pi\varepsilon_0\alpha^2}\sum_{j\neq i}\sum_{\mathbf{n}}\frac{\mathbf{r}'_{i,j\mathbf{n}}}{\left|\mathbf{r}'_{i,j\mathbf{n}}\right|^3}\left\{\operatorname{erfc}\left(\frac{\left|\mathbf{r}'_{i,j\mathbf{n}}\right|}{\sqrt{2}\gamma'}\right) + \sqrt{\frac{2}{\pi}}\frac{\left|\mathbf{r}'_{i,j\mathbf{n}}\right|}{\gamma'}\exp\left(-\frac{\left|\mathbf{r}'_{i,j\mathbf{n}}\right|^2}{2\gamma'^2}\right)\right\}. \tag{5}$$

is taken over all $j \neq i$ ions and their $\mathbf{n}$ periodic images with comoving separations $\mathbf{r}'_{i,j\mathbf{n}} = \mathbf{x}'_i - \left(\mathbf{x}'_j + \mathbf{n}L_0\right)$, which uses the complementary error function $\operatorname{erfc}(z) = 1 - \operatorname{erf}(z)$. The side length of the periodic boundary for a simulation of N ions at initial density n' is $L_0 = (N/n')^{1/3}$. The reciprocal space sum

$$\mathbf{F}_i^{(2)} = \frac{2e^2}{4\pi\varepsilon_0\alpha^2 L_0^2}\sum_{j\neq i}\sum_{\mathbf{h}\neq\mathbf{0}}\frac{\mathbf{h}}{|\mathbf{h}|^2}\exp\left(-2\left(\frac{\gamma'\pi}{L_0}\right)^2|\mathbf{h}|^2\right) \times \sin\left(\frac{2\pi}{L_0}\mathbf{h}\cdot\mathbf{r}'_{i,j\mathbf{0}}\right) \tag{6}$$

is taken over $\mathbf{h}$ reciprocal lattice vectors in integer units of the simple-cubic periodic boundary. We used the approximation of Ref. [40] where the sums converge for the choice of parameters $\gamma' = L_0/\sqrt{2}$ with sums over $\mathbf{n}$ so that $\left|\mathbf{r}'_{i,j\mathbf{n}}\right| \leq 2.6\,L_0$, and $|\mathbf{h}| \leq 8$.

We define the temperature from the comoving velocities, which accounts for the effects of adiabatic cooling, as

$$T = \frac{k_B m_i \alpha^2}{3\beta N}\sum_i^N\left|\frac{d\mathbf{x}'_i}{dt}\right|^2. \tag{7}$$

The factor β corrects for the reduction of disorder induced heating associated with the cubic order of the simulation boundary conditions. We can predict this factor for a disordered distribution in a volume of side-length L_0, where the simple-cubic periodicity introduces an initial binding energy per particle in the initial state [41]

$$u_{sc} = -1.4186487\frac{e^2}{4\pi\varepsilon_0 L_0}. \tag{8}$$

For our periodic-boundary simulations with $N = 1000$ and $n' = 1\times10^{16}\,\mathrm{m}^{-3}$, inclusion of the residual initial binding energy in the Percus-Yevick model for a disordered distribution predicts an equilibrium coupling parameter of $\Gamma_{\mathrm{PY}} = 2.51$, increased from the prediction of $\Gamma_{\mathrm{PY}} = 2.23$ for an infinite distribution. Using $\beta = 2.23/2.51$ for these parameters removes the influence of the periodicity so that the simulation represents the behavior of an infinite distribution. Using this correction factor for blockaded distributions, we find good agreement between our simulations and theoretical prediction of the equilibrium coupling parameters.

Adaptive time steps in the Bulirsch-Stoer integrator were calculated to provide a per-timestep error for the comoving velocities less than one part in 10^6 of a velocity

* scholten@unimelb.edu.au

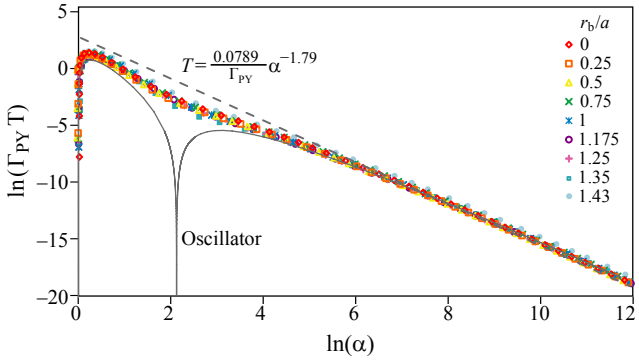

Supp. Fig. 1. Universal asymptotic temperature behavior in the free Coulomb expansion of Rydberg-blockaded initial ion configurations, showing non-adiabatic power-law dependence of the temperature that matches the asymptotic behavior (dashed line) of simple harmonic motion (solid line) in the expanding coordinate system.

scale

$$\Delta v' = e^2 \left(4\pi\varepsilon_0 \alpha a' k_B \Gamma_{\mathrm{eq}} m_i\right)^{-1/2}, \tag{9}$$

taking $\Gamma_{\mathrm{eq}} = 2$ from the expected equilibrium coupling strength of a disordered distribution for an initial Wigner-Seitz radius a', providing a constant error for the emittance in the expanding frame. A limit on the length of a time step was also placed to give a plasma phase difference of at most 1/20th of a full plasma oscillation between steps to ensure clarity of the kinetic energy oscillations.

Harmonic oscillator model for power-law temperature behavior

Ion kinetic energy oscillations can be modelled as harmonic motion at the plasma frequency ω_p. For a single ion, taking an initial displacement $x_0 = 2e^2 \left(4\pi\varepsilon_0 a k_B \Gamma_{\mathrm{PY}} m \omega_p^2\right)^{-1/2}$ from an equilibrium position results in a temperature oscillation about an equilibrium value predicted by the coupling parameter Γ_{PY}. Solving for the motion of the oscillator with expansion in the comoving coordinates shows a temperature with asymptotic power-law dependence on the scale factor α. Supplementary figure 1 shows that the oscillator model predicts the asymptotic behavior of the temperature for all simulations in the range of validity for the Percus-Yevick prediction as $T \propto \Gamma_{\mathrm{PY}}^{-1} \alpha^{1.8}$. The non-adiabatic ($\alpha \neq 2$) temperature law leads to the emittance growth shown in Fig. 3.

PHYSICAL REVIEW E **94**, 021201(R) (2016)

Disorder-induced heating of ultracold neutral plasmas created from atoms in partially filled optical lattices

D. Murphy and B. M. Sparkes*
School of Physics, The University of Melbourne, Victoria 3010, Australia
(Received 30 May 2016; published 8 August 2016)

We quantify the disorder-induced heating (DIH) of ultracold neutral plasmas (UCNPs) created from cold atoms in optical lattices with partial filling fractions, using a conservation of energy model involving the spatial correlations of the initial state and the equation of state in thermal equilibrium for a one-component plasma. We show, for experimentally achievable filling fractions, that the ionic Coulomb coupling parameter could be increased to a degree comparable to other proposed DIH-mitigation schemes. Molecular dynamics simulations were performed with compensation for finite-size and periodic boundary effects, which agree with calculations using the model. Reduction of DIH using optical lattices will allow for the study of strongly coupled plasma physics using low-density, low-temperature, laboratory-based plasmas, and lead to improved brightness in UCNP-based cold electron and ion beams, where DIH is otherwise a fundamental limitation to beam focal sizes and diffraction imaging capability.

DOI: 10.1103/PhysRevE.94.021201

Introduction. Ultracold neutral plasmas (UCNPs) created by photoionizing laser-cooled atoms are a platform for the study of strongly coupled matter, where interparticle interaction energy exceeds thermal kinetic energy. UCNPs provide a laboratory-based resource to study plasma behavior occurring in astrophysical environments, such as the dense high-temperature interiors of gas giants and in white-dwarf stars [1]. UCNPs are characterized by high values of the Coulomb coupling parameter

$$\Gamma = \frac{e^2}{4\pi\varepsilon_0 a k_B T}, \tag{1}$$

where e is the charge of one particle, ε_0 is the vacuum permittivity, the Wigner-Seitz radius $a = (3/4\pi n)^{1/3}$ is the average interparticle separation for particle density n, k_B is the Boltzmann constant, and T is the particle temperature. Γ is the ratio of the interparticle Coulomb potential and kinetic energy. Strong coupling occurs when $\Gamma > 1$, indicating that particle motion within the plasma is dominated by interparticle forces, giving rise to collective effects that result in Wigner crystallization for $\Gamma > 174$ [2]. Strongly coupled UCNPs are also potentially useful as a source of highly focusable electrons and ions suitable for high-resolution coherent diffraction imaging and microscopy [3,4].

When cold atoms in a magneto-optical trap (MOT) are photoionized to produce a UCNP, minimal kinetic energy is imparted by the ionizing laser to the ions and electrons, giving velocity spreads equivalent to less than 1 mK and 10 K, respectively [5]. The low initial temperatures would imply strong coupling for the ions, but UCNP studies have not been able to reach far into the strongly coupled regime due to the disorder-induced heating (DIH) effect [6]. DIH arises from thermalization of random initial interparticle potentials because the ions are created from atoms that have an irregular spatial distribution. The ions gain kinetic energy through mutual Coulomb repulsion, oscillating about dynamic local potential minima at the plasma frequency $\omega = \sqrt{ne^2/\varepsilon_0 m}$, where m is the ion mass, and oscillating in kinetic energy at a frequency of 2ω. Thermalization to an equilibrium coupling parameter $\Gamma_{eq} \sim 1$ occurs in times on the order of one plasma period $2\pi/\omega$ as the kinetic energy oscillations dephase. DIH limits charged particle beam brightness, which is directly proportional to Γ, as particle spatial distributions are uncorrelated at a conventional beam source [7].

In principle, DIH can be suppressed in UCNPs by preparing atoms with spatial correlations prior to ionization, such as in Fermi-degenerate or blockaded Rydberg gases [8,9], which have interatomic interactions that place lower limits on the nearest-neighbor spacings. It has also been predicted that DIH can be entirely prevented in UNCPs created from atoms trapped in optical lattices, which have a crystal-like structure formed in the interference of high-intensity laser beams, if single atoms occupy a high fraction ($f > 0.99$) of the lattice sites [10]. Achieving high filling fractions is experimentally challenging, however, models and simulations to date have not predicted Γ_{eq} for lattice-correlated UCNP at filling fractions $f < 0.99$. Preparation of single atoms in lattice sites is typically limited to $f \leqslant 0.5$, as sites initially holding more than one atom depopulate via pairwise collisions, resulting in an equal probability of being occupied or being vacant [11]. Filling fractions exceeding 0.5 can be achieved through a transition to a Mott insulating state in a condensed gas [12]. It may also be possible to exceed $f = 0.5$ through coherent excitation (and subsequent ionization) of Rydberg atoms to quasicrystalline spatial distributions within a lattice [13].

In this Rapid Communication we calculate the equilibrium Coulomb coupling parameter of UCNPs undergoing DIH created from partially filled ($0 < f < 0.99$) optical lattices. The model is compared to molecular dynamics simulations performed in periodic boundary conditions, accounting for the finite-size effects. Predicting the equilibrium properties of UCNPs as a function of experimental parameters will enable future experiments to target the most promising conditions for obtaining strong coupling for astrophysical simulations [14]. Increased coupling in UCNPs will also enable increased brightness in ion beams extracted from cold atom sources, which serve as a platform for the study of intrabeam Coulomb

*bsparkes@unimelb.edu.au

RAPID COMMUNICATIONS

interactions relevant to future generations of charged particle beam sources [15,16].

Lattice heating calculations. The equilibrium value of the Coulomb coupling parameter after DIH, and its increase through correlations, can be calculated using conservation of energy between the potential energy of the initial lattice distribution and the thermal and binding energy of the equilibrium distribution of a strongly coupled plasma. We model a nonexpanding one-component plasma (OCP), infinite in spatial extent, where electrons in the plasma form a neutralizing background for the ions. Expanding UCNPs do not reach an equilibrium, with Γ increasing in time as a function of system size following DIH [17]. However, the ratio of the coupling parameters for a correlated to a disordered system with expansion is equal to that for a nonexpanding system [16]. Therefore, calculation of Γ as a function of the correlation parameter f quantifies the suppression of DIH independent of the expansion, which depends on the plasma dimensions, and on the electron temperature. The OCP description of a UCNP assumes that the electrons are weakly coupled at high temperature, with no influence on the ion interactions. For UCNPs with low-temperature electrons, inter-ion interactions are reduced to a Yukawa-type potential [18], but, with a generalized definition of Γ including the reduced potential, it can be shown that $\Gamma_{\rm eq}$ is not dependent on the electron temperature [19]. We assume that the UCNP is created in times much less than the DIH time scale ($2\pi/\omega$), which can be achieved using ultrafast photoionizing lasers or pulsed external electric fields [9].

The initial internal binding energy per particle of a system of charged particles with Wigner-Seitz radius a occupying a fraction f of the sites of a lattice is

$$u_{\rm i} = -\frac{e^2}{4\pi\varepsilon_0 a}\frac{f^{2/3}M}{2}, \tag{2}$$

which is f times the Madelung energy of a lattice with Madelung constant M and charge e at each site [20]. An additional factor of $f^{-1/3}$ is included to take into account the average interparticle separation a of only the occupied lattice sites. Atoms with initial temperature $T_{\rm i}$ in lattice sites with harmonic trapping frequency ν are displaced from the lattice sites by standard deviation $\sigma = \sqrt{k_{\rm B}T_{\rm i}/m(2\pi\nu)^2}$ in each axis. Atomic displacement due to thermal motion reduces the initial binding of the ions compared to the zero-temperature case by a value that can be written for small displacements, to first order in the dimensionless quantity $(\sigma/a')^2$, where $a' = f^{1/3}a$ is the Wigner-Seitz radius for the lattice sites, as [10]

$$\Delta = \frac{e^2}{4\pi\varepsilon_0 a}\frac{3f^{2/3}}{2}\left(\frac{\sigma}{a'}\right)^2, \tag{3}$$

which includes the scaling by f as in Eq. (2). The initial energy per particle of the ions is the sum of the binding energy $u_{\rm i}$, the displacement energy Δ, and the initial kinetic energy $k_{\rm i} = 3k_{\rm B}T_{\rm i}/2$.

The binding energy in thermal equilibrium for the strongly coupled fluid phase, occurring for $1 < \Gamma_{\rm eq} < 170$, is

$$u_{\rm eq} = -\frac{e^2}{4\pi\varepsilon_0 a}\left(A + B\,\Gamma_{\rm eq}^{-2/3} + C\,\Gamma_{\rm eq}^{-1}\right), \tag{4}$$

where the factor $A = 0.9$ gives the lower bound to the OCP energy [21] and factors $B = -0.590\,673$ and $C = 0.265\,69$ are given by fits of a known form of the OCP equation of state to simulation data [22]. The total energy per particle in equilibrium is $u_{\rm eq}$ plus the equilibrium kinetic energy written in terms of the equilibrium coupling parameter as $k_{\rm eq} = 3e^2/8\pi\varepsilon_0 a\Gamma_{\rm eq}$.

Equating the initial and equilibrium energies, excluding the relatively small $k_{\rm i}$, results in the expression

$$\frac{1}{2}f^{2/3}\left[M - 3\left(\frac{\sigma}{a'}\right)^2\right] = A + B\,\Gamma_{\rm eq}^{-2/3} + \left(C - \frac{3}{2}\right)\Gamma_{\rm eq}^{-1}, \tag{5}$$

from which $\Gamma_{\rm eq}$ can be calculated in terms of M, f, and σ/a'. At typical UCNP ion densities of $n = 10^{16}$ m^{-3} and initial temperatures $T_{\rm i} < 1$ mK, exclusion of $k_{\rm i}$ has a negligible effect for $f < 0.99$, so that $\Gamma_{\rm eq}$ can be calculated with only the dimensionless quantities of Eq. (5).

Molecular dynamics simulations. We simulated DIH for ^{85}Rb ions (mass $m = 1.41 \times 10^{-25}$ kg) in partially filled lattices of simple cubic (sc), face-centered-cubic (fcc), and body-centered-cubic (bcc) geometries, which are experimentally realizable with suitable choices of laser geometry [23–25], and have Madelung constants $M_{\rm sc} = 1.760\,12$, $M_{\rm fcc} = 1.791\,75$, and $M_{\rm bcc} = 1.791\,86$, respectively [26]. Molecular dynamics simulations were initialized with ion positions set at lattice sites for a range of filling fractions, choosing the cubic lattice dimensions so that the number of ions N was closest to 1000 for consistency. Ion density in simulation was kept constant at $n = 10^{16}$ m^{-3} by varying the lattice spacing, giving one-to-one correspondence between the temperature and coupling parameter across our simulations. Experimentally, lattice spacings are fixed by the laser wavelength and geometry so that low filling fractions will typically correspond to low density, but our main result in predicting $\Gamma_{\rm eq}$ as a function of f is dimensionless and independent of density. Figure 1(a) shows a two-dimensional representation of the initial positions for ions of different filling fraction but equal density.

Ions from lattice-trapped atoms with thermal displacement were simulated for a trapping frequency of $\nu = 15$ kHz. Each particle was assigned a random velocity using a Gaussian thermal distribution, for the chosen σ/a' parameter, and a random phase for the oscillatory harmonic motion in each axis, which together define a spatial displacement relative to the lattice site. For simplicity, we assume that photoionization is instantaneous, though we observe negligible differences in the equilibria of simulations repeated with ionization times up to 7 ns, or 1.6×10^{-2} times the DIH time scale, typical of the duration of pulsed lasers used to ionize atoms in a UCNP.

Equations of motion for the set of $\mathbf{N} = \{1,2,\ldots,N\}$ ions with positions $\mathbf{x}_{i\in\mathbf{N}}$, interacting via Coulomb forces in cubic periodic boundaries, were taken from the gradient of Ewald-summed interparticle potentials [27,28], splitting the calculation into two separately convergent sums of the interparticle forces as

$$\frac{d^2\mathbf{x}_i}{dt^2} = \frac{1}{m}\left(\mathbf{F}_i^{(1)} + \mathbf{F}_i^{(2)}\right). \tag{6}$$

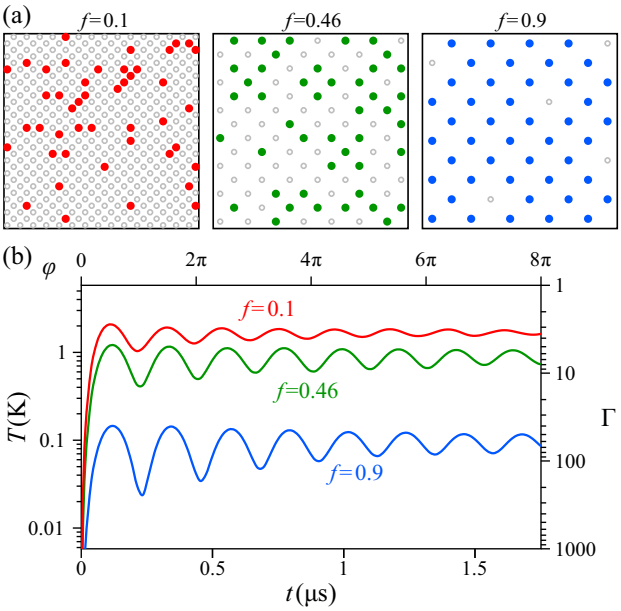

FIG. 1. (a) Two-dimensional lattices with different filling fraction f but equal atom density. The solid circles represent the position of atoms, and the open circles represent vacant lattice sites. (b) Simulations of disorder-induced heating in ionized rubidium atoms located at the sites of a three-dimensional body-centered-cubic lattice with filling fraction f. All simulations have equal density, allowing a direct comparison of temperature T to the coupling parameter Γ, and time following ionization t to the plasma phase $\varphi = \omega t$. Lattices of high filling fraction equilibrate to lower temperature and higher coupling parameter, reflecting increased interparticle spatial correlations in the initial distribution.

The Ewald method shields the long-ranged, positive-valued ionic Coulomb potentials with Gaussian negative-charge distributions of standard deviation γ, allowing a convergent sum of the shielded forces in real space,

$$\mathbf{F}_i^{(1)} = \frac{e^2}{4\pi\varepsilon_0}\sum_{j\neq i}\sum_{\mathbf{n}}\frac{\mathbf{r}_{i,j\mathbf{n}}}{|\mathbf{r}_{i,j\mathbf{n}}|^3}\left[\operatorname{erfc}\left(\frac{|\mathbf{r}_{i,j\mathbf{n}}|}{\sqrt{2}\gamma}\right) + \sqrt{\frac{2}{\pi}}\frac{|\mathbf{r}_{i,j\mathbf{n}}|}{\gamma}\exp\left(-\frac{|\mathbf{r}_{i,j\mathbf{n}}|^2}{2\gamma^2}\right)\right]. \quad (7)$$

Equation (7) uses the complementary error function $\operatorname{erfc}(z) = 1 - \operatorname{erf}(z)$, taken over all $j \neq i$ ions for cubic-boundary lattice vectors $\mathbf{n} \in \mathbb{Z}^3$ with separation vectors $\mathbf{r}_{i,j\mathbf{n}} = \mathbf{x}_i - (\mathbf{x}_j + \mathbf{n}L)$, where the boundary length is $L = (N/n)^{1/3}$ for a simulation of N ions at density n. The contributions to the forces from the negative shielding potentials are counteracted by adding equally placed positive-charge Gaussian potentials and taking the sum of forces in reciprocal space,

$$\mathbf{F}_i^{(2)} = \frac{2e^2}{4\pi\varepsilon_0 L^2}\sum_{j\neq i}\sum_{\mathbf{h}\neq\mathbf{0}}\frac{\mathbf{h}}{|\mathbf{h}|^2}\exp\left[-2\left(\frac{\gamma\pi}{L}\right)^2|\mathbf{h}|^2\right] \times \sin\left(\frac{2\pi}{L}\mathbf{h}\cdot\mathbf{r}_{i,j\mathbf{0}}\right), \quad (8)$$

over the reciprocal lattice vectors $\mathbf{h} \in \mathbb{Z}^3$ of the simple-cubic periodic boundary. We used the approximation of Ref. [29] where the sums converge for the choice of parameters $\gamma = L/\sqrt{2}$ with sums over $\mathbf{n}$ so that $|\mathbf{r}_{i,j\mathbf{n}}| \leqslant 2.6L$, and $|\mathbf{h}| \leqslant 8$. Once initialized, the equations of motion were integrated using the Bulirsch-Stoer method with polynomial-function extrapolation [30] with respect to the dimensionless plasma phase $\varphi = \omega t$, where t is the time following ionization. The maximum integral step in the plasma phase was limited to $0.05 \times 2\pi$ in order to resolve the kinetic energy oscillations [seen in Fig. 1(b)].

Simulations are affected by the finite size of the periodic boundaries, as the repeating images of the system introduce effective correlations into the ion position distribution at the scale of the boundary length [31]. In the initial binding energy calculation of Eq. (2) it is assumed that the lattice vacancies are distributed randomly, but the periodic boundary conditions give the vacancies a simple-cubic repeating structure. Each ion that is "removed" from a lattice site under periodic boundaries causes the remaining ions to retain one unit of simple-cubic binding energy relative to the removal of an equivalent fraction of ions from an infinite distribution. This residual binding energy can be accounted for by introducing an additional term in the calculation of the initial energy

$$u_{\mathrm{PBC}} = -\frac{e^2}{4\pi\varepsilon_0 a}\frac{(1-f)M_{\mathrm{sc}}}{2N^{1/3}}, \quad (9)$$

which is the vacant fraction lattice energy for the simple-cubic structure of the periodic boundaries, for a simulated ion number N.

Calculations of Γ_{eq} including the boundary-correction term (9) in the initial energy of the system can accurately predict the results of the simulations with finite-size effects. Instead, to give results for a system without periodic boundary conditions, we compensate for the finite-size effects by using a correction factor for the coupling parameter evaluated in the simulations. The correction factor is equal to the expected factor by which the prediction of Γ_{eq} for a finite-sized system would differ from the prediction of Γ_{eq} for an infinite system with $u_{\mathrm{PBC}} \to 0$. Simulations for different lattice geometries and filling fractions differ slightly in ion number N due to the cubic scaling of N with lattice dimensions, and therefore also differ in correction factor.

Examples of simulations of ions with zero initial temperature created in a three-dimensional bcc lattice with different filling fractions are shown in Fig. 1(b), corrected for the influence of the periodic boundaries. The ion temperature is plotted against time following ionization, or in dimensionless terms plotted for the coupling parameter against plasma phase φ, exhibiting the damped kinetic energy oscillations expected of an equilibrating UCNP. Ions with a high lattice filling fraction equilibrate to a lower temperature and higher coupling parameter than ions with a low filling fraction, reflecting the increased initial correlations.

Results and discussion. The equilibrium coupling parameter Γ_{eq} was evaluated from the simulations by taking the average of the periodicity-corrected coupling parameters at each time step between plasma phases 8π and 16π. Figure 2 shows the simulated results for zero initial temperature ions

RAPID COMMUNICATIONS

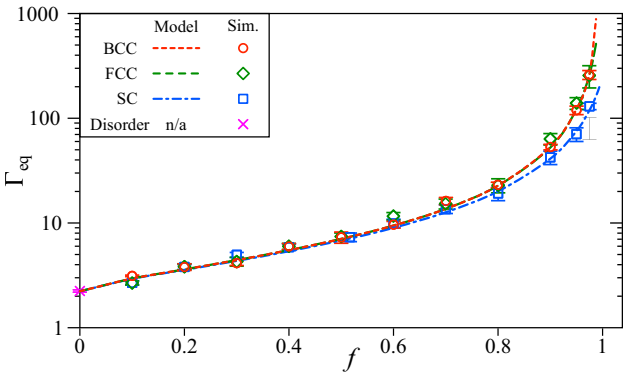

FIG. 2. Calculated (lines) and simulated (points) equilibrium coupling parameters Γ_{eq} for body-centered-cubic (bcc), face-centered-cubic (fcc), and simple-cubic (sc) lattices at different atomic filling fractions f, for atoms of zero initial temperature. High filling fractions lead to increased coupling parameter Γ_{eq} in equilibrium compared to random placement (disorder), which is equivalent to $f = 0$. Γ_{eq} was evaluated in simulation over plasma phases φ between 8π and 16π, with uncertainty as one standard deviation in that period. Differences in Γ_{eq} between lattices result from the different binding energies in the initial state, with the bcc and fcc lattices reaching higher coupling than the sc lattice at fixed f.

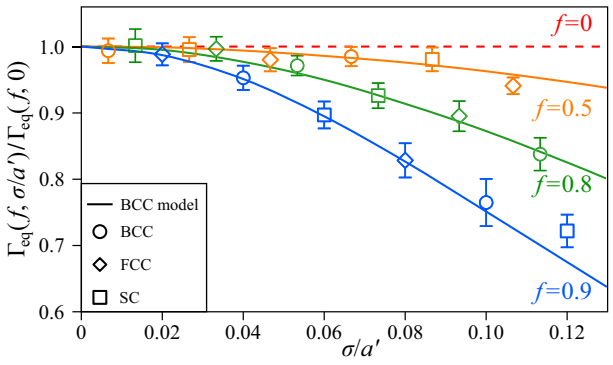

FIG. 3. Lowering of the equilibrium coupling parameter due to thermal broadening of lattice sites, expressed as the ratio of the equilibrium coupling parameters for displaced to nondisplaced atoms in lattices with filling fraction f. The atomic displacement σ is normalized to the Wigner-Seitz radius a' for the lattice sites. Simulations (data points) are performed for the simple-cubic (sc), face-centered-cubic (fcc), and body-centered cubic (bcc) lattices at different filling fractions, averaging the ratios over the evaluation period between plasma phases of 8π and 16π with error bars as one standard deviation, and the theoretical calculations (solid lines) are shown for the bcc lattice only.

($\sigma/a' = 0$) for the body-centered-, face-centered-, and simple-cubic lattices at different filling fractions. These give strong agreement to the theoretical predictions for the dependence of the equilibrium coupling parameter on the filling fraction for each lattice, and to the results for a disordered distribution with randomly placed ions, equivalent to a lattice with $f = 0$, which has $\Gamma_{eq} = 2.2$. Uncertainties in the simulation data result from residual kinetic energy oscillations during the evaluation period for Γ_{eq}. The bcc and fcc lattice results are similar, owing to their nearly equal Madelung constants, while the sc lattice tended to have lower Γ_{eq} at high values of f due to its lower Madelung constant.

Ions with initial thermal displacement from the lattice sites have lowered Γ_{eq} compared to ions from lattices of the same f with zero initial temperature, as the displacements reduce the initial interparticle correlations. Figure 3 shows theoretical predictions and simulation results for the factor by which Γ_{eq} for thermally displaced atoms is reduced compared to the zero-temperature result. The data points are the averages of the coupling parameter ratios for the displaced and zero-temperature simulations at each time step over the $8\pi < \varphi < 16\pi$ evaluation period, with uncertainties as one standard deviation. Simulations were performed for the sc, fcc, and bcc lattices, however, we only show the predictions for the bcc lattice as the ratios are not strongly dependent on the Madelung constant. Thermal displacements have a greater impact on Γ_{eq} for lattices of high f, reducing the otherwise high spatial correlations, than for lattices of low f. For example, distributions with $f = 0$ gain no additional disorder when the atoms are displaced. The simulations agreed with the predictions up to $\sigma/a' = 0.1$, a relatively high parameter for lattice-trapped atoms. For example, the experiments of Ref. [32] achieve $\sigma/a' = 0.087$ for cesium atoms at 10 μK in a 4.9 μm site-separation ($a' = 3.0$ μm) simple-cubic lattice with trapping frequency $\nu = 15$ kHz.

A UCNP created from the above example SC lattice with $\sigma/a' = 0.087$, at the typical experimental limit of $f = 0.5$, would have $\Gamma_{eq} = 6.7$, compared to $\Gamma_{eq} = 2.2$ for disordered atoms. Our results show that by creating UCNP from optical-lattice trapped atoms, even with imperfect filling fraction, an increase in Γ_{eq} may be achieved that is comparable to the expected increases using doubly ionized [33] or Rydberg-blockade correlated atoms [9,16]. Achieving an increase in Γ_{eq} by greater than an order of magnitude compared to disordered ions would require $f > 0.8$ and cooling of the atoms to near the vibrational ground state of the lattice trapping potential.

Conclusion. In summary, we have shown that the coupling parameter in ultracold neutral plasmas can be increased by spatially correlating the cold atoms, prior to ionization, using an optical lattice even with imperfect filling. We have presented a model for calculating the equilibrium coupling parameter following disorder-induced heating of lattice-correlated ions as a function of the lattice geometry, filling fraction, and initial atomic temperature. Calculations using the model are consistent with detailed molecular dynamics simulations, when the additional correlations resulting from periodic boundary effects are accounted for. Increased coupling parameters will allow for observation of strongly coupled plasma processes using UCNP, and will increase the brightness of cold ion beams using the UCNP source beyond the otherwise fundamental limit imposed by disorder-induced heating.

Acknowledgments. We acknowledge helpful discussions with R. E. Scholten. B.M.S. gratefully acknowledges the support of a University of Melbourne McKenzie Fellowship. This work was supported by the Australian Research Council Discovery Project No. DP140102102.

[1] T. C. Killian, Science **316**, 705 (2007).
[2] S. Ichimaru, Rev. Mod. Phys. **54**, 1017 (1982).
[3] B. J. Claessens, S. B. van der Geer, G. Taban, E. J. D. Vredenbregt, and O. J. Luiten, Phys. Rev. Lett. **95**, 164801 (2005).
[4] J. L. Hanssen, E. A. Dakin, J. J. McClelland, and M. Jacka, J. Vac. Sci. Technol. B **24**, 2907 (2006).
[5] T. C. Killian, S. Kulin, S. D. Bergeson, L. A. Orozco, C. Orzel, and S. L. Rolston, Phys. Rev. Lett. **83**, 4776 (1999).
[6] D. O. Gericke and M. S. Murillo, Contrib. Plasma Phys. **43**, 298 (2003).
[7] J. M. Maxson, I. V. Bazarov, W. Wan, H. A. Padmore, and C. E. Coleman-Smith, New J. Phys. **15**, 103024 (2013).
[8] M. S. Murillo, Phys. Rev. Lett. **87**, 115003 (2001).
[9] G. Bannasch, T. C. Killian, and T. Pohl, Phys. Rev. Lett. **110**, 253003 (2013).
[10] T. Pohl, T. Pattard, and J. M. Rost, J. Phys. B: At. Mol. Opt. Phys. **37**, L183 (2004).
[11] M. T. DePue, C. McCormick, S. L. Winoto, S. Oliver, and D. S. Weiss, Phys. Rev. Lett. **82**, 2262 (1999).
[12] J. F. Sherson, C. Weitenberg, M. Endres, M. Cheneau, I. Bloch, and S. Kuhr, Nature (London) **467**, 68 (2010).
[13] J. Schachenmayer, I. Lesanovsky, A. Micheli, and A. J. Daley, New J. Phys. **12**, 103044 (2010).
[14] D. Comparat, T. Vogt, N. Zahzam, M. Mudrich, and P. Pillet, Mon. Not. R. Astron. Soc. **361**, 1227 (2005).
[15] D. Murphy, R. W. Speirs, D. V. Sheludko, C. T. Putkunz, A. J. McCulloch, B. M. Sparkes, and R. E. Scholten, Nat. Commun. **5**, 4489 (2014).
[16] D. Murphy, R. E. Scholten, and B. M. Sparkes, Phys. Rev. Lett. **115**, 214802 (2015).
[17] T. Pohl, T. Pattard, and J. M. Rost, Phys. Rev. Lett. **94**, 205003 (2005).
[18] T. K. Langin, T. Strickler, N. Maksimovic, P. McQuillen, T. Pohl, D. Vrinceanu, and T. C. Killian, Phys. Rev. E **93**, 023201 (2016).
[19] M. Lyon, S. D. Bergeson, and M. S. Murillo, Phys. Rev. E **87**, 033101 (2013).
[20] The total electrostatic energy of a lattice where the charge is reduced by a factor of f scales as f^2, but this energy is shared between only the sites containing charge, so the energy per charged particle scales as f.
[21] M. Baus and J. P. Hansen, Phys. Rep. **59**, 1 (1980).
[22] D. H. E. Dubin and T. M. O'Neil, Rev. Mod. Phys. **71**, 87 (1999).
[23] I. Bloch, Nat. Phys. **1**, 23 (2005).
[24] G. Grynberg, B. Lounis, P. Verkerk, J.-Y. Courtois, and C. Salomon, Phys. Rev. Lett. **70**, 2249 (1993).
[25] C. S. Adams, S. G. Cox, E. Riis, and A. S. Arnold, J. Phys. B: At. Mol. Opt. Phys. **36**, 1933 (2003).
[26] R. M. Martin, *Electronic Structure: Basic Theory and Practical Methods* (Cambridge University Press, Cambridge, UK, 2004).
[27] C. Kittel and P. McEuen, *Introduction to Solid State Physics* (Wiley, New York, 1986).
[28] L. Hernquist, F. R. Bouchet, and Y. Suto, Astrophys. J. Suppl. Ser. **75**, 231 (1991).
[29] M. J. L. Sangster and M. Dixon, Adv. Phys. **25**, 247 (1976).
[30] W. H. Press *et al.*, *Numerical Recipes in C* (Cambridge University Press, Cambridge, UK, 2012).
[31] G. Makov and M. C. Payne, Phys. Rev. B **51**, 4014 (1995).
[32] K. D. Nelson, X. Li, and D. S. Weiss, Nat. Phys. **3**, 556 (2007).
[33] M. Lyon and S. D. Bergeson, Contrib. Plasma Phys. **55**, 399 (2015).

PHYSICAL REVIEW A **94**, 023404 (2016)

Stimulated Raman adiabatic passage for improved performance of a cold-atom electron and ion source

B. M. Sparkes, D. Murphy, R. J. Taylor, R. W. Speirs, A. J. McCulloch, and R. E. Scholten*
School of Physics, University of Melbourne, VIC 3010, Australia
(Received 10 March 2016; published 8 August 2016)

We implement high-efficiency coherent excitation to a Rydberg state using stimulated Raman adiabatic passage in a cold-atom electron and ion source. We achieve an efficiency of 60% averaged over the laser excitation volume with a peak efficiency of 82%, a 1.6 times improvement relative to incoherent pulsed-laser excitation. Using pulsed electric field ionization of the Rydberg atoms we create electron bunches with durations of 250 ps. High-efficiency excitation will increase source brightness, crucial for ultrafast electron diffraction experiments, and coherent excitation to high-lying Rydberg states could allow for the reduction of internal bunch heating and the creation of a high-speed single-ion source.

DOI: 10.1103/PhysRevA.94.023404

I. INTRODUCTION

Cold-atom electron and ion sources (CAEISs) [1–6], based on the photoionization of laser-cooled gases, offer the potential for dramatic improvements for electron diffraction, nanofabrication, and microscopy. One of the main drivers for the development of a CAEIS is the long-term goal of creating "molecular movies": to probe dynamic processes with atomic spatial and temporal resolution. Substantial advances towards this goal have been demonstrated with electron [7–13] and x-ray [14–20] single-shot ultrafast diffraction.

A key metric for ultrafast diffraction is the normalized beam brightness [21]. Conventional electron sources are not sufficiently bright for collecting single-shot diffraction signals from weakly scattering molecules or nanocrystals. Beam brightness is proportional to particle flux, which for a CAEIS depends linearly on the density of the cold-atom cloud and the photoionization probability or efficiency. To date, most CAEIS experiments have used photoexcitation with pulsed lasers in the presence of a static ionizing electric field. The incoherent nature of the excitation has limited the peak efficiency to 50%, while requiring high laser power due to saturation of the conventional excitation process.

Stimulated Raman adiabatic passage (STIRAP) [22] offers a mechanism for increasing the CAEIS excitation efficiency, particular in an optically dense cold atom target, and therefore improving source brightness. Here we are specifically interested in excitation to Rydberg states of rubidium-85 in a three-level ladder system (Fig. 1) [23]. By first illuminating the atoms with light of a frequency ω_{23}, resonant with the $|2\rangle \rightarrow |3\rangle$ transition, and then a second temporally overlapping light field of frequency ω_{12}, a dark state is formed by a coherent superposition of states $|1\rangle$ and $|3\rangle$. As the intensity of the light fields change, the atomic state transitions from state $|1\rangle$ to $|3\rangle$, bypassing $|2\rangle$. Figure 1 shows the population of the three states during the above-mentioned "counterintuitive" pulse sequence, simulated using optical Bloch equations for a ladder system [24] with Rabi frequencies Ω_{12} and Ω_{23}.

STIRAP is a robust technique and, provided the adiabatic condition is met ($\Omega_{\text{eff}}\,\tau > 10$, where $\Omega_{\text{eff}} = \sqrt{\Omega_{12}^2 + \Omega_{23}^2}$ is the effective Rabi frequency and τ is the interaction time), high-efficiency excitation is possible with a variety of different individual Rabi frequencies, pulse delays, and shapes. Experiments to date have demonstrated peak excitation efficiencies up to 90% [25–27], which would increase the brightness of a CAEIS by a factor of 1.8.

STIRAP also enables a method for producing very short bunches, and therefore for observing atomic-scale dynamics, by following excitation with pulsed-electric-field ionization [28]. This method will lead to a longitudinal compression of the bunch following ionization: the electrons liberated at later times will be accelerated by a larger field, allowing for ultra-short bunches at the sample without ultra-high electron densities, and therefore large Coulomb-driven expansion, at the source. Rydberg states have long lifetimes (tens to hundreds of microseconds) and relatively low ionization thresholds (600 V cm^{-1} for $30S_{1/2}$), easing experimental demands on the pulsed electric field supply. The coupling strength of Rydberg transitions is much higher in the absence of an electric field, so that much lower laser power is required with a pulsed electric field compared to excitation in a static field, making STIRAP excitation a viable option. Combining STIRAP excitation and fast pulsed-field ionization has the potential to create bunches that are cold, bright, and ultrafast, which is difficult to replicate with incoherent ultrafast laser ionization [4,29].

The large dipole moments of Rydberg atoms enable Rydberg blockade, where excitation of one atom inhibits the excitation of other atoms nearby [23,24]. Rydberg blockade can, in principle, reduce disorder-induced heating [30,31] and thereby reduce emittance and increase focusabiltiy in a CAEIS [32]. By enforcing a separation between Rydberg atoms larger than the laser excitation volume, blockade can allow selective excitation of discrete separated atoms and thereby create a deterministic single ion source [33–35].

With the much-reduced laser power required, STIRAP can also be used for high-efficiency continuous operation, with increased average current relative to pulsed trap-based CAEISs [36–39]. Continuous sources are preferred for sub-nanometer ion beam milling, imaging, and doping in semiconductor device fabrication. A continuous source of cold ions

*scholten@unimelb.edu.au

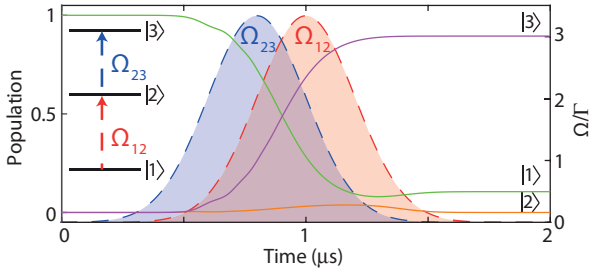

FIG. 1. Simulation of high-efficiency excitation using stimulated Raman adiabatic passage in a three-level ladder system. Solid lines represent atomic state populations (left-hand axis), dashed and filled lines represent Rabi frequencies Ω normalized to the intermediate state decay rate Γ (right-hand axis).

has recently been demonstrated using Rydberg excitation with a current of up to 130 pA [40], a 40-fold increase over direct, above-threshold ionization methods, illustrating the advantage of coherent excitation methods.

Here we present a CAEIS based on STIRAP excitation in a magneto-optical trap (MOT), with a volume-averaged excitation efficiency of 60% and a corresponding peak efficiency of 82%, 1.6 times the maximum possible with direct excitation. We also use a streak method to investigate the temporal profile of the bunches created via electric-field ionization, and finally we discuss how STIRAP could be implemented in an atomic beam-based CAEIS.

II. METHOD

The CAEIS setup is based around a MOT of rubidium-85 atoms located between two accelerator electrodes, as described in previous work [3,29] and shown in Fig. 2(a). A typical experimental sequence is shown in Fig. 2(b), starting with the MOT being loaded for approximately 100 ms. After this time all laser and magnetic fields are switched off and allowed to decay for 4 ms to ensure a field-free excitation region. The atomic density after 4 ms of expansion was measured to be $\rho_a = 5 \times 10^9$ atoms cm^{-3} using absorption imaging.

In contrast to previous CAEIS experiments, which used a large-bandwidth pulsed 480 nm blue laser for direct ionization via a Stark-shifted manifold [3,41–43], here we used a frequency-doubled and amplified 960 nm laser diode. The continuous laser provided a high-power (300 mW), narrow-linewidth (<500 kHz) source of 480 nm light to couple the intermediate $5P_{3/2}$ state to a Rydberg level ($28S_{1/2}$). The frequency was stabilized using an ultrastable optical reference cavity.

The STIRAP process [see level structure; Fig. 2(a)] was driven by an infrared 780 nm narrow-line width (200 kHz) diode laser with 60 nW of power and a frequency 27 MHz blue-detuned from the $5S_{1/2} \rightarrow 5P_{3/2}$ transition to reduce incoherent absorption by atoms outside the interaction volume. The continuous blue laser was red-detuned 27 MHz from the $5P_{3/2} \rightarrow 28S_{1/2}$ transition. We define the one-photon detuning as $\Delta = +27$ MHz.

Temporal control of the excitation fields was achieved via double-pass acousto-optic modulators. Rectangular pulses were used, as illustrated in Fig. 2(c), and we define the

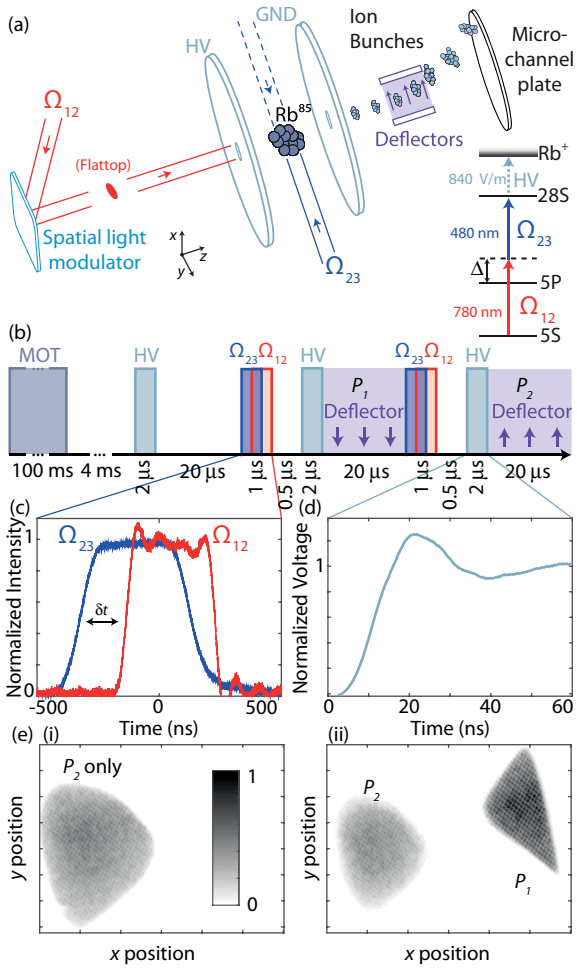

FIG. 2. (a) Cold-atom ion source: HV refers to the high-voltage supplied to the front accelerator plate; GND is the grounded plate; and Ω_{12} and Ω_{23} refer to the two STIRAP fields. Inset shows the level structure of Rb^{85} used here, including the electric field ionization strength required and the one-photon detuning Δ. (b) Timing sequence for STIRAP excitation, field ionization, and two-pulse measurements, using electrostatic deflectors to spatially separate the two pulses (P_1 and P_2). (c) STIRAP pulse sequence, with temporal separation $\delta t < 0$. (d) Time dependence of front accelerator potential, for $V_{max} = 100$ V. (e) Example MCP images showing (i) just pulse two (P_2) and (ii) both pulses. Color bar in (i) shows scaling used for both MCP images.

delay between the pulses δt to be negative if the blue pulse started before the red. The excitation region was determined by the spatial overlap of the two laser beams. The spatial profile of the infrared laser beam, controlled via a spatial-light modulator, was a uniform circular cross section with a radius of $R_r = 150$ μm in the plane perpendicular to the direction of charged particle propagation. The blue laser beam was focused to a ribbon with Gaussian standard deviations of approximately $\sigma_x = 150$ μm by $\sigma_z = 20$ μm in the perpendicular and longitudinal directions respectively. The optical excitation was driven without an external electric field to avoid Stark splitting and loss of coupling strength. A potential difference was then applied to the electrodes, with a rise time of 4 ns [Fig. 2(d)]. The threshold electric field strength required for ionization

of the $28S_{1/2}$ is 840 V cm^{-1}. Typically an accelerator field of 1400 kV cm^{-1} was applied to ensure complete ionization. The liberated electrons or ions (depending on the polarity of the electric field) propagated 70 cm before detection with a micro-channel plate (MCP) combined with a phosphor screen and CCD camera.

STIRAP was performed twice in quick succession using ion bunches to determine the ionization efficiency. The total charge in the first and second bunches, N_1 and N_2 respectively, are related to the efficiency $\mathcal{E}(x,z)$ by

$$N_1 \propto \iiint_V \mathcal{E}(x,z)\,dx\,dy\,dz, \tag{1}$$

$$N_2 \propto \iiint_V \mathcal{E}(x,z)[1-\mathcal{E}(x,z)]\,dx\,dy\,dz, \tag{2}$$

where the spatial dependence of $\mathcal{E}(x,z)$ comes from the intensity profile of the blue laser (the product of two independent Gaussians in x and z), and the interaction volume V is bounded by the size of the infrared laser ($x^2+y^2=R_r^2$). The total volume-averaged efficiency can be determined from the overall charge present:

$$\mathcal{E}_{\text{int}} = 1 - \frac{N_2}{N_1}. \tag{3}$$

This two-pulse method therefore provides a measure of efficiency that is independent of the atomic density, excitation volume and MCP efficiency [25,26] if we assume minimal atomic movement inside the MOT between the two STIRAP events.

$N_{1,2}$ are determined by area integration of the MCP images for pulses $P_{1,2}$ shown in Fig. 2(e). The phosphor screen on the MCP detector has a decay time on the order of milliseconds, too long to be able to temporally separate the signals from the two pulses. Instead, a deflector was used to spatially separate the two bunches. We used a variant on the two-pulse method to remove dependence on the MCP sensitivity, which is not perfectly uniform across the detector. Measurements were made with just the second pulse to give N_1 [Fig. 2(e)(i)], and then at the same location with both pulses spatially separated to determine N_2 [Fig. 2(e)(ii)].

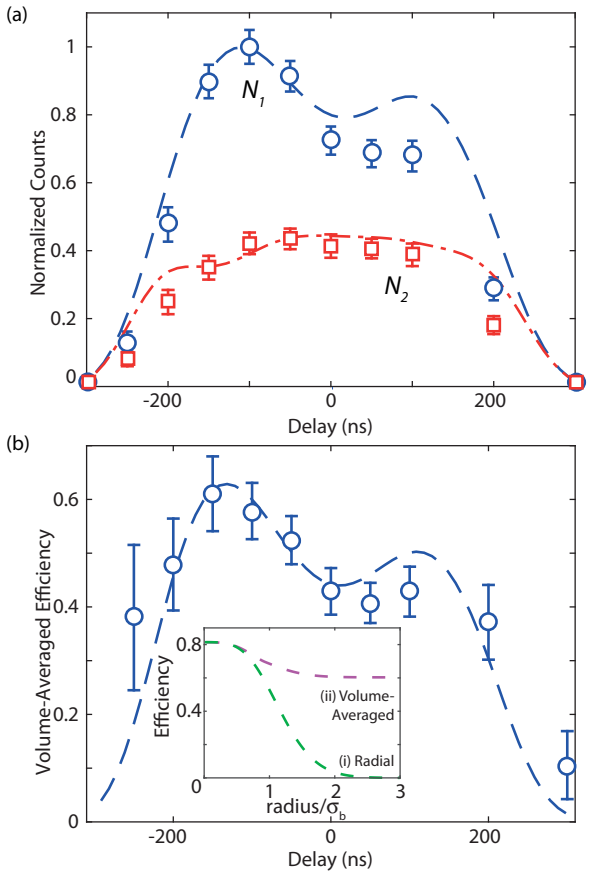

FIG. 3. (a) MCP Counts in first pulse (N_1, blue, circles) and second pulse (N_2, red, squares) as a function of the relative delay between the two excitation fields. Points indicate experimental data, with error bars determined from the standard deviation of 100 images, and lines indicate simulations using 200 ns flattop pulses, peak Rabi frequencies $\Omega_{12}=\Omega_{23}=15$ MHz, laser linewidths $\Gamma_{12}=\Gamma_{23}=500$ kHz, and $\Delta=27$ MHz. (b) Efficiency calculated from the ratio of N_2 to N_1 using Eq. (3). Points indicate experimental data, and lines indicate simulation. The inset shows (i) the calculated radial efficiency and (ii) the volume-averaged efficiency as a function of the blue laser beam radius, normalized to the Gaussian σ_b, at the optimal delay $\delta t=-150$ ns.

III. RESULTS AND ANALYSIS

A. STIRAP efficiency

Figure 3(a) shows the total integrated counts as a function of the delay between the pulses δt. Figure 3(b) shows the volume-averaged efficiency calculated from the relative signals using Eq. (3), with the characteristic high efficiency seen when $\delta t < 0$ (maximum of 60% at $\delta_t=-150$ ns).

Simulations were performed using optical Bloch equations [24] with experimentally realistic parameters (peak Rabi frequencies $\Omega_{12}=\Omega_{23}=15$ MHz, $\Delta=27$ MHz, intermediate state decay rate $\Gamma=6$ MHz, laser linewidths $\gamma_{12}=\gamma_{23}=500$ kHz, for 200 ns rectangular pulses with 100 ns linear rise and fall times). Inset (i) of Fig. 3(b) shows the simulated radial efficiency $\mathcal{E}[r]$ for a blue laser beam with Gaussian electric field profile with an arbitrary $1/e$ width of σ_b. Inset (ii) shows the volume-averaged efficiency $\int_0^r \mathcal{E}[r']\,dr'$ as the radius of integration increases to $\pm r$ in z and either $\pm r$ or $\pm R_r$ in x, whichever is smaller. In the inset we have scaled $\sigma_x=\sigma_z=\sigma_b$ for simplicity and used the fact that $R_r=\sigma_b$. These simulations of the volume-averaged efficiency agree well with the experimental data in Fig. 3. We can therefore infer a peak efficiency for STIRAP in the CAEIS of 82% at the maximum blue intensity. Increasing the blue power would increase the maximum efficiency obtainable. However, with increased intensity comes the possibility of adding random phase and amplitude noise, which can limit the maximum efficiency obtainable [44]. Even without increasing the maximum intensity, for a uniform blue laser profile with intensity such that the Rabi frequency is the same as at the peak of our Gaussian profile, then we expect both volume-averaged and peak efficiencies would be 82%. Nonuniform electric fields within the accelerator region, for example, caused by charged particle accumulation on the electrodes,

will also reduce the coupling strength, broaden the two-photon transition, and reduce the maximum efficiency.

The experimental results show a distinct reduction in signal compared to simulations for $\delta t > 0$. This reduction is the opposite of the increase in signal seen elsewhere [25,26], which was attributed to radiation trapping and Rydberg-Rydberg interactions. We use a large one-photon detuning to avoid absorption of the infrared laser outside the interaction zone. Any background absorption will lead to a large two-photon detuning for the re-radiated light interacting with the off-resonance blue light, causing a reduction in the excitation probability. The accompanying optical pumping of the background atoms into the lower ground state during the first excitation event will reduce the fraction of reradiating atoms for the second event, resulting mainly in a reduction of first pulse counts and, therefore, a reduction in the calculated efficiency.

B. Incoherent excitation efficiency

To quantify the improvement to CAEIS brightness provided by STIRAP, we measured the efficiency of pulsed 480 nm laser ionization using a variant of the two-pulse efficiency method. The pulsed and continuous blue laser beams were overlapped in counterpropagating directions [dashed lines in Fig. 2(a)], perpendicular to the direction of charged particle propagation. The same infrared laser was used for both excitation processes, though the power and detuning were optimized separately for each: on resonance for pulsed-laser excitation and 27 MHz detuned for STIRAP excitation. The accelerator field was applied before pulsed-laser excitation to reproduce "normal" ionization conditions for a CAEIS. N_1 was still defined as the signal for a single STIRAP pulse sequence, and N_2 as the signal for STIRAP excitation following excitation by the pulsed laser. Using this method, the efficiency of the pulsed blue laser as a function of infrared laser intensity and pulsed blue power was measured (Fig. 4).

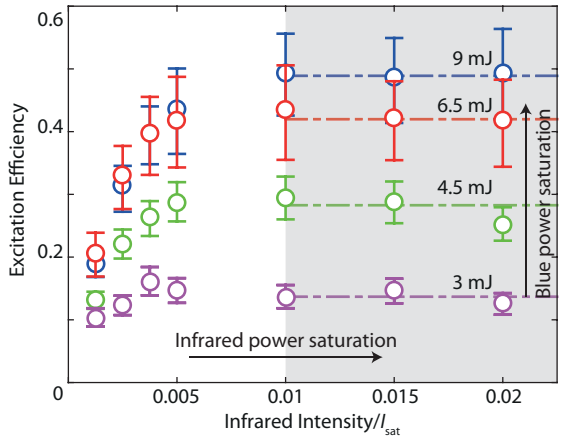

FIG. 4. Pulsed blue ionization efficiency as a function of infrared laser intensity normalized to saturation intensity (I_{sat}) for different blue pulse energies. Numbers indicate the power of the pulsed blue laser, dashed lines show the saturation of ionization efficiency, and shaded region denotes the region where the intermediate state becomes saturated.

The efficiency approaches 50%, the maximum efficiency for incoherent excitation in a two-level system, as infrared laser intensity and pulsed blue energy increase. This limit arises as the blue pulse duration (of order a few nanoseconds) is much faster than the infrared pumping rate, and so the intermediate state will not be refilled on the ionization time scale. Comparing the peak STIRAP excitation to this incoherent excitation peak gives an increase in efficiency by a factor of 60%.

C. Temporal profile

The duration of the electron or ion bunches is an important parameter for most applications of a CAEIS. Coulomb-driven spatial expansion of charged bunches leads to temporal expansion, but the expansion is not significant for electrons because the propagation time from bunch creation to detection is too short. Hence we investigated the temporal bunch shape using a streak method. The electron bunches propagated through deflectors with a rapidly varying transverse potential, causing the bunch to "streak" across the detector, with the position of an electron on the detector being dependent on the time at which it entered the deflector region. The temporal profile of the bunch was then determined from a line profile along the streak, calibrated to the known geometry and time-varying potential difference. The streak measurements are shown in Fig. 5 for bunches created with (a) STIRAP excitation followed by pulsed electric field ionization, and (b) pulsed blue ionization in a constant electric field.

For accelerator fields close to the electric-field ionization threshold of the $28S_{1/2}$ state, a broad secondary peak in the electron temporal distribution can be seen for the STIRAP bunches. This peak could be due to blackbody collisions transferring some atoms to lower energy states with a higher threshold ionization voltage [45]. The appearance of a much narrower secondary peak in both the 5.5 and 7.2 kV results also supports this explanation. Another possibility is nonideal behavior of the high-voltage switch, for example, by fast oscillations in the rising voltage.

The relative pulse heights show that a near-threshold voltage leads to only a small fraction of excited atoms being ionized. Once above the threshold voltage, this fraction approaches one, verified by the detection of only a very weak signal when performing a second electric field ionization pulse after a single STIRAP excitation sequence. The root mean square (RMS) duration of the STIRAP bunches, determined from the streak measurements of Fig. 5(a), was 250 ps, varying only slightly for different accelerator potentials.

With an accelerator rise time on the order of nanoseconds, ionization will be diabatic (hydrogenic). Modeling an accelerator profile on Fig. 2(d), the ionization rate for a "red" state of hydrogen (where Rydberg quantum numbers $m = n_1 = 0$, $n_2 = n - 1$) [46,47] gives an RMS pulse width of 170 ps [Fig. 5(a)], consistent with the initial rise in electron charge seen in the data of Fig. 5(a).

The measured duration of bunches produced with STIRAP excitation and field ionization compares favorably with that for pulsed blue excitation. The bunch duration for incoherent excitation is determined by the temporal profile of the pulsed laser, which has a quoted total pulse length of 5 ns and produces

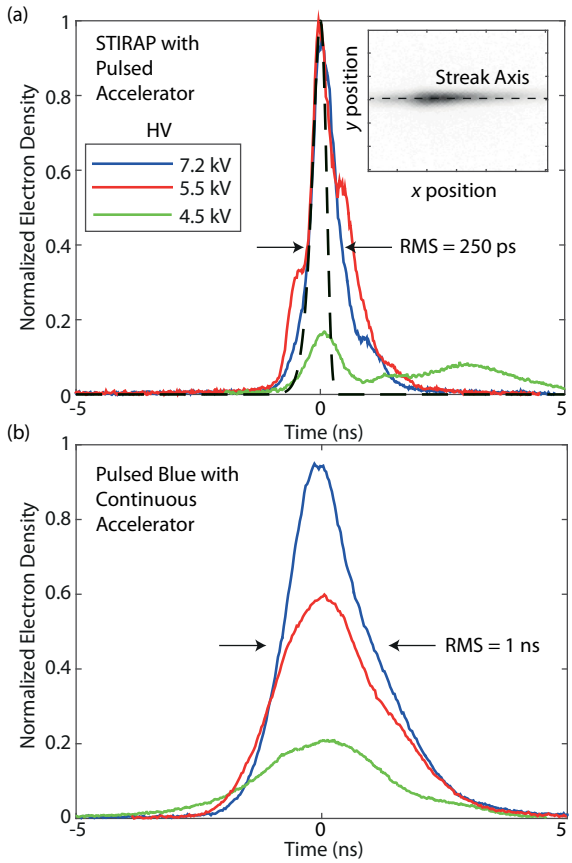

FIG. 5. Streak measurements of electrons created with: (a) STIRAP bunches with pulsed accelerator and (b) pulsed blue laser with continuous accelerator at different accelerator potential differences HV. Inset shows a false-color streaked electron bunch as measured by the MCP. All traces are normalized to the same peak value. Solid lines indicate experimental data, dashed line indicates theory for hydrogenic "red" state with field switching behavior from Fig. 2(d), normalized to height of experimental traces.

bunches with duration of order 1 ns RMS. Ultrafast electron diffraction requires subpicosecond pulses. With accelerator potentials of 30 kV and 30 ns electric field rise times, it has been shown that a bunch length of 80 ps can be achieved [28]. To reduce the bunch duration below 1 ps following STIRAP excitation, the maximum accelerator voltage would need to increase by an order of magnitude, and the switching time reduce to less than 1 ns [1]. Achieving such electric field switching requires careful design of the MOT chamber and accelerator to avoid electrical discharge [28] and a very fast high-voltage switch, potentially using laser-triggered spark gap technology [48]. Alternately, an RF bunch compressor could be used [12].

D. Robustness

The effect of different STIRAP pulse widths w was investigated [Fig. 6(a)]. The robustness of STIRAP excitation is apparent, since a difference in width by a factor of two has very little impact on either the maximum efficiency (50–55%),

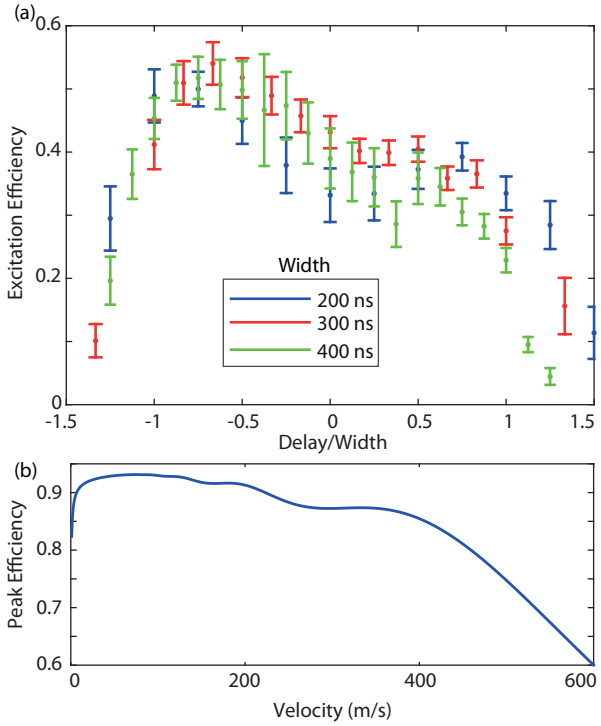

FIG. 6. (a) Efficiency as a function of the ratio of pulse delay δt to flattop pulse width w. (b) Simulated excitation efficiency of STIRAP for an cold atom-beam source, as a function of atomic velocity with $\Omega_{12} = \Omega_{23} = 15$ MHz, $\sigma_z = 15$ μm, and $\delta z = -\sigma_z$.

or the time at which this occurs ($\delta t/w = -0.75$ for the rectangular pulses used).

The robustness of STIRAP makes it ideally suited to next-generation cold-atom ion sources based on atomic beams [36–39]. The experimental situation described above, where atoms are stationary and the optical and electric fields are dynamic, is equivalent to an atomic beam system with atoms moving through spatially separated static optical fields and a region with an electric field gradient. The high temperature of the atoms along the direction of propagation will result in a large velocity spread. For instance, an experimentally practical atom beam temperature of 200 °C would lead to a most-probable velocity of $v_{zp} = 305$ m s^{-1} with standard deviation of 150 m s^{-1}. The different velocities of the atoms are equivalent to a static atom seeing STIRAP fields with different temporal widths but a constant $\delta t/w$. Figure 6(b) shows the peak efficiency calculated for such a system with Gaussian laser beam spatial profiles with $\sigma_z = 15$ μm and $\delta z = -\sigma_z$. The efficiency remains above 80% from 0 to 400 m s^{-1}, so that a large proportion of the atomic population (66%) will be excited with high efficiency.

High ion beam densities achieved using STIRAP excitation could lead to Coulomb explosion and a reduction in the focusability of the source. The density could be reduced by using Rydberg blockade with high principle quantum number $n \approx 100$ [23]. If the excitation volume is reduced to below one blockade radius, it will become possible to isolate separate ions spatially and temporally to create a quasideterministic highly focusable single ion source with heralding provided by the liberated electrons [34,35].

IV. CONCLUSIONS

We have shown that STIRAP can improve the excitation efficiency of a cold-atom electron and ion source by a factor of 1.6, from a peak efficiency of 50% with incoherent excitation, to 82%. Further improvements are expected with higher laser power, greater uniformity of the electric field within the excitation region, and reduced phase noise in the excitation lasers.

We have also shown that STIRAP excitation and fast switching of the ionization electric field produces bunches with an RMS duration of 250 ps. Subpicosecond bunches may be achievable with higher acceleration potentials and faster switching, and with an RF compressor, to satisfy the temporal criterion for imaging dynamic processes with atomic spatial and temporal resolution using ultrafast electron diffraction.

With continuous lasers and an atomic beam, STIRAP excitation will be directly applicable to next-generation continuous atom-beam based cold-electron and ion sources. Finally, by using high efficiency STIRAP excitation to reach higher Rydberg states, the phenomena of Rydberg blockade could be used to create spatial ordering, and therefore reduce the temperature and increase the focusability of the bunches, as well as enabling a new approach to creating a deterministic single ion source.

ACKNOWLEDGMENTS

B.M.S. gratefully acknowledges the support of a University of Melbourne McKenzie Fellowship. This work was supported by the Australian Research Council Discovery Project DP140102102.

[1] B. J. Claessens, S. B. van der Geer, G. Taban, E. J. D. Vredenbregt, and O. J. Luiten, Ultracold Electron Source, Phys. Rev. Lett. **95**, 164801 (2005).

[2] B. J. Claessens, M. P. Reijnders, G. Taban, O. J. Luiten, and E. J. D. Vredenbregt, Cold electron and ion beams generated from trapped atoms, Phys. Plasmas **14**, 093101 (2007).

[3] A. J. McCulloch, D. V. Sheludko, S. D. Saliba, S. C. Bell, M. Junker, K. A. Nugent, and R. E. Scholten, Arbitrarily shaped high-coherence electron bunches from cold atoms, Nature Phys. **7**, 785 (2011).

[4] W. J. Engelen, M. A. van der Heijden, D. J. Bakker, E. J. D. Vredenbregt, and O. J. Luiten, High-coherence electron bunches produced by femtosecond photoionization, Nature Comm. **4**, 1693 (2013).

[5] J. L. Hanssen, S. B. Hill, J. Orloff, and J. J. McClelland, Magneto-optical-trap-based, high brightness ion source for use as a nanoscale probe, Nano Lett. **8**, 2844 (2008).

[6] A. V. Steele, B. Knuffman, J. J. McClelland, and J. Orloff, Focused chromium ion beam, J. Vac. Sci. Technol. B **28**, C6F1 (2010).

[7] J. R. Dwyer, C. T. Hebeisen, R. Ernstorfer, M. Harb, V. B. Deyirmenjian, R. E. Jordan, and R. J. D. Miller, Femtosecond electron diffraction: 'making the molecular movie', Philosophical Transactions. Series A, Mathematical, Physical, and Engineering Sciences **364**, 741 (2006).

[8] B. J. Siwick, J. R. Dwyer, R. E. Jordan, R. J. D. Miller, R. S. Dwyer, R. E. Jordan, and R. J. D. Miller, An atomic-level view of melting using femtosecond electron diffraction, Science **302**, 1382 (2003).

[9] M. Harb, R. Ernstorfer, C. T. Hebeisen, G. Sciaini, W. Peng, T. Dartigalongue, M. A. Eriksson, M. G. Lagally, S. G. Kruglik, and R. J. D. Miller, Electronically Driven Structure Changes of Si Captured by Femtosecond Electron Diffraction, Phys. Rev. Lett. **100**, 155504 (2008).

[10] G. Sciaini, M. Harb, S. G. Kruglik, T. Payer, C. T. Hebeisen, F.-J. M. Z. Heringdorf, M. Yamaguchi, M. H. von Hoegen, R. Ernstorfer, and R. J. D. Miller, Electronic acceleration of atomic motions and disordering in bismuth, Nature (London) **458**, 56 (2009).

[11] S. Tokita, S. Inoue, S. Masuno, M. Hashida, and S. Sakabe, Single-shot ultrafast electron diffraction with a laser-accelerated sub-MeV electron pulse, Appl. Phys. Lett. **95**, 111911 (2009).

[12] T. van Oudheusden, P. L. E. M. Pasmans, S. B. van der Geer, M. J. de Loos, M. J. van der Wiel, and O. J. Luiten, Compression of Subrelativistic Space-Charge-Dominated Electron Bunches for Single-Shot Femtosecond Electron Diffraction, Phys. Rev. Lett. **105**, 264801 (2010).

[13] T. Ishikawa, S. A. Hayes, S. Keskin, G. Corthey, M. Hada, K. Pichugin, A. Marx, J. Hirscht, K. Shionuma, K. Onda, Y. Okimoto, S.-Y. Koshihara, T. Yamamoto, H. Cui, M. Nomura, Y. Oshima, M. Abdel-Jawad, R. Kato, and R. J. D. Miller, Direct observation of collective modes coupled to molecular orbital-driven charge transfer, Science **350**, 1501 (2015).

[14] H. N. Chapman, A. Barty, M. J. Bogan, S. Boutet, M. Frank, S. P. Hau-Riege, S. Marchesini, B. W. Woods, S. Bajt, W. H. Benner, R. A. London, E. Plönjes, M. Kuhlmann, R. Treusch, S. Düsterer, T. Tschentscher, J. R. Schneider, E. Spiller, T. Möller, C. Bostedt *et al.*, Femtosecond diffractive imaging with a soft-x-ray free-electron laser, Nature Phys. **2**, 839 (2006).

[15] H. N. Chapman, P. Fromme, A. Barty, T. A. White, R. A. Kirian, A. Aquila, M. S. Hunter, J. Schulz, D. P. DePonte, U. Weierstall, R. B. Doak, F. R. N. C. Maia, A. V. Martin, I. Schlichting, L. Lomb, N. Coppola, R. L. Shoeman, S. W. Epp, R. Hartmann, D. Rolles, A. Rudenko, L. Foucar, N. Kimmel, G. Weidenspointner, P. Holl, M. Liang, M. Barthelmess, C. Caleman, S. Boutet, M. J. Bogan, J. Krzywinski, C. Bostedt, S. Bajt, L. Gumprecht, B. Rudek, B. Erk, C. Schmidt, A. Hömke, C. Reich, D. Pietschner, L. Strüder, G. Hauser, H. Gorke, J. Ullrich, S. Herrmann, G. Schaller, F. Schopper, H. Soltau, K.-U. Kühnel, M. Messerschmidt, J. D. Bozek, S. P. Hau-Riege, M. Frank, C. Y. Hampton, R. G. Sierra, D. Starodub, G. J. Williams, J. Hajdu, N. Timneanu, M. M. Seibert, J. Andreasson, A. Rocker, O. Jönsson, M. Svenda, S. Stern, K. Nass, R. Andritschke, C.-D. Schröter, F. Krasniqi, M. Bott, K. E. Schmidt, X. Wang, I. Grotjohann, J. M. Holton, T. R. M. Barends, R. Neutze, S. Marchesini, R. Fromme, S. Schorb, D. Rupp, M. Adolph, T. Gorkhover, I. Andersson, H. Hirsemann, G. Potdevin,

H. Graafsma, B. Nilsson, and J. C. H. Spence, Femtosecond x-ray protein nanocrystallography, Nature (London) **470**, 73 (2011).

[16] M. M. Seibert, T. Ekeberg, F. R. N. C. Maia, M. Svenda, J. Andreasson, O. Jönsson, D. Odić, B. Iwan, A. Rocker, D. Westphal, M. Hantke, D. P. DePonte, A. Barty, J. Schulz, L. Gumprecht, N. Coppola, A. Aquila, M. Liang, T. A. White, A. Martin, C. Caleman, S. Stern, C. Abergel, V. Seltzer, J.-M. Claverie, C. Bostedt, J. D. Bozek, S. Boutet, A. A. Miahnahri, M. Messerschmidt, J. Krzywinski, G. Williams, K. O. Hodgson, M. J. Bogan, C. Y. Hampton, R. G. Sierra, D. Starodub, I. Andersson, S. Bajt, M. Barthelmess, J.C. H. Spence, P. Fromme, U. Weierstall, R. Kirian, M. Hunter, R. B. Doak, S. Marchesini, S. P. Hau-Riege, M. Frank, R. L. Shoeman, L. Lomb, S. W. Epp, R. Hartmann, D. Rolles, A. Rudenko, C. Schmidt, L. Foucar, N. Kimmel, P. Holl, B. Rudek, B. Erk, A. Hömke, C. Reich, D. Pietschner, G. Weidenspointner, L. Strüder, G. Hauser, H. Gorke, J. Ullrich, I. Schlichting, S. Herrmann, G. Schaller, F. Schopper, H. Soltau, K.-U. Kühnel, R. Andritschke, C.-D. Schröter, F. Krasniqi, M. Bott, S. Schorb, D. Rupp, M. Adolph, T. Gorkhover, H. Hirsemann, G. Potdevin, H. Graafsma, B. Nilsson, H. N. Chapman, and J. Hajdu, Single mimivirus particles intercepted and imaged with an x-ray laser, Nature (London) **470**, 78 (2011).

[17] S. Boutet, L. Lomb, G. J. Williams, T. R. M. Barends, A. Aquila, R. B. Doak, U. Weierstall, D. P. Deponte, J. Steinbrener, R. L. Shoeman, M. Messerschmidt, A. Barty, T. A. White, S. Kassemeyer, R. A. Kirian, M. M. Seibert, P. A. Montanez, C. Kenney, R. Herbst, P. Hart, J. Pines, G. Haller, S. M. Gruner, H. T. Philipp, M. W. Tate, M. Hromalik, L. J. Koerner, N. Van Bakel, J. Morse, W. Ghonsalves, D. Arnlund, K. Nass, L. Redecke, F. Stellato, N. Timneanu, D. Wang, J. C. H. Spence, H. N. Chapman, and I. Schlichting, High-resolution protein structure determination by serial femtosecond crystallography, Science **337**, 362 (2012).

[18] T. Kimura, Y. Joti, A. Shibuya, C. Song, S. Kim, K. Tono, M. Yabashi, M. Tamakoshi, T. Moriya, T. Oshima, T. Ishikawa, Y. Bessho, and Y. Nishino, Imaging live cell in micro-liquid enclosure by x-ray laser diffraction, Nature Comm. **5**, 3052 (2014).

[19] C. Kupitz, S. Basu, I. Grotjohann, R. Fromme, N. A. Zatsepin, K. N. Rendek, M. S. Hunter, R. L. Shoeman, T. A. White, D. Wang, D. James, J.-H. Yang, D. E. Cobb, B. Reeder, R. G. Sierra, H. Liu, A. Barty, A. L. Aquila, D. Deponte, R. A. Kirian *et al.*, Serial time-resolved crystallography of photosystem II using a femtosecond x-ray laser, Nature (London) **513**, 261 (2014).

[20] P. Nogly, I. Gushchin, A. Remeeva, A. M. Esteves, N. Borges, P. Ma, A. Ishchenko, S. Grudinin, E. Round, I. Moraes, V. Borshchevskiy, H. Santos, V. Gordeliy, and M. Archer, X-ray structure of a CDP-alcohol phosphatidyltransferase membrane enzyme and insights into its catalytic mechanism, Nature Comm. **5**, 4169 (2014).

[21] O. J. Luiten, B. J. Claessens, S. B. Van Der Geer, M. P. Reijnders, G. Taban, and E. J. D. Vredenbregt, Ultracold electron sources, Int. J. Mod. Phys. A **22**, 3882 (2007).

[22] K. Bergmann, H. Theuer, and B. W. Shore, Coherent population transfer among quantum states of atoms and molecules, Rev. Mod. Phys. **70**, 1003 (1998).

[23] R. Löw, H. Weimer, J. Nipper, J. B. Balewski, B. Butscher, H. P. Büchler, and T. Pfau, An experimental and theoretical guide to strongly interacting Rydberg gases, J. Phys. B **45**, 113001 (2012).

[24] S. Sevinçli, C. Ates, T. Pohl, H. Schempp, C. S. Hofmann, G. Günter, T. Amthor, M. Weidemüller, J. D. Pritchard, D. Maxwell, A. Gauguet, K. J. Weatherill, M. P. A. Jones, and C. S. Adams, Quantum interference in interacting three-level Rydberg gases: Coherent population trapping and electromagnetically induced transparency, J. Phys. B **44**, 184018 (2011).

[25] T. Cubel, B. Teo, V. Malinovsky, J. Guest, A. Reinhard, B. Knuffman, P. Berman, and G. Raithel, Coherent population transfer of ground-state atoms into Rydberg states, Phys. Rev. A **72**, 023405 (2005).

[26] J. Deiglmayr, M. Reetz-Lamour, T. Amthor, S. Westermann, A. L. de Oliveira, and M. Weidemüller, Coherent excitation of Rydberg atoms in an ultracold gas, Opt. Commun. **264**, 293 (2006).

[27] T. Takekoshi, L. Reichsöllner, A. Schindewolf, J. M. Hutson, C. R. Le Sueur, O. Dulieu, F. Ferlaino, R. Grimm, and H.-C. Nägerl, Ultracold Dense Samples of Dipolar RbCs Molecules in the Rovibrational and Hyperfine Ground State, Phys. Rev. Lett. **113**, 205301 (2014).

[28] G. Taban, M. P. Reijnders, S. C. Bell, S. B. van der Geer, O. J. Luiten, and E. J. D. Vredenbregt, Design and validation of an accelerator for an ultracold electron source, Phys. Rev. ST Accel. Beams **11**, 050102 (2008).

[29] A. J. McCulloch, D. V. Sheludko, M. Junker, and R. E. Scholten, High-coherence picosecond electron bunches from cold atoms, Nature Comm. **4**, 1692 (2013).

[30] M. S. Murillo, Using Fermi Statistics to Create Strongly Coupled Ion Plasmas in Atom Traps, Phys. Rev. Lett. **87**, 115003 (2001).

[31] S. Kuzmin and T. O'Neil, Numerical simulation of ultracold plasmas: How rapid intrinsic heating limits the development of correlation, Phys. Rev. Lett. **88**, 065003 (2002).

[32] D. Murphy, R. E. Scholten, and B. M. Sparkes, Increasing the Brightness of Cold Ion Beams by Suppressing Disorder-Induced Heating with Rydberg Blockade, Phys. Rev. Lett. **115**, 214802 (2015).

[33] M. Saffman, T. G. Walker, and K. Mølmer, Quantum information with Rydberg atoms, Rev. Mod. Phys. **82**, 2313 (2010).

[34] I. I. Beterov, D. B. Tretyakov, V. M. Entin, E. A. Yakshina, I. I. Ryabtsev, C. MacCormick, and S. Bergamini, Deterministic single-atom excitation via adiabatic passage and Rydberg blockade, Phys. Rev. A **84**, 023413 (2011).

[35] C. Ates, I. Lesanovsky, C. S. Adams, and K. J. Weatherill, Fast and Quasideterministic Single Ion Source from a Dipole-Blockaded Atomic Ensemble, Phys. Rev. Lett. **110**, 213003 (2013).

[36] L. Kime, A. Fioretti, Y. Bruneau, N. Porfido, F. Fuso, M. Viteau, G. Khalili, N. Šantić, A. Gloter, B. Rasser, P. Sudraud, P. Pillet, and D. Comparat, High-flux monochromatic ion and electron beams based on laser-cooled atoms, Phys. Rev. A **88**, 033424 (2013).

[37] B. Knuffman, A. V. Steele, and J. J. McClelland, Cold atomic beam ion source for focused ion beam applications, J. Appl. Phys. **114**, 044303 (2013).

[38] G. ten Haaf, S. H. W. Wouters, S. B. van der Geer, E. J. D. Vredenbregt, and P. H. A. Mutsaers, Performance predictions of a focused ion beam from a laser cooled and compressed atomic beam, J. Appl. Phys. **116**, 244301 (2014).

[39] S. H. W. Wouters, G. ten Haaf, R. P. M. J. W. Notermans, N. Debernardi, P. H. A. Mutsaers, O. J. Luiten, and E. J. D. Vredenbregt, Performance predictions for a laser-intensified thermal beam for use in high-resolution focused-ion-beam instruments, Phys. Rev. A **90**, 063817 (2014).

[40] M. Viteau, M. Reveillard, L. Kime, B. Rasser, P. Sudraud, Y. Bruneau, G. Khalili, P. Pillet, D. Comparat, I. Guerri, A. Fioretti, D. Ciampini, M. Allegrini, and F. Fuso, Ion microscopy based on laser-cooled cesium atoms, Ultramicroscopy **164**, 70 (2016).

[41] S. D. Saliba, C. T. Putkunz, D. V. Sheludko, A. J. Mcculloch, K. A. Nugent, and R. E. Scholten, Spatial coherence of electron bunches extracted from an arbitrarily shaped cold atom electron source, Opt. Express **20**, 3967 (2012).

[42] D. Murphy, R. W. Speirs, D. V. Sheludko, C. T. Putkunz, A. J. McCulloch, B. M. Sparkes, and R. E. Scholten, Detailed observation of spacecharge dynamics using ultracold ion bunches, Nature Comm. **5**, 4489 (2014).

[43] R. W. Speirs, C. T. Putkunz, A. J. McCulloch, K. A. Nugent, B. M. Sparkes, and R. E. Scholten, Single-shot electron diffraction using a cold atom electron source, J. Phys. B **48**, 214002 (2015).

[44] L. P. Yatsenko, B. W. Shore, and K. Bergmann, Detrimental consequences of small rapid laser fluctuations on stimulated Raman adiabatic passage, Phys. Rev. A **89**, 013831 (2014).

[45] T. Wang, S. F. Yelin, R. Côté, E. E. Eyler, S. M. Farooqi, P. L. Gould, M. Koštrun, D. Tong, and D. Vrinceanu, Superradiance in ultracold Rydberg gases, Phys. Rev. A **75**, 033802 (2007).

[46] N. Hoe, B. D'etat, and G. Coulaud, Electric field ionization rate of the hydrogen atom, Phys. Lett. A **85**, 327 (1981).

[47] R. J. Damburg and V. V. Kolosov, A hydrogen atom in a uniform electric field. III, J. Phys. B **12**, 2637 (1979).

[48] G. J. H. Brussaard and J. Hendriks, Photoconductive operation of a laser triggered spark gap, IEEE Trans. Dielectr. Electr. Insul. **14**, 976 (2007).

Suppression of Emittance Growth Using a Shaped Cold Atom Electron and Ion Source

D. J. Thompson,[1] D. Murphy,[1] R. W. Speirs,[1] R. M. W. van Bijnen,[2] A. J. McCulloch,[1] R. E. Scholten,[1,*] and B. M. Sparkes[1]
[1]*School of Physics, The University of Melbourne, Victoria 3010, Australia*
[2]*Eindhoven University of Technology, P.O. Box 513, 5600 MB Eindhoven, The Netherlands*
(Received 20 May 2016; published 3 November 2016)

We demonstrate precise control of charged particle bunch shape with a cold atom electron and ion source to create bunches with linear and, therefore, reversible Coulomb expansion. Using ultracold charged particles enables detailed observation of space-charge effects without loss of information from thermal diffusion, unambiguously demonstrating that shaping in three dimensions can result in a marked reduction of Coulomb-driven emittance growth. We show that the emittance growth suppression is accompanied by an increase in bunch focusability and brightness, improvements necessary for the development of sources capable of coherent single-shot ultrafast electron diffraction of noncrystalline objects, with applications ranging from femtosecond chemistry to materials science and rational drug design.

DOI: 10.1103/PhysRevLett.117.193202

The elimination of Coulomb-driven emittance growth is crucial for the development of high brightness charged particle beam sources for high-energy accelerator injection [1], high-brightness x-ray sources [2], electron and ion microscopy [3,4], and ultrafast electron diffraction (UED) [5]. Single-shot UED experiments in particular require high bunch charge and short bunch duration, conditions that result in severe Coulomb-driven expansion [6,7]. For bunches with nonuniform charge density, the expansion leads to emittance growth and reduced bunch brightness and focusability. Overcoming Coulomb-driven emittance growth is, therefore, a key step towards achieving advances across fields ranging from femtosecond chemistry [8] to rational drug design [9,10] and materials science [5].

Uniformly filled three-dimensional (3D) ellipsoidal distributions, which have linear internal Coulomb fields, are ideal for the preservation of low emittance and high bunch brightness [11,12] because the bunch expansion can be fully reversed using linear electron optics. Three-dimensional ellipsoidal bunches have been created in thermal photocathode electron sources by using 2D laser pulse-shaping techniques to create "pancake" electron bunches which have a half-spherical transverse radial density profile. Provided the longitudinal profile is much narrower than the transverse radius, a pancake bunch will evolve into a uniformly filled ellipsoid under Coulomb-driven expansion [13]. The expansion properties of ellipsoidal bunches have been measured experimentally with photocathode sources [14–19], but demonstrating improved beam brightness has not been possible due to the inherently high electron temperature ($T > 1000$ K). At such temperatures, thermal diffusion quickly destroys the spatial structure of the bunch, preventing detailed observation of the effects of space-charge repulsion. High temperature also limits the initial bunch coherence, focusability and brightness of an electron source.

Cold atom electron and ion sources (CAEISs) are being developed [20–23] with the promise of orders of magnitude improvement in these key bunch metrics. The CAEIS is based on the photoionization of a laser-cooled atomic gas with two overlapping orthogonal laser beams, producing electrons and ions with low temperatures (10 K [21] and 1 mK [24], respectively), and correspondingly low emittance, high brightness, and high coherence. The initial charge distribution can be controlled by manipulating the laser beam profiles [21], allowing for full 3D shaping of the charged particle bunches at the optical resolution limit of a few micrometers [25]. Using this precise shaping ability to produce cold uniform ellipsoidal bunches is an important step towards creating a source capable of single-shot ultrafast coherent diffraction imaging of noncrystalline targets [26].

In this Letter, we describe experiments that demonstrate suppression of space-charge induced emittance growth for improved focusability and brightness, using shaped charged particle bunches from a CAEIS. Cold ions were used rather than electrons because their much lower temperature, and hence, negligible thermal diffusion, enhances the visibility of space-charge dynamics. In a CAEIS, measurements of the charge distribution for nanosecond duration ion bunches are directly analogous to picosecond electron bunches, because the heavier ion bunches disperse much more slowly than low-mass electrons within the accelerator region, retaining their high charge density and, therefore, exhibiting much stronger space-charge effects [27].

We quantify the beam expansion in terms of emittance, a measure of the phase-space volume occupied by the bunch, where low beam emittance corresponds to the desirable characteristics of high focusability and brightness. In thermal equilibrium, the transverse emittance can be defined along an axis x transverse to the beam propagation direction z, as

$$\epsilon_x = \sigma_x \sqrt{\frac{k_B T_x}{mc^2}}, \quad (1)$$

where σ_x is the root mean square (rms) beam width, k_B is the Boltzmann constant, m is the mass of the beam particles, and c is the speed of light. The axial particle temperature can be defined as $T_x = m\sigma_{v_x}^2(1 - R_{x,v_x}^2)/k_B$, where σ_{v_x} is the rms velocity in the x axis and R_{x,v_x} is the correlation coefficient measuring the linearity of the particle position x and velocity v_x phase-space profile. Nonlinear space-charge forces cause distortion of the beam phase-space profile, increasing beam emittance. The normalized transverse beam brightness $\mathcal{B}_{n\perp}$ varies as ϵ_x^{-2}; hence, a reduction in the emittance will lead to an increase in the transverse beam brightness.

Ion bunches were created via two-color, near-threshold photoionization of an ensemble of rubidium atoms cooled to a temperature of 100 μK in a magneto-optical trap (see Fig. 1). The cloud of cold atoms had a Gaussian spatial density profile with a standard deviation of 500 μm and peak density of 3.0×10^{16} atoms m^{-3}. A 780 nm wavelength laser beam was used to excite atoms from the $5S_{1/2}$ ground state to the $5P_{3/2}$ excited state for 500 ns, with a transverse intensity profile shaped by a spatial-light modulator (SLM). Beam shaping was performed with a speckle-free protocol based on iterative feedback [25]. Atoms in the excited state were coupled to the ionization continuum with a 480 nm wavelength, 5 mJ, 5 ns laser pulse propagating through the atom cloud perpendicular to the excitation beam. The ionization beam was focused to a narrow ribbon at the cold atom cloud with rms intensity widths $\sigma_z = 15$ μm along the longitudinal direction of ion propagation and $\sigma_y > 1$ mm in the axis perpendicular to both the excitation and ionization laser propagation directions. The two-color ionization process produced ion bunches that initially had a very narrow longitudinal distribution compared to the length of the accelerator region (50 mm), ensuring that the longitudinal energy spread was only a few eV. Provided the intensity of the excitation laser beam is below the saturation intensity of the $5S \rightarrow 5P$ transition, the transverse excited atomic density profile $\rho_e(r)$ is proportional to $\Omega_e(r)$, the Rabi frequency for the driven transition. Control of the bunch charge was achieved by altering the excitation laser beam power and, thus, the overall population of the intermediate state prior to ionization by the 480 nm laser. The duration of the ion bunches was determined by the 480 nm laser pulse length

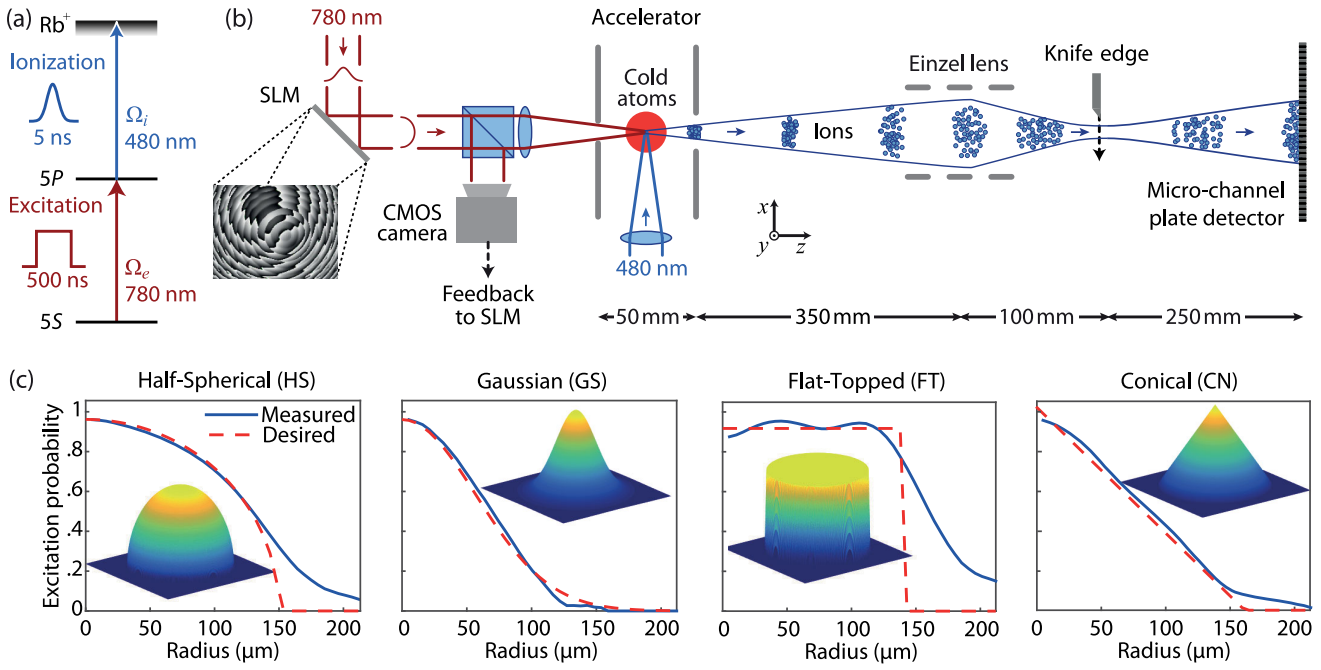

FIG. 1. (a) Two-color laser excitation scheme used to ionize laser-cooled ^{85}Rb atoms. (b) Cold atom electron and ion source with bunch shaping. The intensity profile of the excitation laser coupling the $5S$ ground state to the $5P$ intermediate state was shaped using a spatial-light modulator (SLM) with iterative feedback provided via a CMOS camera [25]. Atoms were ionized with a 5 ns pulsed blue laser, focused to a narrow ribbon perpendicular to the excitation laser. The ions were accelerated into a drift region and focused with an einzel lens. A knife edge was inserted into the bunch around the focus to determine the transverse focal spot width. Spatial bunch profiles and bunch charges were measured with a phosphor-coupled microchannel plate (MCP) detector combined with a CCD camera (not shown). (c) Measured radially averaged excitation laser profiles (solid lines) and desired profiles (dashed lines), plotted as the relative excitation probability. Insets show desired transverse bunch density profiles as shaded false-color renderings. All radial averages and density profiles are individually normalized.

(5 ns), analogous to an electron bunch duration of 13 ps [27].

To investigate the effect of transverse bunch shape on emittance growth, we studied four bunch distributions: half-spherical (HS), required to make pancake bunches; Gaussian (GS), i.e., an "unshaped" laser beam; flat-topped (FT), a uniform transverse profile with complementary application to pancake distributions [28]; and conical (CN), chosen as an example of a nonideal distribution. The excitation laser intensity profile $I_e(r) \propto \Omega_e^2$ was controlled by the SLM to create each initial transverse bunch distribution. Radial distributions of the excitation probability shown in Fig. 1(c) were calculated from each measured laser intensity profile. There was generally good agreement between the measured and desired distributions, with some loss of definition at the edges of the flat-topped and half-spherical distributions.

We initially studied the expansion of the shaped ion bunches for free propagation. Ion bunches with a range of charge densities were accelerated to 6 keV and propagated 700 mm to the detector where the transverse particle distributions were measured using a phosphor-coupled microchannel-plate (MCP) and camera. The initial radius encompassing 95% of the charge was $r_{95} = 139$ μm for all distributions, satisfying $r_{95} \gg \sigma_z$ required for the HS distribution to create a pancake bunch. Figure 2(a) shows the final transverse bunch distributions for ion numbers $N = 2.0 \times 10^3$, where there is negligible space-charge expansion, and $N = 7.1 \times 10^4$, where the growth is dominated by space-charge expansion. For higher charge, all distributions obtain a dense ring structure due to scattered 780 nm light absorbed by atoms outside the interaction region. These atoms were subsequently ionized by the 480 nm light pulse, creating a diffuse halo of electrons. The core ion bunch will expand much faster than the halo due to its higher charge density, resulting in transverse velocity bunching at the edges [27].

Bunches with linear space-charge forces undergo self-similar expansion, where the beam charge density profile is magnified by a single scaling factor. To assess the self-similarity of the CAEIS bunch expansion, we measured the transverse radii containing 50%, 75%, 90%, and 95% of the bunch charge for the different distributions at the detector. We then took the ratio of these radii to their initial values from the laser distribution to obtain the expansion factors denoted e_{50}, e_{75}, e_{90}, and e_{95} [Fig. 2(b)].

At low ion numbers, bunch expansion is mainly determined by lensing in the accelerator structure such that all shapes show approximately equal linear expansion by a factor of 20. As the ion number increases, and space-charge effects become more significant, the central radii expansion factors e_{50} and e_{75} of the GS and CN distributions increase more than the factors for the outer radii (e_{90} and e_{95}) due to the large initial central densities. The opposite behavior is true for the FT, with e_{50} and e_{75} increasing above e_{90} and

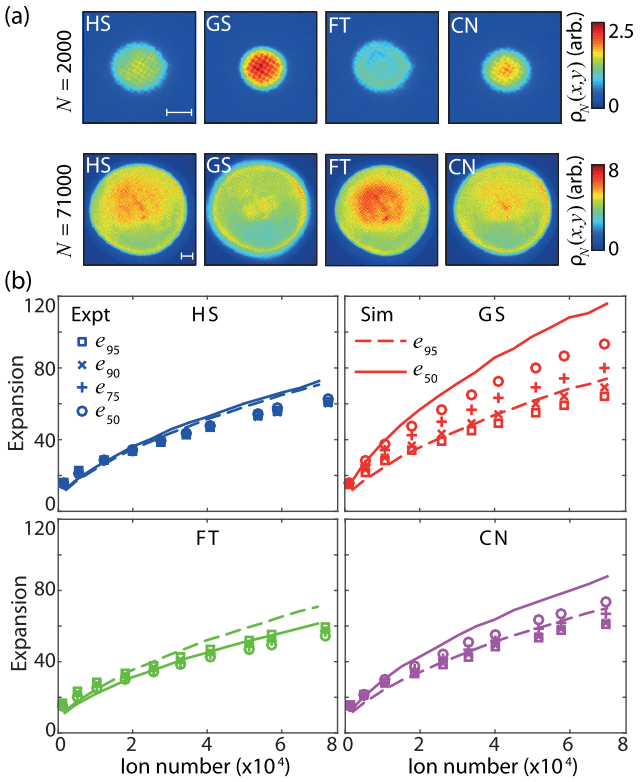

FIG. 2. (a) Experimentally measured transverse ion beam density profiles $\rho_N(x, y)$ for ion number $N = 2\,000$ and 71 000, for HS, GS, FT, and CN initial distributions (scale bar, 2 mm). (b) Radial expansion factors against ion number for each shape individually, with circle, plus, times, and square corresponding to the transverse radii containing 50%, 75%, 90%, and 95% of the bunch charge, respectively. The divergence of the expansion factors at high ion numbers indicate nonlinear space-charge forces, most prevalent in the GS and CN bunches. Simulated expansion factors e_{95} (dashed lines) and e_{50} (solid lines) for each shape are also shown. Measured radii are averaged from 100 ion bunches.

e_{95}, due to the lower initial central density. For the HS initial distribution, the expansion factors remain equal as the ion number increases, signifying linear self-similar space-charge expansion and formation of the desired uniform ellipsoid [13,29].

We simulated the acceleration, propagation, and expansion of the ion bunches using particle tracking software [30] for ideal spatial and measured temporal profiles, and an initial ion temperature of 1 mK. From these simulations, we extracted the expected expansion factors shown in Fig. 2(b). The simulations agree well with the experimental data, especially for the HS distribution. The smaller expansion of the experimental bunches at higher charge is attributed to the ions in the halo discussed earlier, which contribute to the measured ion number but not to the space-charge expansion. The greater deviation seen for the highly peaked GS and CN

distributions could also indicate saturation of the $5S \rightarrow 5P$ transition in the center.

At a beam waist, the transverse emittance [Eq. (1)] is the product of beam width and angular divergence. Measurement of the focal spot width for beams with different initial distributions, therefore, provides a measure of their relative emittance. To investigate the space-charge-induced emittance growth, an einzel lens situated 350 mm from the accelerator was used to focus the expanding bunches. The same transverse rms bunch width $\sigma_x = \sigma_y = 67\ \mu$m was used for all distributions to allow direct emittance comparison. A knife edge was scanned transversely through the propagating bunches at a range of z locations approximately 100 mm from the einzel lens. The rms width $\sigma_r(z)$ was determined from a fit of each profile to an error function (erf) [Fig. 3(a)]. The minimum focused bunch width σ_f was found from a parabolic fit of $\sigma_r(z)$ [Fig. 3(b)].

Figure 3(c) shows how σ_f varies for the different initial spatial distributions as the total ion number increases. The

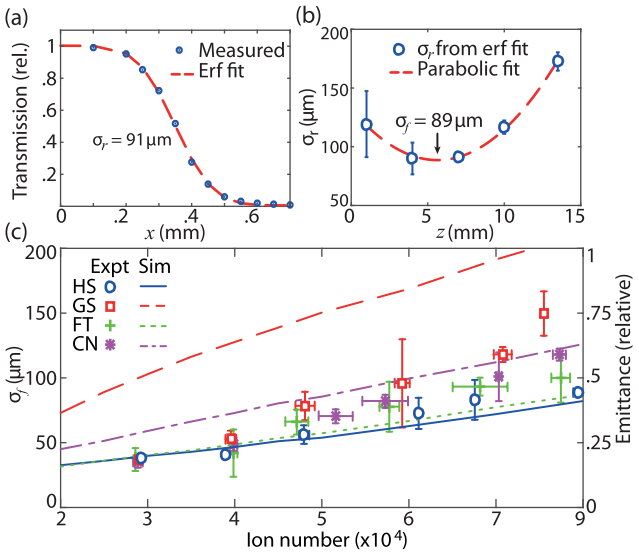

FIG. 3. (a) Example knife-edge plot of relative transmission (points) and erf fit (dashed line) to determine the transverse rms width σ_r at a given z position. (b) Example z scan of knife-edge transmission around the focus. Points indicate the knife-edge measurement and the dashed line is a weighted parabolic fit to determine the minimum rms width σ_f. Error bars are 95% confidence intervals determined from the fit in (a). (c) Experimentally measured minimum rms width (left-hand axis, points) and simulated emittance of freely expanding bunches (right-hand axis, lines) as a function of ion number for the four transverse spatial profiles: HS (blue, circles, solid line), GS (red, squares, dashed line), FT (green, crosses, dotted line), and CN (purple, stars, dashed-dotted line). Uncertainty in ion number is determined from standard deviation of ion numbers from all knife-edge measurements used to determine $\sigma_f(z)$, uncertainty in σ_f is determined from standard error of fitted parabolas in (b). Ion temperature for simulations was taken to be $T = 1$ mK.

GS and CN distributions, which demonstrated the most nonlinear growth in Fig. 2(c), show the greatest increase in emittance with bunch charge, while the linearly expanding HS distribution demonstrates the smallest increase as expected. Aperturing of the bunches in the accelerator structure limited the maximum number of ions to $N = 8 \times 10^4$, where we observe a 50% reduction in focused bunch width and, therefore, transverse emittance for the HS compared to GS distributions.

Particle tracking simulations of the free-expansion emittance for the four distributions exhibit the same behavior, though with a greater variation between the distributions. The greatest deviation is seen at low N, where space-charge expansion is negligible and bunch emittance will mostly be determined by accelerator aberrations and effects such as disorder-induced heating [31]. As N increases and space-charge dominates the emittance growth, there is much closer agreement between the experimental results and simulations, with the GS distribution showing the greatest difference. As with the free-expansion results, the discrepancies can be attributed to a combination of the formation of a ring structure, which will be more prominent for distributions created with higher peak 780 nm intensity, and saturation at the center. The separation between experimentally measured FT and HS waists is attributed to the imperfect flat-topped laser profile [Fig. 1(c)(ii)]. Nevertheless, the HS profile again matches very well with the simulations and shows that bunch shaping with a CAEIS can lead to a marked reduction in emittance growth relative to conventional Gaussian bunches.

In this Letter, we have experimentally demonstrated improvement of charged particle beam brightness through control of transverse bunch density distribution. The low temperature of the cold atom source has enabled detailed observation of space-charge effects, for the first time clearly distinguishing the variation in nonlinear growth for different initial particle distributions. For space-charge-dominated bunches with $N = 7.1 \times 10^4$ particles, a reduction in emittance growth of nearly 50% was achieved for a half-spherical rather than Gaussian transverse distribution, corresponding to a brightness increase by a factor of 4. Further improvements in beam brightness are expected if the spatial width of the pulsed blue laser beam is reduced to better satisfy the requirements for a half-spherical pancake distribution to transform into a uniformly filled ellipsoid [13].

The 5 ns ion bunches used for our demonstrations are directly analogous to ultrafast 13 ps electron bunches [27,31] with the same bunch charge. Achieving ultrafast single-shot diffraction will require much higher charge density, and much higher bunch charge such as the $N = 5 \times 10^5$ electron bunches we have previously produced with a cold atom source [32]. The effects of Coulomb-driven emittance growth will then severely limit the beam focus and brightness for unshaped Gaussian

bunches. Indeed, other cold atom sources using ultrafast electron bunches have been limited to a few hundred electrons per bunch due to the degrading effects of space charge, requiring thousands of bunches to create a satisfactory diffraction image [33]. Demonstrating the suppression of space-charge-induced emittance growth through shaping of the initial bunch profile is, therefore, a critical milestone in the development of cold electron sources, necessary for harnessing their inherent coherence, focusability, and brightness to perform single-shot ultrafast diffraction of noncrystalline targets.

B. M. S. acknowledges the support of a University of Melbourne McKenzie Fellowship. This work was supported by the Australian Research Council Discovery Project No. DP140102102.

*scholten@unimelb.edu.au

[1] S. Bernal, H. Li, T. Godlove, I. Haber, R. A. Kishek, B. Quinn, M. Reiser, M. Walter, Y. Zou, and P. G. O'Shea, Phys. Plasmas **11**, 2907 (2004).
[2] R. W. Schoenlein, W. P. Leemans, A. H. Chin, P. Volfbeyn, T. E. Glover, P. Balling, M. Zolotorev, K. Kim, S. Chattopadhyay, and C. V. Shank, Science **274**, 236 (1996).
[3] N. M. Buckanie, J. Göhre, P. Zhou, D. von der Linde, M. Horn-von Hoegen, and F. J. Meyer zu Heringdorf, J. Phys. Condens. Matter **21**, 314003 (2009).
[4] J. Orloff, Rev. Sci. Instrum. **64**, 1105 (1993).
[5] B. J. Siwick, J. R. Dwyer, R. E. Jordan, and R. J. D. Miller, Science **302**, 1382 (2003).
[6] Z. Tao, H. Zhang, P. M. Duxbury, M. Berz, and C.-Y. Ruan, J. Appl. Phys. **111**, 044316 (2012).
[7] F. O. Kirchner, A. Gliserin, F. Krausz, and P. Baum, Nat. Photonics **8**, 52 (2014).
[8] J. C. Williamson, J. Cao, H. Ihee, H. Frey, and A. H. Zewail, Nature (London) **386**, 159 (1997).
[9] L. W. Hardy, J. S. Finer-Moore, W. R. Montfort, M. O. Jones, D. V. Santi, and R. M. Stroud, Science **235**, 448 (1987).
[10] I. D. Kuntz, Science **257**, 1078 (1992).
[11] O. D. Kellogg, *Foundations of Potential Theory* (Springer-Verlag, Berlin, 1929).
[12] I. M. Kapchinskij and V. V. Vladimirskij, in *Proceedings of the International Conference on High Energy Accelerators* (CERN, Geneva, 1959), p. 274.
[13] O. J. Luiten, S. B. van der Geer, M. J. de Loos, F. B. Kiewiet, and M. J. van der Wiel, Phys. Rev. Lett. **93**, 094802 (2004).
[14] P. Musumeci, J. T. Moody, R. J. England, J. B. Rosenzweig, and T. Tran, Phys. Rev. Lett. **100**, 244801 (2008).
[15] J. T. Moody, P. Musumeci, M. S. Gutierrez, J. B. Rosenzweig, and C. M. Scoby, Phys. Rev. ST Accel. Beams **12**, 070704 (2009).
[16] Y. Li, S. Chemerisov, and B. Shen, New J. Phys. **12**, 123011 (2010).
[17] B. O'Shea, J. B. Rosenzweig, G. Asova, J. Bähr, M. Hänel, Y. Ivanisenko, M. Khojoyan, M. Krasilnikov, L. Staykov, F. Stephan *et al.*, Phys. Rev. ST Accel. Beams **14**, 012801 (2011).
[18] R. K. Li, K. G. Roberts, C. M. Scoby, H. To, and P. Musumeci, Phys. Rev. ST Accel. Beams **15**, 090702 (2012).
[19] P. Piot, Y. E. Sun, T. J. Maxwell, J. Ruan, E. Secchi, and J. C. T. Thangaraj, Phys. Rev. ST Accel. Beams **16**, 010102 (2013).
[20] B. J. Claessens, S. B. van der Geer, G. Taban, E. J. D. Vredenbregt, and O. J. Luiten, Phys. Rev. Lett. **95**, 164801 (2005).
[21] A. J. McCulloch, D. V. Sheludko, S. D. Saliba, S. C. Bell, M. Junker, K. A. Nugent, and R. E. Scholten, Nat. Phys. **7**, 785 (2011).
[22] A. J. McCulloch, D. V. Sheludko, M. Junker, and R. E. Scholten, Nat. Commun. **4**, 1692 (2013).
[23] W. J. Engelen, M. A. van der Heijden, D. J. Bakker, E. J. D. Vredenbregt, and O. J. Luiten, Nat. Commun. **4**, 1693 (2013).
[24] N. Debernardi, M. P. Reijnders, W. J. Engelen, T. T. J. Clevis, P. H. A. Mutsaers, O. J. Luiten, and E. J. D. Vredenbregt, J. Appl. Phys. **110**, 024501 (2011).
[25] R. M. W. van Bijnen, C. Ravensbergen, D. J. Bakker, G. J. Dijk, S. J. J. M. F. Kokkelmans, and E. J. D. Vredenbregt, New J. Phys. **17**, 023045 (2015).
[26] T. van Oudheusden, E. F. de Jong, S. B. van der Geer, W. P. E. M. Op't Root, O. J. Luiten, and B. J. Siwick, J. Appl. Phys. **102**, 093501 (2007).
[27] D. Murphy, R. W. Speirs, D. V. Sheludko, C. T. Putkunz, A. J. McCulloch, B. M. Sparkes, and R. E. Scholten, Nat. Commun. **5**, 4489 (2014).
[28] S. B. Van der Geer, M. J. De Loos, and O. J. Luiten, in *European Particle Accelerator Conference: Proceedings* (Genoa, Italy, 2008), Vol. 8, p. 151.
[29] L. Serafini, AIP Conf. Proc. **413**, 321 (1997).
[30] http://www.pulsar.nl/gpt/.
[31] D. Murphy, R. E. Scholten, and B. M. Sparkes, Phys. Rev. Lett. **115**, 214802 (2015).
[32] R. W. Speirs, C. T. Putkunz, A. J. McCulloch, K. A. Nugent, B. M. Sparkes, and R. E. Scholten, J. Phys. B **48**, 214002 (2015).
[33] M. W. van Mourik, W. J. Engelen, E. J. D. Vredenbregt, and O. J. Luiten, Struct. Dyn. **1**, 034302 (2014).

Microsc. Microanal. 20, 1008–1014, 2014
doi:10.1017/S1431927614000774

Microscopy AND Microanalysis

High-Coherence Electron and Ion Bunches From Laser-Cooled Atoms

Ben M. Sparkes, Daniel J. Thompson, Andrew J. McCulloch, Dene Murphy, Rory W. Speirs, Joshua S. J. Torrance, and Robert E. Scholten*

School of Physics, ARC Centre of Excellence for Coherent X-Ray Science, The University of Melbourne, Parkville, VIC 3010, Australia

Abstract: Cold atom electron and ion sources produce electron bunches and ion beams by photoionization of laser-cooled atoms. They offer high coherence and the potential for high brightness, with applications including ultra-fast electron-diffractive imaging of dynamic processes at the nanoscale. The effective brightness of electron sources has been limited by nonlinear divergence caused by repulsive interactions between the electrons, known as the Coulomb explosion. It has been shown that electron bunches with ellipsoidal shape and uniform density distribution have linear internal Coulomb fields, such that the Coulomb explosion can be reversed using conventional optics. Our source can create bunches shaped in three dimensions and hence in principle achieve the transverse spatial coherence and brightness needed for picosecond-diffractive imaging with nanometer resolution. Here we present results showing how the shaping capability can be used to measure the spatial coherence properties of the cold electron source. We also investigate space-charge effects with ions and generate electron bunches with durations of a few hundred picoseconds. Future development of the cold atom electron and ion source will increase the bunch charge and charge density, demonstrate reversal of Coulomb explosion, and ultimately, ultra-fast coherent electron-diffractive imaging.

Key words: ion beam, electron beam, electron diffraction, space charge, cold atom physics, coherence

Introduction

The ultimate goal of X-ray and electron imaging is the ability to create "molecular movies" of the dynamics of atomic-scale processes (Dwyer et al., 2006). Molecular movies, with atomic spatial and temporal resolution, will enable dramatic advances in our understanding of critical phenomena underlying biology, materials sciences, and technological applications. For instance, rational drug design relies on knowing the molecular structure and function of membrane proteins (Pinto et al., 1992), motivating development of many different technologies including billion-dollar X-ray-free electron lasers, which attempt to produce sufficient brightness in an X-ray beam for single-shot imaging of noncrystalline objects (Chapman et al., 2011).

Electrons offer an alternative to very bright X-ray sources, which, in any case, require a bright- and low-emittance electron source. The sample interaction is 10^4–10^6 times stronger for electrons compared to X-rays (Sciaini & Miller, 2011) but electron imaging is limited by the space-charge effect: that is, the Coulomb interaction within an electron bunch that dramatically reduces the source brightness and coherence. Coulomb-driven explosion of the electron bunch can be reversed if the electron bunch has a uniform ellipsoidal distribution (Luiten et al., 2004).

The ability to shape electron bunches into appropriate ellipsoidal distributions is one of the motivations behind the development of a cold atom electron/ion source (CAEIS) (Claessens et al., 2005). Other advantages of a CAEIS include high source coherence due to the low temperature of the electrons and ions, and the promise of high brightness, with up to 10^6 particles/bunch. Here we present an overview of our CAEIS, investigation of space-charge effects, and the creation of ultra-fast cold electron bunches.

Received November 14, 2013; accepted March 21, 2014
*Corresponding author. scholten@unimelb.edu.au

Materials and Methods

Cold Atom Source

In our experiments we laser-cool and trap rubidium-85 atoms. We use an effusive oven to produce hot rubidium, which is then cooled via a Zeeman slower before entering the trapping region. This provides a high-flux source of slow atoms, described in more detail in a study by Bell et al. (2010). The atoms are then confined in a magneto-optic trap (MOT) located between two accelerator plates separated by 50 mm. Using this method, up to 10^9 atoms at $\sim$70 μK can been trapped with a Gaussian width of <1 mm, leading to densities up to 10^{11} cm^{-3}, similar to or greater than other CAEIS experiments (Knuffman et al., 2011; Engelen et al., 2013). Densities of 10^{12} cm^{-3} have been achieved using a dark spot in a sodium MOT (Ketterle et al., 1993). The maximum density is important as it will ultimately limit the number of electrons or ions that can be produced for a region of a certain size. Recently, proposals have been made to use atom beams as opposed to trapped atoms to increase the flux (Kime et al., 2013; Knuffman et al., 2013).

Creating Shaped Bunches

To create electron and ion bunches, a two-stage ionization process is used (Fig. 1b). First, the trapping and cooling lasers, as well as the magnetic fields of the MOT, are turned off. A pulse of laser light resonant with the $F = 3 \rightarrow F' = 4$ transition (780 nm) and duration of order microseconds is then directed onto the atoms perpendicular to the accelerator plates. A 5 ns 480 nm pulsed laser beam is directed onto the excited atoms in a direction parallel to the accelerator plates. The wavelength of the pulsed blue laser can be changed over tens of nanometers to allow for either direct ionization of the already-excited atoms, or to excite them to a high-lying Rydberg state, where the static accelerator field induces field ionization.

The pulsed blue laser is focused into a ribbon of light at the MOT, with a full-width at half-maximum (FWHM) of approximately $\sigma_z = 150\,\mu$m. The size of the blue laser ribbon is important as it will determine the energy spread σ_u of the electrons and ions produced via $\sigma_u = e\sigma_z F$, where e is the fundamental electron charge and F the strength of the accelerating electric field. For a field of 40 kV/m, we obtain $\sigma_u = 6$ meV. The temporal length of the laser pulse determines the bunch length, 10 cm and 3 mm for pulse durations of 5 ns and 150 ps.

The 780 nm excitation laser profile is transformed into an arbitrary shape using a spatial light modulator (SLM). This combination of laser wavelengths and orientations creates the shaped electron and ion bunches, as shown in Figure 1a. Approximately 10^5 electrons were produced in each bunch. The repetition rate of the experiment is 10 Hz, limited by the repetition rate of the pulsed blue laser.

Detection

We select electrons or ions by appropriate choice of polarity for our accelerator front plates (e.g. electrons in Fig. 1a). After constant acceleration, the electrons or ions are propagated for 21.5 cm in a null field, then detected on a phosphor-coupled microchannel plate detector (MCP) and imaged with a CCD camera to provide two-dimensional spatial resolution of the bunch, as shown in Figure 1c. Temporal evolution of the bunch can be determined by monitoring the potential of the grounded component of the MCP.

Results

Temperature and Coherence Length Measurements of Cold Electron Bunches

The temperature of the electron source can be determined from the divergence of the bunches, calculated from the derivative of the edge of the image of the propagated bunch and the propagation distance. Using our ability to shape the excitation laser using a SLM, we produced a beam with sharply defined edges. The edge width before propagation was defined by the resolution of the excitation intensity profile, which in turn is defined by the optical resolution of the excitation laser imaging system, ~10 μm. The transverse thermal velocity of the electron cloud determines the angular spread after propagation (Sheludko et al., 2010):

$$\frac{dQ_e}{dr} = e\kappa \frac{d_1}{2d_1 + d_2} \sqrt{\frac{eF}{d1(k_B T_0 + \Delta E)}}, \qquad (1)$$

where Q_e is the detector signal proportional to charge, r the radial coordinate, e the electron charge, κ the linear magnification, d_1 and d_2 the distances through which the bunch is accelerated and freely propagated, F the accelerator field magnitude, k_B the Boltzmann constant, ΔE the excess energy of the electrons after ionization, and T_0 the minimum electron temperature (i.e., when $\Delta E = 0$). The excess electron energy can be varied by changing the wavelength of the blue laser (Fig. 2a), and the data fitted to equation 1 to determine κ and T_0. The minimum temperature of the electrons was found to be $T_0 < 10 \pm 5$ K (McCulloch et al., 2011) for a bunch containing 10^5 electrons (20 fC). The electron temperature is much higher than the cold atom temperature (70 μK) owing

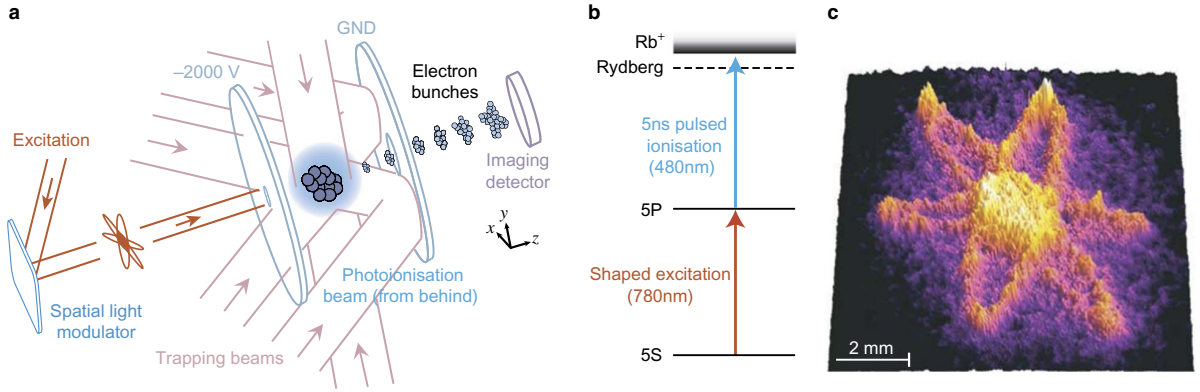

Figure 1. a: Experimental set-up of the cold atom electron/ion source. **b:** Energy-level diagram showing two-stage ionization process. **c:** False-color image of electron cloud detected on microchannel plate detector. From McCulloch et al. (2011).

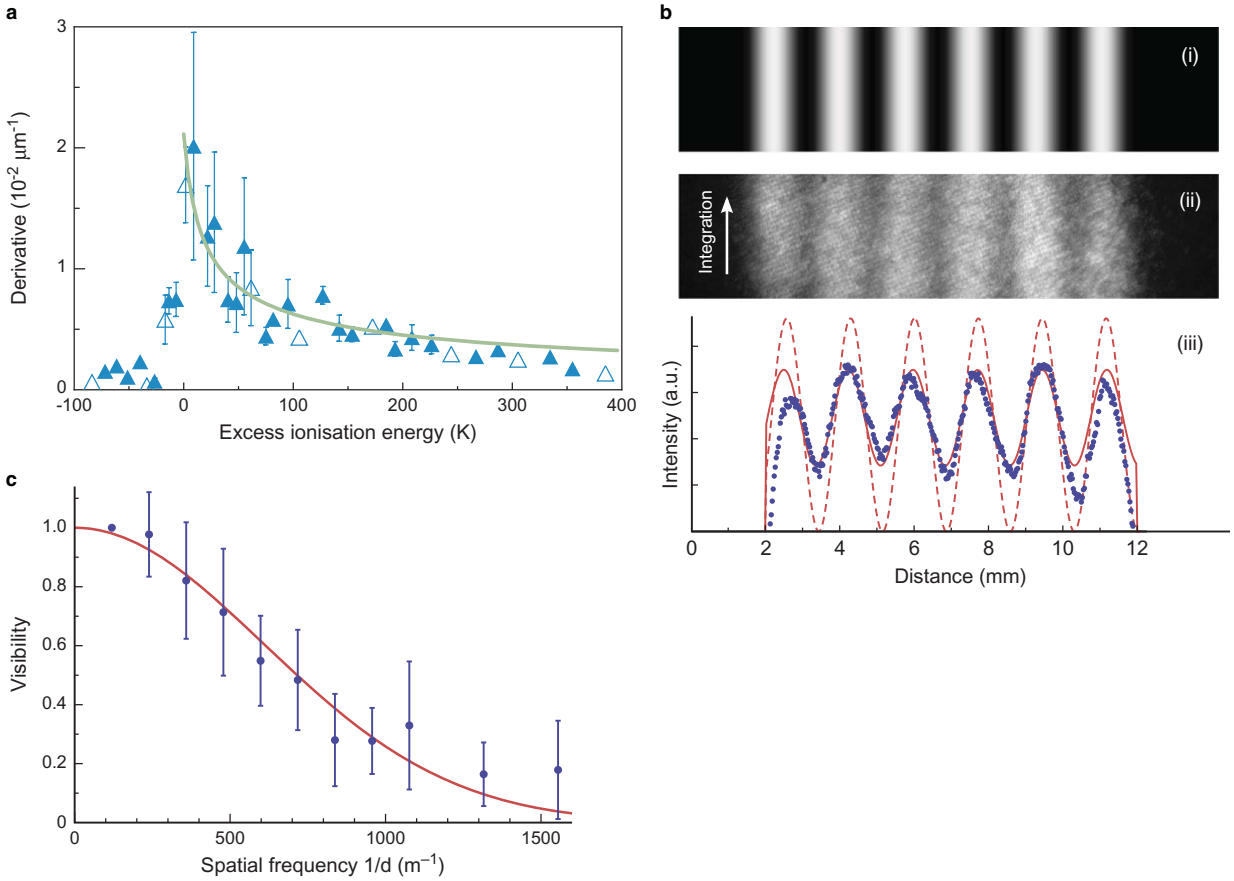

Figure 2. **a:** Measuring electron bunch divergence from edge acuity. Error bars indicate one standard deviation over 30 shots, including statistical and systematic uncertainties. An upper limit to source temperature of $T_0 = 10 \pm 5$ K is extracted for a bunch of 10^5 electrons by fitting equation 1 to the data (solid line) with excess ionization energy $\Delta E_c \geq 0$ K. From McCulloch et al. (2011). **b:** (i) Desired excitation laser beam intensity profile used to create the spatial light modulator phase mask. (ii) Image of resulting shaped electron bunch on microchannel plate detector. (iii) Integrated line profile of the calculated fully coherent electron distribution (red, dashed), the recorded electron image (blue points), and a fit to the recorded data (red, solid). **c:** Visibility of electron bunch pattern as a function of spatial frequency, with a Gaussian fit to the visibility function resulting in $L_c = 7.8 \pm 0.9$ nm. The systematic uncertainty in measuring d was 3%. From Saliba et al. (2012).

to the intrinsic heating processes encountered during ionization, such as disorder-induced heating.

From this minimum temperature we can determine the transverse coherence length of the electron bunch:

$$L_c = \hbar / \sqrt{m_e k_B T_0}, \quad (2)$$

where m_e is the mass of the electron. Using the value for T_0 obtained above gives $L_c > 10 \pm 3$ nm.

The arbitrary shaping ability of the CAEIS can also be used to directly measure the coherence length. This was achieved by using a sinusoidally shaped excitation laser and measuring the visibility of the electron pattern as a function of spatial frequency (Figs. 2b, 2c), resulting in a measurement of $L_c = 7.8 \pm 0.9$ nm following the procedure outlined in a study by Saliba et al. (2012). A coherence length of 10 nm at the source is already sufficient for imaging small biomolecules such as bacteriorhodopsin, where the unit cell length is of order 10 nm. In contrast, high-brightness conventional electron sources based on photoemission, with electron bunch temperatures of order 10^4 K, have an associated coherence length of just 0.3 nm.

Cold atom ion bunch temperatures are on the order of milliKelvins, limited by disorder-induced heating (Bannasch et al., 2013).

Ultra-Fast Cold Electrons

Ultra-fast electron diffraction enables the study of molecular structural dynamics with high resolution at sub-picosecond timescales. This is important for understanding biochemical dynamics such as protein folding and regulation, as well as the formation of cracks in novel materials (Schotte et al., 2003; Sciaini & Miller, 2011). Ultra-fast exposure times will also allow high-intensity imaging of radiation sensitive

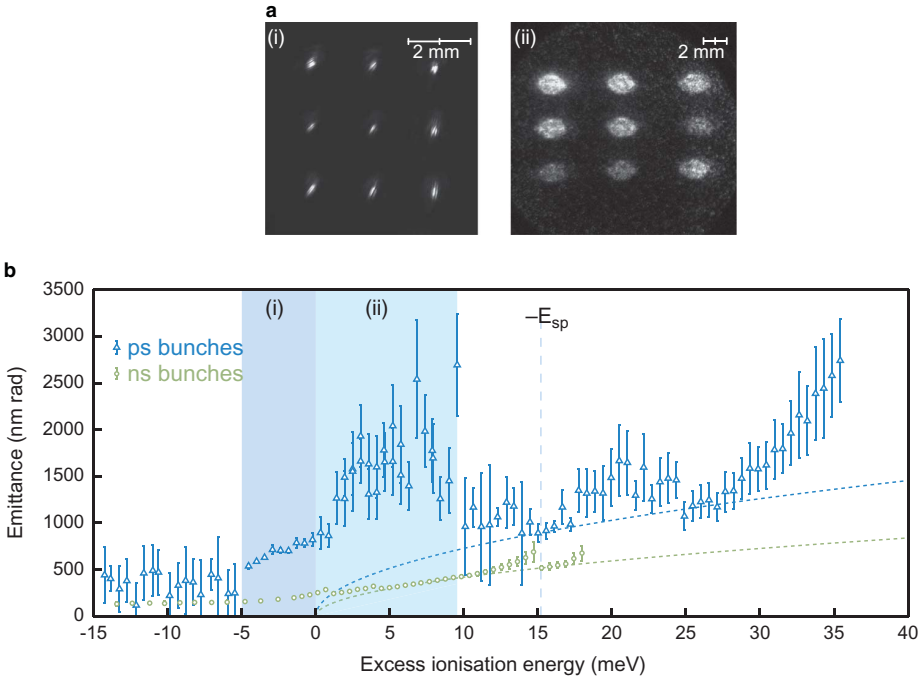

Figure 3. a: Typical pepperpot images used to extract the emittance of femtosecond-excited cold atom electron/ion source electron bunches with a charge of 100 fC. (i) A charge-coupled device image of the laser pulse used to excite the atoms. (ii) Detected electron signal on microchannel plate detector for an ionization wavelength of 478.00 nm. **b:** Measured radial emittance as a function of excess ionization energy. Each point represents 50 single-shot measurements with the error bars indicating one standard deviation combined from the statistical deviation and systematic uncertainties. The dashed lines are theoretical plots of the emittances using the experimentally determined temperature and beam radii [see equation (3)]. For more information see McCulloch et al. (2013).

samples, such as biologically active molecules, to obtain sufficient information about the molecule before it dissociates, known as "diffract-before-destroy" imaging.

To achieve this with our CAEIS, we replaced the continuous wave (CW) 780 nm excitation laser with a femtosecond laser, with a full-width-half-maximum (FWHM) of 40 nm. With femtosecond excitation, the initial electron pulse duration is limited by the spatial and temporal extent of the overlap between the new femtosecond pulses and the 5 ns pulses of 480 nm light. The overlap produces a shaped pulse of electrons or ions with a minimum duration of 150 ps (McCulloch et al., 2013). The charge of the electron bunches produced was 100 fC.

The high bandwidth inherent to short laser pulses might be expected to increase the excess energy spread of the electrons and thus destroy their transverse coherence. We performed an emittance measurement using the pepperpot method. Instead of using a physical pepperpot, we shaped the femtosecond excitation as shown in Figure 3ai and measured the spatial distribution of the electron bunches at the MCP detector. By knowing the initial and final electron beamlet distributions, the emittance ε_γ can be calculated (McCulloch et al., 2013). The pepperpot measurements were performed for a series of different blue laser wavelengths, similar to the temperature measurements discussed in Materials and Methods section, and compared to results with CW excitation.

From the results (Fig. 3b) it can be seen that in region i, just below the field-free ionization threshold, the emittance increases, coinciding with an increase in ionization efficiency and therefore an increase in space-charge effects. In this region the electron bunches that are produced are ultra fast and still highly coherent. Below region i the ionisation efficiency is poor, reflected in the large error bars. In region i the blue laser couples the $5P_{3/2}$ state to one or more field-ionizing Rydberg states, resulting in an electron bunch with minimal spread. Above threshold, in region ii, the emittance increases dramatically owing to the opening of an alternative ionization pathway: when the energy of the ionization laser is above threshold, the blue laser couples the $5P_{3/2}$ state directly to the continuum. In this case the large near-resonant bandwidth of the 780 nm femtosecond pulse substantially increases the energy spread.

As the excess ionization energy increases further, the emittance approaches the theoretical emittance growth function:

$$\varepsilon_r = \sigma_r \sqrt{\frac{k_B T}{m_e c^2}}, \tag{3}$$

where σ is the root mean square bunch width and T the electron temperature. As can be seen, the emittance will

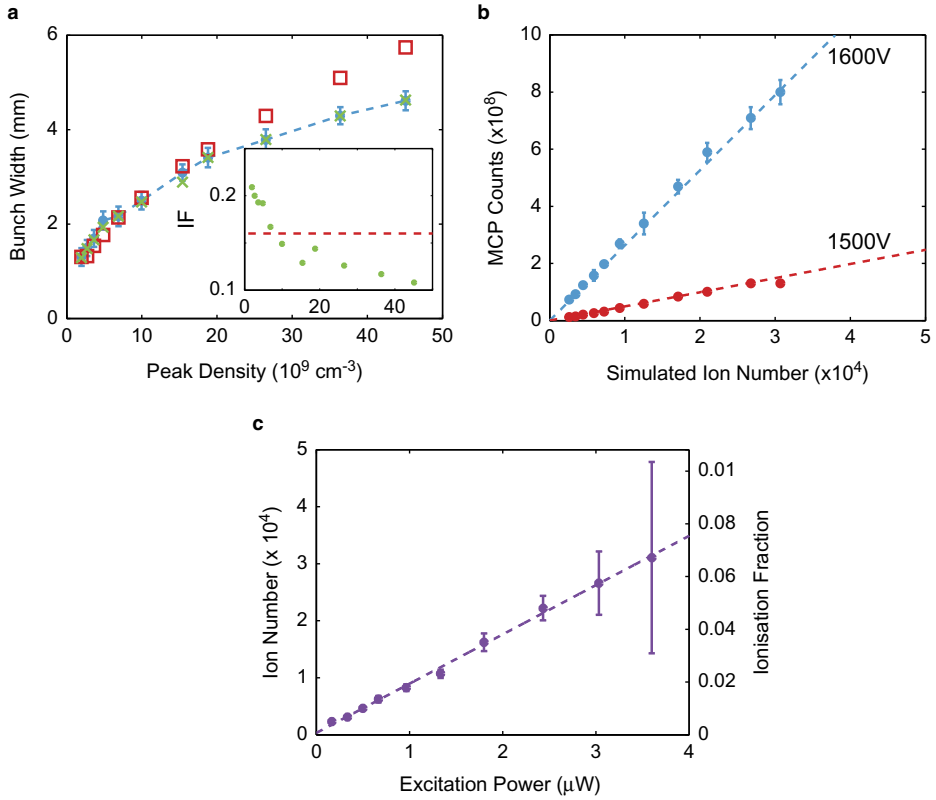

Figure 4. a: Gaussian bunch widths as a function of peak atom density. Blue circles indicate experimental data, with the error bars determined from the standard deviation of ~100 measurements; dashed blue line is to guide the eye; red squares indicate general particle tracer (GPT) simulations determined from the peak density and a 0.16 ionization fraction (IF) within the interaction region determined by the sizes of the excitation and ionization lasers; green crosses indicate GPT simulations with an ionization fraction chosen to match the experimental data. The inset shows the ionization fraction chosen for each density (green points) compared with the 0.16 constant value (red dashed line). **b:** Measured counts from the microchannel plate detector (MCP) as a function of the simulated ion number from the ionization fraction shown in inset of (**a**) for an MCP potential of 1,500 (red) and 1,600 V (blue). Points indicate experimental data, error bars from standard deviation of ~100 measurements and dashed lines indicate linear fit to data. **c:** Ion number, determined using the calibration from (**b**), as a function excitation pulse power for measured data. The right-hand axis shows the ionization fraction, determined from the atom density and ionization laser sizes. Each data point represents 100 single-shot measurements with the error bars indicating one standard deviation combined, the dashed line represents a linear fit to the data.

increase with the temperature of the electron produced, which, in turn, will depend on the excess ionization energy (see Fig. 2a). The difference from this theoretical line is most likely due to space-charge effects or other heating processes that occur during ionization and extraction, which equation 3 does not take into account. This shows that the bandwidth of the femtosecond laser is not contributing appreciably to the energy spread.

Below region i the emittance is approximately constant ($\varepsilon_r = 538 \pm 26$ nmrad), limited by heating during the extraction process. In the same region, the emittance with CW excitation was 141 ± 7 nmrad. Though the femtosecond emittance is larger, the corresponding coherence length is still relatively large for an electron source, at $L_c = 4.0 \pm 0.2$ nm (McCulloch et al., 2013). The difference in emittance and temperature (and therefore coherence length) between the nanosecond and picosecond bunches is because of the increased space-charge repulsion that will occur in a bunch with the same charge but density 30 times greater.

Observing Space-Charge Effects

Space-charge effects within clouds of electrons or ions cause bunch expansion. This is normally an irreversible process and leads to a loss in coherence and brightness. However, if the bunch shape is a uniform ellipsoid then the internal fields are linear, and though the bunch will still expand, the expansion can be reversed by refocusing with conventional linear-charged particle optical systems, preserving the initial coherence and brightness of the source. It has been theoretically shown that an initial bunch with a semi-circular transverse distribution and a very narrow

longitudinal distribution will evolve into a uniform ellipsoid (Luiten et al., 2004).

Creating such a distribution experimentally is challenging. The spatial distribution of the initial bunch depends not only on the excitation beam profile, but also on the initial density of the cold atom cloud, and the time-dependent behavior of the excitation process. We have simulated these effects using optical Bloch equations, and modeled the evolution of the bunch shape using general particle tracer (GPT) simulations (http://www.pulsar.nl/gpt).

We have investigated space-charge effects using ions rather than electrons because of their greater mass and lower velocity and consequently longer interaction times. The ion temperature is also orders of magnitude lower than for electrons, so the effects of thermal diffusion are minimal. In combination, the effects of Coulomb interactions within the bunch are much more clearly discernible.

By increasing the delay between the time when the MOT fields are turned off and the ionization beams are turned on, we are able to study the effect of atomic density on space-charge expansion of the ion bunches by making use of the thermal expansion of the atomic cloud, this is shown in Figure 4a, which shows the bunch size for varying initial density. As expected, as the atomic density increases the bunch width also increases, in good agreement with GPT simulations for a fixed ionization fraction of 0.16 (Fig. 4a), up to a density of around $3 \times 10^{10}\,\mathrm{cm}^{-3}$. At higher density, we postulate that the reduced ionization fraction seen experimentally is because of absorption of some of the excitation beam by the atoms at the leading edge of the atom cloud, outside the interaction region, reducing the number of photons in the interaction region available to ionize the atoms and therefore reducing space-charge effects. The inset to Figure 4a shows the individual ionization fraction that best matched simulation and data for each initial atomic density.

By matching the simulations to the space-charge expansion data we have been able to calibrate the detection system to determine the ion number from the counts measured by the phosphor-coupled MCP and CCD imaging system. This was achieved by comparison of the integrated counts recorded on the CCD with the ion number used in GPT to obtain the correct bunch width shown in Figure 4a. The calibration is shown in Figure 4c for two different detector potentials. In both cases the R^2 coefficient was >0.99, indicating a strong linear relationship between the MCP counts and the simulated number of ions. We examined the effect between ion number and excitation power further at low power (well below the saturation limit of ~10 mW) to illustrate how absorption of the excitation laser outside the interaction laser could lead to a reduction in ion number. As can be seen from Figure 4c, the ion number (calculated with the calibration obtained from Fig. 4b) increases linearly with excitation power. We also calculated the ionization fraction using the sizes of the ionization beams and the peak atomic density of the MOT.

Our investigations have also led to the discovery of some interesting effects such as the formation of density waves around an initially uniform circular ion bunch. This can be explained by the formation of a diffuse halo of charges around the central core of the bunch. The halo is created by reabsorption of spontaneous emission from the directly excited atoms. The dense core then expands into the halo, due to space-charge repulsion, and creates a high-density ring. We have also investigated the space-charge interaction of parallel beamlets to see the influence of overlapping self-fields. Our studies show good agreement between simulations and experiments. The simulations reveal the sensitivity of the visibility of the high-density features to the initial ion temperature: the structure is lost at temperatures of a few tens of Kelvin, highlighting the advantages of the cold atom source in comparison with conventional sources, which operate at room temperature or above, for studying these effects.

Discussion

We have presented our CAEIS, including characterization of the temperature of the source and the corresponding transverse coherence lengths of the electron bunches. We have also investigated the effect of space charge on ion bunches as an analog to the much faster expansion of electron bunches, showing substantial space-charge effects. One of our main priorities is to overcome the space-charge expansion using the unique beam-shaping ability of cold atom sources to produce uniform ellipsoidal bunches. Our shaping ability is currently limited by speckle in the excitation beam image produced from the SLM owing to the hologram-production algorithm used. Overcoming this will involve implementing alternate algorithms and feedback control over the phase pattern on the SLM, by monitoring the excitation laser profile with an independent imaging detector.

Apart from space charge, another phenomenon limiting the minimum temperature of the ions produced from the CAEIS is disorder-induced heating. Nonuniform Coulomb interactions of the initially randomly distributed electrons and ions leads to an initial spread in the temperature of the bunch. For ions, this increases the temperature of the bunch by at least an order of magnitude (Bannasch et al., 2013). One way of overcoming disorder-induced heating is to use the phenomenon of Rydberg blockade, where the van der Waals' potential caused by an atom in a highly excited state prohibits nearby atoms from also being excited (Bannasch et al., 2013; Robert-de Saint-Vincent et al., 2013). We have recently developed an alternative blue laser system using a frequency locking scheme based on electromagnetically induced transparency (Abel et al., 2009). With this new laser we have produced preliminary results demonstrating blockade behavior with the 30S state and measurements of the temperature effects are in progress.

By overcoming both space-charge and disorder-induced heating effects we should be able to produce ion bunches capable of sub-nanometer resolution (van der Geer et al., 2007).

Conclusion

We have developed a CAEIS with the ultimate goal of producing single-shot electron diffraction of biological samples.

On the path to producing these we have developed a source with a coherence length of ~10 nm with electron temperature of 10 K. By using a femtosecond pulsed laser we have also produced ultra-fast bunches with a minimum duration of 150 ps, with a maximum coherence length of 4 nm. We have shown that space-charge effects are readily observable without the obfuscation of thermal diffusion, potentially providing a new approach to investigating subtle Coulomb interactions in high-current-charged particle sourcs. Finally, we have investigated the effects of space charge on the ion bunches produced with our system, and observed the formation of surprising structures. To improve the emittance and brightness of the source further, we are investigating reducing the temperature by using Rydberg blockade to overcome disorder-induced heating effects, and using our shaping ability to overcome space-charge effects. By implementing these advances, single-shot ultra-fast coherent-diffractive imaging with nanoscale resolution should become feasible, allowing for the creation of "molecular movies."

Acknowledgments

We thank D. V. Sheludko for his technical assistance. This work was supported by the Australian Research Council Discovery Project DP10960625.

References

Abel, R.P., Mohapatra, A.K., Bason, M.G., Pritchard, J.D., Weatherill, K.J., Raitzsch, U. & Adams, C.S. (2009). Laser frequency stabilization to excited state transitions using electromagnetically induced transparency in a cascade system. *Appl Phys Lett* **94**, 071107.

Bannasch, G., Killian, T.C. & Pohl, T. (2013). Strongly coupled plasmas via Rydberg blockade of cold atoms. *Phys Rev Lett* **110**, 253003.

Bell, S.C., Junker, M., Jasperse, M., Turner, L.D., Lin, Y.-J., Spielman, I.B. & Scholten, R.E. (2010). A slow atom source using a collimated effusive oven and a single-layer variable pitch coil Zeeman slower. *Rev Sci Instrum* **81**, 013105.

Chapman, H.N., Fromme, P., Barty, A., White, T.A., Kirian, R.A., Aquila, A., Hunter, M.S., Schulz, J., DePonte, D.P., Weierstall, U., Doak, R.B., Maia, F.R.N.C., Martin, A.V., Schlichting, I., Lomb, L., Coppola, N., Shoeman, R.L., Epp, S.W., Hartmann, R., Rolles, D., Rudenko, A., Foucar, L., Kimmel, N., Weidenspointner, G., Holl, P., Liang, M., Barthelmess, M., Caleman, C., Boutet, S., Bogan, M.J., Krzywinski, J., Bostedt, C., Bajt, S., Gumprecht, L., Rudek, B., Erk, B., Schmidt, C., Hömke, A., Reich, C., Pietschner, D., Strüder, L., Hauser, G., Gorke, H., Ullrich, J., Herrmann, S., Schaller, G., Schopper, F., Soltau, H., Kühnel, K.-U., Messerschmidt, M., Bozek, J.D., Hau-Riege, S.P., Frank, M., Hampton, C.Y., Sierra, R.G., Starodub, D., Williams, G.J., Hajdu, J., Timneanu, N., Seibert, M.M., Andreasson, J., Rocker, A., Jönsson, O., Svenda, M., Stern, S., Nass, K., Andritschke, R., Schröter, C.-D., Krasniqi, F., Bott, M., Schmidt, K.E., Wang, X., Grotjohann, I., Holton, J.M., Barends, T.R.M., Neutze, R., Marchesini, S., Fromme, R., Schorb, S., Rupp, D., Adolph, M., Gorkhover, T., Andersson, I., Hirsemann, H., Potdevin, G., Graafsma, H., Nilsson, B. & Spence, J.C. (2011). Femtosecond X-ray protein nanocrystallography. *Nature* **470**, 73–77.

Claessens, B., van der Geer, S., Taban, G., Vredenbregt, E. & Luiten, O. (2005). Ultracold electron source. *Phys Rev Lett* **95**, 164801.

Dwyer, J.R., Hebeisen, C.T., Ernstorfer, R., Harb, M., Deyirmenjian, V.B., Jordan, R.E. & Miller, R.J.D. (2006). Femtosecond electron diffraction: "Making the molecular movie". *Phil Trans R Soc A* **364**, 741–778.

Engelen, W.J., van der Heijden, M.A., Bakker, D.J., Vredenbregt, E.J.D. & Luiten, O.J. (2013). High-coherence electron bunches produced by femtosecond photoionization. *Nat Commun* **4**, 1693.

Ketterle, W., Davis, K.B., Joffe, M.A., Martin, A. & Pritchard, D.E. (1993). High densities of cold atoms in a dark spontaneous-force optical trap. *Phys Rev Lett* **70**, 2253–2256.

Kime, L., Fioretti, A., Bruneau, Y., Porfido, N., Fuso, F., Viteau, M., Khalili, G., Šantić, N., Gloter, A., Rasser, B., Sudraud, P., Pillet, P. & Comparat, D. (2013). High-flux monochromatic ion and electron beams based on laser-cooled atoms. *Phys Rev A* **88**, 033424.

Knuffman, B., Steele, A.V. & McClelland, J.J. (2013). Cold atomic beam ion source for focused ion beam applications. *J Appl Phys* **114**, 044303.

Knuffman, B., Steele, A.V., Orloff, J. & McClelland, J.J. (2011). Nanoscale focused ion beam from laser-cooled lithium atoms. *J Phys* **13**, 103035.

Luiten, O., van der Geer, S., de Loos, M., Kiewiet, F. & van der Wiel, M. (2004). How to realize uniform three-dimensional ellipsoidal electron bunches. *Phys Rev Lett* **93**, 94802.

McCulloch, A.J., Sheludko, D.V., Junker, M. & Scholten, R.E. (2013). High-coherence picosecond electron bunches from cold atoms. *Nat Commun* **4**, 1692.

McCulloch, A.J., Sheludko, D.V., Saliba, S.D., Bell, S.C., Junker, M., Nugent, K.A. & Scholten, R.E. (2011). Arbitrarily shaped high-coherence electron bunches from cold atoms. *Nat Phys* **7**, 785–788.

Pinto, L.H., Holsinger, L.J. & Lamb, R.A. (1992). Influenza virus M2 protein has ion channel activity. *Cell* **69**, 517–528.

Robert-de Saint-Vincent, M., Hofmann, C.S., Schempp, H., Günter, G., Whitlock, S. & Weidemüller, M. (2013). Spontaneous avalanche ionization of a strongly blockaded Rydberg gas. *Phys Rev Lett* **110**, 045004.

Saliba, S.D., Putkunz, C.T., Sheludko, D.V., Mcculloch, A.J., Nugent, K.A. & Scholten, R.E. (2012). Spatial coherence of electron bunches extracted from an arbitrarily shaped cold atom electron source. *Opt Exp* **20**, 3967–3974.

Schotte, F., Lim, M., Jackson, T.A., Smirnov, A.V., Soman, J., Olson, J.S., Phillips, G.N., Wulff, M. & Anfinrud, P.A. (2003). Watching a protein as it functions with 150-ps time-resolved X-ray crystallography. *Science* **300**, 1944–1947.

Sciaini, G. & Miller, R.J.D. (2011). Femtosecond electron diffraction: Heralding the era of atomically resolved dynamics. *Rep Prog Phys* **74**, 096101.

Sheludko, D.V., McCulloch, A.J., Jasperse, M., Quiney, H.M. & Scholten, R.E. (2010). Non-iterative imaging of inhomogeneous cold atom clouds using phase retrieval from a single diffraction measurement. *Opt Exp* **18**, 623–626.

van der Geer, S.B., Reijnders, M.P., de Loos, M.J., Vredenbregt, E.J.D., Mutsaers, P.H.A. & Luiten, O.J. (2007). Simulated performance of an ultracold ion source. *J Appl Phys* **102**, 094312.